UV Photodesorption and photoconversion of interstellar ices: the laboratory perspective

Bulak, M.

Citation

Bulak, M. (2021, December 9). *UV Photodesorption and photoconversion of interstellar ices: the laboratory perspective*. Retrieved from https://hdl.handle.net/1887/3245781

UV Photodesorption and Photoconversion of Interstellar Ices

- the laboratory perspective

Michał Bulak

UV Photodesorption and Photoconversion of Interstellar Ices

- the laboratory perspective

Proefschrift

ter verkrijging van
de graad van Doctor aan de Universiteit Leiden,
op gezag van rector magnificus prof.dr.ir. H. Bijl,
volgens besluit van het college voor promoties
te verdedigen op donderdag 9 december 2021
klokke 10:00 uur
door

Michał Bulak

Born in Zamosc, Poland
in 1992

Promotiecommissie

Promotores: Prof. dr. H. V. J. Linnartz
Prof. dr. A. G. G. M. Tielens

Overige leden: Prof. dr. H. J. A. Röttgering
Prof. dr. P. van der Werf
Prof. dr. P. Caselli (Max-Planck-Institute for Extraterrestrial Physics)
Dr. M. Bertin (Sorbonne Université)
Dr. S. Ioppolo (Queen Mary University of London)

CONTENTS

1 | INTRODUCTION

Until 1992, our knowledge about planets was limited to the nine planets (at that time) in our Solar System (Wolszczan & Frail 1992). Since then, our view of stellar systems has been revolutionized by detections of thousands of planets surrounding other stars. These exo-planets exhibit an incredible diversity, in terms of size, composition, and distance to their star, illustrated in Figure 1.1. The characteristics of these new distant worlds significantly defy the known extremities: gas giants larger than Jupiter, planets locked in permanent freeze or extremely hot rocky bodies with their surface covered in hot lava. Among these, are also planets which are Earth-like, with a similar rocky composition and a temperature allowing to sustain liquid water. This invites to revisit the questions asked since the dawn of times: is it possible that life originated on other planets as well?
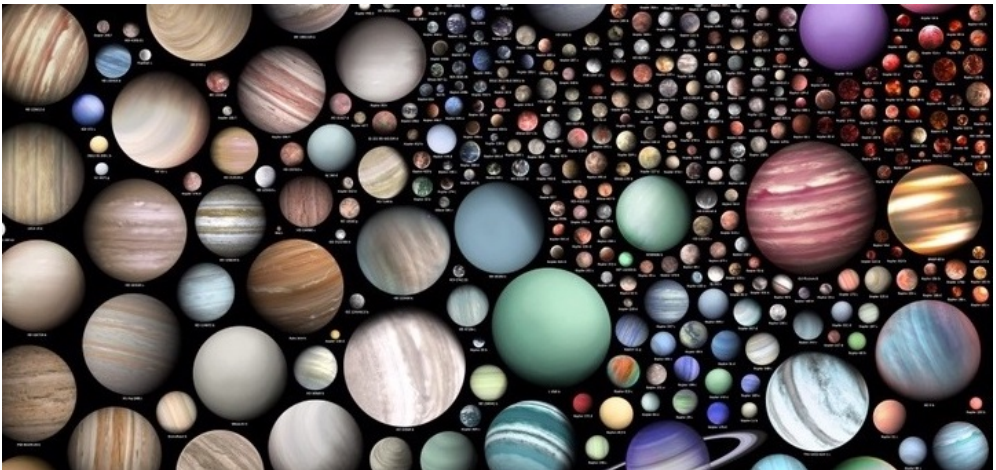
Figure 1.1: Diversity of worlds. Recreated with permission from the artist: Martin Vargic.

To address this question, it is important to understand the chemical evolution of matter during the process of star and planet formation. This process starts already in the large and highly dilute interstellar clouds that fill the space between stars. The subsequent formation of prestellar cores and protoplanetary disks ultimately results in the formation of a young stellar object surrounded by one or more newly born planets. More specifically, we need to understand how the physical conditions along this evolutionary track govern chemical processes that result in the molecular species that

are needed to create life, as we know it, e.g. small molecules like water, but also more complex organic molecules, like sugars and amino acids.

The interstellar medium (ISM) consists of regions which can be linked to particular stages of a star formation cycle, beginning in molecular clouds. The relevant local physical conditions span a wide range in density (10^2 - 10^6 particles cm^{-3}), temperature (10 - 10^3 K), and exposure to different types of radiation and particles (cosmic rays, ultraviolet (UV) photons, free atoms and energetic electrons). These conditions determine the ongoing chemistry, both in the gas phase and in the solid state, that is in icy mantles that cover the surface of micrometer sized dust grains. Such icy grains provide a chemical reservoir that also acts as a catalyst for surface reactions. These involve mostly radicals, which are produced upon 'energetic' processing, or via hydrogen addition and abstraction reactions (referred to as 'non-energetic' processing). The balance in molecular abundances between ice and gas phase is controlled by accretion and desorption processes, and the latter are triggered by an increase in temperature (sublimation), or via non-thermal mechanisms: photodesorption, electron stimulated desorption, or a release of energy following a chemical reaction (e.g. Hollenbach et al. 2009; Thrower et al. 2010; Acharyya et al. 2020).

Radiation from the interstellar radiation field, typically in the vacuum-UV (VUV), or at later stages emitted by young stellar objects, plays a special double-sided role at each stage of the stellar evolution cycle. It can cause molecules to fragment (dissociation), with the resulting fragments reacting to form other molecules and increasing the chemical complexity in the ice (photoconversion, see Herbst & van Dishoeck 2009), or it triggers a non-thermal desorption of ice mantles. This thesis provides an experimental study to quantitatively determine the role of VUV radiation on interstellar ice analogues, in the context of the early stages of the stellar formation cycle. Topics that are discussed focus on the formation of new complex molecules, accurate photodesorption rates as well as an explanation for the large amounts of molecular oxygen ice found on comets in our solar system.

1.1   Ices during star formation sequence

The composition of the ISM is divided by mass, between gas (99%) and dust (1%). The gas-phase component is dominated by hydrogen and helium, with only a small fraction of heavier elements ($\sim$0.1%). The dust grains are mostly made of silicates or carbonaceous material with their sizes varying between 10 nm - 0.5 μm. Billions of stars in our Galaxy participate in a continuous recycling of this material in the ISM. The stars (and planets) are formed from the available matter, through gravitational collapse of a large interstellar cloud, and after a number of evolutionary stages (prestellar core, protoplanetary disk and planetary system) matter is ejected back into the ISM when a star explodes at the end of its life. Depending on the size of the star, this process can span periods ranging from several hundred millions of years up to several tens of billions of years. The formation and evolution of the low-mass stars (less than two solar masses) has been previously described in detail (Shu et al. 1987; Draine 2010; Tielens 2005) and the results presented in this thesis concern processes along this evolutionary track. The processes taking place during high mass star formation differ to some extent (Zinnecker & Yorke 2007).
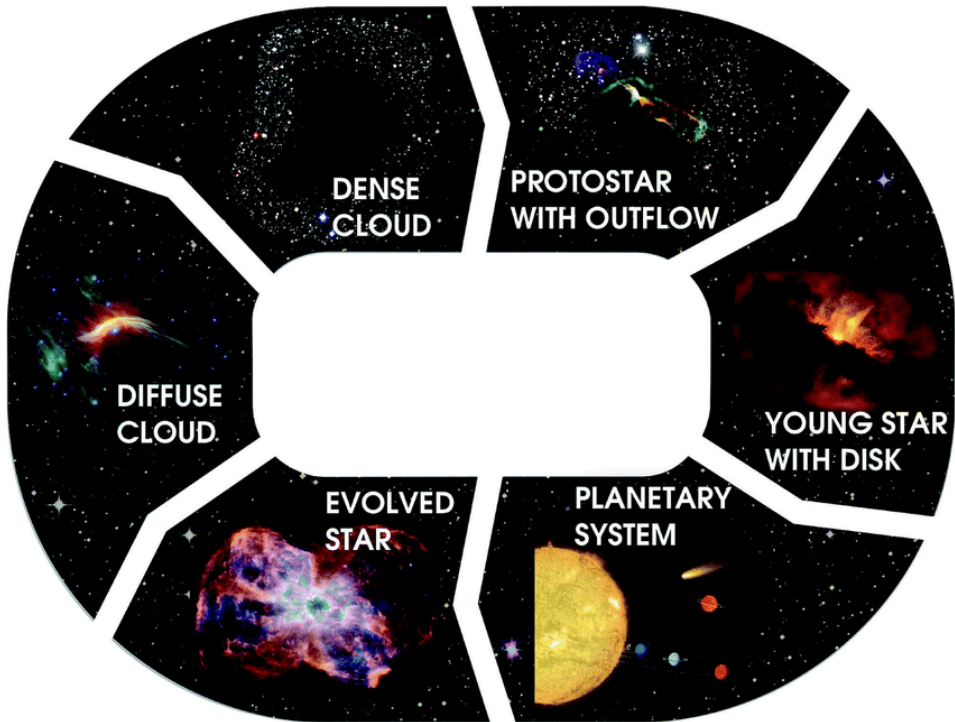
Figure 1.2: Recycling of matter in the ISM during the star and planet formation sequence. Credit: M. Persson, NASA/ESA/ESO/ALMA

The main stages of the stellar formation cycle for a solar-type system are represented in Figure 1.2. The cycle begins in molecular clouds, which can be further divided based on their density, between diffuse, translucent and dense dark clouds. The diffuse clouds have a typical density of 50 - 100 particles cm^{-3}, and a visual extinction (A_V) of less than 1 ($A_V < 1$ mag, where 1 mag = 2.5 times reduction of intensity), allowing the interstellar radiation field (ISRF) to penetrate the cloud. The ISRF represents the average radiation in a galaxy, with multiple components including stellar UV radiation between 6 - 13.6 eV, with a photon flux equal to 10^7 cm^{-2}s^{-1} (Mathis et al. 1983). The interstellar medium is also pervaded by cosmic rays, energetic (>10 MeV/nucleon) particles (Gredel et al. 1989). The diffuse cloud composition is a mixture of bare dust grains with mostly atomic (H, C, O, N) and ionic species (C$^+$), and weak traces of simple molecules, such as H$_2$, CO and H$_2$CO (Snow & McCall 2006; Liszt & Lucas 2001). It is likely that also larger species reside in these clouds, giving rise to diffuse interstellar bands (DIBs), which remain largely unassigned (Snow 2013).

Density fluctuations within a diffuse cloud (e.g., upon stellar winds or supernovae explosions) lead to local over-density regions, where gravity starts playing a role. The result is a dense, gravitationally bound cloud with its interior shielded from the external UV radiation. The local physical parameters with the densities around 10^3 - 10^4 cm^{-3}, A_V of 1 - 5, and temperatures around 10 - 20 K, are typical for a dense

molecular cloud. The low temperature results in a gradual freeze-out of atomic and molecular species on top of dust grains, that also start reacting with each other. This marks the onset of interstellar ice formation, which has a profound impact on the chemical inventory available during star formation, discussed further in Section 1.3 (Herbst & van Dishoeck 2009). In parallel, a low temperature gas-phase chemistry largely based on ion-molecule and radical-radical reactions results in the formation of diverse species (Bergin & Tafalla 2007). The chemical composition at this stage is regulated by UV radiation, which results in a competition between molecular dissociation and formation (Bergin et al. 2004). The edge of dense clouds, fully exposed to the ISRF, is referred to as a photon dominated region (PDR). At its front only atomic and ionic species survive, however, behind the front, efficient gas-phase chemistry results in molecular complexity (Hollenbach & Tielens 1997; Guzmán et al. 2014).

The inner region of the dense cloud reaches a density above 10^5 cm^{-3} and cools down to temperature of 10 K (Pagani et al. 2007). This substructure is referred to as a cloud core, and it is where the star will eventually form. Under these physical conditions, all species, except for H and H$_2$, rapidly freeze-out on top of the dust grains, forming multilayered icy mantles. The low temperature gas-phase chemistry continues, however, it is accepted that for these conditions with generally low gas-phase reaction efficiencies, the chemical evolution is largely steered by solid state processes, that is reacting molecules that are part of the icy mantles coating small dust grains. Solid state astrochemical reactions within the dense clouds can take place upon impacting particles (atoms, electrons, cosmic rays) or upon UV photolysis. The external UV field does not penetrate the dense cloud, however, there exists an alternative source of VUV photons. The interactions of cosmic rays with molecular hydrogen lead to its ionization or excitation. This creates a cascade of secondary electrons as well as VUV photons, generating a so-called secondary UV field. The VUV spectral energy distribution includes a strong Ly-α emission at 121.6 nm, a large number of discrete H$_2$ lines and a broad molecular emission between 140 and 165 nm (Prasad & Tarafdar 1983). The cosmic ray-generated photon flux in dense clouds is a few orders of magnitude lower compared to ISRF, and equals (1-10) $\times$ 10^3 cm^{-2}s^{-1} (Gredel et al. 1989; Shen et al. 2004a). The interactions of the VUV photons, with the icy mantles results in a number of processes, introduced in more detail in section 1.3.2, and these are discussed throughout this thesis.

As the dense core becomes more massive (density of 10^5 - 10^7 cm^{-3}), it becomes opaque and starts to heat up as gravitational collapse occurs. The resulting protostar is surrounded by a debris disk, comprising of leftover dust and gas that carries the chemical inheritance from the diffuse and dense cloud stages, all embedded within a large molecular envelope. In order to preserve angular momentum, disk formation is accompanied with perpendicular outflows. At this point, the cloud character of the region is lost and the object is referred to as a young stellar object (YSO). The newly formed protostar emits infrared radiation and rapidly heats up its surrounding to a temperature above 100 K, which triggers a complete sublimation of the nearby icy mantles. This region around a low mass protostar is referred to as a hot corino (for high mass stars it is called a hot core). Over the last few decades a highly diverse chemical complexity has been found towards these sources, based on gas phase identifications. It is generally assumed that these species, or at least a substantial fraction provides a good representation of the chemical composition of icy mantles (for an overview, see Jørgensen et al. 2016; Drozdovskaya et al. 2019).

Over the following 1 - 10 millions of years the protostellar system evolves and the remaining material from the molecular envelope is either dispersed of accreted. This leaves a pre-main sequence star surrounded by a protoplanetary disk. The chemical composition of the disk is of great interest, as it determines the chemical inventory available for planets. This includes access to water and molecules relevant for life (reviews by Williams & Cieza 2011; Öberg & Bergin 2021). The chemical structure of the protoplanetary disks is less known due to their compactness, and weak molecular emission, however, some smaller complex organic molecules have already been detected, such as CH_3OH and CH_3CN (Öberg et al. 2015; Walsh et al. 2016; Booth et al. 2021). These detections demonstrate that species linked to prebiotic molecules are present at the onset of planet formation. Their origin, however, is not firmly constrained (Drozdovskaya et al. 2014). The leftover material, which does not get incorporated into planets and their moons, ends up in other celestial bodies, such as comets, asteroids, or boulders and dust. In particular comets are very interesting objects, as these are frozen remnants of the protoplanetary disks, and provide the most pristine view on the chemical composition of the Solar System (Mumma & Charnley 2011).

Depending on how massive the star is, it can live for several billions of years. Once the star burns through most of its fusion material, its outer atmosphere becomes a factory ejecting dust and other species back into the interstellar medium. This material provides the (chemically enriched) constituents required for the next generation of stars to be formed.

1.2   Interstellar ices

The focus in this thesis is on interstellar ices. Their presence has been first proposed by Eddington (1937), however it was not until the 1970s, when the first solid state signature of water was identified (Gillett & Forrest 1973). Since then, astronomical observations of ices on interstellar dust grain surfaces, and combined with dedicated laboratory data, allowed to identify other components of interstellar ices in various stages of star formation sequence. The dominating components of interstellar ices, as shown in Figure 1.3, include: H_2O, CO_2, CO, CH_4, CH_3OH, and NH_3. Some other constituents are less abundant or still under debate (see Table 1.1). It is expected that with the upcoming James Webb Space Telescope (JWST) mission, new ice constituents will be identified, possibly also including complex organic molecules. This is important, as the interstellar ice species are subject to energetic and non-energetic processing, and it is generally expected that this transforms simple solid state precursors into larger species, but observational evidence is still lacking (e.g. Terwisscha van Scheltinga et al. 2018). In addition, the desorption of species present in the ice via thermal and non-thermal mechanisms affects the ice-gas balance in the ISM.

1.2.1   Ice demographics

The identification and determination of abundances of interstellar ice components relies on infrared absorption spectroscopy. Species present in the ices absorb the light emitted by a background source, such as a protostar (or YSO), at molecule-specific wavelengths in the near- and far- infrared regime. Each molecule has a series of char-
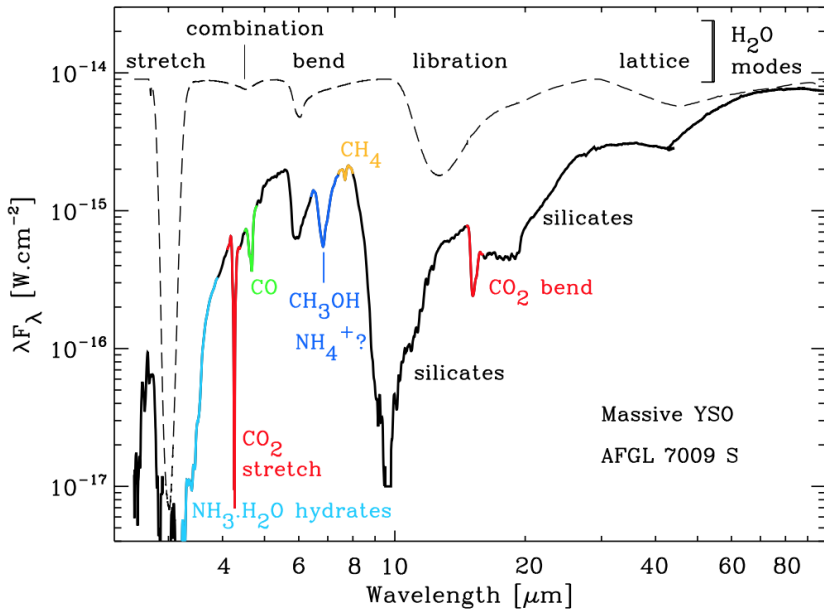
Figure 1.3: An ice spectrum towards the massive YSO AFGL 7009S, published by Boogert et al. (2015). The major interstellar ice components are identified with the marked vibrational modes. A complete vibrational signature of pure H_2O ice is shown at the top of the figure.

acteristic absorption features, the molecular spectrum, that in the infrared region corresponds to the excitation of intrinsic vibrational modes. In the ice, the molecules are immobilized, hence only (hindered) vibrations are possible, which are excited by the infrared radiation (e.g. Hagen et al. 1980; Gerakines et al. 1995; Gibb et al. 2004). In principle, it is also possible to investigate electronic transitions in ices (e.g. Bouwman et al. 2009), but recent applications involve mainly polycyclic aromatic hydrocarbons (PAHs) and this is beyond the scope of this thesis.

Ground observations of ices in the IR are obstructed by the strong telluric pollution of atmospheric H_2O and CO_2. This can be overcome by using space-based or air-born telescopes. The Infrared Space Observatory (ISO) and the Spitzer Space Telescope (SST), have opened up the required infrared spectral windows, in the range of 2.3 - 200 μm (see e.g., Whittet et al. 1996; Gibb et al. 2000, 2004), and 3 - 37 μm, respectively (see e.g., Boogert et al. 2008; Öberg et al. 2011a; Boogert et al. 2015). The interpretation of the resulting astronomical observations was only possible following accurate laboratory experiments recording interstellar ice spectra for different species and for different temperatures (e.g. Hudgins et al. 1993; Gerakines et al. 1995; Ehrenfreund et al. 1996; Bisschop et al. 2007a; Terwisscha van Scheltinga et al. 2018). Currently, many of the available ice data are summarized and available online through the Leiden Database for Ice[1] or NASA Goddard Cosmic Ice Laboratory IR spectra database[2].

A typical ice absorption spectrum collected towards a YSO is shown in Figure 1.3, with clear assignments of features to the main components of the interstellar ices, as

---

[1]https://icedb.strw.leidenuniv.nl
[2]https://science.gsfc.nasa.gov/691/cosmicice/spectra.html

Table 1.1: Interstellar ices and (a range of) their abundances normalized to the water ice column density (in %).

	Species	MYSOs	LYSOs	Mol. clouds	Comets
Secure	H_2O	100	100	100	100
	CO	3 - 26	<3 - 85	9 - 67	0.4 - 30
	CO_2	11 - 27	12 - 50	14 - 43	4 - 30
	CH_3OH	3 - 31	<1 - 25	<1 - 12	0.2 - 0.7
	NH_3	∼7	3 - 10	<7	0.2 - 1.4
	CH_4	1 - 3	1 - 11	<3	0.4 - 1.6
Likely	OCN^-	0.1 - 1.9	<0.1 - 1.1	<0.5	-
	H_2CO	∼2 - 7	∼6	-	0.11 - 1.0
	OCS	0.03 - 0.16	<1.6	<0.22	0.1 - 0.4
Possibly	HCOOH	<0.5 - 6	<0.5 - 4	<2	0.06 - 0.14
	CH_3CH_2OH	<0.5 - 6	<0.5 - 4	<2	0.06 - 0.14
	$HCOO^-$	0.3 - 1.0	∼0.4	<0.1	-
	NH_4^+	9 - 34	4 - 25	4 - 13	-
	SO_2	<0.9 - 1.4	∼0.2	-	0.2
	PAH	∼8	-	-	-
	O_2	<15	<39	-	2 - 5.4[a]
	H_2O_2	<2 - 17	-	-	-
	CH_3CN	-	-	-	0.008 - 0.04[a]
	N_2	-	-	<0.2 - 60	0.07 - 0.11[a]

Notes. The table is adapted from Boogert et al. (2015) and references therein, with added cometary ice abundances from Rubin et al. (2019) ([a]) and references therein; upper limit values are marked by "<" signs.

well as "likely" and "possibly" identified carriers (Boogert et al. 2015). To securely identify a constituent of an interstellar ice, its observational spectrum should provide an excellent fit to the laboratory data. This is often challenging due to the large width of ice absorption features in the solid state and an overlap of typical vibrational modes (e.g., C-H or C-O stretching mode), originating from different species and complicating unambiguous identifications. This problem increases with increasing molecule size. Moreover, there is an uncertainty in the exact position of absorption features as these shift depending on the ice morphology (ice composition and ice structure and temperature). Finally, the derived ice column density needs to be balanced with the gas-phase abundance. Species which are "likely" in the ice mantle, such as OCN^-, require only one securely identified band, however, their complete signature needs to fit into the full absorption spectrum along with the derived abundances. The "possibly" identified species, such as CH_3CN or PAHs, lack a convincing full profile fit, or have been detected in an indirect way, for example, in the gas phase in a region dominated by sublimating ice species.

The column density of an ice species is determined by integrating the optical depth of a characteristic band and dividing it by the integrated band strength, measured in the laboratory. The resulting column density of water ice ranges between 10^{17} - 10^{19} cm^{-2} for different YSOs. The abundances of other ice components are often normalized to water. The composition of ice mantles can vary between different molecular clouds, however, certain trends are observed. Table 1 shows the ice abundances rel-

ative to water ice in different environments - massive young stellar objects (MYSO), low and intermediate young stellar objects (LYSO), dense clouds and cores, as well as comets. The table is divided into three sections, with secure, likely and possible identifications of species, as explained earlier. Water is the most abundant constituent in all environments, and the median relative amount of species such as CO or CO_2 is within the same range, although the variation for each type of an environment can be by a factor of a few. The observations of a molecular cloud as a function of depth into the cloud, show the layered structure of the icy mantles with the H_2O-rich layer coated by a CO-rich ice. This is due to the fact that CO is highly volatile and only freezes out at higher densities and very low temperatures. In the literature the H_2O-rich layer is called the polar ice phase, the CO-rich layer is referred to as the a-polar ice phase.

1.2.2   Rosetta revolution

While the ice abundances in regions outside of the solar system (MYSOs, LYSOs, molecular clouds) are largely derived based on their IR signatures, different options apply for the comets whose orbits come closer to Earth, providing a unique opportunity to probe their composition *in-situ*. Space missions *Giotto* and more recently *Rosetta* probed the cometary comae of comets 1P/Halley (1P) and 67P/Churyumov-Gerasimenko (67P), respectively. *Rosetta* mission followed the comet 67P, illustrated in Figure 1.4, along its orbit around the Sun, measuring the release of gas and dust during the different phases. The composition of the coma was used to derive the composition of the nucleus of the comet, that could be considered to be a large dirty snowball. The measurements were done with an on board mass spectrometer, the Rosetta Spectrometer for Ion and Neutral Analysis (ROSINA). This detection method solves (some) of the challenges inherent to IR ice spectroscopy, and provides a more sensitive and unambiguous identification technique. The analysis of the data from the ROSINA instrument resulted in an impressive number of different species, doubling the number of previously detected cometary molecules (currently 66), including small COMs (e.g. CH_3OH, CH_3CN), polycyclic aromatic hydrocarbons (PAHs), sugars (glycolaldehyde, $(HC(O)CH_2OH)$) and even the simplest amino acid (glycine, NH_2CH_2COOH) (Altwegg et al. 2016, 2017; Rubin et al. 2019). Approximately two-thirds of the species detected in comets, have been previously detected in clouds of low and high mass stars. In addition, the relative abundances of the species detected at the early evolutionary stages are similar to the cometary values, supporting the primordial (inherited from prestellar stage) origin of the cometary chemical composition (Altwegg et al. 2019).

   One of the surprising results from the *Rosetta* mission was the detection of a large amount of molecular oxygen (O_2), at level of a ∼3% with respect to H_2O ice (Bieler et al. 2015). This finding motivated a re-analysis of the data from the *Giotto* mission, which resulted in a similarly high ratio in comet 1P (Rubin et al. 2015). These cometary O_2/H_2O values were significantly above the expected gas-phase ratio in the interstellar medium (ISM) (Woodall et al. 2007; Yıldız et al. 2013). The origin of the high abundance of O_2 in the cometary ice is still debated (Luspay-Kuti et al. 2018), and it may be that it is inherited from the ices formed in the dense molecular clouds (Bockelée-Morvan et al. 2000; Cleeves et al. 2014; Drozdovskaya et al. 2014). The two comets originate from different parts in the Solar System, with chemically and physically different conditions. 1P has its origin in the Oort cloud and 67P is considered a Kuiper Belt Object (Balsiger et al. 1995; Altwegg et al. 2015). The consistent relative
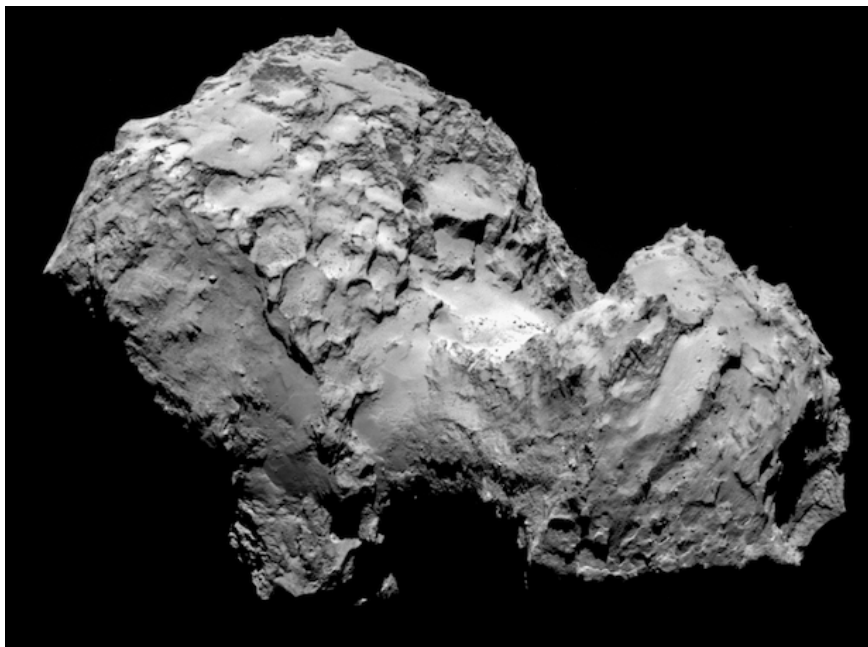
Figure 1.4: Image of comet 67P/Churyumov-Gerasimenko taken by Rosetta's OSIRIS narrow-angle camera on 3 August, 2015 from a distance of 285 km. Copyright: ESA/Rosetta/MPS

O_2 abundances for both bodies is in line with a common (primordial) origin of the observed O_2. The primordial origin of O_2 ice cannot be observationally verified, due to its homo-nuclear diatomic nature, which turns this molecule nearly invisible in the infrared and millimeter wavelength regime.

1.3   Complexity in interstellar ices

Icy dust grains in space provide a surface where molecules 'accrete, meet and greet', that is, where they freeze-out forming a molecular reservoir, where they can interact, directly or following diffusion in the ice (Linnartz et al. 2015). The ice mantle supports the increase in chemical complexity in two major ways. It acts as a solid state sink of gas phase atoms and molecules, where species have a higher chance to meet (compared to the gas phase). In addition, the icy surface acts as a chemical catalyst, providing a third body that allows to absorb energy from an exothermic reaction, stabilizing the reaction product. As stated earlier, different chemical triggers are at play, both leading to a formation of radicals in the ice, so called 'non-energetic' (dark) and 'energetic' (light) processing. Radicals are highly reactive species containing at least one unpaired electron in the valance shell. The dark chemistry is driven by atom and radical addition/abstraction reactions and is dominant during early stages of star formation, in dark and dense molecular clouds. The 'energetic' processing of ices is expected to play a larger role in the later stages of stellar evolution, triggered by im-

pacting cosmic rays, X-rays, UV photons, or energetic electrons. Another trigger for chemistry is an increase in temperature, which takes over when ices are heated (but not sublimated yet). All these processes have been studied in specialized laboratory experiments, providing the driving mechanisms and parameters needed for astrochemical modelling (e.g. Watanabe & Kouchi 2002; Muñoz Caro et al. 2002; Fuchs et al. 2009; Öberg et al. 2009c; Fillion et al. 2014; Dulieu et al. 2019). In the next sections several of these studies are discussed.

1.3.1   Dark ice chemistry

In dark clouds ice chemistry is mostly driven by atom addition reactions at temperatures typical for molecular clouds (10 - 20 K) between the most abundant elements: H (D), O, C, N. The involved chemical reactions are experimentally demonstrated and reviewed by Linnartz et al. (2015). The dominant abundance of H atoms promotes the importance of hydrogenation reactions, where H atoms stick on the grain, diffuse over the grain surface and find species to react with. This so-called *Langmuir-Hinshelwood* mechanism is used to explain the formation of abundant interstellar ice molecules: H_2O, CH_4 and NH_3 (Ioppolo et al. 2008, 2010; Qasim et al. 2020; Fedoseev et al. 2015b). For example, the formation of water ice proceeds via sequential hydrogenations of O atoms (or O_2 and O_3), which has been also verified by chemical modelling (Cuppen et al. 2010; Lamberts et al. 2013). In parallel, CO_2 ice is formed via reactions between CO and the OH radicals (O + H), and to a lesser extent between CO and O (Oba et al. 2010; Garrod et al. 2008; Ioppolo et al. 2011). Formation of more complex methanol, has been suggested and verified to proceed via hydrogenation reactions of the solid CO, particularly during the a-polar ice stage, when CO forms an ice coating (Tielens & Hagen 1982; Watanabe & Kouchi 2002; Fuchs et al. 2009).

Upon further hydrogenation of these species (H_2CO and CH_3OH) larger radicals are formed in the ice, such as HCO, CH_3O and CH_2OH (Chuang et al. 2016). The following radical-radical reactions result in the formation of COMs, such as methyl formate, glycolaldehyde, ethylene glycol, and even glycerol - a three carbon containing species necessary for the formation of membranes of living cells (Chuang et al. 2016; Fedoseev et al. 2017). A schematic representation of a part of the involved chemical network is provided in Figure 1.5. Finally, it has been recently shown that species as complex as the amino acid glycine, can be formed with 'non-energetic' chemistry in a water-rich ice. The final chemical step leading to NH_2CH_2COOH formation is between the NH_2CH_3 radical and HOCO (Ioppolo et al. 2021). Whereas methylamine (NH_2CH_3) as a precursor species has been identified in the ISM, the detection of glycine in dense molecular clouds remains to be confirmed (Kaifu et al. 1974).

1.3.2   Energetic processes

Different forms of energetic particles (cosmic rays, photons, electrons) interact with solid state species, both on the ice surface and in the bulk. Dense dark clouds, even though shielded from the ISRF, are penetrated by the cosmic rays, highly energetic particles, which produce energetic electrons and a secondary UV (VUV) field in the inner regions of the molecular clouds. These trigger dissociation, followed by radical-driven chemistry forming other species, including larger COMs, which become detectable
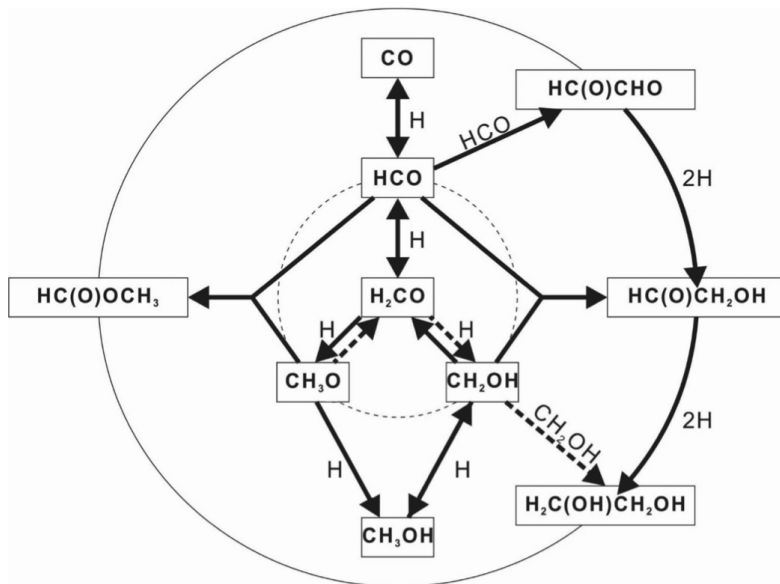
Figure 1.5: Non-energetic formation pathways showing sequential hydrogenation of CO, leading first to formaldehyde (H_2CO) and methanol (CH_3OH). Subsequent radical-radical or radical-molecule recombinations, or hydrogenation of reaction products result in the formation of methyl formate ($HC(O)OCH_3$), glycolaldehyde ($HC(O)CH_2OH$) and ethylene glycol ($H_2C(OH)CH_2OH$). The latter COMs have been identified in the gas phase in the ISM. Figure taken from Chuang et al. (2016).

following an ice sublimation. Alternatively, energetic processing of ices results in a non-thermal desorption mechanism regulating the balance between ice and gas in cold regions of the ISM. The focus of this section will be on processes following the irradiation of an ice analogue with VUV photons, as this is the main topic of this thesis.

Figure 1.6 shows a simplified overview of feasible processes following VUV photolysis of solid state species on a grain surface in cold regions in the ISM or in laboratory experiments on an ice formed on a gold-coated copper substrate. A molecule in the ice matrix is electronically excited following an absorption of a VUV photon (1). The photon absorption cross-sections of the main constituents of interstellar ices have been derived experimentally and all species except for (a possible constituent) N_2 absorb efficiently in the VUV range (Cruz-Diaz et al. 2014a,b). The energy released upon the relaxation of the excited molecule to its ground state (2), can have different outcomes. If its transferred to the neighboring molecule, it can result in neighbor's indirect desorption from the ice (3a, e.g. Bertin et al. 2013). Alternatively, the excited molecule can use its energy to directly photodesorb (3b, Fayolle et al. 2011) or photodissociate and form radicals (4). The formed radicals species can participate in dissociative or reactive photodesorption, where the excited radicals desorb from the ice surface (3c, Muñoz Caro et al. 2010; Andersson & van Dishoeck 2008), or 'kick-out' their neighbor (molecule or fragment) into the gas phase (3d, Andersson & van Dishoeck 2008). Finally, the formation of radicals can also result in their recombination into new molecules (6, photochemistry), which either stabilize in the ice or desorb (3e, photochemidesorption as in Martín-Doménech et al. 2016). Photoconversion is char-
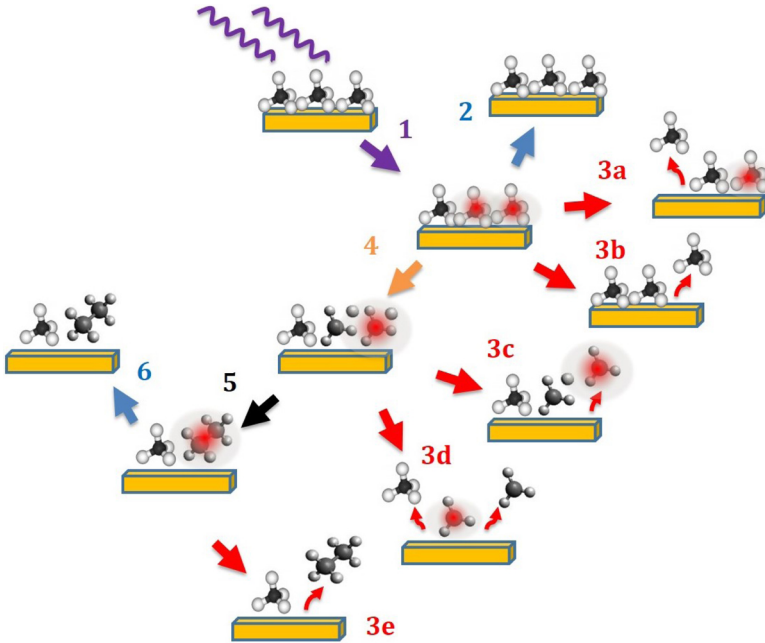
Figure 1.6: Competition between processes taking place in solid state species upon an absorption of a VUV photon. Photodesorption processes (in red) are only possible for the top layers of the ice. All other processes can happen in both the ice bulk and on the surface. The schematic applies to ices at a temperature excluding thermal desorption, typically ≤ 20 K. Figure from (Bulak et al. 2020).

acterized by a combination of photochemistry (6), and reactions of nondissociated, photoexcited molecules (1), with neighboring neutral species. Both types of reactions provide formation pathways of many of the observed simple and complex species (e.g. Gerakines et al. 1996; Jin & Garrod 2020).

The desorption processes described above (3a - 3e) are expected to be possible only in the top few layers of the ice. In case of CO and H_2O, the top 3 ML (1 ML = 10^{15} molecules cm^{-2}) participate in photodesorption (Andersson & van Dishoeck 2008; Bertin et al. 2012). The photodissociation branch (4) is accessible when an absorbed photon carries enough energy to dissociate the molecule in the ice. This threshold is given by a molecular bond dissociation energy, BDE. The main constituents of interstellar ices, such as H_2O, CO_2, CH_4, NH_3, CH_3OH, have their BDE in the energy range between 4 - 10.2 eV allowing to be dissociated by the VUV field. An exception to this is the CO molecule, which requires 11.2 eV to be dissociated. Upon photodissociation, radicals are formed and their mobility in the ice is dependent on the temperature. At 20 K, H atoms are expected to diffuse through the ice, however, larger radicals, such as CH_3, OH, CH_2OH or CH_2CN have limited mobility, in a range up to a few layers (Andersson et al. 2006; Garrod et al. 2008). The following radical-radical and radical-molecule interactions in the ice, result in many detected complex organic species, including alcohols, sugars, nitriles, amides, and the building blocks of life - aminoacids, (e.g. Bernstein et al. 1995; Muñoz Caro et al. 2002; Öberg et al. 2009c; Ligterink et al. 2018a; Bulak et al. 2021). The separation and quantification of

these competing processes (photodesorption and photoconversion) is an experimental challenge for pure ices, and even more so, for ice mixtures. This is another topic that is addressed in detail in this thesis.

The role of the remaining type of energetic processing, thermal, is activated upon the formation of the protostar, when its environment begins to heat up resulting in processing of the surrounding icy mantles. Prior to the sublimation, the increased ice temperature results in more efficient diffusion or radicals and molecules, ultimately increasing the reaction rates. It also allows some acid-base reactions to proceed more efficiently (van Broekhuizen et al. 2004; Theulé et al. 2013). In addition, structural changes to the ice may occur, such as crystallization (transition from the amorphous to crystalline ice phase) and ice segregation (Ehrenfreund et al. 1998; Öberg et al. 2009a; Isokoski et al. 2014).

1.4 Link between ice and gas

1.4.1 Thermal desorption of COMs

The local composition of ice and gas in the warm regions (above 20 K) is regulated by thermal desorption characteristics of interstellar ices. One of the implications is related to the chemical inventory available for exoplanet formation. In particular, a temperature gradient in protoplanetary disks (decreasing temperature as a function of distance from the protostar), results in a varied gas phase composition linked to sublimation of water (temperature of 135 K) and CO (20 K). The location of these so-called snowlines determines the gas phase C/O ratio, which is available to be incorporated into new planetary systems (Öberg et al. 2011b).

Sublimation of interstellar ices is also linked to the first detections of COMs. In a massive-star forming region, where the young stars heat up their surroundings (hot cores), both CH_3OH and CH_3CN could be detected (Ball et al. 1970; Solomon et al. 1971). In these environments, the ice mantles are sublimated rapidly, hence the gas phase composition of hot cores is thought to give a good representation of the composition of the interstellar ices. Examples of high mass star forming regions are Orion KL and Sagittarius B2, while their low-mass equivalents include IRAS-16293 and NGC 1333-IRAS2A.

Since the 1970s, over 50 COMs have been detected in different environment associated with star formation, from prestellar cores, through hot cores and corinos, to protoplanetary disks and comets (e.g., Bisschop et al. 2007b; Öberg et al. 2010a; Jiménez-Serra et al. 2016; Calcutt et al. 2018). The gas phase species are studied with (sub)millimeter wave telescopes such as *Herschel*, or *Atacama Large Millimeter/submillimeter Array* (ALMA) and detections of new molecules continue on a yearly basis (McGuire 2018). Recent highlights include species detected in hot corinos containing three carbon atoms, such as acetone and propanal (Lykke et al. 2017), and species of prebiotic interest such as glycolaldehyde (Jørgensen et al. 2012) and formamide (Kahane et al. 2013). The wealth of the observations is summarized in (Jørgensen et al. 2020). These detections reinforce the importance of understanding the low-temperature grain surface chemistry for the formation of prebiotic molecules seen in hot corinos in the gas after sublimation of the entire ice mantle. Further evidence supporting the (partial) solid state origin of (some) COMs is found in astrochemical

models. The models have shown that gas-phase chemistry alone cannot explain the observed abundances of COMs. This includes methyl formate, dimethyl ether, glycolaldehyde, and ethanol, for which solid state formation schemes have been investigated and for which accurate solid state spectra have become available (Garrod et al. 2008).

The high spatial resolution of observation of COMs in star forming regions can provide additional chemical hints about their origin, that is a grain surface production and sublimation versus gas-phase formation scenario. This is illustrated by figure 1.7, where emission lines from several oxygen- and nitrogen- bearing COMs (O-, and N-bearing COMs) are mapped out. A spatial differentiation of COMs is clearly visible, with the N-bearing COMs (e.g., cyanides) peaking toward the protostar, while the O-bearing COMs (alcohols) toward two spots offset from the protostar (Csengeri et al. 2019). The N-bearing COMs demonstrate a typical thermal sublimation of ices possibly followed by warm gas-phase chemistry, while the O-bearing species peak at locations associated with accretion shocks (Csengeri et al. 2019). A similiar spatial differentiation has been seen towards other sources, such as a massive YSO NGC7538 IRS9 (Öberg et al. 2013). Here, the analysis of the emission of CH_3OH, CH_3CN, and CH_3CCH toward the YSO revealed a change in COM chemistry at temperatures above 25 K, likely reflecting the onset of an efficient ice chemistry above this temperature. Recent studies discussing detections and interpretations of varying distributions of O-, and N-bearing COMs are found in van Gelder et al. (2020a) and Nazari et al. (2021), respectively.
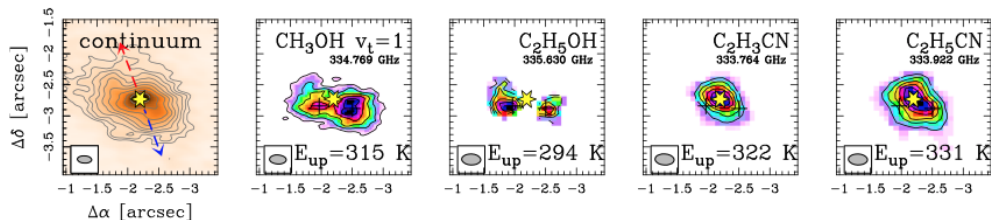
Figure 1.7: Continuum emission (left panel) and integrated intensity maps of transitions of several COMs (other panels) toward the young high-mass protostar G328.2551-0.5321 obtained with ALMA. O-bearing COMs (CH_3OH and CH_3CH_2OH trace two spots (black crosses) offset from the protostar (yellow star) that are associated with the accretion shocks. In contrast, the emission of N-bearing COMs (CH_2CHCN and CH_3CH_2CN) peaks on the protostar. Figure adapted from Csengeri et al. 2019.

The low-temperature grain-surface chemistry leading to O-bearing COMs, such as CH_3CH_2OH, or CH_3OCH_3, $HCOOH$, $HCOOCH_3$ is often linked to energetic processing of CH_3OH ice (Bennett et al. 2007; Öberg et al. 2009c; Paardekooper et al. 2016a). For the N-bearing COMs (cyanides, amides, amines) the dominant solid state precursors and chemical pathways are less clear. The structural equivalent of CH_3OH in nitrogen chemistry is acetonitrile (CH_3CN), which has been been indirectly detected to be a part of interstellar ices (e.g. Lee et al. 2019). Its potential as a precursor, mixed with H_2O and irradiated by ion bombardment has been tested by Hudson et al. (2008). The resulting residual material was extracted and analyzed *ex-situ*, following acid hydrolysis, yielding a range of amino acids. Despite demonstrating a potential to form building blocks of proteins, it was not possible to disentangle the involved chemical pathways or *in-situ* low-temperature ice chemistry. In another experiment, VUV

processing of interstellar ice constituents $HNCO/OCN^-$ mixed with CH_4 has been demonstrated to form species with a peptide bond (which build up amino acids), such as acetamide (CH_3CONH_2), formamide (NH_2CHO) and urea NH_2CONH_2 (Ligterink et al. 2018a). Photoprocessing of NH_3 was also tested and while it does not lead to a formation of large molecules on its own, it provides the NH_2 radical, which in combination with, for example CH_3OH, can yield a plethora of N-bearing COMs (Muñoz Caro et al. 2014). Mixtures containing NH_3 and CH_3OH are not expected to be abundantly present in the interstellar ices. Despite the ubiquity of large N-bearing species found towards different sources and their prebiotic potential, formation pathways (in the solid state or gas phase) towards already detected pecies, such as CH_3CH_2CN, $HOCH_2CN$, $(CH_2CN)_2$, or $(NCCN)/(CNCN)$, remain unclear, or unknown. In this thesis it is shown that VUV photolysis of CH_3CN ice (in water) provides solid state pathways to a number of CN-containing species.

1.4.2   Non-thermal desorption

In cold interstellar regions exposed to UV photons, the desorption of simple and complex species can occur via different non-thermal mechanism driven by UV photons (see Fig. 1.6). This process is responsible for the presence of cold molecular gas of molecules, such as CO and H_2O, in environments where molecules should be frozen out on grains. This conclusion is based on state-of-art gas-grain astrochemical models such as one of molecular cloud composition by Hollenbach et al. (2009). These complex studies derive the compositon of gas and ice as a function of depth into the cloud. The considered contributing effects include: thermal balance, gas-phase chemistry, simple surface chemistry, accretion of gas-phase species to grain surfaces, and various desorption processes such as photodesorption, thermal desorption, and cosmic-ray desorption. The model successfully reproduces the ice and gas abundances of H_2O, OH, O and (where relevant) O_2 towards molecular cloud B68, a star forming cloud in Orion, NGC 2024, and ρ Ophiuchus (Larsson et al. 2007; Hollenbach et al. 2009). The results show that UV-driven competition between photodissociation and photodesorption has a major effect on the gas phase chemical composition from the edge until intermediate depths into the cloud. At the onset of water ice formation, the majority (98%) of gas phase water is due to UV photodesorption of water from the grain surfaces. Deeper into the cloud, the percentage drops to 70%, and at intermediate depths into the cloud, goes up again to 92%. The photodesorption is also necessary to explain observed abundances towards other regions in the ISM: photon dominated regions of molecular clouds (Snell et al. 2000; Wilson et al. 2003), prestellar cores (Caselli et al. 2012), outer parts of protostellar envelopes (Schmalzl et al. 2014) and protoplanetary disks (Dominik et al. 2005; Willacy 2007; Hogerheijde et al. 2011).

The photodesorption process has been studied in the laboratory for the main constituents of interstellar ices: H_2O, CO, CO_2, CH_4, CH_3OH (Westley et al. 1995a; Öberg et al. 2007b; Paardekooper et al. 2016c; Fillion et al. 2014; Dupuy et al. 2017; Bertin et al. 2016; Cruz-Diaz et al. 2016). Despite the investigation of this topic for over 20 years, the photodesorption rates reported in the literature still vary by a few orders of magnitude. Among all ice constituents, the 'simple' case of CO photodesorption has been studied the most extensively, as CO does not dissociate upon VUV photolysis (Sect. 1.3.2). Fig. 1.8 shows an overview of all experimental studies on photodesorption of CO. There exist experimental differences between these studies
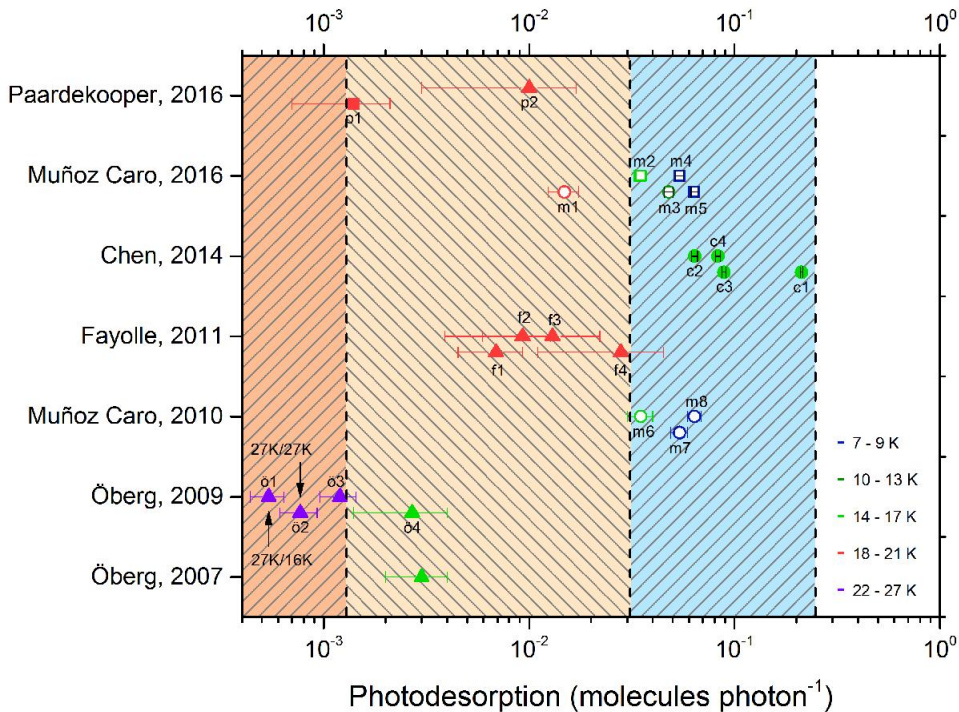
Figure 1.8: Overview of all the experimental CO photodesorption studies from (Paardekooper et al. 2016c). The colour code refers to the deposition and photolysis temperature. Studies at different photon energies by Fayolle et al. (2011) are labelled as: f1 = 10.2 eV, f2 = 11.2 eV, f3 = 9.2 eV, f4 = 8.2 eV. Flux calibration methods are distinguished with filled symbols (NIST photodiode) and empty symbols (actinometry). Detection technique; triangles and circles: IR spectroscopy; square: mass spectrometry. The labelling of c1, c2, c3, and c4 refer to different spectral energy distribution of a UV lamp in Chen et al. (2014). The labelling p1 and p2 refers to a direct measurement and derivation of the photodesorption rate in Paardekooper et al. (2016c).

explained in more detail in the next section, including the type of UV source, calibration methods, ice temperature and analytical techniques used to measure the rate. It is hard to understand, though, how these differences can account account for two orders of magnitude difference between the resulting rates of 2.3×10^{-1} molecules photon^{-1} (Chen et al. 2014) and 2.7×10^{-3} molecules photon^{-1} Öberg et al. 2009e). One should note, however, that photodesorption values of CO were set to 10^{-6} molecules photon^{-1}, before the experimental studies were performed. From this perspective, experiments still contributed substantially to a better quantitative understanding of this desorption process.

Besides broad band studies, also wavelength dependent photodesorption experiments have been performed using synchrotron facilities (Fayolle et al. 2011). In these experiments the molecular origin of the excitation mechanism - desorption induced by electronic transition - could be studied and also more information was obtained on the location of excited and desorbed ice species (Bertin et al. 2013).

The measurements of photodesorption of COMs, or smaller species that photodis-

sociate within the VUV energy range, is more challenging as it requires to separate the effects of photodesorption from photoconversion (see Fig. 1.6). This is reflected by missing photodesorption values for COMs, such as CH_3CN, CH_3CH_2OH, or $HCOOH$ and differences in the reported values for intact photodesorption of CH_3OH (Öberg et al. 2009c and Bertin et al. 2016 or dissociative desorption of OH from H_2O ice ((Cruz-Diaz et al. 2018; Fillion et al. 2021)). These differences in the literature or the lack of measured photodesorption rates motivate further laboratory investigations of this mechanism, specifically for species which can be photoconverted in the VUV range.

1.5 Laboratory astrophysical approaches

A prime objective of laboratory astrophysical studies has been to record signatures of molecules allowing to identify the species in astronomical observations. In the case of interstellar ices, a few decades ago a typical laboratory system for solid state investigations comprised a chamber under high vacuum conditions (10^{-7} mbar) with a substrate cooled down below to 10 K and an IR spectrometer. In an experiment, after deposition of a pure or mixed ice of interest, infrared spectra of species were recorded using a Fourier transform infrared spectrometer (FTIR) and used for interpretation of observations, as shown in Fig. 1.3 (Hudgins et al. 1993). Today, these systems have been updated to ultra high vacuum conditions (10^{-10} mbar) and the infrared spectrometers to higher sensitivity and spatial resolution. This combination provides more accurate spectra of ice species in preparation for the JWST launch, planned towards the end of 2021 (e.g. Terwisscha van Scheltinga et al. 2018; Rachid et al. 2020).

Since the identification of the main components of the interstellar ices, dynamical studies have been performed in laboratories, focusing on the involved solid state chemical processes, for example, by irradiating ice analogues with microwave discharge hydrogen lamps (MDHL), a source of VUV radiation, resembling the secondary UV field in the ISM. Photoconversion of simple ice species was investigated and the formation of new species during the UV photolysis was traced. In the very first studies by *ex-situ* investigation of remaining residues (Greenberg 1983; Bernstein et al. 1995), and later with *in-situ* methods, such as FTIR, which is well-suited for detection of molecules with a dipole moment (Gerakines et al. 1996). In complex ice mixtures, this technique is less powerful as the identification and quantification of species suffers from overlapping signatures of molecules with the same functional groups. For this reason, IR spectroscopy (in transmission or reflection-absorption mode, RAIRS) is often used in combination with quadrupole mass spectrometry (QMS) and temperature programmed desorption (TPD). Upon linear heating of the sample, ice constituents desorb into the gas phase, each at a characteristic temperature corresponding to the binding energy between molecules or molecule and the substrate (Collings et al. 2004). The desorbing species are detected with a QMS, which inherently measures an equilibrated gas-phase composition in the experimental chamber. This means that molecules, prior to being detected, may interact with the walls and other inner parts of the setup, which are typically at room temperature. Experiments with TPD can include the thermally induced processes, resulting in the chemical changes in the ice (Öberg 2009; Ioppolo 2010).

An alternative *in-situ* technique to these two methods has been implemented by Abplanalp et al. 2016, who have combined the TPD with a tunable single photon

ionization source and a time-of-flight mass spectrometer (TOF MS). The soft tunable ionization source, allows for minimal fragmentation and isomer-specific identification based on the ionization potential of the probed molecule. Successful application of this method allowed to identify the formation of polycyclic aromatic hydrocarbons from the energetically processed C_2H_2 ices (Abplanalp & Kaiser 2020).

Photodesorption of interstellar ices can be measured indirectly via monitoring the depletion of the ice or directly by measuring the photodesorbed species in the gas phase. Photodepletion of the ice - a decrease in abundance of the parent species as a function of UV photon fluence is a combined result of photodesorption and photoconversion. In the original photodesorption study by Westley et al. 1995a, the depletion of water ice was monitored by a quartz micro balance and linked to the photodesorption rate of H_2O. Over a decade later, Öberg et al. (2009d) monitored the depletion of the water ice with RAIRS and simultaneously measured the species in the gas phase with a calibrated QMS, detecting the dissociative desorption. In other studies (Fayolle et al. 2011) used the signal measured with a QMS to convert it to a photodesorption rate of CO. This method was later applied to other molecules (Bertin et al. 2016; Cruz-Diaz et al. 2018).

Most common laboratory UV sources are microwave discharge hydrogen lamps (MDHL), in which the excitation of H atoms (and H_2) results in emission of Lyman-α (121.6 nm) and features around 160 nm from de-excitaiton of H_2. The photon flux and spectral energy distribution of this lamp are sensitive to its operation conditions, described in detail by Ligterink et al. 2015. An alternative UV source is provided by tunable synchrotron radiation which allows to investigate the photodesorption efficiency as a function of UV photon energy (Fayolle et al. 2011).

The results of this thesis are based on experiments on MATRI^{2}CES - Mass Analytical Tool for Reactions in Interstellar ICES (Paardekooper et al. 2014). This setup follows a different experimental approach to quantitatively probe the composition of the ice as a function of VUV fluence at low temperatures (down to 20 K). The *in-situ* probing sequence is initiated by a desorption of the ice with unfocused laser shot, resulting in a gas phase plume representing the composition of the ice. The plume is ionized via electron impact and extracted into the time-of-flight mass spectrometer. This scheme is referred to as Laser Desorption Post Ionization Time-of-Flight Mass Spectrometry (LDPI TOF MS) and allows to simultaneously probe the effects of photoconversion and derive photodesorption rates of astronomically relevant ices in an ultra-sensitive manner. Much of the work described in the next chapters only became possible because of the experimental tools MATRI^{2}CES offers.

1.6 This thesis

This thesis is an experimental study of the UV irradiation of the interstellar ice analogues, relevant for the different stages of the star and planet formation sequence. It describes in detail photodesorption and photoconversion processes, and as such, contributes to worldwide efforts that aim at understanding how chemistry in space could have contributed to the origin of life on Earth and possibly planets around other stars. Our contribution to address this idea, is to investigate the potential of UV photolysis of astronomically relevant species as solid state precursors of the detected chemical

complexity, and molecules linked to life (photoconversion, Chapters 4 and 6). In parallel to photoconversion, UV photolysis triggers a non-thermal desorption mechanism which quantified, contributes to the ice - gas balance in cold regions of the ISM exposed to UV (photodesorption Chapters 3 and 5). The results from Chapters 3 and 5 can be used as a direct input for astrochemical modelling.

Chapter 2 details the experimental system MATRI^{2}CES, the apparatus used in this thesis to study the UV photoprocesses in ices. Under ultra high vacuum conditions (UHV), simple ice analogues are deposited and irradiated with vacuum UV photons. The chemical composition of the ice at low temperature is quantitatively traced as a function of UV photon fluence via laser desorption post ionization time-of-flight mass spectrometry (LDPI TOF MS), an *in-situ* experimental method, relatively new in the field of laboratory astrochemistry. The measurement toolbox on MATRI^{2}CES is described with examples of time-of-flight mass spectrometry traces contributing to the data analysis.

Chapter 3 presents a novel experimental approach to discriminate between photoconversion and photodesorption upon VUV photolysis of interstellar ice analogues. It is based on a comparison between the effects of photolysis of pure ices with ices coated with an Argon layer. The inert coating is transparent to the VUV photons (does not affect the UV fluence), but it quenches the photodesorption processes. A quantitative comparison of the photodepletion of the parent species between the (un)coated experiments is used to derive its total photodesorption rate. The method is first validated using the well-studied case of CO and extended to CH_4, CH_3OH, and CH_3CN.

Chapter 4 includes an investigation of a potential role of acetonitrile (CH_3CN) as a parent molecule to N-bearing COMs, motivated by its omnipresence in the ISM and structural similarity to another well-known precursor species, CH_3OH. In addition a mixture relevant to the interstellar ices, embedding CH_3CN in an H_2O matrix, is investigated. The UV photolysis of pure CH_3CN ice yields larger nitriles including NC-CN/CNCN, CH_3CH_2CN and $NCCH_2CH_2CN$. The UV photolysis of an astronomically relevant H_2O:CH_3CN ice at 20 K, leads to the formation of larger (at least up to 6-7 C/N/O-containing) molecules with the functional groups of: imines, amines, amides, large nitriles, carboxylic acids, and alcohols. Many of these species already have been identified in gas phase studies, while other species that have not been identified yet may be well present in the ISM.

Chapter 5 is motivated by previous experimental and theoretical studies which provide a range of photodesorption rates for H_2O ice and hint at a convoluted competition between photodesorption and photoconversion. A novel experimental approach presented in Chapter 5 is applied to the case of water ice. The UV photolysis of porous amorphous water (H_2O) ice at 20 K water ice is repeated with an Argon coating and the chemical composition and ice thickness are traced with the LDPI TOF MS technique. The role of the Argon coating is to quench any type of photon-triggered desorption, with a minimal effect on photoconversion. Upon a comparison of the (un)coated experiments a photodesorption rate of water ice was derived, with an upper limit on intact, dissociative and reactive photodesorptions. The results can be used as direct input for astrochemical modelling. The main finding of this fully independent approach is

that the photo desorption value of water ice is close in the range of previously found values.

Chapter 6 explores a new (primordial) scenario which might (partially) contribute to the formation of the surprisingly large abundance of O_2 and its correlation with water in the cometary ices of comets 1P and 67P. In this chapter the formation of O_2 and (H_2O_2) is detected and quantified upon VUV irradiation of pure H_2O and mixed H_2O:CO_2 ice at 20 K. For an UV photon fluence representative of dense molecular clouds and innermost regions of protoplanetary disks ($\approx 10^{18}$ photons cm^{-2}), UV irradiation of porous amorphous H_2O ice at 20 K leads to formation of O_2 and H_2O_2 in the solid state at the maximum abundances of (O_2/H_2O) and H_2O_2/H_2O equal to (0.9 $\pm$ 0.2)% and (1.3 $\pm$ 0.3)%, respectively. The relative formation efficiency of (O_2/H_2O) increases with the presence of CO_2 in the initial mixture. The abundances of O_2/H_2O found in our experiments are sufficient to account for at least part of the observed cometary abundances.

2 | MATRI²CES

Abstract

Interstellar ices have a profound impact on the physical and chemical processes during star and planet formation sequence. In an experimental setup, MATRI²CES (Mass Analytical Tool to study Reactions in Interstellar ICES), ice analogues are synthesized and irradiated with vacuum-ultraviolet photons at low temperature (20 K). The photochemical evolution of the ice is quantitatively traced with a combination between laser-desorption and time-of-flight mass spectrometry, a toolbox unique for astrochemistry. In this chapter, a detailed description of the setup is provided, including an experimental upgrade, which resulted in a current detection limit of 3×10^{11} molecules cm^{-2}. The key calibration procedures are demonstrated, followed by a step-by-step analysis of the resulting data. MATRI²CES offers a sensitive experimental tool, complementary to more common techniques like RAIRS and TPD-QMS, which is applied to investigate the solid-state origin of species, including complex organic molecules. In addition, it is used to accurately determine the UV photodesorption rates of interstellar ices, important for the balance between ice and gas in cold regions representing various stages of star and planet formation.

2.1   Introduction

In this chapter, a description of the experimental setup used for this thesis is provided. MATRI^{2}CES (Fig. 2.1), the Mass Analytical Tool to study Reactions in Interstellar ICES, is an apparatus designed to simulate the interstellar ices in different regions of the ISM. The system in its original form was built in 2013 (Isokoski 2013) and upgraded over the last years to gain sensitivity and allow more sophisticated ice chemistry experiments, with details described in Paardekooper et al. (2014) and Bulak et al. (in prep). The basic concept of this setup differs from those applied in ice setups used elsewhere and allows to combine laser desorption and time-of-flight mass spectrometry, resulting in an *in-situ* probing technique that allows quantitative analysis of photon-triggered processes in ices. The fundamental principle and approaches of the different types of measurements with MATRI^{2}CES, as well details of the data analysis are provided in the next sections.

A. Main chamber
B. Flight tube
C. Cryostat
D. z–translator
E. y–translator
F. Gate valve
G. Substrate
H. Extraction optics
I. Gas inlet tube
J. Ablation laser
   (beam path)
K. Ionization source
   (electron gun)
L. UV source
   (discharge lamp)
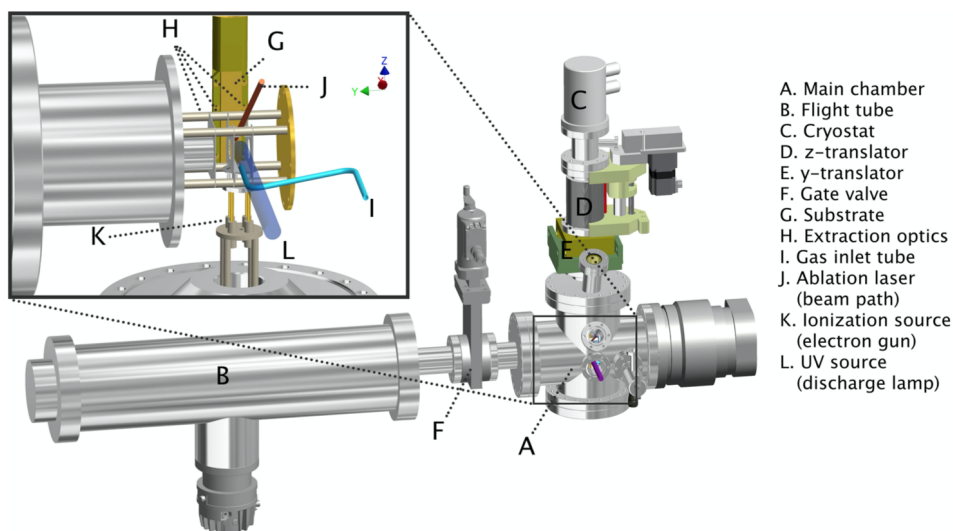
Figure 2.1: A schematic view of the experimental setup MATRI^{2}CES used in this thesis. Figure is adapted from Paardekooper et al. (2014)

2.2   System description

A schematic 3D view of the experimental system MATRI^{2}CES is shown in figure 2.1 along with its main components. The system consists of two vacuum chambers: the main chamber (A in Fig. 2.1) and the time-of-flight mass spectrometer tube (B, Jordan TOF products, Inc.), both at a base pressure of $\sim 10^{-10}$ mbar (equivalent to $\sim 10^6$ particles cm^{-3}). The main chamber houses a closed-cycle helium cryostat (C, Advanced Research System, DE 202), which cools down a gold-coated copper block, used as a substrate for ice deposition (G). The temperature of the substrate is controlled between 20-300 K, through resistive heating of the copper block that is continuously cooled by the cryostat, using a temperature controller (Lakeshore 331). Temperature

values are measured using chromel-gold/iron alloy thermocouples with an absolute accuracy of ± 1 K. The cryostat is mounted on top of two translation stages (D, E), allowing a linear shift in the position of the substrate in two dimensions (y- and z-directions). The translation along the z-direction (50 mm) is motorised, allowing to control the vertical motion of the substrate with variable speeds. The position of the substrate in the y-direction is adjusted manually (15 mm). The ices are deposited under fully controlled conditions via an inlet gas tube (I), connected to a gas manifold, with a base pressure in the range of $\sim 10^{-4}$ mbar. The ice deposition rate is calibrated using He-Ne laser interference measurements (Section 2.3.1).

The spectral energy distribution (SED) of the interstellar radiation field includes Lyman-α (121 nm), a molecular H_2 emission (130 - 165 nm), and can be closely simulated by a microwave discharge H_2 lamp (MDHL). The MDHL is connected to the main chamber via a magnesium fluoride viewport, opposite from the substrate, at a distance of 14 cm (L). The lamp (borosilicate) has a F-type design with an Evenson cavity placed on it, characterized in detail by Ligterink et al. (2015). The H_2 plasma is powered by a microwave generator (Sairem, 2.45 GHz, 80 Watts) and the lamp is operated with a continuous flow of H_2 gas maintaining a pressure of 1.4 mbar. The calibration of the resulting VUV photon flux is key in accurately describing the photon-triggered process, hence the calibration procedure is described in separately in Section 2.3.2.

The probing of the ice composition is initiated by laser ablation of a small spot (diameter of ~ 1 mm) on the deposited ice with an unfocused laser beam of a Nd:YAG laser (J, Polaris II, New Wave Research, 3-4 nanoseconds). The energy of the laser pulse (typically between 10 and 55 mJ cm^{-2}) is calibrated for each species and ice thickness to be sufficient for complete desorption of the ablated spot. This results in a gas phase plume of species with a net velocity vector away from the substrate (x-direction). The travelling plume is ionized via dissociative electron impact ionization (electron gun, K). The continuous electron beam is guided along the z-axis in the near vicinity of the substrate, and has an average electron energy of 70 eV. The involved electrons do not interact with the ice substrate. The average electron energy corresponds to the highest electron ionization cross sections for most species, resulting in a maximized ion formation efficiency. The ionization event also induces fragmentation of the species, which offers an additional tool to guide unambiguous identification (if the fragmentation pattern is available). In the case of overlapping mass fragments from multiple molecules, the mass analysis is complicated. It is possible to (partially) overcome this issue by using lower electron energies (i.e., 20 eV) that come with less fragmentation and moreover different fragment intensities, as well as the explicit use of isotopically enriched precursor species.

Ions are generated within the ion extraction optics (H) - metal plates oriented orthogonally to the substrate, each carrying a voltage of 1050 V. After a preset time delay (Fig. 2.2) following the laser shot, a fast (4 μs) decrease in the voltage (by 100 V) on one of the plates results in an extraction of the ions towards the electric-field-free time-of-flight tube (81.28 cm). Before entering the tube, the ions are gently steered along the x-direction in order to guide them towards the detector, which is off-center. This is done via a constant potential difference (100 V) applied to V_x plates in Fig. 2.3. During the drift in the time-of-flight tube, ions are separated according to their mass over charge ratio (m/z). Lower masses arrive earlier than heavier masses and this time resolution allows to record mass selective signals. To improve the mass resolution of

our spectra, the TOF MS is operated in a reflectron mode. This means that at the end of the time-of-flight tube, ions are reflected back, allowing to minimize the effect of variations in the initial kinetic energy within the plume. The detector is a 40 mm microchannel plate (MCP), with a high electric field applied across its plates (2400 - 3000 V). This allows a single ion to trigger an electron cascade, with the signal gain regulated by the MCP voltage. For each ion (m/z) a time-of-flight between the extraction optics and the MCP detector is recorded with a Data Acquisition card (DAQ) at a sampling rate of 2.5 GHz and used to ultimately derive the composition of the probed ice.
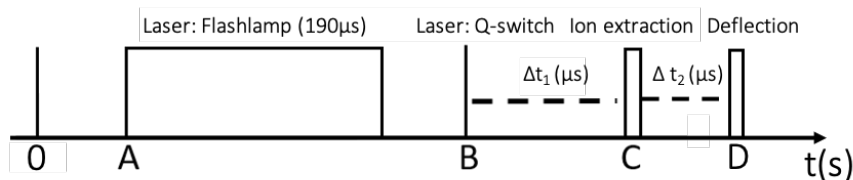

Figure 2.2: Relative timing sequence of LDPI TOF MS technique including the laser shot (A, B) and ion extraction (C) into the TOF MS. The time delay of the ion extraction (t = B + Δt_1) is varied in order to optimize detection settings for a particular product or probe the complete distribution of the plume. The timing of deflection (t = C + Δt_2) is relevant only for the last section of this chapter.

The timing of the LDPI TOF MS probing sequence (laser shot, ion extraction, data acquisition) is shown in Fig. 2.2. It is controlled with a time/delay generator (DG 535, Stanford Research System), which is triggered 100 times at a frequency of 5 Hz. This is synchronized with the vertical motion of the substrate (z-direction) allowing each laser shot to probe a 'fresh' spot along a column of the ice. To probe the changes in the ice composition and thickness as a function of UV radiation dose, the substrate is shifted along the y-axis and a fresh column of ice is probed (9 non-overlapping columns). The recorded 100 spectra are averaged (at the same timing sequence), to improve the signal to noise ratio, and used for further analysis. Alternatively, the time delay (Δt_1) can be varied every 10 spectra, to collect a complete distribution of the plume profile.

2.2.1   Limit of detection

The sensitivity of MATRI^{2}CES to detect low abundances of photoproducts has been limited by the dynamic range of the MCP. The amount of signal generated by the parent species (typically a molecular ion) causes saturation of the detector at the voltages of 2500 V across the MCP detector. A repeated saturation of the detector (signal above 1 V) leads to damage, hence the MCP has been operated at relatively insensitive settings. A solution has been implemented to utilize the full potential of the system. A high voltage pulser with a nanosecond rise time was added to the setup and connected to the V_x plates in Fig. 2.3. A short voltage pulse (0.2 - 5μs) is applied to the ion optics at a precisely calibrated delay (t = B + Δt_2) to deflect the most abundant ions (minimum deflected range of 3 - 5 atomic mass units). This prevents

the most abundant species from reaching the detection, i.e. to go into saturation, and allows to increase the gain across the MCP, successfully lowering the limit of detection (LoD) in other parts of the mass spectrum (Section 2.5).
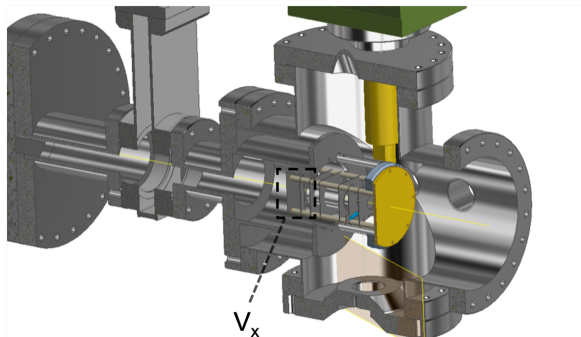
Figure 2.3: A short voltage applied to the V_X metal plate (duration of 0.2 - 5μs, 50 V) is timed to deflect the most abundant ions, ultimately to increase the sensitivity (improving the detection limit) on MATRI^{2}CES.

2.3   Calibration measurements

2.3.1   Ice thickness

An all-metal high-precision leak valve controls the ice deposition rate. It connects the gas manifold used for sample preparation with a gas tube in the main chamber, under an angle of 85° with respect to the substrate. Laser interference measurements are used to calibrate the ice deposition rate (Hudgins et al. 1993). During an ice growth, a He-Ne laser beam (wavelength 632.8 nm) is reflected from the substrate at an incident angle of 3°(θ). The reflected light is collected with a photodiode (Thorlabs PDA36A) and its intensity is recorded with an oscilloscope as a function of time. Figure 2.4 shows data collected for a deposition of CO ice at 20 K with a preset needle valve setting (15) and CO pressure in the gas manifold equal to 40 mbar. The resulting interference pattern of subsequent minima and maxima can be used to derive the ice deposition rate (τ). First, the ice thickness (d) is described as a function of the number of interference fringes (m) as in equation 6.2:

$$d = \frac{m \cdot \lambda}{2 \cdot \frac{n_1}{n_0} \cdot \cos \theta},$$

(2.1)

where λ is 632.8 nm, n_0 and n_1 are refractive indices of the vacuum (1) and ice, and θ is the angle of refraction (3°). The ice growth rate (in mol. cm^{-2}s^{-1}) can be determined from:

$$\tau = \frac{d \cdot \rho \cdot N_A}{M \cdot t},$$

(2.2)
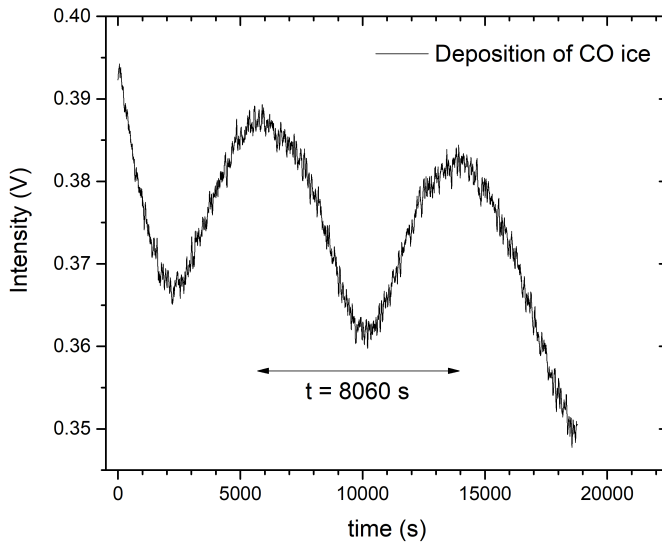
Figure 2.4: An interference pattern recorded during the CO growth at 20 K. The overall loss in the intensity is caused by scattering of the light in the ice, which does not affect the interference period.

where t is the time corresponding to the thickness d (calculated using equation 6.2), N_A is Avogadro's number (6.022×10^{23} mole^{-1}), ρ is the ice density in (g cm^{-3}), and M is the molar mass of the species (in g mole^{-1}). To calculate the CO ice deposition rate, the following values are used: molar mass of 28 g mole^{-1}, ice density equal to 0.8 g cm^{-3}, n_1 equal to 1.27 and the period for one fringe of 8060 s (Roux et al. 1980). These values are plugged into Eq. 2.2 and result in an ice deposition rate of 5.3×10^{13} molecules cm^{-2}s^{-1}. A deposition of a typical ice thickness of 20 monolayers (1 ML = 1×10^{15} molecules cm^{-2}) takes around 6 minutes.

2.3.2 Microwave discharge hydrogen lamp

The VUV photon flux of the MDHL used in our experiments has been determined at the position of the substrate, with a 1 cm^2 NIST-calibrated AXUV-100 photodiode. The photocurrent corresponding to the amount of radiation on the photodiode is measured with a Keithley 485 picoammeter. To separate the contribution of the photons in the visible range, a second MDHL lamp has been operated at the identical conditions, with a seal (fused silica) that transmits in the visible range with 90% efficiency and absorbs photons in the VUV ($\lambda < 230$ nm). The difference between the two measurements (MDHL sealed and not sealed) allows to subtract the photocurrent linked to visible photons, and to derive the VUV photon flux (F(λ)) using equation 2.3:

$$F(\lambda) = \frac{i(\lambda}{e \cdot \epsilon(\lambda)}, \tag{2.3}$$

where $i(\lambda)$ is the VUV photocurrent (Ampere), e is the electron charge (1.6×10^{-19} C) and $\epsilon(\lambda)$ is the number of electrons per absorbed photon of the NIST photodiode (quantum efficiency). The SED of the lamp at the operating conditions has been measured for a large number of different settings in (Ligterink et al. 2015). The derived VUV photon flux based for the conditions applied in this thesis research project is $(2.5 \pm 0.5) \times 10^{14}$ photons cm^{-2}s^{-1}.

2.4   Data analysis

The analysis of the LDPI TOF MS spectra consists of three steps: mass calibration, integration of the area under the mass peaks, and conversion of the calculated signal into a column density of identified species. The first step in the data analysis is the mass calibration of the time-of-flight spectra. This is done via a two-point calibration, where two known ions (m/z based on the initial composition of the ice) are used to solve the conventional equation of the time-of-flight (TOF):

$$TOF = A + B \cdot \sqrt{m/z}, \qquad (2.4)$$

An example of a mass calibrated spectrum of H$_2$O ice acquired via LDPI TOF MS is shown in Figure 2.5. The thickness of the ice is 100 ML, following the ice deposition rate calibration described in Section 2.3.1. The mass resolution of the peaks calculated with M/ΔM 300. Here gives M the m/z value and ΔM is the full width half maximum of the peak. The mass peaks at m/z = 16, 17, 18 represent fragments of H$_2$O created upon electron impact ionization, in agreement with the NIST database (Kim et al. 2014). In addition, peaks at m/z = 18·n+1, where n = 1, 2 represent protonated water clusters formed upon laser desorption of water ice; these species are not formed upon VUV irradiation and do not influence the ongoing ice chemistry (Gudipati & Yang 2012). The intensities of the mass peaks (integrated area) are proportional to a linear combination of species present in the plume (Paardekooper et al. 2014). This allows to express an integrated mass spectrum, M_t, at a given irradiation time, t, by:

$$M_t = \sum_{i=1}^{n} a_i \cdot \sigma_i \cdot M_i, \qquad (2.5)$$

where a$_i$ is the molecular abundance of species i, σ_i is the electron impact ionization cross section (at 70 eV), and M$_i$ is the corresponding fragmentation fraction. The area under each mass peak is calculated by fitting a Pearson IV distribution, which provides an excellent fit to the data by taking into account the asymmetry of the peaks and "spikiness" (Pearson 1895; Castellanos et al. 2018). An example of a fit is given by Fig. 2.6. The error associated with the fit is estimated by calculating the root mean square over the residual within one standard deviation from the center.   The sum of the integrated area of the mass peaks between m/z = 16 and 18, is linked with the column density of water ice via Equation 2.5. After taking into account the ionization cross-section for water (2.275 Å^2, Kim et al. 2014), the resulting value is set equal to 100 ML of water ice or 1×10^{17} molecules cm^{-2}. This value is then used as a reference to calculate the photodepletion of the parent or formation of photoproducts, after taking into account the fragmentation pattern and ionization cross-section. For
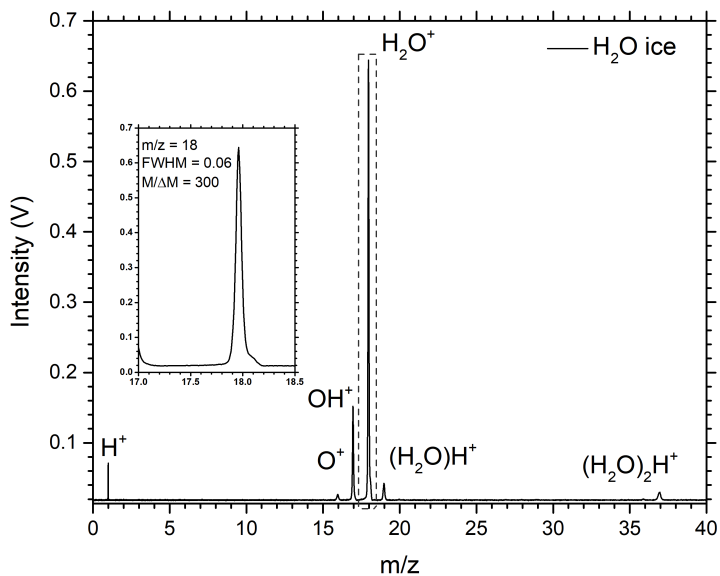
Figure 2.5: LDPI TOF MS of H_2O ice deposited at 20 K. The ice thickness in 100 ML. The inset shows the mass signal corresponding with H_2O^+ ion at m/z = 18, to demonstrate the mass resolution of the spectra.
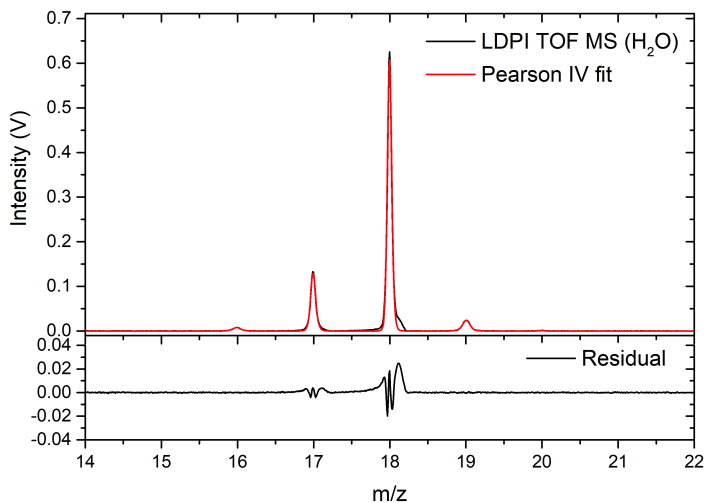
Figure 2.6: A Pearson IV fit to the LDPI TOF MS. The lower panel shows the residual to the corresponding fit.

example, for photoformation of O_2, the molecular ion at m/z = 32) is integrated, however a part of its fragmentation pattern overlaps with a water fragment (m/z = 16), preventing from clearly disentangling the contribution of each molecules. This is solved by considering the fragmentation pattern available at NIST, with 22% of O_2 residing in the fragment of m/z = 16 (Kim et al. 2014). After including the ionization cross section of O_2 (2.441 Å^2), the resulting value is converted with respect to the initial column density of water, allowing to trace its formation as a function of VUV fluence. A further option to circumvent overlapping masses is to work with isotopically enriched species, as will be shown later in this thesis for several experiments.

2.5   Measuring toolbox

This section focuses on the different types of measurement/data analysis methodologies performed with MATRI^{2}CES, as these provide the basis for quantifying the impact of a photon-triggered process. The most valuable is the capacity to measure the chemical kinetics at low ice temperature. The second concerns the identification of formed photoproducts using Temperature Programmed Desorption. The third topic deals with an improvement in the limit of detection on MATRI^{2}CES.

2.5.1   VUV photolysis at 20 K

The LDPI TOF MS traces of CH_3CN ice upon VUV photolysis at 20 K are collected; already for a small dose of VUV photon fluence, a multitude of new features appears in the spectra. The assignment of these mass peaks to particular products is a multi-

Figure 2.7: *Left panel:* Molecular abundances of species during the UV photolysis of CH_3CN ice as function of photon fluence. *Right panel:* Zoom in of the low fluence region indicated in the left panel.

step process, which begins with considering the radical species which are formed upon VUV photodissociation. The recombination of radicals typically dominates the photoconversion, however, radical-neutral inter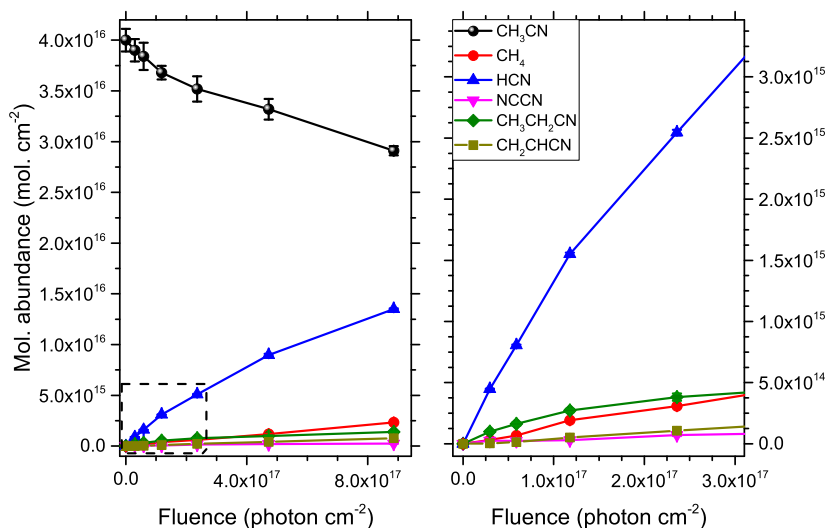actions can also play a role. In this case, two of the products can be immediately suggested: CH_4 (CH_3+H) and HCN (CN+H). Indeed their mass spectral signatures fit the collected LDPI TOF MS. Experiments with a deuterated acetonitrile (CD_3CN) confirm these assignments. In these experiments, the observed mass peak shifts correspond to the substitution of HCN (m/z = 27) $\rightarrow$ DCN (m/z = 28) and CH_4 (m/z = 16) $\rightarrow$ CD_4 (m/z = 20). The data analysis is performed as described in Section 2.4 and as a result, chemical kinetics of the parent species and photoproducts derived at 20 K, are shown in Fig. 2.7. The demonstrated photodepletion of the parent species is a combined effect of photoconversion and photodesorption. To separate these two processes, an experiment with a UV-transparent Argon cap is performed, which literally blocks the photodesorption, but has a minimum effect on the photoconversion (Chapters 3 and 5).

2.5.2 Temperature Programmed Desorption with TOF MS

In typical temperature programmed desorption, species desorb from the ice at characteristic temperatures, which provides a complimentary tool for product identification. On MATRI^{2}CES, the typical TPD is only possible for temperatures above the sublimation threshold of the parent species. This is due to a risk related to operating high voltages at a high pressure (up to 10^{-6} mbar upon the thermal desorption of the parent), which can cause an electrical spark with devastating effects on the electronics of MATRI^{2}CES. An alternative is a comparison of mass peak intensities collected via LDPI TOF MS at different temperatures, allowing for stabilizing the temperature of the substrate and the pressure in the chamber, prior to turning on the high voltages. As an example, following a VUV irradiation of CH_3CN at 20 K, the ice is probed with LDPI TOF-MS in specific temperature ranges, typically above and below the desorption temperature of an abundantly formed photoproduct. As a result, an intensity decrease of characteristic mass peaks is observed. This process can be explained by the thermal desorption of a photoproduct. This is demonstrated for CH_4 and HCN in Fig. 2.8. A comparison between mass spectra at 60 K and 130 K shows a decrease in the mass peak at m/z = 27, which is a characteristic peak of HCN, expected to desorb around 120 K. In addition, thermal desorption of remaining CH_4 trapped in the ice is observed at m/z = 16. The integrated (difference) mass spectra demonstrate the thermal desorption of CH_4 and HCN at expected temperatures and can be used as a supplementary identification tool.

Classical temperature programmed desorption has been performed on MATRI^{2}CES for the first time, following VUV photolysis of CH_3CN and starting at a temperature above the sublimation threshold of CH_3CN, around 150 K. The data acqusition sequence, without the laser, can be run at a much higher frequency (500 Hz). This results in an improvement in the signal to noise of the data. The substrate is heated at a rate of 2 K/minute and the species recorded with the TOF have been binned into 30 K intervals, shown in Fig. 2.9. The identification of photoproducts in Chapter 5 has been cut off at the second generation of products (m/z of around 80), due to uncertainties related to their identification. Despite that, the figure shows the incredible chemical complexity that can form upon VUV photolysis of CH_3CN, with the largest species consisting of 10 atoms (C/N/O). Identifying the typical fragmentation
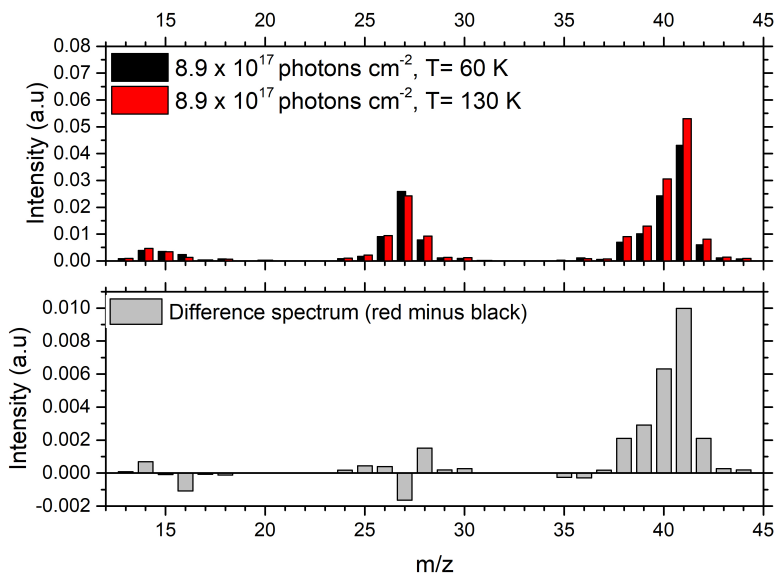
Figure 2.8: Top panel: integrated LDPI TOF-MS signals for an UV-irradiated CH_3CN ice at 20 K that is subsequently heated to a temperature of 60 K (black sticks) and 130 K (red sticks). The identification of HCN formation in the ice becomes visible when subtracting the 130 K and 60 K data as HCN thermally desorbs around 120 K. This is shown in the lower panel; at m/z = 27 this results in a negative value. In addition, thermal desorption of remaining CH_4 trapped in the ice is observed at m/z = 16.
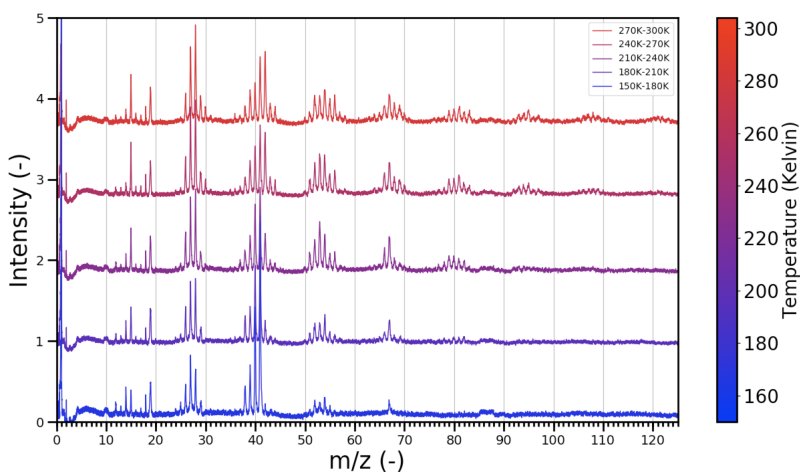
Figure 2.9: TPD TOF MS between 150 K - 300 K following a VUV photolysis of the CH_3CN ice. The mass spectra collected continuously during the heating up of the substrate, without the use of LDPI.

patterns of different families of species (amides, nitriles, carboxylic acids, etc.) is the next step in interpretation of this rich dataset.

2.5.3 Increasing the detection sensitivity

Finally, the most recent development on the setup has been an addition of a high voltage pulser, calibrated to deflect the ions that typically saturate the MCP detector (see Fig. 2.3). To test the limit of detection before and after the implementation of the pulser, we designed a scheme, in which the 3σ detection can be described in terms of detected ice column density (molecules per cm^2). An argon ice is deposited at 20 K with column density of 17.5 ML. Argon has been chosen as it has three natural isotopes with masses 36, 38, and 40 at low natural abundances of 0.334%, 0.063%, and 99.604%, respectively. With the 'old' settings, the ^{36}Ar peak is clearly detected with the S/N of 7σ (MCP of 2520 V), where the S/N is calculated by dividing the absolute intensity of the feature by standard deviation of the noise level in the spectrum, see Fig. 2.10. The 7σ detection corresponds to 1.4×10^{13} mol.cm^{-2}, hence the LoD at 3σ is 6×10^{12} mol.cm^{-2}. This trace is labeled 'Pulser OFF'. It is important to note that at the used MCP value of 2520 V, the molecular ion (m/z = 40) nearly saturates the detector (limit on the signal is 1V). In the same spectrum, an argon cluster peak $((Ar)_2^+$ at m/z = 80) is detected at S/N of 23σ, which will be used to demonstrate the role of the new pulser. Originally, the target was the doubly ionized Ar^{2+} (m/z = 20), however, during testing we found out that this peaks quickly saturates the detector, forcing the use of a peak with lower intensity.
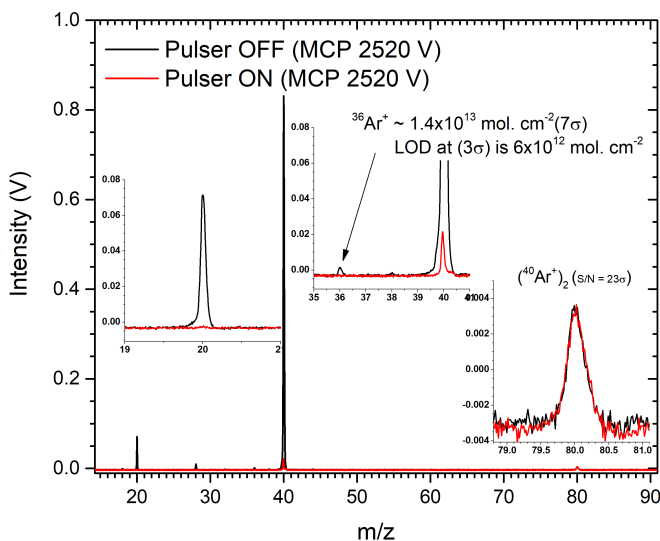
Figure 2.10: LDPI TOF MS of Argon ice at 20 K with a thickness of 17.5 ML with the pulser on and off at a low MCP value. The limit of detection (LoD) is calculated based on the natural abundance of ^{36}Ar at m/z = 36.
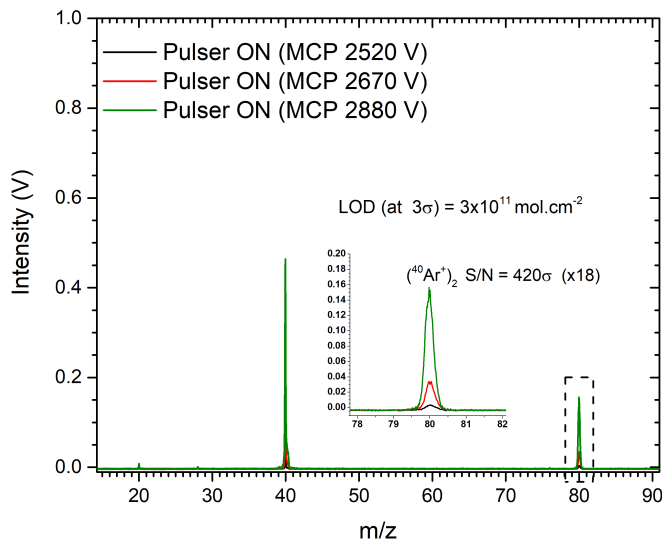
Figure 2.11: LDPI TOF MS of Argon ice at 20 K with a thickness of 17.5 ML with the pulser on allowing to increase the MCP value. The new limit of detection (LoD) is calculated based on an increase in the S/N of the $(Ar)_2^+$ mass peak at m/z = 80.

The pulser settings have been calibrated to deflect all ions including and below m/z = 40. This corresponds to a time delay setting of $\Delta t_2 = 1.95$ μs, with the voltage dip of 50 V, for 2 μs. It is shown in Fig. 2.10 ('Pulser ON' trace) that the pulser efficiently deflects (most) ions below the set threshold, and does not affect the measurement of $(Ar)_2^+$. This deflection window can be shorter, down to 0.2 μs, however, for the purpose of this test, it is kept wide. With the pulser deflecting the ions, the MCP voltage is increased in three steps and this corresponds to the S/N of the peak at m/z = 80, equal to 420, shown Fig. 2.11. In comparison the to the measurements with the pulser off, it as an improvement by a factor of 18. Under the assumption that the gain of the detector is similar in the mass range between m/z = 36 - 80, we estimate that the new LoD for MATRI^{2}ICES is equal to 3×10^{11} molecules cm^{-2}.

2.6   Conclusion

MATRI^{2}ICES is an experimental system using Laser Desorption Post Ionization Time-of-Flight Mass Spectrometry to probe and quantify photon-triggered processes in interstellar ice analogues. In the field of astrochemistry this is a unique setup. In this section the setup has been described, along with the key calibration experiments and measuring techniques, proving its potential to investigate the VUV photolysis of interstellar ices.

3 | Novel approach to distinguish between vacuum UV-induced ice photodesorption and photoconversion

Abstract

In cold regions of the interstellar medium (ISM) with intense ultraviolet (UV) radiation fields, photodesorption has been suggested as a nonthermal desorption mechanism promoting the transition of molecules from the solid state to the gas phase. Laboratory experiments measuring photodesorption rates are crucial in attempting to explain high molecular gas phase abundances of species that are expected to form in the solid state, such as methane, methanol, and acetonitrile, and to aid astrochemical modeling. Due to the convoluted competition between photodesorption and photoconversion, it is far from trivial to derive accurate photodesorption rates. In this chapter a new methodology is described that aims at discriminating between the two processes. The method has been validated using the well-studied case of CO and extended to CH_4, CH_3OH, and CH_3CN. Comparing the laser desorption post ionization time-of-flight mass spectrometry (LDPI TOF MS) of the ices with and without the Ar coating provides information on the different interactions of the VUV photons with the ice. We show here that the newly developed experimental technique allowed for a derivation of photodesorption rates for ices at 20 K of: CO $(3.1 \pm 0.3) \times 10^{-3}$ mol. photon^{-1}, CH_4 $(3.1 \pm 0.5) \times 10^{-2}$ mol. photon^{-1}, and upper limits for CH_3OH ($<6 \times 10^{-5}$ mol. photon^{-1}) and CH_3CN ($<7.4 \times 10^{-4}$ mol. photon^{-1}); in the latter case, no literature values have been reported yet. Photoconversion cross sections are presented in the 7-10.2 eV range. The possible role of photodesorption and photoconversion in the formation of interstellar COMs is discussed.

3.1 Introduction

Astronomical observations show that the interstellar medium (ISM) contains many different complex organic molecules (COMs), which, by definition, are carbon bearing species made up from six or more atoms (Herbst & van Dishoeck 2009). As their gas phase formation rates are low, it is generally accepted that COMs form on icy dust grains, as shown in a number of dedicated laboratory experiments (Gerakines et al. 1996; Watanabe & Kouchi 2002; Fuchs et al. 2009; Fedoseev et al. 2015a; Abplanalp & Kaiser 2019). Thermal desorption efficiently releases ice species into the gas phase (Collings et al. 2004); however, COMs are also observed in interstellar regions with temperatures well below their thermal desorption temperatures, requiring alternative mechanisms to explain the observed gas phase abundances (Cernicharo et al. 2012; Guzmán et al. 2013; Vastel et al. 2014; Öberg et al. 2015; Goto et al. 2021). In recent decades, a number of mechanisms have been investigated in an attempt to explain the nonthermal desorption of frozen molecules. These include direct cosmic-ray-induced desorption, X-Ray-induced desorption, vacuum ultraviolet (VUV) photodesorption, reactive desorption, and different types of codesorption (Dartois et al. 2015; Dupuy et al. 2017, 2018; Chuang et al. 2018b; Ligterink et al. 2018b; Oba et al. 2018).

In particular, VUV photodesorption is considered to be an effective mechanism with regard to CO ice high rates on the order of 10^{-3} to a few times 10^{-2} mol. photon $^{-1}$, which were determined in the laboratory (for an overview see Fig. 5 in Paardekooper et al. 2016 and references therein). As a result, state-of-the-art astrochemical gas-grain models include photodesorption rates based on laboratory works (Garrod & Pauly 2011; Walsh et al. 2014a; Kalvāns 2015). However, the number of molecules studied in laboratory experiments is limited. Models commonly use a rate of 10^{-3} mol. photon $^{-1}$ when no value has been reported.

A major challenge in an experimental ice VUV photolysis study boils down to separating multiple phenomena that can happen within the ice upon photon absorption.Fig. 3.1 is a simplified summary of feasible processes in solid state species on a grain surface in cold regions in the ISM or in laboratory experiments on a gold-coated copper substrate. A molecule embedded in the ice matrix is electronically excited by an absorbed photon (1). Upon relaxation back to the ground state (2), the molecule can transfer its energy to neighboring species, followed by the neighbor's desorption (3a, indirect desorption as in Bertin et al. 2013; van Hemert et al. 2015). Alternatively, the excited species can directly photodesorb (3b) or photodissociate (4). The latter process can be followed by dissociative photodesorption (3c, transfer of excited radicals into the gas phase demonstrated in Muñoz-Caro et al. 2010; Fillion et al. 2014), the "kick-out" of a fragment or parent species by an excited radical (3d, e.g., kick-out of H_2O or OH by an energetic H atom as in (Andersson & van Dishoeck 2008)), or product formation (5). If the newly formed species are in an excited state, they either desorb (3e - reactive photodesorption and photochemidesorption as in Martín-Doménech et al. 2016 and Andersson et al. 2008) or dissipate their energy and remain in the ice (6). The photodissociation branch is typically accessible when a molecule is excited by a photon that carries more energy than the bond dissociation energy (BDE). In that case, chemical bonds can be broken, which is the origin of radical species. The radicals at 20 K have a limited mobility; however, for small fragments, such as H or OH, diffusion across a few layers of ice may occur (Andersson & van Dishoeck 2008). Alternatively, if radicals are near each other, they react with little
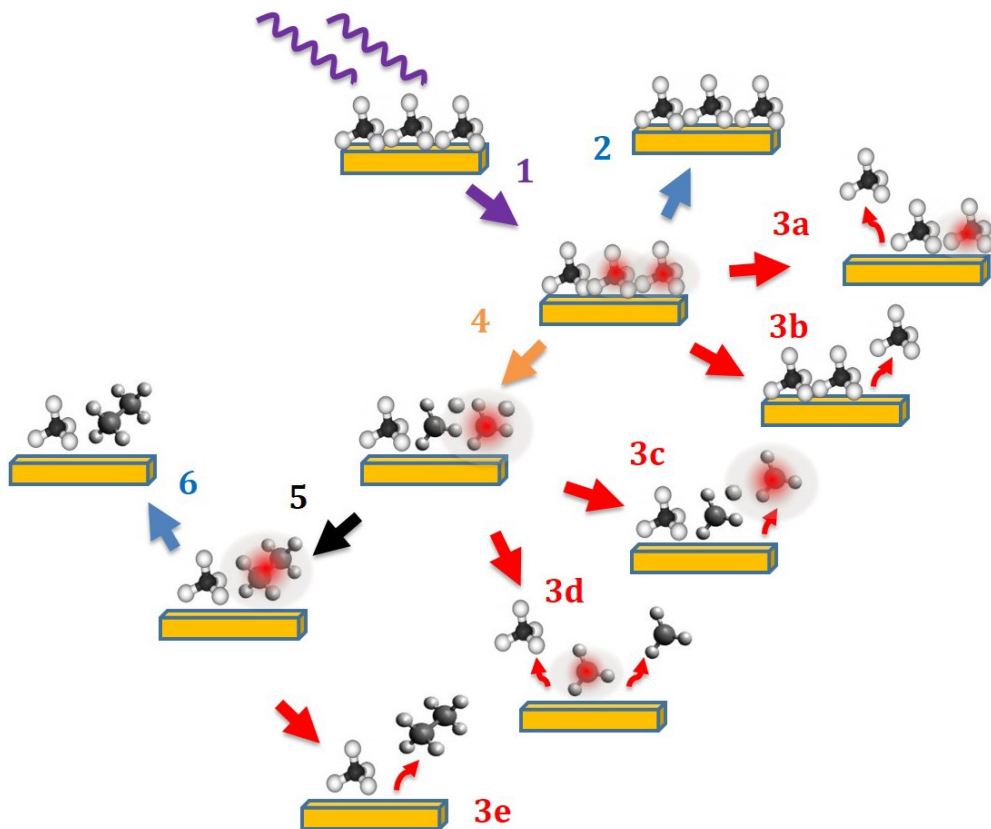
Figure 3.1: Competition between processes taking place in solid state species upon an absorption of a photon. Photodesorption processes (in red) are only possible for the top layers of the ice. All other processes can happen in both the ice bulk and surface. The schematic applies to ices at a temperature excluding thermal desorption, typically ≤ 20 K.

or no barrier to form larger molecules. The desorption processes described above (3a, 3b, 3c, 3d) are expected to occur for molecules in the surface layers of the ice. It has been shown that for CO ice, only the top 3 ML (1 ML = 10^{15} molecules cm^{-2}) can be photodesorbed, which are considered surface layers in this work (Bertin et al. 2012).

Besides photodesorption, a decrease in the abundance of the parent species is caused by photoconversion. Here, the photoconversion rate is characterized by a combination of the following two solid state processes: photodissociation, followed by recombination reactions into species other than the parent molecule, that is, photoproducts, and reactions of nondissociated, photoexcited molecules, with neighboring neutral species, which also lead to the production of other species. The focus in this work is on CO, CH_4, CH_3OH, and CH_3CN.

In order to simulate interstellar radiation fields in a laboratory setting, we used a light source with the photon energy range 7-10.2 eV. In this range, CO, the second most abundant molecule in the ISM, does not dissociate (BDE of CO is 11.16 eV from Kalescky et. al (2013)); therefore, it is a relevant and an "easy" case to study. During CO ice photoprocessing, the decrease in an abundance of CO can be linked to intact

photodesorption. For this reason and the fact that CO is an abundant constituent of the interstellar ices, CO photodesorption has been studied in much detail by several research groups. The first experiments monitored the initial amount and subsequent loss of CO ice (as a function of VUV fluence) using reflection-absorption infrared spectroscopy (RAIRS). During the same experiments, a quadrupole mass spectrometer (QMS) signal of m/z=28 can be recorded, which allows for the calibration of the gas phase QMS readings to the decline of the abundance of solid state CO detected by infrared (IR) spectroscopy (Öberg et al. 2009e; Fayolle et al. 2011).

A limitation of the IR-based method is that similar vibrational modes of different species may overlap. This is particularly true for COMs. In addition, unknown (temperature and environment dependent) IR band strengths add uncertainty to quantifying results. For molecules with a BDE that is lower than 10.2 eV, it is challenging to disentangle the effects of dissociation and desorption since both these processes simultaneously deplete the parent species. In addition, RAIRS cannot be applied to molecules without IR active modes.

A QMS can be used for a gas phase analysis of desorbed species. In order to quantify results using this method, a mathematical conversion is necessary to correlate the gas phase QMS signal of a molecule (e.g., methane or methanol) to the previously measured gas phase CO signal (i.e., calibrated with solid state C≡O stretching mode in the IR). Factors that need to be considered for this conversion are the setup and the molecule specific QMS detector sensitivity, varying pumping speeds for different molecules, electron ionization cross-sections, and fragmentation patterns. For a discussion on the calibration see Zhen & Linnartz (2014).

Methane has been identified as a component of ice mantles toward multiple sources (e.g., Young Stellar Objects) in abundances ranging from 1 to 10 % with respect to H_2O (Boogert et al. 2015). The detection has motivated multiple experimental studies, which show that, in contrast to CO, methane can be dissociated by impacting photons with an energy below 10.2 eV (H−CH_3 bond energy of 4.5 eV from Ruscic 2015). Hence, methane photolysis is an example of the competition between photodesorption and photodissociation followed by an increasing chemical complexity. Pure ice photolysis results in various products including C_2H_2, C_2H_4, C_2H_6, and larger hydrocarbons (Gerakines et al. 1996; Paardekooper et al. 2014; Lo et al. 2015). The dissociation results in effective branching ratios of CH_3:CH_2:CH equal to 95:4:2 (Bossa et al. 2015), which is quite different from similar studies performed in the gas phase (Gans et al. 2013). Intact CH_4 photodesorption at 12 K was investigated recently in a wavelength-dependent study at the SOLEIL synchrotron (Dupuy et al. 2017). This work resulted in an intact photodesorption rate of 2.2×10^{-3} mol. photon^{-1} in a photon energy range of 9.1 - 13.6 eV. The photodesorption yield in that range follows the trend of the absorption spectrum of solid state methane. To date, this is the only published measurement of intact methane photodesorption. In 2016, reactive photodesorption of H_2CO from a photoprocessed CH_4:H_2O mixture was demonstrated, whereas intact photodesorption was not (Martín-Doménech et al. 2016), which suggests that multiple desorption mechanisms play a role in understanding the process as a whole.

Solid state methanol has been detected as a significant component of the ice mantles of interstellar dust grains with abundances varying between 3 % and 12 % with respect to water in dense clouds (Chiar et al. 1996; Boogert et al. 2011). VUV processing of methanol ice yields more complex organics, including methyl formate, glycolaldehyde, ethylene glycol, and many others, thus making methanol one of the pillars of the inter-

stellar chemical network (Gerakines et al. 1996; Öberg et al. 2009c; Boamah et al. 2014; Henderson & Gudipati 2015; Maity et al. 2014; Paardekooper et al. 2016b; Chuang et al. 2017). Öberg and coworkers in 2009 were the first to study the photodesorption of methanol. A partial decrease in the IR signature was assigned to intact photodesorption and a rate of $(2.1 \pm 1.0) \times 10^{-3}$ mol. photon^{-1} was derived (Öberg et al. 2009c). Photodesorption and photodissocation were fit separately by explicitly assuming that photodesorption is a 0th order surface and photodissociation is mainly a 1st order bulk process. In 2016, a study by Cruz-Diaz et al. determined an upper limit for intact methanol desorption to be in the 10^{-5} mol. photon^{-1} range. Simultaneously, Bertin et al. (2016) measured photodesorption of methanol in a wavelength-dependent study, using the VUV DESIRS beamline at the SOLEIL synchrotron facility. The average photodesorption rate derived for the UV interstellar radiation field profile (Mathis et al. 1983) was $(1.2 \pm 0.6) \times 10^{-5}$ mol. photon^{-1}. The measured photodesorption was proposed to result from a recombination reaction of the CH_3O or CH_2OH radical with a hydrogen atom. The same study also demonstrated the dissociative photodesorption of CH_3, OH, and H_2CO at similar efficiencies to intact photodesorption. Both laboratory studies of Bertin et al. 2016 and Cruz-Diaz et al. 2016, find lower photodesorption rates of methanol by 2-3 orders of magnitude compared to previous work. When the updated laboratory photodesorption rates were applied to gas grain astrochemical models of protoplanetary disks, it was concluded that photodesorption alone is insufficient in explaining the observed gas phase methanol abundances and that other mechanisms have to be invoked (Ligterink et al. 2018b).

Methyl cyanide, or acetonitrile (CH_3CN), has been detected within the Solar System: in Titan's atmosphere (Cordiner et al. 2015), in comet 67P/Churyumov-Gerasimenko (Goesmann et al. 2015), and in cometary comae of Hale-Bopp (Woodney et al. 2002). In addition, there were multiple detections toward sources outside of the Solar System, including molecular clouds Sgr A and Sgr B (Solomon et al. 1971), protoplanetary disks around T Tauri stars (Bergner et al. 2018), and high and low-mass protostars (Purcell et al. 2006; Calcutt et al. 2018). CH_3CN has also been recently detected to be a part of the icy mantle in a circumstellar disk around V883 Ori. The detection was possible due to a shifted sublimation front, which was caused by an outburst of a young star (Lee et al. 2019).

Acetonitrile (CH_3CN) plays an important role in the nitrile-based chemistry. With available solid state formation routes (Garrod et al. 2008) and a high thermal desorption temperature ($\sim$140 K in laboratory conditions), energetic processing of CH_3CN ice becomes an important subject. It has been investigated in a number of largely qualitative studies (Hudson & Moore 2004; Abdulgalil et al. 2013). Final products of VUV photolysis of pure acetonitrile have been identified to be as follows: HCN, CH_4, $(CH_2CN)_2$, and isomerization to CH_3NC and H_2CCNH (Hudson & Moore 2004; Hudson et al. 2008). Ion-irradiation and hydrolysis of $CH_3CN:H_2O$ mixtures yield a variety of amino acids (Hudson et al. 2008), which supports CH_3CN as an important element of the N-bearing chemical network. A quantitative photodesorption study of acetonitrile ice is currently lacking. This is due to experimental challenges associated with disentangling VUV-induced solid state processes. In this work, we address these challenges by applying our new measurement method.

3.2   Experimental

In order to provide more insight into the photon-driven competition in the solid state, we developed a new method to measure photodesorption rates of COMs. VUV irradiated ices at 20 K are first studied as a pure ice species and subsequently with a protecting argon (Ar) coating on top. The latter quenches photodesorption, which becomes clear when comparing the time-of-flight mass spectra of the probed (un)coated ices. The following subsections provide information on the experimental setup, measurement principle, and applied methodology.

3.2.1   Setup overview

The experiments were carried out in MATRI^{2}CES (Mass Analytical Tool for Reactions in Interstellar ICES), an ultra-high vacuum (UHV) apparatus. A thorough description of the system is given by Paardekooper et al. (2014) and in Chapter 2.

The vacuum system consists of two parts: a main chamber and a time-of-flight chamber, which are connected with each other by a gate valve. Both are evacuated by turbomolecular pumps, which are supported by a prepump. The base pressure in the chambers, measured by inverted magnetron gauges, is in the 10^{-10} mbar range. The pressure is comparable to a density of 10^7 H$_2$ particles cm^{-3} which, combined with low temperature, make for a reasonable representation of a dense cloud core. In the main chamber, a gold-coated copper block serves as a nonreactive substrate onto which the ices are grown. It is in thermal contact with a closed-cycle helium cryostat, which allows for surface temperatures as low as 20 K. The temperature of the substrate is controlled by a thermocouple and a resistive heater connected to a temperature regulator. The available temperature range is between 20 and 300 K, and it is set with an absolute precision of less than 1 K. The cryostat is mounted on a two-dimensional translation stage. A stepper motor allows for automized control of the position of the substrate and of the ices that are grown onto it in the vertical direction (z-axis). In the horizontal direction (y-axis), manual control is supported by a translation stage.

Ices are formed on the substrate via front deposition, which is controlled by a calibrated high precision leak valve. The gas mixing line is evacuated by a turbomolecular pump that is supported by a scroll pump, which allows pressures in the 10^{-4} mbar range. Samples in both the gas phase and liquid phase can be introduced to the main chamber. In the experiments, we used CO (Linde, 99.997 %), CH$_4$ (Praxair, 99.999 %), CH$_3$OH (Sigma-Aldrich, Chromasolv, 99.99 %), CH$_3$CN (VWR, < 10ppm of water), CD$_3$CN (Sigma-Aldrich, $\geq$ 99.8 % D), and Ar (Linde, $\geq$99,999 % Ar). To prevent contamination from the air, all liquid samples were taken through two freeze-pump-thaw cycles prior to deposition. The front deposition proceeds at an angle of 85° with respect to the substrate's surface plane.

The spectral energy distribution (SED) of the interstellar radiation field includes Lyman-α (121 nm), a molecular H$_2$ emission continuum (130 - 165 nm), and can be closely simulated by a microwave discharge hydrogen lamp (MDHL). To accurately determine the photoprocessing rates, it is crucial to calibrate the wavelength dependent flux of the light source. The SED of the lamp is strongly dependent on its operational conditions (Ligterink et al. 2015). We used an H$_2$ pressure of 1.44 mbar and 80 W of microwave power, which results in an SED, which is shown in Fig. 4 in

Paardekooper et al. (2016c). The lamp is attached to the chamber via a MgF$_2$ UHV viewport, which directly faces the substrate. To measure the emitted photon flux, a calibrated silicone photodiode was placed at the position of the substrate (following the approach in Paardekooper et al. 2016c). The measured photocurrent includes contributions from photons in both VUV and visible ranges. In order to specifically determine the VUV flux, at the same plasma conditions, we operated a sealed lamp with a glass seal inserted between the lamp and MgF$_2$ window, which absorbs photons at $\lambda < 300$ nm and transmits at 90 % efficiency in the visible range. The difference in the photocurrent ($i(\lambda)$) between the two lamp settings was used to calculate the VUV photon flux contribution. The flux, $F(\lambda)$, was determined to be $(2.5 \pm 0.5) \times 10^{14}$ photons cm^{-2}s^{-1}, using the equation below:

$$F(\lambda) = \frac{i(\lambda)}{e \cdot \epsilon(\lambda)}.$$ (3.1)

It takes the quantum efficiency of the photodiode, $\epsilon(\lambda)$, and the elementary charge, e, equal to 1.602 x 10^{-19} C, into account.

Probing the photoprocessed ice is done with laser desorption post-ionization time-of-flight mass spectrometry (LDPI TOF-MS). It should be noted that this laser-induced desorption is, in fact, nothing more than a direct ablation process, which is not related in any way with the VUV-induced processes we want to study here. In the following, we use "ablation" to avoid confusion. For ablation, a Nd:YAG laser's third harmonic frequency is used. The 3-4 ns pulses at 355 nm carry up to 3-11 mJ per pulse (molecule-dependent) at 5 Hz. The unfocused beam is trimmed to a diameter of 1 mm and pointed toward the substrate at an angle of 30°. Synchronization of the vertical motion of the substrate and laser shots allows one to probe a "fresh" spot with every laser shot. Each shot desorbs a plume of material that floats in the direction orthogonal to an ionizing sheet of electrons (70 eV). After an optimized time delay, generated cations are extracted from the main chamber into the field-free time-of-flight tube. The ions are reflected using a reflectron at the end of the flight tube. The reflectron increases the separation between ions with a different m/z and minimizes the initial velocity distribution within the desorption plume. After reflection, the ions pass through the field-free tube again and are detected with a 40 mm micro-channel plate (MCP) detector. The signal from the detector is recorded via a data acquisition card (DAQ) as the voltage versus time delay, which can be converted to a mass over charge ratio. Timing of the laser shots, ion extraction, and data acquisition is set through a delay generator and is controlled via a custom-made Labview routine. Typically 85 TOF spectra, which correspond to fresh spots along one column on the substrate, are collected and averaged to one mass spectrum. Afterwards, the substrate can be manually moved to a different y-axis position and the measurement can be repeated to probe the effects for further increasing VUV fluence.

3.2.2   Thickness measurements

The ice deposition procedure has been calibrated using a series of measurements with an intensity stabilized He-Ne laser (Hudgins et al. 1993). For each ice growth, the gas pressure in the mixing line, needle valve setting, and temperature are recorded. During the deposition, a photodiode records a laser interference pattern as the laser beam is reflected from the ice surface and the substrate. The equation expressing the

ice thickness (d) as a function of the number of interference fringes (m) is given by:

$$d = \frac{m \cdot \lambda}{2 \cdot \frac{n_1}{n_0} \cdot \cos \theta},$$

(3.2)

where λ is the wavelength of the He-Ne laser (632.8 nm), n_0 and n_1 are refractive indices of the vacuum and ice, and θ is the angle of refraction (3). The growth rate (τ, in molecules $cm^{-2}s^{-1}$) can be determined from:

$$\tau = \frac{d \cdot \rho \cdot N_A}{M \cdot t},$$

(3.3)

where t is the time corresponding to the thickness d (calculated in Eq. 2), N_A is Avogadro's number (6.022×10^{23} mole^{-1}), ρ is the ice density in (g cm^{-3}), and M is the molar mass of the species (in g mole^{-1}). The ice thickness (in molecules cm^{-2}, or mol. cm^{-2}) has the same units as column density and is controlled by changing the deposition time while keeping all of the other parameters constant.

We performed these measurements for Ar, CO, CH_4, CH_3OH, and CH_3CN. Respective densities and refractive indices used to calculate the growth rates are: 1.76 g cm^{-3} (Dobbs et al. 1956) and 1.29 (Sinnock & Smith 1968); 0.8 g cm^{-3} and 1.27 (Roux et al. 1980); 0.4 g cm^{-3} and 1.329 (Brunetto et al. 2008); and 0.64 g cm^{-3} (Luna et al. 2018) and 1.33 (Weast 1972), 0.8 g cm^{-3}, and 1.34 (assumed to be the same as for liquid at room temperature (Riddick et al. 1986)). The deposition method allows one to reproduce ices with the thickness varying within 5-10 %. This was concluded after a comparison of time-of-flight signals probing nonoverlapping spots across the substrate surface.

The laser interference calibration method is limited to ices for which refractive indices are known (pure species). This might change as a result of a recently introduced new broad band technique, which holds the potential to also derive such parameters for mixed ices (Kofman et al. 2019).

3.2.3 Experimental procedure

A series of two structurally different experiments were performed for each of the ices. The first experiment probed the effects of VUV photoprocessing of an ice at 20 K (photodissociation, photodesorption, radical recombination). For the second experiment, an additional layer of Ar (around 50 ML) was deposited on top of the ice of interest, while the same procedure was utilized to probe the VUV photoprocessing of the ice. Here, it should be noted that given the large volume of the sample holder, 20 K is the lowest temperature that is achievable. This temperature is several Kelvin higher than the typical 12-15 K values used in previous ice experiments, but it is still well below the accretion onset of CO and other astronomically relevant species in the ISM. The extra Ar layer is added to fully quench the photodesorption process; surface species, typically restricted to the upper few monolayers, are prohibited from leaving the surface; photodissociation, however, can still take place, like in the original ice without Ar coating. At 20 K, diffusion of molecules or an energy transfer between more than a few monolayers is negligible (Cuppen & Herbst 2007). Therefore in experiments with the Ar layer, intact, dissociative, and reactive photodesorption (being surface or subsurface processes) are effectively quenched. Ar, as a noble gas, does not

react with our species of interest. Moreover, it does not absorb light in the VUV range (Schnepp & Dressler 1960), which allows for a comparison of coated and uncoated experiments (same flux). The direct consequence of this approach is that a difference between the (un)coated ices can be directly linked to a difference that originates from photodesorption and photoconversion compared to photoconversion only.

To understand the principle concept of the method applied here, it is important to realize that we recorded all species remaining in the ice rather than selected species leaving the ice. The resulting mass spectra include contributions from molecular ion peak signals, respectively: m/z=28, 16, 32, 41 for CO, CH_4, CH_3OH, and CH_3CN, as well as molecule-specific fragmentation patterns that arise due to the used electron ionization method.

A previous photodesorption study on CO ice using MATRI^{2}CES demonstrates a linear relation between the integrated signal from a laser-desorbed plume, which was collected and summed up over multiple extraction timings, and the surface coverage and column density in the ice (Paardekooper et al. 2016c). In other words, the intensity of a signal in the MCP detector is linearly dependent on the abundance of the species in the ice. Given the initial column density of the molecule in the ice (see Section 3.2.2), it is possible to monitor its decrease as a function of VUV fluence by recording mass spectra as a function of irradiation time. This is confirmed for methane for a constant extraction time; this can be seen in Figure 3.2, which shows the integrated molecular ion signal at m/z=16 as a function of ice thickness as well as the characteristic fragmentation pattern resulting from the electron impact ionization. The linear dependence of the signal is demonstrated for ices of up to 150 ML. In our photodesorption experiments, the maximum ice thickness amounts to 105 ML, that is, in a range where the signals can be used to determine the methane column density. This procedure along with well-calibrated deposition rates, allows for the recording of absolute column density of the species throughout experiments.

We recorded the LDPI TOF-MS spectra of pure ices for all of the species under investigation. These spectra directly correspond to the fragmentation pattern of the molecules as available on the NIST database. During our analysis, the fractional contribution of fragments of the parent species were subtracted from their respective m/z signals and added to the molecular ion signal. By using this method, we were able to trace the fragments of photoproducts (along the same channels as the fragments of the parent species), which were being formed during the experiments. It should be noted that the fragmentation pattern of any photoproduct does not overlap with the molecular ion peak of the parent and, therefore, it does not complicate the analysis.

There is a fundamental limitation to photolysis experiments. Ideally, an experiment would entail thin ices and long irradiation times, which allow for spread-out data that expose the subtle, surface photodesorption process. However, when photodissociation is an available channel, the parent species deplete rapidly, which increases the difficulty of tracing subtle photodesorption processes. For each species, we used a different initial ice thickness and total photon fluence. We ensured that all ices were at least 5 ML or thicker during the full experiment; as for thinner ices, the photodesorption may run into a nonlinear regime (Muñoz Caro et al. 2010; Fayolle et al. 2011). The particular thicknesses for methane and methanol experiments (55 and 40 ML) were motivated by previous studies performed on the setup with the aim to compare our results against previously published work (Bossa et al. 2015; Paardekooper et al. 2016b). In case of acetonitrile (8ML), we chose to deposit a thin ice to magnify the surface versus
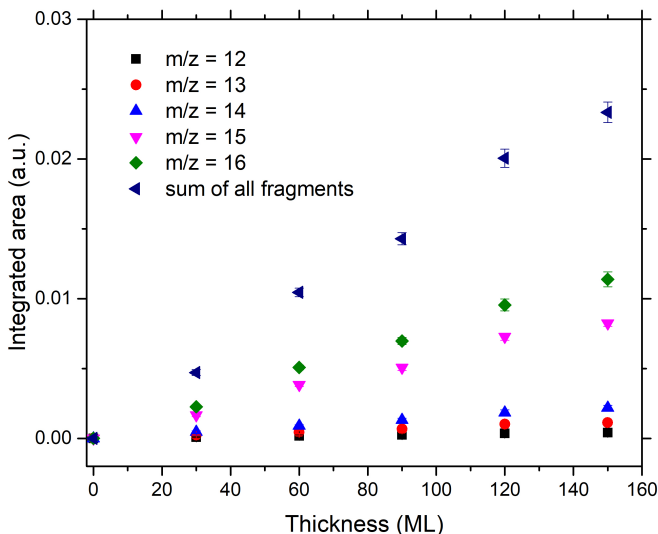
Figure 3.2: Linear dependence between the thickness of the ice and intensity of methane mass peaks, arising from the electron ionization. Thickness is given in monolayers (1 ML = 10^{15} molecules cm^{-2}).

the bulk processes. A drawback specific to our method is that the Ar cap, despite being inert, may increase the efficiency of chemistry on the ice surface. Quenching the photodesorption of radicals, allows for a higher probability that their recombination forms bigger species in the ice (not necessarily back into the parent), also known as the "cage effect". Previous studies show an efficiency of dissociative photodesorption for methanol to be between 10^{-5} - 10^{-6} mol. photon $^{-1}$ (Bertin et al. 2016). However, only a fraction of these photodesorbed fragments would have recombined into the parent and therefore influenced the rates derived here. The efficiency of this process is likely to be molecule dependent and in this work it is assumed to be below the detection levels.

Associated with our method of probing the ice by laser ablation is also a possibility of thermally triggered chemistry. That effect can only be seen when using full laser power for the capped ices. To prevent that, the laser power was tuned to the minimum, thus still allowing a good time-of-flight signal.

3.2.4   Analysis methods

We derived the photodesorption rates by fitting a linear function to the difference between Ar coated and uncoated ice photolysis experiments. The next analysis step is applicable to molecules that photodissociate within the used photon energy range: methane, methanol, and acetonitrile. When an Ar layer quenches photodesorption, a decrease in the abundance of the parent species is caused by photoconversion. A photoconversion cross section can be derived by fitting the coated experimental data

with an exponential function:

$$N(t) = N_0 \, e^{-\phi t \sigma_{\text{photoconv}}}, \tag{3.4}$$

where $N(t)$ and N_0 are time dependent and initial column densities in mol. cm^{-2}, ϕ is flux in photons cm^{-2}s^{-1}, t is the irradiation time in seconds, and $\sigma_{\text{photoconv}}$ is the photoconversion cross section in cm^2.

Under low VUV fluence, when the recombination reactions in the ice are not very significant, photoconversion following an exponential decay can be approximated by a linear fit. In that case, the slope of the fit yields photoconverted mol. photon^{-1}.

In order to better compare our results to different experimental conditions from other studies, all derived rates (per incident photon) can be converted to effective yields (per absorbed photon). This is discussed in more detail in Section 4.2. This way, experiments with ices of a different thickness and with a different photon flux can be compared. When the intensity of the incident VUV photons, I$_{\text{inc}}$, crosses the ice, the light intensity (I) follows the Beer-Lambert absorption law:

$$I = I_{\text{inc}} \, e^{-\sigma(\lambda)_{\text{abs}} N} \tag{3.5}$$

where I_{inc} is in photons cm^{-2}s^{-1} (see section 3.2.1), σ_{abs} is the average absorption cross-section (in cm^2, taken from the literature), and N is the column density in mol. cm^{-2}. By applying the absorption cross section of species from the literature (an average value for the wavelength range 120-165 nm), we can determine how many photons are absorbed by a specific ice column density. For example, for CO (see the next subsection), the absorption cross section is 4.7×10^{-18} cm^2 and the top 3 ML absorb $\sim$1.5 % of photons, while the whole ice, 21 ML absorb 10 % of incident photons (Cruz-Diaz et al. 2014).

3.2.5   Proof of concept with CO

Carbon monoxide is one of the most abundant constituents of the ice mantles on interstellar dust grains, yet, it is also detected in the gas phase in regions where the temperature is below its freeze-out (Willacy & Langer 2000). That motivated detailed experimental studies of photodesorption of CO (Öberg et al. 2009b; Muñoz Caro et al. 2010; Fayolle et al. 2011; Chen et al. 2013; Paardekooper et al. 2016d). It makes a good case study because the BDE of the C≡O bond, 11.16 eV, excludes photodissociation in our experiments (Kalescky et al. 2013). The CO ionization potential is well above the used energies. The photodesorption rates across previous studies are consistent and range from 10^{-3} to a few times 10^{-2} mol. photon^{-1}. The differences are most likely associated with varying experimental conditions (deposition and sampling temperature, spectral energy distribution, and flux of the used VUV lamps).

Two distinct experiments have been performed on CO ice at 20 K. In the first experiment, a pure layer of CO ice (thickness = 21 ML) was irradiated with VUV photons and LDPI TOF mass spectra were recorded at different irradiation times. During the second experiment, an additional Ar layer of about 50 ML was deposited on top of the 21 ML of CO. In both experiments, the ice was irradiated with a fluence of about 4.4×10^{18} photons cm^{-2}. Figures 3.3 and 3.4 show TOF mass spectra taken at different VUV fluences. For clarity purposes of the plot, we show four out of six spectra taken at different times during the experiment. Figure 3.3 demonstrates decreasing
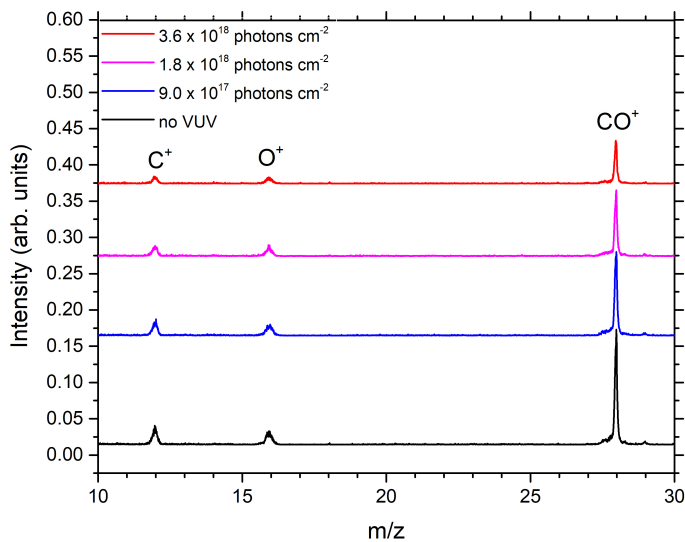
Figure 3.3: LDPI TOF mass spectra of CO ice acquired at different VUV fluences. An offset between mass spectra has been inserted for clarity as is the case for other figures in this work.
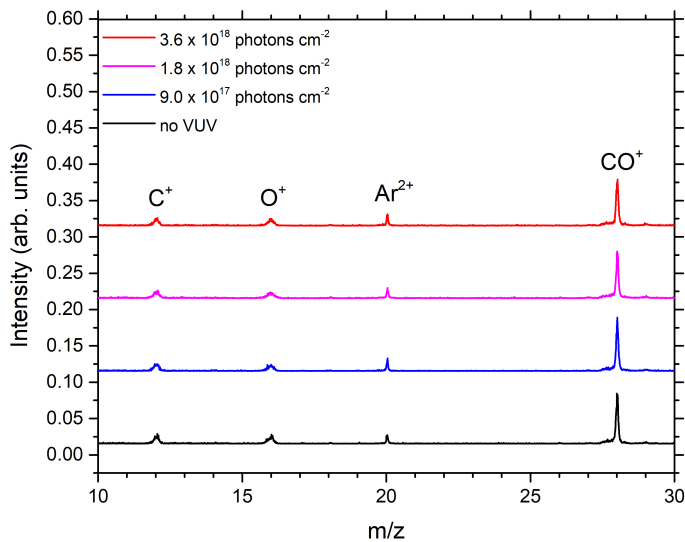

Figure 3.4: LDPI TOF mass spectra of CO with Ar coating acquired at different VUV fluences.
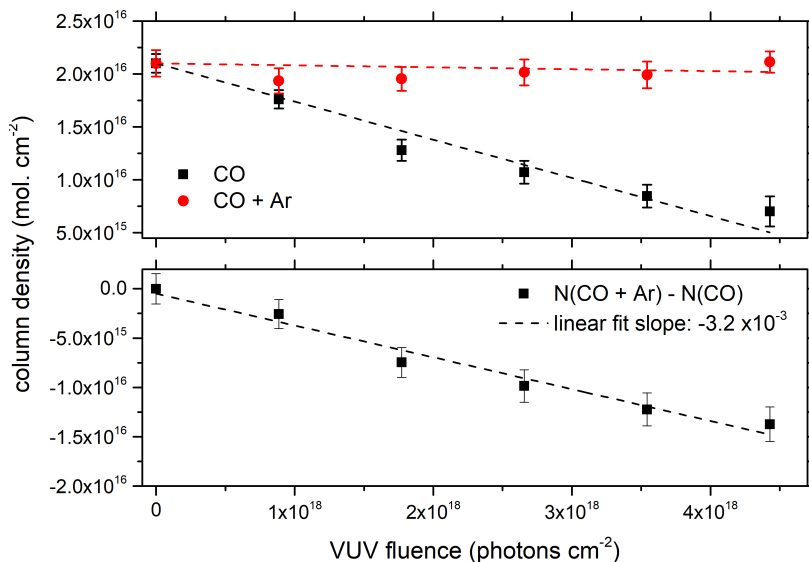
Figure 3.5: Upper panel shows CO abundance during the photolysis of CO with and without the Ar coating at 20 K. Bottom panel represents the difference between the CO and CO+Ar experiments resulting in a CO photodesorption rate.

intensities of peaks at m/z = 12, 16, and 28, which can be directly linked to ongoing photodesorption. In Fig. 3.4, intensities of CO peaks stay constant, which means that the Ar layer effectively quenched photodesorption.

In order to calculate the intensity of each peak, a Pearson IV function was fit (Castellanos et al. 2018). A Pearson IV distribution, unlike a Gaussian, allows for peak asymmetry and therefore provides a very good fit for our experimental data. The error bars shown on plots were calculated with the root-mean-square over the residual within one standard deviation from the center of the m/z peak.

To derive the photodesorption rate, we calculated the difference in CO abundance between the two experiments (i.e., CO+Ar and CO) for every data point and we fit a linear function to obtain the slope as shown in Fig. 3.5. The analysis yields an average photodesorption rate of $(3.1 \pm 0.3) \times 10^{-3}$ mol. $photon^{-1}$ in the 7 - 10.2 eV range, which is in agreement with previous studies. As mentioned in the Introduction, reactions involving photoexcited CO should be considered. We calculated the efficiency of the CO to CO_2 conversion in our experiments to be at 3.5 % after a fluence of 4.4×10^{18} photons cm^{-2}. This constitutes a minor depletion channel for CO and is in fact within the photodesorption experimental error.

The strength of our method is in comparing the same molecular peaks between two experiments, which eliminates the uncertainty related to calibrating the QMS detector (Martín-Doménech et al. 2015a), overlapping IR bands and their absorption coefficients, measuring molecule-dependent pumping speeds, different fragmentation patterns, etc. This illustrates that our photodesorption measurement method works well as it reproduces previous literature values.

3.3   Results

3.3.1 CH_4

Solid state CH_4 strongly absorbs light around Ly-α with an average cross-section value of 5.7×10^{-18} cm^2 for the wavelengths 120-165 nm, while demonstrating almost no absorption at longer wavelengths of the MDHL lamp spectrum (Cruz-Diaz et al. 2014b). The decrease in the methane ice abundance in the photolysis experiments is due to photoconversion (in the bulk and on the surface) as well as photodesorption (only on the surface).

Figure 3.6: CH_4 abundance during the photolysis of CH_4 with and without the Ar coating at 20 K. Bottom panel represents the difference between the CH_4 and CH_4+Ar experiments resulting in a CH_4 photodesorption rate.

Methane ice of 55 ML was deposited at 20 K and irradiated by a fluence of up to 2.3×10^{17} photons cm^{-2}. In the following experiment, an additional Ar layer of about 50 ML was deposited on top of the 55 ML methane ice and the same experimental procedure was followed. The resulting mass spectra have been analyzed using the procedure described in Sections 3.2.3 - 3.2.5. The upper panel of Fig. 3.6 shows integrated mass peaks of methane (contributions from m/z = 12, 13, 14, 15, 16) for the two types of experiments. The bottom panel shows the difference between the experiments due to photodesorption. It is fit by a linear function resulting in an average photodesorption yield for methane of $(3.1 \pm 0.5) \times 10^{-2}$ mol. photon^{-1} in the 7 - 10.2 eV range.

During the analysis of the coated experiment, the unique process that depletes the methane abundance is photoconversion. Given the low total photon fluence, more than 70 % of the original species were left in the ice at the end of the experiment. We applied a linear fit to coated methane photolysis data and derived an incident pho-
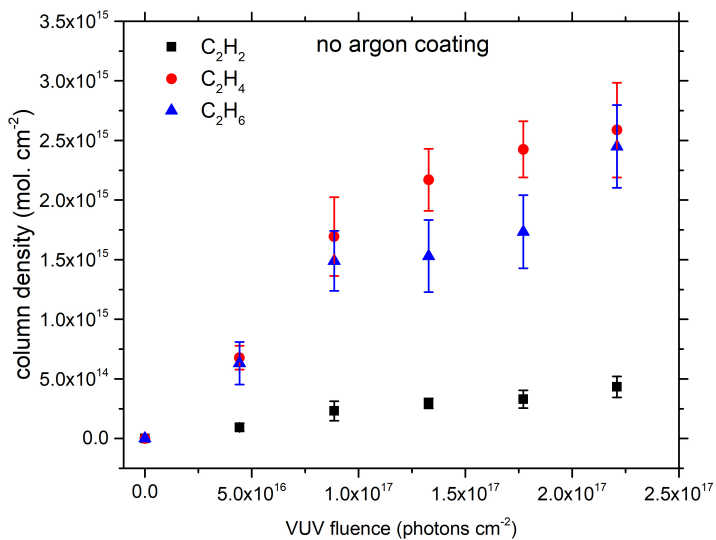
Figure 3.7: The obtained C_2H_2, C_2H_4, C_2H_6 kinetic curves for photolysis of CH_4.
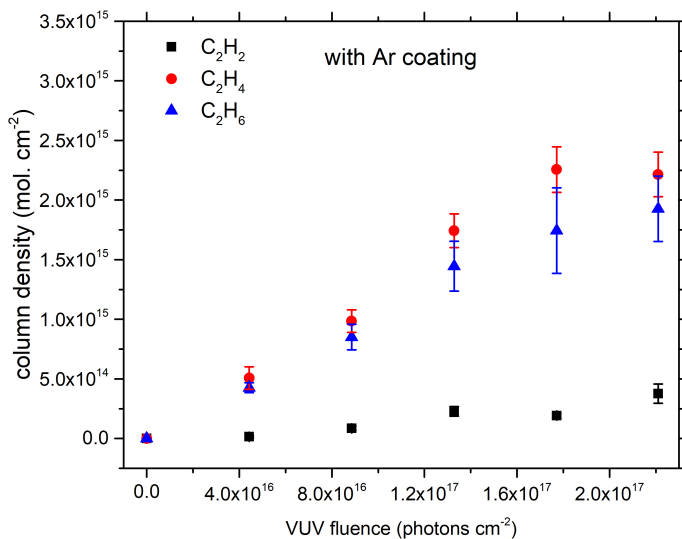
Figure 3.8: The obtained C_2H_2, C_2H_4, C_2H_6 kinetic curves for photolysis of CH_4+Ar.

toconversion rate of 7×10^{-2} mol. photon^{-1}. First order photodissociation products are the following radicals: CH, CH$_2$, and CH$_3$· Given their high reactivity, it is not possible to detect them directly. Nonetheless, we monitored the relative growth of the following second generation photoproducts: acetylene (C$_2$H$_2$, molecular ion m/z=26), ethylene (C$_2$H$_4$, m/z=28), and ethane (C$_2$H$_6$, m/z=30). During the derivation of the yields, different electron ionization cross sections at 70 eV and resulting fragmentation patterns were taken into account for CH$_4$, C$_2$H$_2$, C$_2$H$_4$, and C$_2$H$_6$ and the ionization cross sections are 3.524, 4.374, 5.115, and 6.422 Å^2, respectively (Kim et al. 2014). Figures 3.7 and 3.8 compare the product formation kinetics for both types of experiments. In both experiments, ethylene is the most abundant product, followed closely by ethane, while acetylene is produced in very small amounts. A contribution from fragments of larger products (C$_3$H$_y$ where y = 4, 6, 8) toward C$_2$H$_x$ (x = 2, 4, 6) was very small; therefore, this was not taken into account.

Theoretically, a difference in yields of the same photoproduct between (un)coated experiments could be assigned to a combination of dissociative and reactive photodesorption. However, as photoproducts mostly form in the bulk of the ice (90 % of the ice volume), these subtle surface effects are not detected in our data. Additional studies on thin, pure C$_2$H$_2$, C$_2$H$_4$, C$_2$H$_6$ ices with and without Ar coating are necessary to investigate their intact photodesorption.

Larger hydrocarbons species were formed in both experiments. It was not our primary focus to investigate the chemical pathways, however it is interesting to note that we recorded signals of large species, containing even up to five carbon atoms (see Fig. 3.11).

3.3.2 CH$_3$OH

The solid state CH$_3$OH absorption spectrum is a decreasing continuum with an average value of 4.4×10^{-18} cm^2 for the wavelengths 120-165 nm (Cruz-Diaz et al. 2014a). The decrease in the methanol ice abundance in the photolysis experiments is due to photoconversion (in the bulk and on the surface) as well as photodesorption (only on the surface).
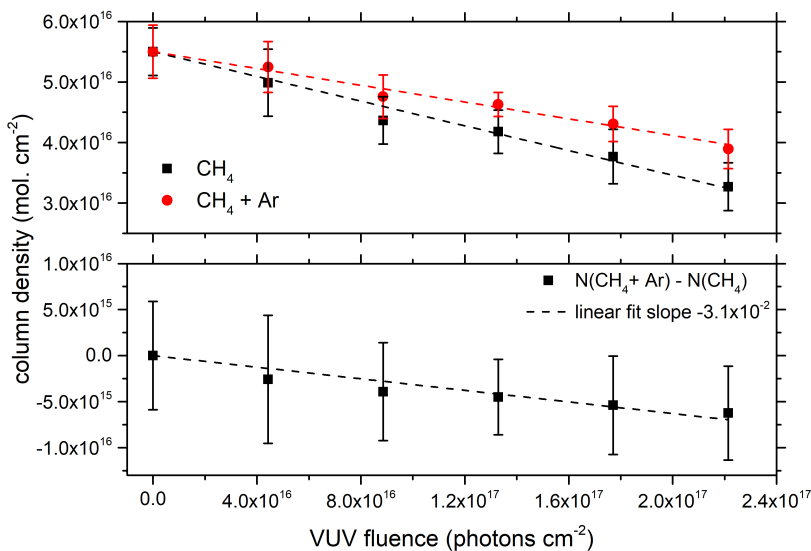
Methanol ice of 40 ML was deposited at 20 K and irradiated by a fluence of 5.3×10^{17} photons cm^{-2}. In the following experiment, we added an Ar layer of about 50 ML and applied the same experimental procedure. Integrated signals of methanol remaining in the ice in both experiments are shown in Figure 3.9 (combined methanol-only contributions to signals at m/z= 15, 29, 30, 31, 32). The upper panel demonstrates no visible difference between the coated and uncoated experiments, which suggests photodesorption to be insignificant. The analysis was performed in the same manner as previously described and it results in an upper limit for the desorption efficiency equal to 6×10^{-5} mol. photon^{-1}. Dissociative and reactive photodesorption processes are also below the detection limits. This is in line with recent studies by Bertin et al. (2016) and Cruz-Diaz et al. (2016). In contrast to photodesorption, the photoconversion of methanol is very efficient. By fitting a linear fit to methanol data, we find a photoconversion rate of 9×10^{-2} mol. photon^{-1} and by the end of the experiment, 70 % of the parent species were converted. The subsequent increase in chemical complexity of methanol photoproducts has been studied extensively before (Öberg et al. 2009c; Paardekooper et al. 2016d). Our data also demonstrate the importance of methanol as a precursor of other solid state COMs in space (e.g., CH$_4$,

Figure 3.9: CH$_3$OH abundance during the photolysis of CH$_3$OH with and without the Ar coating at 20 K. Bottom panel represents the difference between the CH$_3$OH and CH$_3$OH+Ar experiments resulting in a CH$_3$OH photodesorption rate. The lower panel shows the linear fit of a difference between the experiments in an attempt to constrain the upper limit for CH$_3$OH photodesorption rate.

H$_2$CO, HCOOCH$_3$, CH$_3$CHO, see Fig. 3.11).

To confirm that all desorption processes were indeed blocked, we summed up all signals collected by the TOF and tracked the molecular budget during the photolysis, which yields a constant value. We did not take the cross-sections of particular photoproducts into account, but as we compared two experiments with the same products (i.e., same cross sections), this should not affect our conclusion.

3.3.3   CH$_3$CN

A series of experiments with 8 ML of acetonitrile ice at 20 K was performed. A layer of about 50 ML of Ar was used to prevent photodesorption processes. Integrated signals of acetonitrile remaining in the ice in both experiments are shown in Figure 5.1 (combined acetonitrile-only contributions to signals at m/z= 12, 13, 14, 15, 25, 26, 27, 28, 38, 39, 41). Multiple series of experiments do not demonstrate a detectable level of photodesorption, but this allowed us to determine an upper limit. The linear slope of the difference between capped and uncapped experiments yields 7.4×10^{-4} mol. photon^{-1}, which we consider to be an upper limit for the photodesorption of acetonitrile.

CH$_3$CN experiments were run for a fluence of 1.6×10^{17} photons cm^{-2}. During the experiment, 35 % of the parent species were photoconverted. The photoconversion rate derived here is 3×10^{-2} mol. photon^{-1}, which should be considered to be its lower limit since acetonitrile isomerizes to isonitrile and ketenimine, which cannot be

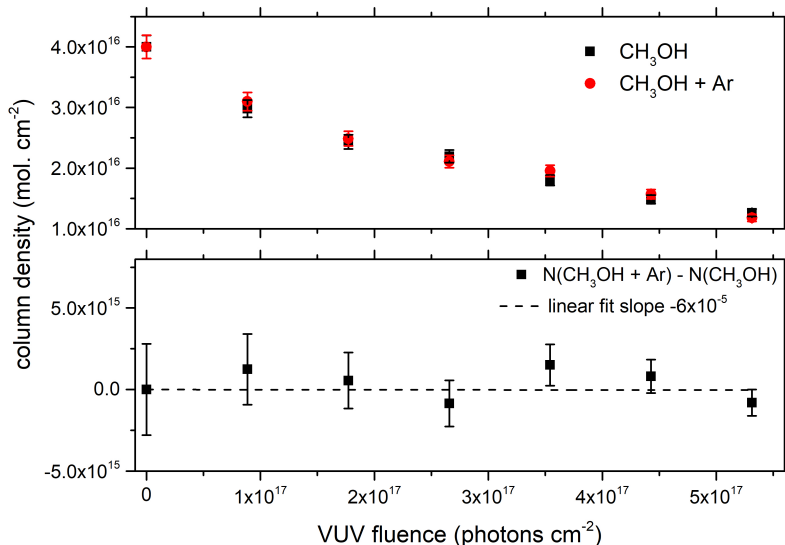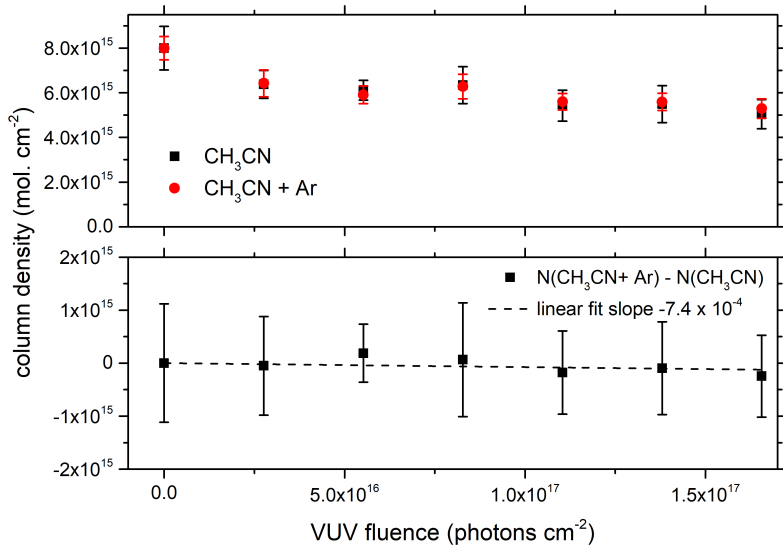**Figure 3.10:** CH$_3$CN abundance during the photolysis of CH$_3$CN with and without the Ar coating at 20 K. Bottom panel represents the difference between the CH$_3$CN and CH$_3$CN+Ar experiments resulting in a CH$_3$CN photodesorption rate. Lower panel shows the linear fit of a difference between the experiments in an attempt to constrain the upper limit for CH$_3$CN photodesorption rate.

separated from the parent species using mass spectrometry (Hudson & Moore 2004). The efficiencies of these processes are unknown, moreover, these two species are not the only photoproducts. Other products, that we could monitor in our experiments, include CH$_4$, HCN/HNC, CH$_3$CH$_2$CN, and even larger species (assignments made on the basis of Hudson et al. 2008, see Fig. 3.11).

3.4 Discussion

3.4.1 Comparison with other studies

Literature values for photodesorption rates of different molecules range between 10^{-1} and 10^{-6} mol. photon^{-1} (e.g., Chen et al. 2014, Bertin et al. 2016). We first compare our results to previous studies. For CO, our rate ($(3.1 \pm 0.3) \times 10^{-3}$ mol. photon^{-1}) is in agreement with the literature values from experiments as well as theory (e.g., see Paardekooper et al. 2016 for an overview of experimental studies, van Hemert et al. 2015 for the theoretical study), proving that our method is reliable for the quantification of photodesorption. In the case of methane, intact photodesorption has only been detected by Dupuy et al. (2017), at a rate about an order of magnitude lower than in this work ($(2.2 \pm 1.1) \times 10^{-3}$ mol. photon^{-1}). Several reasons may explain this. The intact photodesorption rate measured by Dupuy et al. accounts for species that

desorb from the surface, as a CH_4 molecule, through multiple mechanisms (processes 3a, 3b, 3d in Figure 3.1). In comparison, the rate derived in our study includes all of the processes mentioned above as well as dissociative desorption (3c). The Ar cap blocks any of the species from leaving the ice surface, including the radicals. In Andersson et al. (2008), dissociative desorption has been shown to be 1-2 orders of magnitude more efficient than in intact desorption (see Table 3.1 therein). This gives a hint that dissociative desorption can easily account for the difference in the desorption efficiencies between Dupuy et al. 2017 and our study of methane. Additionally, the increased yield derived here may also be related to a higher temperature of the ice: 20 K in this work, compared to 8-12 K in the former study. A similar behavior was previously shown for H_2O and CO ices (Westley et al. 1995b; Arasa et al. 2010; Cruz-Diaz et al. 2018; Öberg et al. 2009b).

As in the case of CO, one order of magnitude deviations are currently considered to be within the experimental acceptance limits. An upper limit derived in the present study for methanol ($< 6 \times 10^{-5}$ mol. photon^{-1}) is in agreement with the other recent studies (Bertin et al. 2016; Cruz-Diaz et al. 2016). The photolysis results indicate that photoconversion into other products is the preferred process following a photon absorption. Methanol fragment photodesorption as well as reactive desorption have been studied before, demonstrating a low efficiency of these processes. The derivation of a photodesorption upper limit of acetonitrile is, to our knowledge, the first quantitative study in the field allowing one to gauge the efficiency of photon triggered transfer of species from a solid state to a gas phase ($< 7.4 \times 10^{-4}$ mol. photon^{-1}). Despite deriving an upper limit, rather than a specific rate, this result can be applied to the state-of-the-art astrochemical models that currently assume a rate in the 10^{-3} mol. photon^{-1} range. Similarly to methanol, acetonitrile ice exhibits an efficient photoconversion upon VUV irradiation.

3.4.2 Effective yields

To complete this analysis, an important assumption had to be made regarding the thickness of the ice involved in photodesorption (surface layers). It is based on the findings of previous experimental work investigating the number of CO monolayers that are actually affected by photodesortion. Bertin et al. (2012) conclude that this process is limited to the upper 2-3 ML. In earlier work by Muñoz Caro et al. (2010), a value of 5 ML is reported. For other molecules, the approximate size of this border region has not been investigated. Here, we therefore assume as a first order approximation that a value of about 3 ML is representative for the molecules investigated in this study (CH_4, CH_3OH, CH_3CN), even though we realize that these species are different in the sense that they also hold the potential to bind through H-bridges. In using the absorption cross section for solid state species from the literature (an average value for the wavelength range 120-165 nm), we can determine how many photons are absorbed by a specific ice column density (Section 3.2.4, Eq. 3.5). In particular, the top 3 ML of CO ice absorb ~ 1.5 % of photons, while the bulk and surface combined, 21 ML, absorb 10 % of incident photons (absorption cross section of 4.7×10^{-18} cm^2 from Cruz-Diaz et al. 2014a). The resulting effective photodesorption yield of CO is one desorbed molecule per five photons absorbed in the top three layers - 20 % efficiency. This is in decent agreement with theoretical work by van Hemert et al. (2015), where effective photodesorption yields of amorphous CO ice at 18 K was found to be 12.5 %

for the surface and subsurface combined (radius of 12.5Å $\sim$ 3 ML).

In the case of methane, by calculating the effective yields, we are able to gauge the competition between the photoconversion, photodesorption, and relaxation. Photoconversion takes place in both the bulk and surface of the ice; we assume that the efficiency of photoconversion for the ice bulk is the same as for the surface layers. We calculated the number of absorbed photons in the top 3 ML (1.7 % photons) and the whole ice, 55 ML (31 % of incident photons). The derived incident photoconversion rate (7×10^{-2} mol. photon^{-1}) corresponds to an effective yield of 20 converted molecules per 100 absorbed photons; the energy from the remaining 80 absorbed photons is distributed to the ice matrix. When considering the surface layers, a photodesorption rate of 3.1×10^{-2} mol. incident photon^{-1} corresponds to 180 depleted methane molecules per 100 absorbed photons. Twenty out of the 180 molecules are photoconverted resulting in 160 photodesorbed methane molecules, per 100 absorbed photons.

A similar analysis can be performed for methanol. We note that 1.4 % of the incident photons are absorbed by the surface layers, while 16 % of photons are absorbed by 40 ML of methanol ice. On average, every 100 photons that are absorbed in the bulk of the ice convert 50 methanol molecules to other species, while the energy from the remaining 50 photons is dissipated in the ice matrix. The effective yield derived in this work is consistent with Cruz-Diaz et al. (2016) where the effective dissociation yield was found to be 0.5 mol. per absorbed photon. The efficiency of photoconversion is more than double compared to CH$_4$. The same photoconversion efficiency applies to the surface layers. However, in order to desorb one methanol molecule, at least 250 photons are required.

The solid state absorption cross section of acetonitrile has not been measured before. Hence, for the purpose of a complete discussion of effective yields, we estimated the solid state absorption cross section of acetonitrile in the following way. Cruz-Diaz et al. (2014a) demonstrate that solid state absorption features are broadened and blue shifted with respect to their corresponding gas-phase absorption spectra. Considering that they are related to each other, we calculated the ratio of the gas phase to the solid state absorption cross section for methanol (8.2×10^{-18} cm^2 from Salahub & Sandorfy 1971 and 4.4×10^{-18} cm^2 from Cruz-Diaz et al. (2014a), respectively) and applied it to calculate the cross section of acetonitrile in the solid state from its average gas phase absorption cross section (1.4×10^{-17} cm^2 from Suto & Lee 1985). This simplified calculation yields an average absorption cross section of 7.5×10^{-18} cm^2 for solid state CH$_3$CN in the range 120 - 165 nm. Taking into account the estimated cross section, the top 3 ML absorb 2 % of the incident photons, while 8 ML of the ice absorb 6 % of the incident photons. Thus, upon the absorption of 100 photons, 50 molecules dissociate and form other species with the same efficiency in the bulk and surface layers. The upper limit of photodesorption is converted to one desorbed molecule per at least 30 absorbed photons. The summary of the calculated effective yields is presented in Table 3.1, normalized to 100 photons.

3.4.3   Photodesorption mechanisms

The total absorption cross section for each of the studied molecules is of the same order of magnitude, which excludes it as the key factor that determines the competition between photodesorption and photoconversion. In an attempt to explain the difference

Table 3.1: Summary of effective yields of photon-triggered processes for investigated solid state species. Yields are given in molecules per 100 absorbed photons. First row for each molecule corresponds to processes in the active surface layers (3 ML), while the second row represents the ice bulk. The uncertainty for these values is estimated to be $\pm$ 10 %.

Species	Photodesorption yield (mol.)	Photoconversion yield (mol.)	Relaxation (mol.)
CO	20	-	80
	-	-	100
CH_4	160	20	80
	-	20	80
CH_3OH	<0.04	50	50
	-	50	50
CH_3CN	<0.3	50	50
	-	50	50

in orders of magnitude in photodesorption rates for the molecules studied here, one needs to investigate the different mechanisms driving this process and its competition with photoconversion. The present study, with a wider scope thanks to results from other work, allows one to link the physical parameters to the possible mechanism involved.

For CO, desorption induced by electronic transitions (DIET) is an indirect process responsible for photodesorption below 10 eV range. Electronic excitation energy that is redistributed to neighbors provides energy to surface molecules in order to overcome (van der Waals type) bond energies that bind them to the ice (Fayolle et al. 2011). Photodissociation and ionization of CO are both negligible processes.

The photodesorption mechanism for dissociative species (e.g., methane, methanol, acetonitrile) is not fully understood. It is likely that different mechanisms are at play, either simultaneously or sequentially. For the molecules studied here, photodissociation can occur through the loss of a single hydrogen atom, which can carry energy to a surface molecule leading to its desorption. This H atom kick-out mechanism has previously been proposed by molecular dynamics (MD) simulations of water ice (Andersson & van Dishoeck 2008) and may more generally apply as is discussed below.

If we make the assumption that the H atom does not lose any energy in the ice until it collides with a surface molecule, this can lead to desorption given that the intermolecular bond energy is overcome. The initial energy of the H atom is determined by the remaining energy after dissociation. In our calculations, we assumed that all energy goes into the kinetic energy of the H atom. Following the laws of conservation of energy and momentum, we calculated the upper limit of the energy transferred to the surface molecule. Comparing this with the intermolecular bond strength gives a hint about the efficiency of the kick-out desorption mechanism by H atoms. The results of these calculations are summarized in Table 3.2, and they are discussed in detail in the following paragraphs.

The dissociation of condensed methane is initiated by photon absorption (average energy of 9 eV), and subsequently the $H-CH_3$ bond is broken (BDE of 4.5 eV). We assume that the H atom inherits all remaining energy in the form of kinetic energy (4.5 eV). The energetic fragment moves through the ice and collides with a surface

Table 3.2: Summary of parameters that impact the efficiency of the kick-out photodesorption mechanism. The last column is the ratio of the upper limit for energy transferred to surface species to the intermolecular bond energy (See text below for details).

Species	Intermol. bond energy (eV)	Diss. threshold energy (eV)	Energy trans. to a surface species (eV)	Ratio
CH_4	0.1	4.5	<0.99	9.9
CH_3OH	0.38	4.5	<0.58	1.5
CH_3CN	0.39	4	<0.46	1.2

molecule to transfer up to 0.99 eV. This value exceeds the energy required to break the intermolecular bond of methane (0.1 eV, Smith et al. 2015) with a factor of 10. This particularly high ratio might help to account for the effective photodesorption rate of methane (see Table 3.1).

The photodissociation of methanol liberates the H atom through breaking the $H-CH_2OH$ bond (4.16 eV) or CH_3O-H (4.5 eV) (Blanksby & Ellison 2003). The same calculation procedure as for methane yields an upper limit of the energy transferred to the surface molecule of 0.58 eV. A comparison with the strong hydrogen bonding energy of the methanol ice (0.38 eV, Martín-Doménech et al. 2014) yields a ratio of 1.5. This low ratio can indicate that kick-out desorption is a possible mechanism for methanol, but given our idealistic assumptions, it is unlikely to be efficient. The case of acetonitrile is similar to methanol. The H atom can transfer up to 0.46 eV of energy to a strongly bound surface molecule (intermolecular bonding energy of 0.39 eV, Abdulgalil et al. 2013). The ratio of the upper limit for transferred energy to the intermolecular bonding is 1.2. In an ideal case, this should be sufficient for desorption, but in reality the H atom loses some energy when traveling through the ice before colliding with the surface molecule. Hence, this mechanism is expected to be less efficient.

If we consider the kick-out mechanism to be a dominant photodesorption process for dissociative species, our data suggest a trend related to their efficiency. In particular, the photodesorption rate can be roughly estimated by comparing the upper limit for the energy transferred to the surface via perfect collision and intermolecular bonding energy. This ratio can possibly be linked to the measured photodesorption rate. If this trend holds true, then under the made assumptions, photodesorption of larger molecules, that are strongly bound, likely fall below 10^{-3} mol. photon^{-1}, the current default astrochemical model value.

The efficiency of the kick-out process has been discussed in the context of pure ices, but more importantly, it is likely that this process also plays a role in the interstellar medium. If this is the case, our results can be extrapolated toward realistic conditions. For example if we look at the water-rich phase of interstellar ices. These ices contain minor abundances of CH_4, CO_2, and NH_3 (Garrod & Pauly 2011), which are likely to be isolated in a water matrix or on a surface bound to the water ice. The kick-out photodesorption efficiency of these species can be determined by the comparison of energy binding them to the water ice (for overview see Table 2 in Das et al. 2018) and the energy which can be transferred to these species by an intermediate carrier, such as an H atom. We can then follow the same procedure as in Table 3.2. We assume

that the H atom is created upon water dissociation and can transfer its energy to a surface CH_4, CO_2, or NH_3 molecule. The resulting ratios suggest that the kick-out mechanism is the most efficient for methane (ratio of 10.3), then CO_2 (1.8) and NH_3 (1.7). To complete these calculations, the following binding energies were used: 0.08 eV (Raut et al. 2007), 0.2 eV (Minissale et al. 2016), and 0.48 eV (Collings et al. 2004), respectively.

It is important to mention that the kick-out mechanism is not the only mechanism capable of photodesorption. Alternatively, for a surface methane molecule, the fragments CH_3 and H can recombine following an exothermic reaction with 4.5 eV excess energy. Upon comparison with the intermolecular bond energy, this is sufficient to desorb from the surface (Chase Jr & Tables 1998). Recombination reactions of gas phase radicals, which are formed in this way, have been proposed as a starting point for a gas phase formation route to CH_3OH (Bertin et al. 2016).

Theoretical studies, such as for CO (van Hemert et al. 2015) and H_2O (Andersson & van Dishoeck 2008), are essential for investigating the mechanisms behind VUV photodesorption. Hence, molecular dynamics studies of methane, methanol, and acetonitrile are necessary to confirm or disprove our hypothesis.

3.4.4   Astrophysical implications

As mentioned in the Introduction, photodesorption has been considered to be an effective way to transfer, newly formed, solid state species into the gas phase. In the case of the nondissociative VUV excitation of CO, this
seems to apply; the measured photodesorption rates, presented here and in previous studies, are high enough to explain CO gas phase observations toward the prestellar core B68 (Bergin et al. 2006). This result is even more relevant, since icy dust grains are expected to be coated with a CO-rich layer, as CO is the last abundant molecule to freeze out. Determining the relevance of photodesorption as a mechanism that bridges the solid state and gas phase becomes much more challenging when looking for other species, such as H_2O or CO_2, which easily dissociate upon VUV excitation.

The new technique presented here has an advantage that it can be used to study several photoprocesses taking place simultaneously (i.e., photodesorption and photoconversion). Due to this, the method has been applied to CO, dissociating CH_4, and CH_3OH ices, largely confirming data from previous work. This confirmation is of particular interest for CH_3OH, since this study also shows that it is very hard to photodesorb intact methanol. Additionally, dissociative desorption may be an important mechanism, as suggested for the case of CH_4. It may be very well possible that the resulting radicals recombine in the gas phase, that is, reflecting a solid state triggered gas phase chemistry. For the dissociative VUV irradiation of CH_3CN, no earlier photodesorption values have been presented and an upper limit has been derived here that is about a factor 10 lower than the values typically used in astrochemical models. There is a second advantage regarding the new method. The existing techniques have focused on pure ices. The only exceptions concern studies focusing on codesorption or reactive desorption experiments, such as for mixed $CO:N_2$, $CO:CH_3OH$, and $CH_4:H_2O$ ices (Fayolle et al. 2013; Bertin et al. 2013; Martín-Doménech et al. 2016). The LDPI TOF MS method discussed here is also capable of dealing with mixed, that is, astronomically more realistic ices. It will be interesting to know how different ice constituents determine each other's photodesorption properties, as a function of the
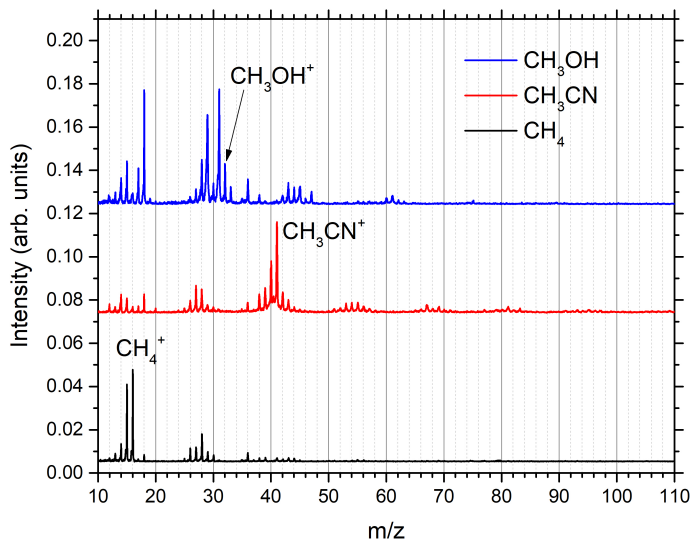
Figure 3.11: LDPI TOF MS of CH_4, CH_3OH, and CH_3CN after a photon fluence of 1.8×10^{17} photon cm^{-2}. Peaks at m/z higher than the molecular ion represent products created during photoconversion of the species.

mixing ratio, but also, for example, for different temperatures. This is currently a work in progress. From the work presented here, it is already clear that photoconversion increases the number of ice constituents substantially. This is illustrated in Figure 3.11. The photoconversion not only decreases the abundance of precursor material, but it also increases the molecular complexity in the ice. The figure shows the TOF mass spectra for methanol, acetonitrile, and methane ices upon VUV irradiation for an irradiation of only 12 minutes. As discussed earlier (Öberg et al. 2009c; Paardekooper et al. 2016d), larger COMs are formed in this process as well. It is clear that photodesorption and photoconversion are two intimately mixed processes.

From the present work, another astronomically relevant conclusion can be drawn. The coating on top of the ices prohibits surface radicals, which normally desorb, to leave the ice. It is a logical step to assume that these radicals are, therefore, forced to recombine in the ice, enhancing the overall photoconversion. Such a process could take place in space as well, as interstellar ices are shown to have layered structures, that is, the CO-coating on top of a H_2O rich ice could enforce chemistry involving OH-radicals. Here, the impact of the coating as a reaction thriving mechanism could not be confirmed.

To summarize, the present work on pure ices, comprising of molecules dissociating upon VUV irradiation, cannot explain the observed gas phase abundances of methanol and acetonitrile. It is very likely, that for even larger complex organic molecules, the intact desorption efficiency will go even further down. Nevertheless, the detection of such species on cometary surfaces as well as the proof for their thermal release from icy dust grains (Lee et al. 2019) clearly hints at a solid state origin for these species. This is also fully in line with the data presented here, see Fig. 3.11. A possible ex-

planation for this inconsistency is that most studies have focused on pure ices so far and the processes in mixed ices may be different (e.g., efficient reactive desorption). The new method that is introduced here holds the potential to study these processes further; also it provides a versatile tool that is able to discriminate between direct photodesorption and photoconversion.

3.5   Conclusions

We introduce a new method for gauging the competition between photon-triggered processes in solid state species. By comparing time-of-flight mass spectra of laser ablated (un)coated ice experiments upon VUV irradiation, we are able to distinguish between the effects of photodesorption and photoconversion. The new approach has been demonstrated on the example of CO, and then applied to CH_4, CH_3OH, and CH_3CN. The derived rates are average values in the 7-10.2 eV photon energy range and are shown in Table 3.3.

Table 3.3: Summary of photon-triggered processes of solid state species at 20 K in the 7-10.2 eV photon energy range.

Species	Photodesorption rate (in mol. photon^{-1})	Photoconversion cross section (in cm^2)
CO	$(3.1 \pm 0.3) \times 10^{-3}$	-
CH_4	$(3.1 \pm 0.5) \times 10^{-2}$	3.7×10^{-18}
CH_3OH	$< 6.0 \times 10^{-5}$	2.8×10^{-18}
CH_3CN	$< 7.4 \times 10^{-4}$	3.0×10^{-17}

For CH_3CN, for the first time, a value for the photodesorption rate is presented that provides an upper limit that is about a factor of 10 lower than what is currently used in astrochemical models. Moreover, upon comparison of the values determined for pure species studied here and in some earlier work, the following trend is suggested: the VUV desorption efficiency for dissociative species seems to depend on the balance between the extra energy available after dissociation, intermolecular bonding energy, and the relative mass of fragments and parent species. This implies that for even larger complex organic molecules (compared to CH_3OH and CH_3CN), the intact photodesorption rate likely falls below the currently used rate of 10^{-3} mol. photon^{-1}. It should be noted that this behavior has been observed in laboratory experiments containing pure ices, with a few exceptions in binary mixtures (Bertin et al. 2016; Zhen & Linnartz 2014); whereas, in the ISM, ices are generally mixed. Since the new technique also allows one to study realistic ices analogs, future studies will help in quantitatively disentangling the role that impacting VUV photons play in interstellar chemistry.

4 | PHOTOLYSIS OF ACETONITRILE IN A WATER-RICH ICE AS A SOURCE OF COMPLEX ORGANIC MOLECULES: CH_3CN AND $H_2O:CH_3CN$ ICES

Abstract

Many C-, O-, and H-containing complex organic molecules (COMs) have been observed in the interstellar medium (ISM) and their formation has been investigated in laboratory experiments. An increasing number of recent detections of large N-bearing COMs motivates our experimental investigation of their chemical origin. We investigate the potential role of acetonitrile (CH_3CN) as a parent molecule to N-bearing COMs, motivated by its omnipresence in the ISM and structural similarity to another well-known precursor species, CH_3OH. The aim of the present work is to characterize the chemical complexity that can result from vacuum UV photolysis of a pure CH_3CN ice and a more realistic mixture of $H_2O:CH_3CN$. The CH_3CN ice and $H_2O:CH_3CN$ ice mixtures were UV irradiated at 20 K. Laser desorption post ionization time-of-flight mass spectrometry was used to detect the newly formed COMs *in-situ*. We examined the role of water in the chemistry of interstellar ices through an analysis of two different ratios of $H_2O:CH_3CN$ (1:1 and 20:1). We find that CH_3CN is an excellent precursor to the formation of larger nitrogen-containing COMs, including CH_3CH_2CN, NCCN/CNCN, and $NCCH_2CH_2CN$. During the UV photolysis of $H_2O:CH_3CN$ ice, the water derivatives play a key role in the formation of molecules with functional groups of: imines, amines, amides, large nitriles, carboxylic acids, and alcohols. We discuss possible formation pathways for molecules recently detected in the ISM.

4.1   Introduction

Astronomical detections of over 200 different molecules demonstrate the chemical diversity of the interstellar medium (ISM). Besides many smaller species, typically di- and triatomics, also a large amount of C-, O-, N- and H-bearing species has been identified that contain 6 or more atoms. From an astrochemical perspective these species are considered complex organic molecules (COMs) and make up 25 percent of the detected molecules (van Dishoeck 2014; McGuire 2018). Of special interest are 'prebiotic' species, a molecular subgroup that is relevant in the formation of amino acids or other molecules important for emergence of life. Nitriles are often considered as prebiotic molecules due to their ability to produce amides and carboxylic acids (including amino acids) upon hydrolysis in aqueous solutions. Acetonitrile (CH_3CN) is a part of this family as the simplest of the alkyl nitriles (Bernstein et al. 2002; Hudson et al. 2008).

   CH_3CN is a symmetric top molecule with a large dipole moment of 3.92 D and in the gas phase it has been detected through its strong millimeter transitions. CH_3CN has been observed both in our Solar System and beyond (Cordiner et al. 2015; Goesmann et al. 2015; Woodney et al. 2002; Solomon et al. 1971; Bergner et al. 2018; Purcell et al. 2006; Calcutt et al. 2018). Whereas identifications so far are limited to the gas phase, it is generally assumed that CH_3CN is present on icy dust grains and plays an important role in solid state nitrogen chemistry (e.g. Loomis et al. 2013). Recently CH_3CN was identified towards the circumstellar disk around V883 Ori (Lee et al. 2019) where its origin as well as that of several other COMs - methanol, acetone, acetaldehyde and methyl formate - was directly linked to species sputtered from icy dust grains. These observations are in line with the idea that COMs form on icy dust grains through surface reactions that are triggered by impacting atoms, upon UV irradiation, electron bombardment, cosmic ray interactions or through thermal processing. In recent years many efforts have been taken to study such processes under fully controlled laboratory conditions. The results are then linked to astronomical observations or used as physical chemical input for astrochemical models. (e.g. Garrod & Herbst 2006; Garrod et al. 2008; Walsh et al. 2014b)

   The majority of the identified COMs has been detected towards high-mass hot cores. Specific detections of nitriles and other nitrogen bearing species, including that of astrobiological importance, are: hydrogen cyanate (HCN), isocyanic acid (HNCO), formamide (NH_2CHO), methylamine (CH_3NH_2), methyl isocyanate (CH_3NCO), amino acetonitrile (NH_2CH_2CN), ethyl cyanide (CH_3CH_2CN), vinyl cyanide (CH_2CHCN), cyanoacetylene (HCCCN), acetamide (CH_3CONH_2), urea (NH_2CONH_2), (tentatively) N-methyl formamide (CH_3NHCHO), and more recently glycolonitrile ($HOCH_2CN$) and propargylimine (HCCCHNH) (Snyder & Bhul 1971; Bisschop et al. 2007b; Fourikis et al. 1974; Halfen et al. 2015; Ligterink et al. 2017; Belloche et al. 2009; Calcutt et al. 2018; Hollis et al. 2006; Belloche et al. 2019, 2017; Zeng et al. 2019; Bizzocchi et al. 2020).

   In light of these detections and the prebiotic relevance of many nitriles, several studies have been focused on the involved formation pathways (Raunier et al. 2004; Jones et al. 2011; Danger et al. 2012). In comparison, many C-, O- and H-bearing COMs have been linked to UV irradiated CH_3OH ices (Öberg et al. 2009c; Paardekooper et al. 2016b). CH_3CN - even though less abundant in space - can be regarded as another promising parent molecule to yield its own branch of COM derivatives. Whereas the

formation of methanol through CO hydrogenation is well accepted (Watanabe et al. 2003; Fuchs et al. 2009; Linnartz et al. 2015), the interstellar formation pathways of CH_3CN are less known. In fact, both gas phase and solid state routes have been proposed. In the gas phase formation may proceed through radiative association:

$$HCN + CH_3^+ \rightarrow C_2H_4N^+ + \text{photon} \tag{4.1}$$

and followed by dissociative recombination:

$$C_2H_4N^+ + e^- \rightarrow CH_3CN + H \tag{4.2}$$
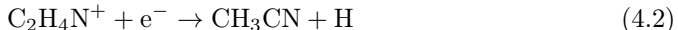
as proposed by Mackay 1999; Willacy et al. 1993; Vigren et al. 2008. In the solid state, formation of CH_3CN is possible through radical recombination, CH_3+CN (Garrod et al. 2008) or hydrogenation of C_2N (Belloche et al. 2009). Recent observational work by Loomis et al. 2018 indicates that the molecular origin of CH_3CN in the protoplanetary disk TW Hya is dominated by solid state pathways, in line with the already mentioned studies by Lee et al. (2019).

The first studies using CH_3CN as a solid state starting point in the formation of larger COMs were reported by Hudson & Moore 2004, Hudson et al. 2008 and Abdulgalil et al. 2013. Upon UV irradiation, the following photolysis products were identified: HCN, CH_4, and $(CH_2CN)_2$. It was also found that the parent species isomerizes to CH_3NC and H_2CCNH. When mixed with H_2O ice, photolysis of the $CH_3CN:H_2O$ ice mixture yields OCN^-, one of the few charged ice species identified in space (van Broekhuizen et al. 2005) and characteristic of acid base chemistry forming a salt, $NH_4^+OCN^-$. Hudson et al. 2008 also showed that CH_3CN mixed with H_2O and bombarded with ions (at low temperature), resulted in the identification of amino acids after hydrolysis at room temperature. Danger et al. 2011 found that thermal processing of CH_3CN ice mixed with ammonia resulted in the formation of amino acetonitrile. Hydrolysis of amino acetonitrile in liquid solution at room temperature is known to form glycine.

Whereas UV photolysis of CH_3CN ice clearly showed to trigger solid state chemical processes, hydrogenation of CH_3CN by thermalised H atoms was found to be rather inefficient due to a high energy barrier for the first H atom addition (Nguyen et al. 2019). Conversely, for the hydrogenation of isonitrile CH_3NC the barrier was found to be lower and lead to the formation of secondary amines (CH_3NHCH_3). Other chemical routes may also be relevant in the formation of N-bearing prebiotics. Gerakines et al. 2004 studied the photolysis and proton irradiation of $H_2O:HCN$ mixture, which yielded isocyanic acid (HNCO), formamide (NH_2CHO), OCN^- and NH_4^+, and recently Ligterink et al. 2018a demonstrated solid state pathways to form amides upon UV irradiation of an $CH_4:HNCO$ ice mixture.

In the present work the focus is on UV induced reactions in pure CH_3CN ice and $H_2O:CH_3CN$ ice mixtures. The aim is to demonstrate the formation of heavier COMs. This becomes possible through application of a new ultra-sensitive detection method based on laser desorption post ionization time-of-flight mass spectrometry, with experimental details described in section 4.2. The primary goal is to improve our understanding of solid state astrochemical reactions that extend existing networks resulting in the formation of (N-bearing) COMs. The results are presented and discussed in section 4.3. Information on the underlying reaction network showing how imines, amines, amides and nitriles chemically connect and the "catalytic" role of water are presented. The manuscript concludes with the astronomical relevance of this work.

4.2   Experimental

The experiments are performed in an ultra-high vacuum (UHV) system, MATRI^{2}CES (Mass Analysis Tool to study Reactions in Interstellar ICES). This section provides the relevant information, while a detailed description of MATRI^{2}CES can be found in Paardekooper et al. 2014. The experimental procedures as well as an overview of the experiments performed are discussed.

4.2.1   Setup and analysis tools

MATRI^{2}CES is a two chamber system, with a base pressure in the 10^{-10} mbar range. The main chamber houses a closed cycle Helium cryostat which cools a 2.5 cm x 5 cm large gold coated copper substrate to a temperature of 20 K. A thermocouple and a resistive heater are attached to the cold finger, allowing a Lakeshore 331 temperature controller to regulate the temperature of the substrate between 20 and 300 K with roughly 1 K precision. Ice growth on the substrate proceeds via needle valves that guarantee a continuous and stable deposition pressure in the main chamber. The needle valve on the front is connected to a tube which faces the sample at an angle of 85 degrees with respect to the substrate. Acetonitrile (CH$_3$CN, VWR, <10ppm of water), and acetonitrile-D3 (CD$_3$CN, Sigma-Aldrich, $\geq$ 99.8% D) are used. In order to simultaneously admit water vapor (H$_2$O, miliQ or H$_2$^{18}O, Sigma-Aldrich, 97% ^{18}O), an additional needle valve located behind the substrate is used. Prior to deposition, atmospheric gases trapped in the samples are removed by several freeze-pump-thaw cycles. The growth rates are determined in advance by HeNe interference measurements as discussed in previous works (Baratta & Palumbo 1998; Paardekooper et al. 2016c; Bulak et al. 2020).

UV irradiation of the ice is accomplished with a microwave discharge hydrogen flowing lamp (MDHL, F-type), which is connected to the main chamber by a magnesium fluoride (MgF$_2$) viewport and directly faces the substrate. The lamp produces vacuum UV photons with energies in the 7-10.2 eV range and simulates interstellar radiation fields. Throughout all experiments, the lamp is run at a H$_2$ pressure of 1.4 mbar and 80 W of microwave power. The corresponding SED contains both Lyman-α (121.6 nm) and molecular H$_2$ emission continuum (130 - 165 nm); the full SED is given in Fig. 4 in Paardekooper et al. 2016c. The impacting radiation causes various processes in the ice molecules, e.g., excitation, dissociation, desorption or even ionisation in the case if ionization threshold is below the energy of the present UV photons. For an overview of photo-induced processes see Fig 1 in Bulak et al. 2020. The photon flux of the MDHL is measured at the location of the substrate with a NIST calibrated photodiode and found to be $(2.5 \pm 0.5) \times 10^{14}$ photons cm^{-2}s^{-1}.

As analytical technique, laser desorption post ionisation time-of-flight mass spectrometry (LDPI TOF-MS) is applied to probe the composition of the ice at different vacuum UV fluences. The light of an unfocused ($\sim$1 mm) Nd:YAG laser beam (355 nm and 4-5 ns pulse length) is used as an ice ablation source. Typical laser pulse energies of 65 mJ cm^{-2} are applied. Ice species that are desorbed are subsequently ionized in the gas phase using 70 eV electrons and guided by ion optics located in front of the substrate into the second chamber, which contains a field free TOF system. The latter is operated in reflectron mode to increase mass resolution (Δm/m $\sim$250). In order to select different parts of the photoprocessed ice for sequential laser ablation

steps, the position of the cryostat (and substrate) can be moved using a two dimensional translation stage. In the vertical direction, translation is driven by a stepper motor, and in the horizontal direction, it is manually controlled. The motorized vertical translational stage allows for synchronization with laser shots resulting in each shot probing a fresh location on the ice, while ensuring that the location of the desorption plume with respect to the ion optics remains the same. This approach results in minimal shot-to-shot fluctuations, while ensuring that multiple averages can be used to increase the overall signal-to-noise. Every mass spectrum presented in this study is based on 100 averages obtained at different locations on the ice coated substrate. To trace the changes in the chemical composition of the ice, raw TOF spectra are collected at different photon fluences. In order to determine the elemental compositions of the new signals in the mass spectra, each experiment is performed for two isotopes. For the pure ice, CH_3CN and CD_3CN, and for the mixed ices, $CH_3CN:H_2^{16}O$ and $CH_3CN:H_2^{18}O$ are used.

The dominating process driving the reactions in the ice is photodissociation followed by radical-radical and radical-molecule interactions. Hence, the combination of elemental composition of the new ions, with fragmentation patterns of the expected products from the NIST database, allows to tentatively identify the newly formed photoproducts. In addition, based on the order of appearance of the new mass peaks, assigned species can be roughly separated into first and second generation photoproducts.

Quantitatively, the mass spectra are analysed by calculating the integrated area of each peak by fitting a Pearson IV distribution (Castellanos et al. 2018). This function allows for peak asymmetry and therefore is able to accurately fit the individual peaks. The resulting intensities of mass peaks can be regarded as a linear combination of multiple individual compounds present in the plume (Paardekooper et al. 2014). Hence, an integrated mass spectrum, M_t, at a given irradiation time, t, can be expressed by:

$$M_t = \sum_{i=1}^{n} a_i \cdot \sigma_i \cdot M_i, \tag{4.3}$$

where a_i is the molecular abundance of species i, σ_i is the ionization cross section and M_i is the corresponding fragmentation pattern. To derive product abundances, we fit our experimental data using a limited memory Broyden–Fletcher–Goldfarb–Shanno (L-BFGS) optimisation algorithm incorporated in Python. This allows to take into account all parameters from equation 4.3 and trace the evolution of different species in the ice throughout the VUV photo-processing. Where available, NIST mass spectra are used as input for the reference mass spectra.

4.2.2 Overview experiments

Table 4.1 summarizes all relevant experiments. The experiments allow to get an insight into the early stages of the photolysis process. At a low photon fluence, the radical concentration in the ice is low, hence, the impact of the second order reactivity, including reversed reactions, is limited. The experiments are extended to be representative for a lifetime of a dense molecular cloud, which may experience a total fluence as high as $(3\text{-}30) \times 10^{17}$ photons cm^{-2}. This value has been estimated using a cosmic ray induced UV flux of $(1\text{-}10) \times 10^3$ photons $cm^{-2}s^{-1}$ and an average molecular cloud life-

Table 4.1: Summary of the performed CH_3CN and $H_2O:CH_3CN$ UV photolysis experiments. The UV irradiation time is given in minutes, with a photon flux of $(1.5 \pm 0.5) \times 10^{15}$ photons $cm^{-2}min^{-1}$.

Composition	Thickness (ML)	Temperature (K)	UV irradiation (min)
CH_3CN*	40	20	0-128
CH_3CN	40	77	0-128
CH_3CN	40	20-285	0-128
CD_3CN*	40	20	0-128
$H_2O:CH_3CN$* ($\sim$1:1)	100	20	0-128
$H_2O:CH_3CN$* ($\sim$20:1)	100	20	0-128
$H_2^{18}O:CH_3CN$* ($\sim$20:1)	100	20	0-128
blank*	0	20, 160-300	60

Notes. Experiments repeated more than once are marked with an asterisk (*)

time of up to 10^7 years (Shen et al. 2004a). The CH_3CN and complimentary CD_3CN experiments are conducted to confirm product assignments. The same approach is used for two different $H_2O:CH_3CN$ ice mixtures. Most experiments are performed at a temperature of 20 K, however, in order to apply the results to different environments, such as the icy surfaces of Titan, data is also collected at 77 K.

To provide an additional tool for identification of photoproducts according to their characteristic desorption temperatures (Paardekooper et al. 2016c), an experiment with a range of temperatures (20-285 K) is performed for CH_3CN. In this experiment, the ice is UV-irradiated at 20 K, then slowly warmed up and probed with LDPI. For example, the mass peaks representing methane, at a temperature above its thermal desorption ($\sim$40 K), decrease in signal, confirming the assignment of methane.

The blank experiment is performed to demonstrate that all detected reaction products form in the deposited ice, rather than externally, i.e., on the walls of the setup or in the ion optics. To test that, the cold substrate (20 K) is UV irradiated and probed via LDPI. This procedure is also performed at higher temperatures, following a deposition of CH_3CN above its thermal desorption threshold (160-300 K). In all experiments, the dominant uncertainty source follows the absolute calibration of the deposition rate and UV flux. The error bars shown in the kinetics diagrams are a result of the fitting routine of the particular mass peaks.

4.3 Results and discussion

This section comprises of three parts. First the photolysis of pure CH_3CN ice is discussed. The LDPI TOF-MS data are presented and photoproducts are assigned. The production yields of first generation photoproducts are calculated. Second, a similar qualitative analysis is done for the UV photolysis of $H_2O:CH_3CN$ ice mixtures. The photoproduct assignments are additionally supported by mass spectra from experiments for two different mixing ratios (1:1 and 20:1). In the third part the chemical
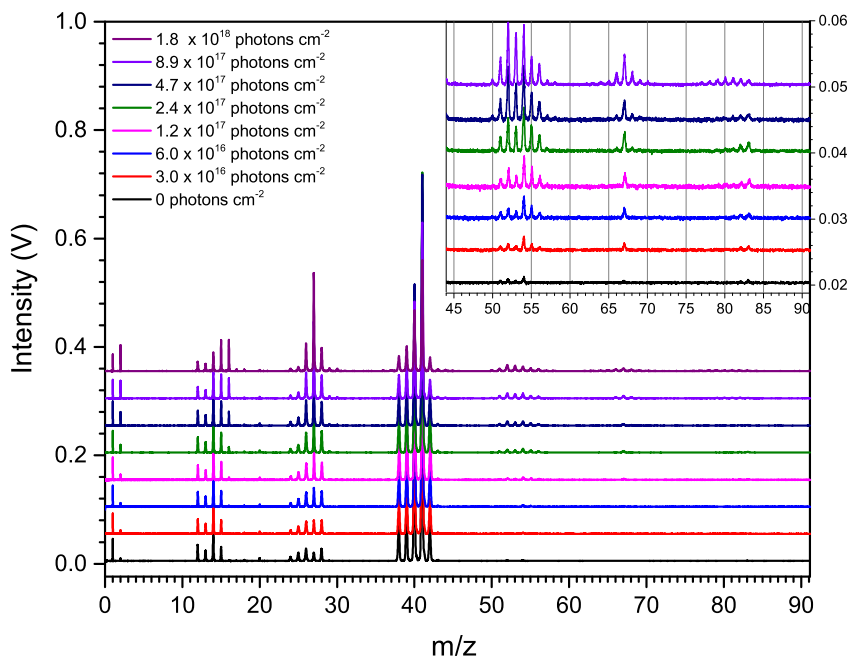
Figure 4.1: LDPI-MS signals for an UV irradiated CH_3CN ice at 20 K for increasing photon fluence. The lowest graph shows the signal without UV irradiation. The inset is a zoom in on the intensity scale for the higher masses.

role of water molecules is presented.

4.3.1   CH₃CN photoproducts

Mass spectra obtained throughout the UV photolysis of pure CH_3CN ice are shown in Figure 6.1 The bottom trace shows the signature of an unprocessed acetonitrile ice with a characteristic fragmentation pattern spread over multiple mass peaks (m/z = 12-15, 24-28, 38-42). It serves as a reference for tracking any changes in the chemical composition of the ice. After 2 min of UV irradiation (3.0×10^{16} photons cm^{-2}, represented by the red trace), new peaks arise at m/z values: 16, 27-29, 51-56, 67, 82, 83. As photolysis proceeds (see the remaining traces) additional peaks appear in the spectra, demonstrating a rapid increase in the total number of species newly formed in the ice. The (inset in the) figure also shows the high detection sensitivity of MATRI^{2}CES and its capability to quickly monitor the formation of larger COMs, up to at least 6-7 C/N-atoms containing species (m/z = 93).

The assignment of the new peaks to specific molecules is not straight forward as the peaks merely reflect fragment masses due to the dissociative ionization method (electron impact ionization): upon dissociation different species may form identical fragments. Also, it is not *a priori* clear which species are expected to form as different

processes are involved. Radicals created via photodissociation recombine with each other to form larger stable products. The MDHL produces photons in the energy range between 7-10.2 eV, which is below the ionization potential of the CH_3CN, but is sufficient to overcome a barrier for two photodissociation pathways: CH_2CN-H and CH_3-CN with thresholds of 4 and 5.2 eV, respectively (Darwent 1970). Moreover, the formed CN radicals can be in electronically excited states (Kanda et al. 1999; Schwell et al. 2008). Given their high reactivity, the radicals do not build up an abundance sufficient to be detected directly. Instead, the stable end products of radical recombination can be studied. The radicals can also react with the abundantly present precursor species (CH_3CN), e.g. by interacting with the triple CN bond. Alternatively, it is possible that newly formed species (e.g. CH_3CH_2CN) can engage in a neutral-radical reactions or be photodissociated to supply a new, large radical for further reactions, as discussed in detail by Fedoseev et al. 2017. It is also possible that the resulting radicals participate in H-atom abstraction reactions (Chuang et al. 2016).

An assignment of the mass peaks shown in Fig. 6.1 to specific species starts with the determination of the elemental composition of the new mass peaks. The observed mass peaks reflect either the ionized (and unfragmented) species formed along one of the three processes described above, or one of the corresponding photoproduct fragments formed upon dissociative ionization. In addition, CD_3CN is used as an isotopically enriched precursor to discriminate between mass peaks shifted because of hydrogen and deuterium contributions. Special care is taken that the overlap between the chosen characteristic peaks is minimum. In this way it is possible to link the majority of the observed mass peaks to an elemental C/N/H composition and this allows to conclude on the formation of several of the formed products, as will be illustrated later. Table 4.2 gives a summary of the observed mass peaks used to derive the elemental product composition and (tentative) assignments of species, newly formed upon VUV photolysis of pure acetonitrile ice.

In Table 4.2 photoproducts formed as a result of isomerization are included, but their identification (and presence in the ice) cannot be confirmed using tof mass spectrometry. Here, tandem mass spectrometry or spectroscopic methods would offer a possible alternative. This applies to most nitriles being restructured into isonitriles (e.g. $CH_3CN \rightarrow CH_3NC$) and acetonitrile isomerizing into ketenimine ($CH_3CN \rightarrow H_2C=C=NH$), which has been discussed by Hudson & Moore 2004.

To demonstrate the approach to photoproduct assignments, Figure 6.2 highlights the isotopic shift between the CH_3CN and CD_3CN experiments. Upon VUV irradiation, an immediate increase in signals at m/z = 16 and 27 is observed for CH_3CN (red trace), which corresponds to an increase at m/z = 20 and m/z = 28 when using the deuterated equivalent. The corresponding elemental compositions are CH_4 and HCN which are obviously assigned to methane and hydrogen cyanide. Possible formation pathways of these species include hydrogenation of the CN and CH_3 radicals, as demonstrated in previous studies (Borget et al. 2017; Qasim et al. 2020). For higher UV fluences (blue and pink traces), the abundance of these products continues to increase, while other peaks demonstrate further changes in the composition of the ice. Towards the end of CH_3CN photolysis, peaks at m/z = 26, 28, 29 and 30 increase.

Table 4.2: Characteristic m/z peaks used for identification of photoproducts of the UV photolysis of the CH$_3$CN ice

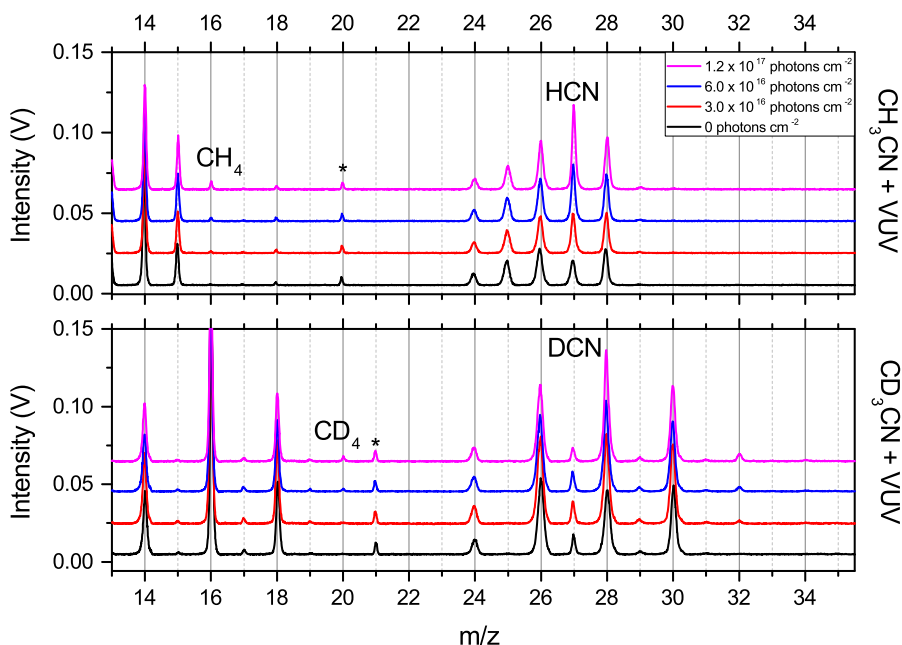| CH$_3$CN m/z	CD$_3$CN m/z	Elemental composition	Proposed molecular species	Name
2	4	H$_2$	H$_2$	mol. hydrogen
16	20	CH$_4$	CH$_4$	methane
26, 27	26, 28	CNH	HCN/HNC	hydrogen (iso)cyanide
40, 41	42, 44	C$_2$NH$_3$	CH$_3$CN/CH$_3$NC/ H$_2$CCNH	acetonitrile/methyl isocyanide/ ketenimine
50, 51	50, 52	C$_3$NH	HCCCN	propiolonitrile
52	52	C$_2$N$_2$	(CN)$_2$	cyanogen
26, 52, 53	26, 54, 56	C$_3$NH$_3$	CH$_2$CHCN	2-propenenitrile
28, 54	30, 58	C$_3$NH$_5$	CH$_3$CH$_2$CN	propanenitrile
29, 55	32, 60	C$_3$NH$_5$	CH$_3$CH$_2$NC	ethyl isocyanide
56	62	C$_3$NH$_6$	-	imine (R-CHNH)
65-69	66, 68, 70, 72, 74	C$_3$N$_2$H$_x$	-	
77-83	78-90	C$_4$N$_2$H$_y$	-	-

Figure 4.2: Low m/z range of LDPI-MS signals of pure CH_3CN (top panel) and CD_3CN (bottom panel) at 20 K, as a function of photon fluence. Peak marked by an asterisk (*) is a doubly ionized CH_2CN^{2+}.

This mass range is characteristic for fragments of large (iso)nitrile species (CH_3CH_2CN, CH_2CHCN and CH_3CH_2NC). However, small species, if present in the ice (methanimine CH_2NH), might also contribute. Following the outcome of the deuterated experiments, these peaks can be matched with the following elemental compositions: CN/C_2H_2, CNH_2/C_2H_4, CNH_3 and CNH_4.

The higher m/z range is analyzed using the same strategy, as shown in Figure 6.3. Newly observed peaks are assigned to elemental compositions of C_2N_2, C_3NH_x, $C_3N_2H_x$ and $C_4N_2H_y$ (x = 1, 3, 5 and y = 1, 3, 5, 7). The mass peak at m/z = 52, which is clearly visible in both experiments, is assigned to (iso)cyanogen (NCCN/CNCN). Based on characteristic mass peaks of (iso)nitriles with three carbon atoms (NIST Chemistry Webbook), the signals at 50-55 amu are assigned to a combination of propiolonitrile (HCCCN), acrylonitrile (CH_2CHCN), propanenitrile (CH_3CH_2CN), and ethyl isocyanide (CH_3CH_2NC). The formation of NCCN/CNCN and CH_3CH_2CN probably proceeds via radical recombination reactions. Peaks representing CH_2CHCN and HCCCN appear later in the photolysis, which can be interpreted as a result of UV-induced dehydrogenation of CH_3CH_2CN.

The peak at m/z = 56 shifts to m/z = 62 in the deuterated experiments. This observation is consistent with C_3NH_6 elematal composition which can only be obtained by hydrogenation of CN bond bond. This leads to imine formation, with a general structure of R-CHNH. As the involved fragmentation pattern is not known, it is unfortunately not possible to unambiguously confirm this assignment.

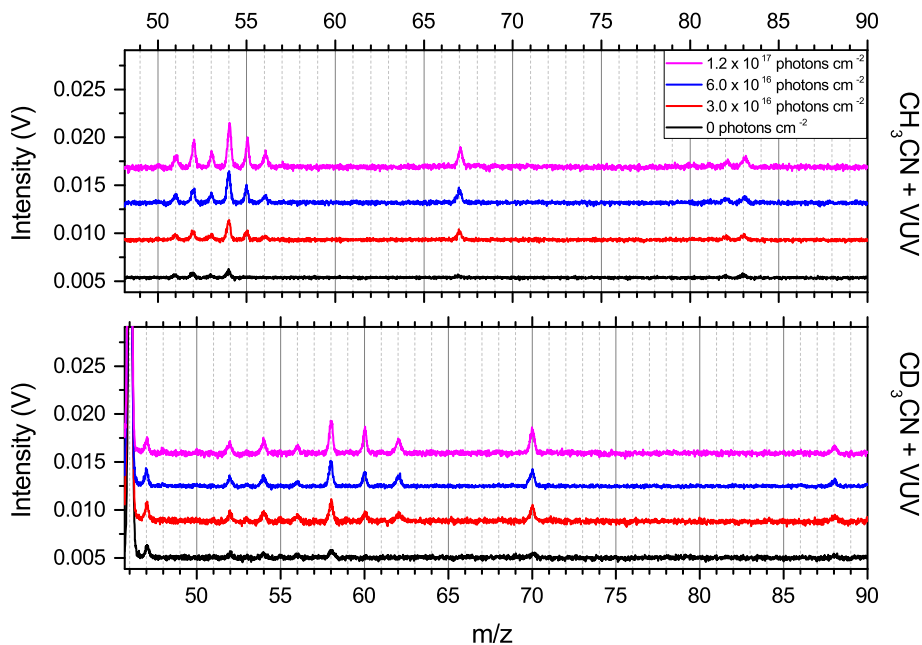Mass peaks in the range of m/z = 65-69 and m/z = 77-83 have been assigned with

Figure 4.3: High m/z range of LDPI-MS signals of pure CH_3CN (top panel) and CD_3CN (bottom panel) at 20 K, as a function of photon fluence.

elemental compositions $C_3N_2H_x$ (x = 1, 3, 5) and $C_4N_2H_y$ (y = 1, 3, 5, 7). Due to the visibility of traces at m/z = 67, 82 and 83 in the reference spectrum (before photolysis), and a significant increase of these signals during the experiments, it is likely that these represent newly formed large photolysis products. For this it is important to exclude that these peaks are a direct consequence of the used laser desorption method or originate from non-volatile residues from previous experiments.

It has been demonstrated that upon laser desorption, species with strong hydrogen bonds, such as H_2O, CH_3OH or CH_3CN, form protonated clusters (e.g. $(H_2O)_nH^+$, where n = 0, 1, 2 and higher from Gudipati & Yang 2012). Mass peaks of these clusters are easily recognized, as the corresponding peaks are evenly spaced and their intensities decrease with the size of the cluster (n). Additionally, the intensity of the cluster peaks follows the abundance of the parent molecule. Hence, if CH_3CN abundance decreases, any peaks assigned to $(CH_3CN)_nH^+$ (where n = 0, 1, 2) should follow this trend (Ribeiro et al. 2020). This behaviour is not seen in our spectra (see Figure 6.1). On the contrary, the peaks at m/z = 65-69 and m/z = 77-83 increase, while the parent species decreases, hence these peaks do not originate from clustering upon laser desorption. Blank experiments are performed, to exclude the role of any non-volatile residue on the substrate left over from previous experiments. At an increased laser power (doubled) and detector voltage (increased by 300 V), some residue is detected. Subsequently, the substrate is irradiated for 1 hr and new small mass peaks are observed in the mass spectra. Special care is taken to tune the experimental settings (laser power and MCP detector voltage) to minimize observations of any resid-

ual material. Consequently, at the standard sensitivity settings (Section 4.2), neither the residue, nor its derivatives, are observed. This leaves the conclusion that the new signals represent newly formed photoproducts arising from CH_3CN photolysis.

After 2 min of UV photolysis, the mass peak at m/z = 67 dominates the higher region of the mass spectrum. The elemental composition of this ion corresponds to a combination of CH_3CN and a CN radical, however, to our knowledge, there are no stable molecules of that composition. This implies that it likely is a fragment of a larger molecule. The simplest scenario is that the fragment at m/z = 67 is the main fragmentation channel (molecular ion minus H) of a molecule with an elemental composition of $C_3N_2H_4$. An intense H-loss channel upon electron ionization, is typical for nitriles. The only stable candidate found in the NIST database that matches this elemental composition is glycinonitrile, n-methylene- $NCCH_2NCH_2$. Unfortunately, due to a lacking fragmentation pattern, it is not possible to confirm this assignment. At longer irradiation times, additional peaks appear near m/z = 67, suggesting subsequent (de)hydrogenation reactions (+2H or -2H). Similarly to m/z = 67, it is not possible to unambiguously assign molecular formulas to these ions.

Due to lack of available fragmentation patterns of large nitriles, the identification of ions at m/z = 77-83, in most cases, follows the assignment of the elemental composition. An exception is succinonitrile ($NCCH_2CH_2CN$), suggested to be a photolysis product in previous studies (Hudson et al. 2008). The fragmentation pattern of $NCCH_2CH_2CN$, with strong peaks at m/z = 79, and 80 fits the experimental spectrum. The assignment is supported via an available formation pathway: a recombination of two CH_2CN radicals, which at a high UV fluence, are abundant in the ice. Peaks which are near succinonitrile features differ in the number or hydrogen atoms, but that can be accounted for by +2H and -2H reactions, resulting in formation of unsaturated nitriles, and imines, respectively.

VUV irradiation of CH_3CN ice at a higher temperature of 77 K shows the same molecular complexity in the ice, with one exception. That is a lower production yield of methane. This can be explained by methane thermally desorbing from the ice, as its desorption temperature (40 K) is below the photolysis temperature of 77 K. We conclude that the ice photochemistry of CH_3CN results in a similar complexity in the temperature range between 20 and 80 K. It also implies that thermally initiated reactions do not play a (major) role in this temperature range.

As mass spectra are recorded for different fluences, it is possible to visualize the formation kinetics for the main CH_3CN photoproducts (20 K), listed in Table 4.2. The absolute ice abundances are shown in Figure 6.4, calibrated using the known initial abundance of the parent molecule. For this, complete fragmentation patterns of products described above were fitted to our data. This was followed by considering the electron impact ionization cross sections of the species which were taken from the NIST database (Kim et al. 2014) or theoretical work (Pandya et al. 2012; Zhou et al. 2019).

The HCN abundance exhibits the fastest increase and appears to be the most abundant product during photolysis. Simultaneously, at a 10 times lower formation rate, CH_3CH_2CN and CH_4 are formed in the ice. A potential origin of the significant difference in formation yields is discussed in section 4.3.3. As the photon fluence increases, methane becomes the second most abundant product. The remaining quantified products are: NCCN/CNCN, and CH_2CHCN, at significantly lower abundances, compared to HCN. The formation of H_2 is also observed, however, its yield is largely
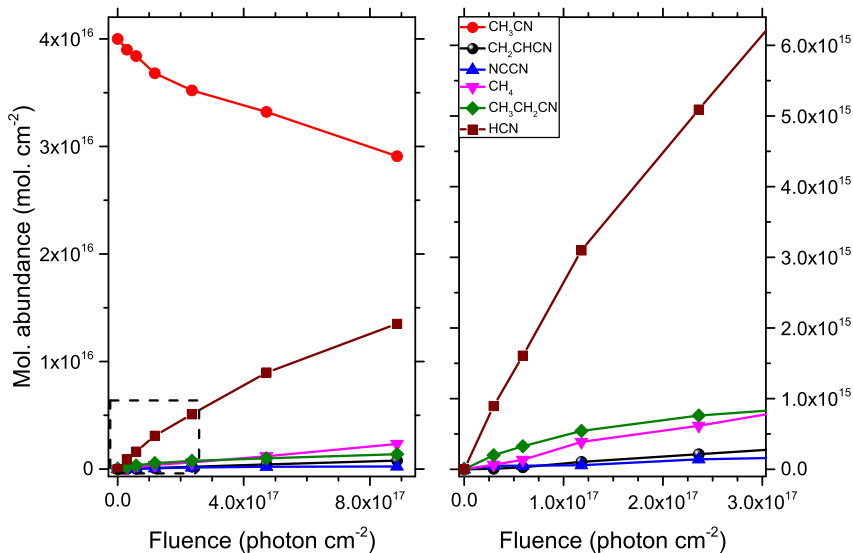
Figure 4.4: *Left panel:* Molecular abundances of species during the UV photolysis of CH$_3$CN ice as function of photon fluence. *Right panel:* Zoom in of the low fluence region indicated in the left panel.

limited by its thermal desorption. The molecular yields of all quantified photoproducts are summed up to check if the formation of new species balances the loss of the parent molecules. That is indeed the case, hence, despite unidentified peaks appearing in the ice, their contributions to the early chemical network are considered insignificant. The formation kinetics for photoproducts of CD$_3$CN at 20 K (not shown here) demonstrate similar trends.

4.3.2 H$_2$O:CH$_3$CN

Two different H$_2$O:CH$_3$CN ice mixing ratios are used (1:1 and 20:1). Figure 6.5 shows the calibrated LDPI TOF-MS data of the photolysed water rich (20:1) mixture for selected VUV fluences. The (black) reference spectrum, before irradiation, shows m/z peaks which can be assigned to fragmentation patterns of H$_2$O (m/z = 16-18), CH$_3$CN (m/z = 12-15, 24-28, 38-42) and protonated clusters of water and water-acetonitrile (m/z = 19, 37, 55, 60, 73). The latter are not formed upon VUV irradiation but are known to form upon laser desorption. After 2 minutes of irradiation, an increase in the following mass signals is observed: 27-34, 42-46, 51-60, 75, 76, 93, 94 (see inset of Fig. 6.5). As the photolysis continues, more peaks are formed. By comparing Figures 6.1 and 6.5 it is immediately clear that the level of molecular complexity is higher in the water containing ice. This is also expected. Upon UV irradiation, the ice contains OH radicals, as well as O- and H-atoms that will expand the chemical network. A systematic analysis of the resulting data is given below.

A comparison of the pure and mixed ice (1:1) allows to identify mass peaks that
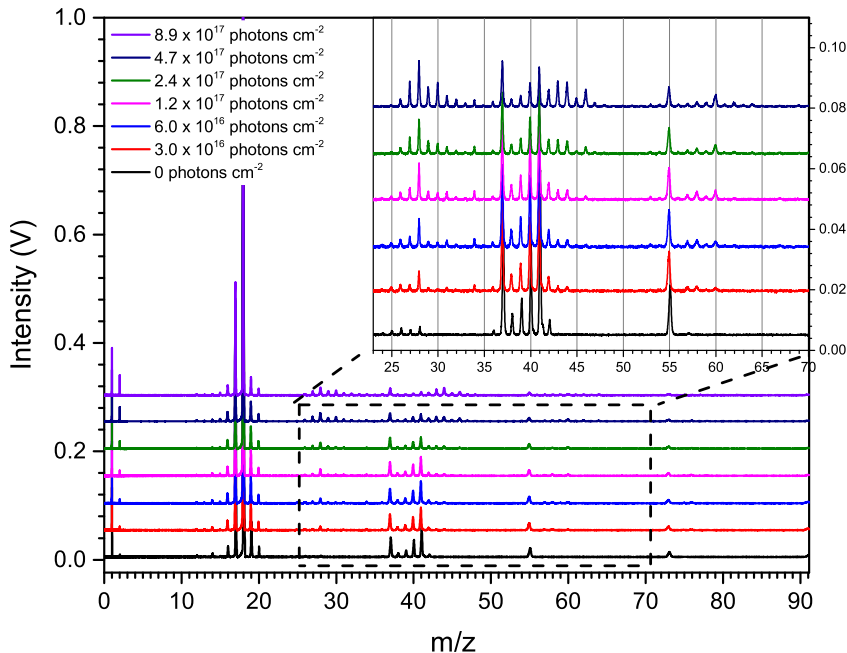
Figure 4.5: LDPI-MS signals for an UV irradiated $H_2O:CH_3CN$ (20:1) ice at 20 K for increasing photon fluence. The lowest graph shows the signal without UV irradiation. The inset is a zoom in on the intensity scale for the higher masses.

can be associated with water chemistry. In the water dominated experiments (20:1) the abundance of these products is expected to further increase. This information, combined with TOF spectra obtained for the $H_2^{18}O$ experiments, allows to assign the elemental compositions of the produced species. Finally, considering the reactions expected to take place in the ice mixture, specific mass peaks can be linked to specific (fragments of) photoproducts, similar to the approach used for pure ices. Table 3.3 shows a summary of all observed mass peaks and their corresponding elemental compositions.

The results of four different photolysis experiments: pure CH_3CN ice, two different $H_2O:CH_3CN$ mixtures (1:1 and 20:1) and a $H_2^{18}O:CH_3CN$ mixture (20:1), are shown in Figures 4.6, 4.7 and 4.8. Each figure shows a different mass range; it is noted that Fig. 4.6 shows the intermediate range (37-50 amu) and Figs 4.7 and 4.8 a lower (24-37 amu) and higher (50-70 amu) mass regime, respectively. In order to compare relative yields of products between the four experiments, all mass spectra are normalized to the amount of CH_3CN in the ice via the mass peak signal at m/z = 39. This particular peak is chosen as a signature of acetonitrile, as it does not with overlap with any other fragments of species present in the ice.

Figure 4.6 shows a mass spectral range between m/z = 37-50. Peaks at 38-42 amu are a part of the fragmentation pattern of CH_3CN ice. The VUV irradiation of the (1:1) ice mixture yields new mass peaks at m/z = 45-48 and signals at m/z = 42, 43,
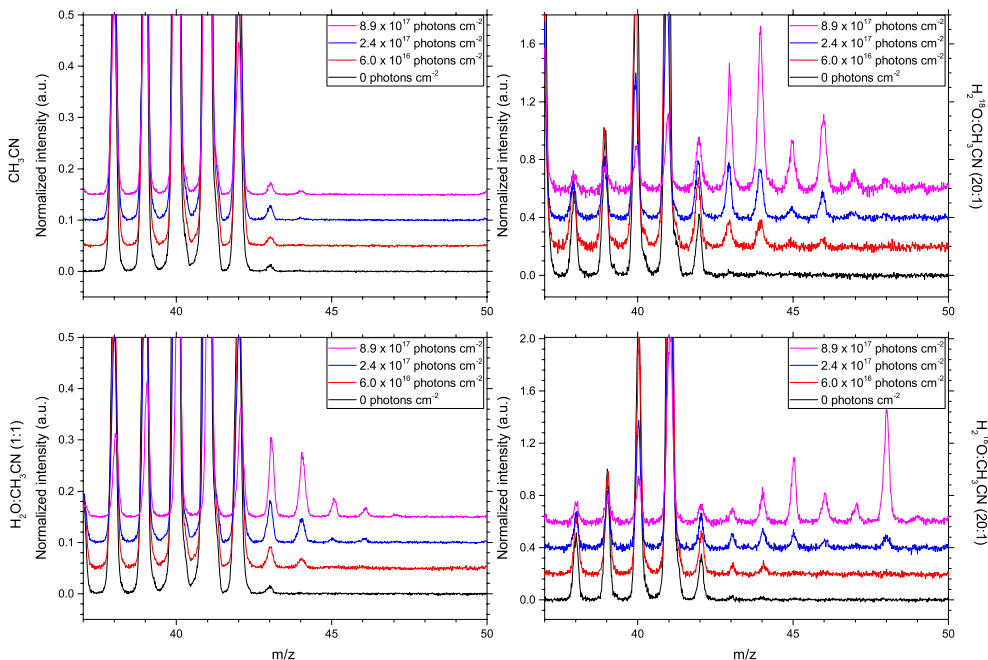
Figure 4.6: Normalized LDPI-MS signals (m/z range: 37-50) for four different photolysis experiments. Top panel from left to right: CH_3CN, H_2O:CH_3CN (20:1). Bottom panel from left to right: H_2O:CH_3CN (1:1) and CH_3CN:$H_2^{18}O$ (20:1).

44 are significantly higher than in the pure ice experiment. The new peaks hint at the presence of O-bearing species, which is consistent with the TOF spectra found for the water dominated experiment (20:1). A comparison of the (20:1) spectra for the ^{16}O and ^{18}O water shows that not all product peaks (42-48 amu) can be assigned to O-bearing species, as only part of the peaks shifts upon ^{18}O substitution.

The observed peak shifts, corresponding to 2 or 4 amu, indicate that O-bearing species/fragments are involved with one or two oxygen atoms. The corresponding elemental compositions are: CHNO, CH_3NO, CO_2H_{2x} and C_2H_yO (where x = 0, 2 and y = 4, 6). Based on the characteristic mass peaks of all considered species, these compositions can be assigned to isocyanic acid (HNCO), carbon dioxide (CO_2), acetaldehyde (CH_3CHO), dimethyl ether (CH_3OCH_3), ethanol (CH_3CH_2OH) and formic acid (HCOOH). Formamide (NH_2CHO) is one of the candidates fitting the CH_3NO composition, and several possible solid state formation routes have been discussed before (Raunier et al. 2004; Jones et al. 2011; Ligterink et al. 2018a), but other isomers cannot be excluded at this stage. The assignment of the elemental formula HCNO to isocyanic acid is guided by a previous study (Gerakines et al. 2004) and the greater stability of HNCO versus its isomers by Crowley & Sodeau 1989.

The contribution from other species in the m/z = 42-48 range is only clearly visible in the ^{18}O experiments. All oxygen containing species shift to m/z = 45 or higher, while peaks at 42, 43, and 44 remain present in the spectra. Molecules which contribute to these peaks lack oxygen. Considering the parent species, it was concluded that these mass signals originate from imines (containing the = NH functional group)
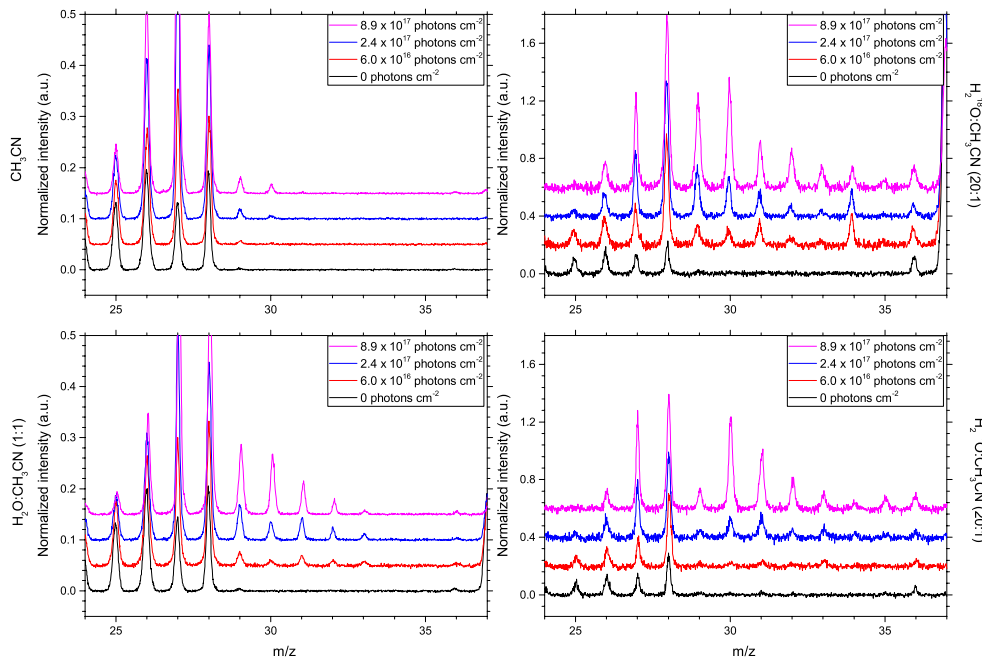
Figure 4.7: Normalized LDPI-MS signals(m/z range: 24-37) for four different photolysis experiments. Top panel from left to right: CH$_3$CN, H$_2$O:CH$_3$CN (20:1). Bottom panel from left to right: H$_2$O:CH$_3$CN (1:1) and CH$_3$CN:H$_2$^{18}O (20:1).

and amines (containing the -NH$_2$ group). It is important to note that as the signals in the ^{18}O experiments are generally less intense, partially due to the presence of 3% of ^{16}O, this does not account for the observed signals at m/z = 42-44. A similar process was demonstrated for HCN, which undergoes hydrogenation reactions, even with cold atoms, to form CH$_2$NH$_2$ (Theule et al. 2011).

The present work demonstrates, for the first time, the hydrogenation of a CN bond for larger nitriles. The formation of imines and amines seems to be significantly enhanced in the presence of water ice. This has two major consequences. Firstly, it underlines the "catalytic" potential of water ice. Secondly, it implies that =NH and −NH$_2$ functional groups are present in the ice, which helps with interpreting the mass signals in the other mass ranges. The addition of water into the ice mixture clearly increases the number of possible chemical pathways and is further discussed in Section 4.3.4.

Figure 4.7 shows a lower mass range (m/z = 24-37) which is the signature region of smaller COMs. A comparison of the UV irradiated pure and mixed ices (1:1), shows that new mass signals appear at m/z = 31, 32, 33, while at m/z = 29 and 30 significantly higher signals are found. The peak at m/z = 32, which further increases with water content (20:1) is determined to have an elemental composition of CH$_4$O. With CH$_3$ and OH radicals available in the ice, the most logical explanation is that this peak corresponds to the ionized methanol (CH$_3$OH$^+$). This assignment is consistent with the shift of the peak (m/z = 32 to m/z = 34) in the ^{18}O experiments and with the increasing intensity of the methanol base peak (m/z = 31, shifted to m/z = 33),
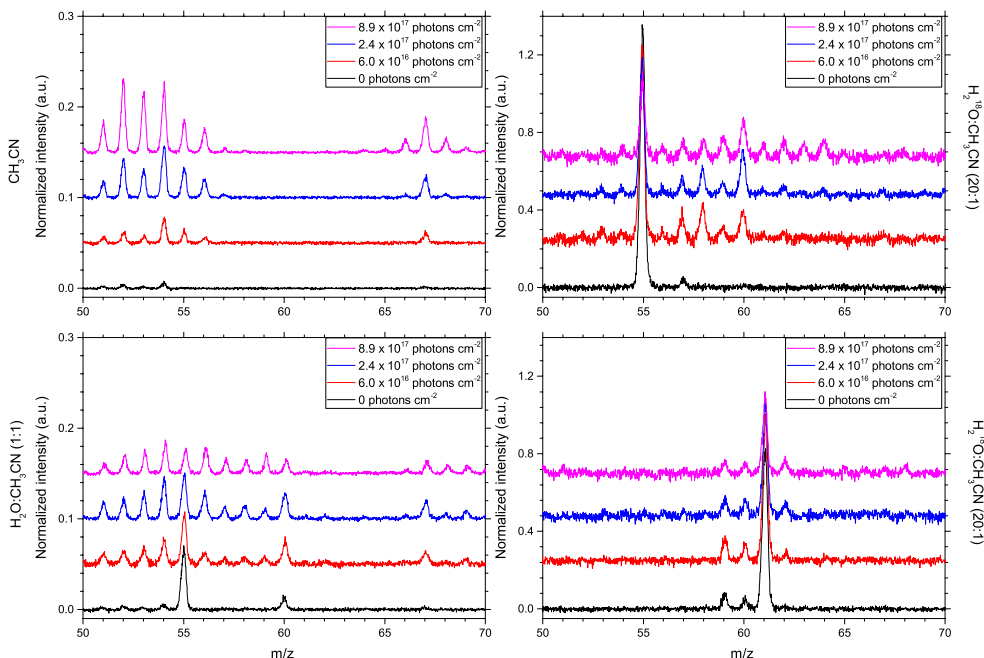
Figure 4.8: Normalized LDPI-MS signals (m/z range: 50-70) for four different photolysis experiments. Top panel from left to right: CH_3CN, $H_2O:CH_3CN$ (20:1). Bottom panel from left to right: $H_2O:CH_3CN$ (1:1) and $CH_3CN:H_2^{18}O$ (20:1).

although it should be noted that this peak is also characteristic for fragment masses of larger COMs. The formation of methanol also indicates that CH_3OH photoproducts as studied by Öberg et al. 2009c and Paardekooper et al. 2016b can be expected.

The mass peak at m/z = 33 is due to species with an elemental composition of NH_3O. The molecular ion of hydroxylamine (NH_2OH) could be a carrier of this signal, as is the case for protonated methanol or a fragment of hydrogen peroxide (H_2O_2). Contributions of the latter two are less likely, as mass signals at m/z = 32 (unfragmented methanol) and 34 (unfragmented hydrogen peroxide) are relatively low. In previous work, NH_2OH was shown to form through hydrogenation of NO (Fedoseev et al. 2012) and was recently detected in space (Rivilla et al. 2020).

In the case of peaks at m/z = 28-30, an increase is due to multiple species. The most likely contributors include carbon monoxide (CO)/N_2, formaldehyde (H_2CO), methanimine (CH_2NH) and fragments of bigger COMs. Specifically, primary amines have their characteristic, strong fragment at m/z = 30 (CH_2NH_2). For the water dominated experiments, the ratio of 29 to 30 is reversed upon longer photolysis, which may reflect a growing presence of a family of primary amines. All these assignments are also consistent for experiments with increased water content and (non)shifts observed for ^{18}O. Formation of imines and amines in the ice might proceed via excited radicals reacting with the CN bond of CH_3CN, for instance:

$$CH_3CN + 2H \rightarrow CH_3CHNH \qquad (4.4)$$

$$CH_3CHNH + 2H \rightarrow CH_3CH_2NH_2 \qquad (4.5)$$

Notes. Species previously detected using gas chromatography-mass spectrometry (GC-MS) after energetic processing of $H_2O{:}CH_3CN$ ice are marked with an asterisk (*) based on Hudson et al. 2008

Table 4.3: Characteristic m/z peaks used for identification of photoproducts of the UV photolysis of the $H_2O{:}CH_3CN$ (1:1 and 20:1) and $H_2^{18}O{:}CH_3CN$ (20:1) ices.

	$H_2O{:}CH_3CN$ m/z	$H_2^{18}O{:}CH_3CN$ m/z	Elemental composition	Proposed molecular species	Name
	2	2	H_2	H_2	mol. hydrogen
	16	16	CH_4	CH_4	methane*
	26, 27	26, 27	HCN	HCN/HNC	hydrogen (iso)cyanide *
	42, 43	42, 43	C_2H_5N	CH_3CHNH	imine (R−CHNH)
	44, 45	44, 45	C_2H_7N	$CH_3CH_2NH_2$	amine (R−CH_2NH_2)
$C_xH_yN_z$	52	52	C_2N_2	CNNC/CNCN	cyanogen/isocyanogen
	26, 52, 53	26, 52, 53	C_3H_3N	CH_2CHCN	2-propenenitrile
	28, 54	28, 54	C_3H_5N	CH_3CH_2CN	propionitrile
	29, 55	29, 55	C_3H_5N	CH_3CH_2NC	ethyl isocyanide
	56	56	$C_2H_4N_2$	-	-
	66-69	66-69	$C_3H_xN_2$	-	-
	77-83	77-83	$C_4H_yN_2$	-	-
	33, 34	37, 38	H_2O_2	H_2O_2	hydrogen peroxide
	28	30	CO	CO	carbon monoxide
	29, 30	31, 32	CH_2O	H_2CO	formaldehyde*
	31, 32	33, 34	CH_4O	CH_3OH	methanol
	44	48	CO_2	CO_2	carbon dioxide
$C_xH_yO_z$	44, 29	46, 31	C_2H_4O	CH_3CHO	acetaldehyde *
	45, 46	47, 48	C_2H_6O	CH_3OCH_3	dimethyl ether
	45, 31	47, 33	C_2H_6O	CH_3CH_2OH	ethanol
	29, 46, 45	31, 50, 49	CHO_2	HCOOH	formic acid
	31, 60	33, 64	$C_2H_4O_2$	$HCOOCH_3/HOCH_2CHO$	methyl formate/glycolaldehyde
	43, 45, 60	45, 49, 64	$C_2H_4O_2$	CH_3COOH	acetic acid

-	$H_2O:CH_3CN$ m/z	$H_2^{18}O:CH_3CN$ m/z	Elemental composition	Proposed molecular species	Name
	31, 62	33, 66	$C_2H_6O_2$	$(CH_2OH)_2$	ethylene glycol
$C_xH_yN_zO_w$	33	35	NH_3O	NH_2OH	hydroxylamine
	43	45	$CNOH$	$HNCO/HOCN/HCNO$	(iso)cyanic acid/fulminic acid
	45	47	CH_3NO	NH_2CHO	formamide
	57	59	C_2H_3NO	$CH_3NCO/HOCH_2CN$	methyl isocyanate/glycolonitrile*
	58	60	C_2H_4NO	-	-
	59	61	C_2H_5NO	CH_3CONH_2/CH_3NHCHO	acetamide*/N-methyl formamide
	60	62	CH_4N_2O	NH_2CONH_2	urea
	62	64	C_2H_7NO	-	amine
	63	67	CH_5NO_2	-	-
	64	68	CH_5NO_2	-	-
other	19, 37, 55, 73	21, 41, 61, 81	$H_{2n+1}O_n$	$(H_2O)_nH^+$	water clusters H+
	60	-	C_2H_6NO	$(H_2O)(CH_3CN)H^+$	water/acetonitrile H+

From Fig. 4.8 it becomes clear that the higher mass range, m/z = 51-65, exhibits a picture of chemical complexity that is largely consistent with the lower mass range. Peaks at m/z = 51-57, associated with nitriles containing three C-atoms, are present in both the pure ice photolysis and in the 1:1 ice mixture. In the water dominated experiment (20:1), these are almost non detectable, most likely, due to an overabundance of water, which lowers the probability for CH_3CN molecules to stay next to each other in the ice.

New peaks, compared to the pure acetonitrile photolysis, appear at m/z = 58-60 and the peak at m/z = 57 is significantly more pronounced. Additionally, water dominated experiments give origin to new peaks at m/z = 61-64. Assigning elemental compositions to all peaks in this mass range (m/z = 51-65) is challenging due to low signals of the ^{18}O experiments, however, a few conclusions can be drawn. The peak at m/z = 57, for which a strong contribution from O-bearing species is visible, has an elemental composition of C_2H_3NO. There are several species consistent with this composition but the most likely candidates are glycolonitrile ($HOCH_2CN$) and methyl isocyanate (CH_3NCO). The first structure can be a direct result of a radical recombination ($OH + CH_2CN$) and the latter can be formed through an O-atom interacting with the triple bond of CH_3CN or its structural isotope, CH_3NC. The assignment of CH_3NCO is also supported by a recent study by Fourré et al. 2020, in which the relative thermodynamical stability of 40 isotopes of C_2H_3NO is compared. The clearly visible peak at m/z = 58 is associated with an elemental composition of C_2H_4NO, which is confirmed with a shift to m/z = 60. Considering the available molecular reservoir, the peak at m/z = 59 can be assigned to an elemental composition of C_2H_5NO. Newly formed species consistent with this observation include acetamide (CH_3CONH_2) and N-methyl formamide (CH_3NHCHO), with the first molecule being the most stable isomer (Lattelais et al. 2010). These may form in O/OH radical reactions involving CH_3CN and its structural isomer CH_3NC, followed by H-atom additions, but as the involved energetics are unknown, such a conclusion only can be treated with care.

Peak 60, which significantly increases for water dominated ices, can be explained by contributions from two stable combinations of elements: $C_2H_4O_2$ or CH_4N_2O. The peak shifts observed in the ^{18}O experiments, point to a major contribution from the species with one oxygen atom. One of the structures, that is potentially present is a molecule of astrobiological context, urea (NH_2CONH_2). This would be consistent with the Wohler synthesis. The previously demonstrated formation pathways of urea on interstellar grains analogues includes radical recombination of NH_2 and $CONH_2$ (Raunier et al. 2004; Ligterink et al. 2018a).

In water dominated experiments, additional peaks appear at m/z = 61-64. These peaks are shifted to 64-68 range in the ^{18}O experiments, indicating a presence of two oxygen atoms in the fragments. A possible corresponding elemental composition is CH_xNO_2, where x = 3-5.

The chemical complexity continues to increase as many peaks are seen in the higher m/z range. This indicates that upon VUV irradiation of CH_3CN (embedded in water) ices, even larger COMs with at least six or more C-, N- and/or O-atoms are formed. A specific assignment is not possible at this stage, but this observation on its own is interesting, as it shows that CH_3CN can act as an efficient precursor species in the formation of large N-containing COMs.

4.3.3   Abstraction reactions in the ice at 20 K

The most abundant product of the photolysis of pure CH_3CN ice is HCN. In order to compare the HCN yield between different experiments, it is helpful to convert the molecular yields to formation rates in molecules per absorbed photon. For this, average photon absorption cross sections in the range 120-165 nm are used, which for CH_3CN and H_2O are 7.5×10^{-18} photons cm^{-2} and 2.3×10^{-18} photons cm^{-2}. For mixed ices, the absorption cross section is derived as an average between the constituents, considering the ratio between them. The efficiency of HCN formation, per destroyed CH_3CN, per absorbed photon, is similar for all studied ices. On average, 1000 absorbed photons lead to the destruction of 230 CH_3CN molecules and the formation of 200 HCN molecules, almost 10 times the amount of CH_4.

The dominating yield of HCN motivates further investigation of its formation route. The radical recombination formation pathway of HCN requires photodissociation of two CH_3CN molecules (CN+H recombination). Additionally, if radical recombination is the dominant reaction mechanism, the CH_4 formation yield should be comparable (CH$_3$+H route). The calculated yields are not in line with a radical-radical recombination scenario, thus, other reaction types need to be considered.

One of the alternative formation routes is an abstraction reaction with the general formula: H-X+CN $\rightarrow$ X+HCN, where X can be CH_2CN, CH_3, etc. This reaction of CH_2CN and a CN radical resulting in formation of HCN is strongly exothermic (99 kJ/mole), while a similar reaction including a CH_3 radical, and resulting in CH_4 formation is barely exothermic (8 kJ/mole). The calculations of enthalpies are based on values from Active Thermochemical Tables available via Argonne National Laboratory (Ruscic et al. 2004). This helps to account for a major difference in production rates of HCN and CH_4. A theoretical study will be necessary to test which is the most efficient formation mechanism of HCN in the H_2O:CH_3CN ice. The reaction type discussed above, of an excited radical with a neutral species, has been recently demonstrated to be efficient also at low temperatures for gas phase CH_3OH+OH and CH_3CN+CN (Shannon et al. 2013; Sleiman et al. 2016). Hence, this type of reactions should be considered in gas-grain astrochemical models, which is already the case in recent work by Jin & Garrod 2020.

4.3.4   Role of water in ice chemistry

Water, as the most abundant constituent of interstellar ice, plays an important role in the solid state chemical networks. The effects of water molecules on the ice chemistry observed in this work are in agreement with previous studies (e.g. Öberg et al. 2010b). In particular, it is found that the formation of O-rich species is increased with the water content. In the water dominated experiment, $m/z = 44$ is assigned to species containing two O atoms, consistent with the observed shift to $m/z = 48$, for ^{18}O experiments. This peak, assigned to CO_2, is less intense in the mixture with 1:1 ratio, in comparison to the mixture with 20:1 ratio, and is not present in the pure CH_3CN ice photolysis. Other O-bearing species exhibit a similar behaviour, which follows the water abundance in the ice. Consequently, as CH_3CN molecules are more diluted in a water rich ice, the abundance of nitrile based photoproducts (e.g. CH_3CH_2CN) decreases proportionally.

H_2O ice provides an environment in which nitriles can efficiently transform into

imines and amines, upon UV-photolysis. Previous studies already reported on these findings. An isomerization of CH_3CN to an imine was demonstrated during UV photolysis by Hudson & Moore 2004, however, this was not studied in the water environment. In another study, Nguyen et al. 2019 performed an experimental and theoretical investigation of hydrogenation of CH_3CN. The study demonstrated a high energy barrier for hydrogenating the CN bond: between 0.06 - 0.22 eV, depending on the used level of theory. The analysis of the mass spectra in figure 4.6 shows evidence for effective hydrogenation of the CN bond, which leads to formation of imines and amines, in a water rich ice. This must be due to the energetic radicals produced in photodissociation of the water molecules. Indeed, the average translation energy carried by an H radical following water dissociation is between 1.5 - 2.5 eV (Andersson & van Dishoeck 2008), larger than the calculated barrier of 0.22 eV. Following the first hydrogenation of the CN bond, subsequent H atom additions have a lower energetical barrier, which eventually leads to a formation of imines and amines.

The chemical complexity observed in the photolyzed mixed ices goes beyond amines, specifically the formation of amides (molecules containing the $-C(=O)NH_2$ functional group) is observed. During the photolysis of the mixed ices, the mass peaks associated with amides (m/z = 57-59) appear after 2 min of irradiation (see Fig. 4.8), hence a formation pathway involving many steps is unlikely. Here, formation of amides is suggested via O-/OH-radical interacting with the triple bond of CH_3CN. Photodissociation of H_2O using photons in an energy range between 8.5-10.5 eV leads to an electronically excited $OH(A^2)$ and $O(^1D)$ (van Harrevelt & van Hemert 2008), which can interact with the CN bond to form amides. This chemical route, however, requires further verification. At least two other pathways to form amides are known. Both might be more relevant towards the end of our experiments, as multiple chemical steps are involved. One pathway is demonstrated by Ligterink et al. 2018a, where formation of CH_3CONH_2 proceeds via recombination of the NH_2CO radical (formed from NH_2+CO) with a CH_3 radical. An alternative route is through breaking of the C-OH bond in any carboxylic acid (e.g. acetic acid, CH_3COOH) and attaching a -NH, NH_2 or -NRH (from ammonia or any amine) to the leftover C=O structure will yield formamide (NH_2CHO).

4.4 Astrophysical implications and conclusions

N-bearing COMs are commonly observed towards diverse environments, yet the chemical network leading to their formation is still unclear. An observational study focused on the origin of N-bearing COMs in the Galactic Center quiescent giant molecular cloud, G+0.693, by Zeng et al. 2018 concluded that species such as CH_3CN, HC_5N, HNCO, and NH_2CHO are transferred to the gas phase from dust grains. The gas phase abundances of CH_3CN observed in protoplanetary disks, photodissociation regions (PDR) and dark, dense molecular cores, also imply that CH_3CN is released from icy mantles (Loomis et al. 2018; Gratier et al. 2013). These findings are in agreement with the laboratory work presented here that shows that upon vacuum UV irradiation of $H_2O:CH_3CN$ ice a large amount of N-bearing COMs can be formed. This is not fully unexpected, as the molecular structure of acetonitrile (CH_3-CN) resembles that of methanol (CH_3-OH) that has been shown to be an important parent molecule to O-bearing COMs. Actually, as methanol is found to be formed upon UV photolysis of

$H_2O:CH_3CN$ ice, the experiments analyzed here also offer pathways towards O-(and N/O-)bearing COMs. It should be noted, though, that methanol is more abundant than CH_3CN; also other nitrogen precursors, such as NO and NH_x radicals may play a role in the formation of N-bearing COMs (see for example Congiu et al. 2012, Muñoz Caro et al. 2014, Jones et al. 2011 and Ioppolo et al. 2021). To fully benefit from the work presented here, modeling will be needed to place the importance of CH_3CN ice chemistry in the larger astrochemical context. For this it also will be important to better understand how CH_3CN forms.

It should also be noted that pure CH_3CN ice does not exist in space, but for the purpose of this study a diluted $H_2O:CH_3CN$ (20:1) mixture simulates the potential role acetonitrile can play. In fact, the involvement of the methyl radical, CH_3, in CH_3CN formation would position its formation stage in the water rich phase (see Öberg et al. 2008; Qasim et al. 2020). There are different astronomical environments where the processes described here may be at play. In dense dark clouds, it is generally assumed that solid state astrochemical processes are driven by atom addition reactions (Linnartz et al. 2015). It is here that smaller molecules like H_2O, NH_3 and HNCO or CH_4 form, as well as larger species including glycerol (Fedoseev et al. 2017). UV induced chemistry is considered to be less important (Chuang et al. 2017), but cannot be excluded. In dark clouds ices are exposed to cosmic ray induced UV irradiation. In the more translucent cloud areas, as well as in protoplanetary disks, UV induced chemistry takes over. During the star formation cycle, these energetically processed ices are eventually desorbed, allowing for the detection of COMs in the gas phase. Hence, it is interesting to compare the products detected during the UV photolysis of the CH_3CN and $H_2O:CH_3CN$ (20:1) ices with astrochemical observations and models.

After an exposure of a pure CH_3CN ice to a photon fluence of 8.9×10^{17} photons cm^{-2}, 25% of CH_3CN molecules are converted to other species. The products which are larger than the parent species, supplying the N-bearing COM reservoir, make up for 25% of the lost parent molecules. The same analysis was performed for the water dominated mixture (20:1). 25% of water molecules were depleted while 85% of acetonitrile molecules were consumed. This demonstrates that water effectively prevents the recombination of CH_3CN and enhances its photoconversion by providing reactive O, OH, and H radicals. Thus, on the dark cloud time scales, a high conversion rate of CH_3CN into the photoproducts can be expected.

The photolysis of pure CH_3CN ice leads to isomerization or formation of other nitrile based species. HCN is the most abundant product of photolysis, but many other species are formed including: CH_3CH_2CN and $NCCH_2CH_2CN$. The types of reactions leading to this complexity are radical-radical recombinations (e.g. $CH_3+CH_2CN \rightarrow CH_3CH_2CN$), radical-molecule interactions (e.g. $CH_3CN+CN \rightarrow HCN+CH_2CN$) and (de)hydrogenation reactions (e.g. $CH_3CH_2CN - 2H \rightarrow CH_2CHCN$ and $CH_3CN + 2H \rightarrow CH_3CHNH$). Specifically for HCN, it is demonstrated that radical-radical interactions alone are not sufficient to account for its formation yield.

The chemical complexity resulting from the pure CH_3CN photolysis is shown in the upper part of Figure 4.9. All photoproducts, except for NCCN and $NCCH_2CH_2CN$, have been observed in the ISM. However, the presence of NCCN in the ISM is implied by detections of two closely related species: a metastable isomer CNCN and the protonated form of cyanogen, NCCNH$^+$ (Agúndez et al. 2015, 2018). Both of the species are detected in dense clouds L483 and TMC-1. The known formation mechanism of NCCN includes an exothermic gas phase pathway via neutral-neutral
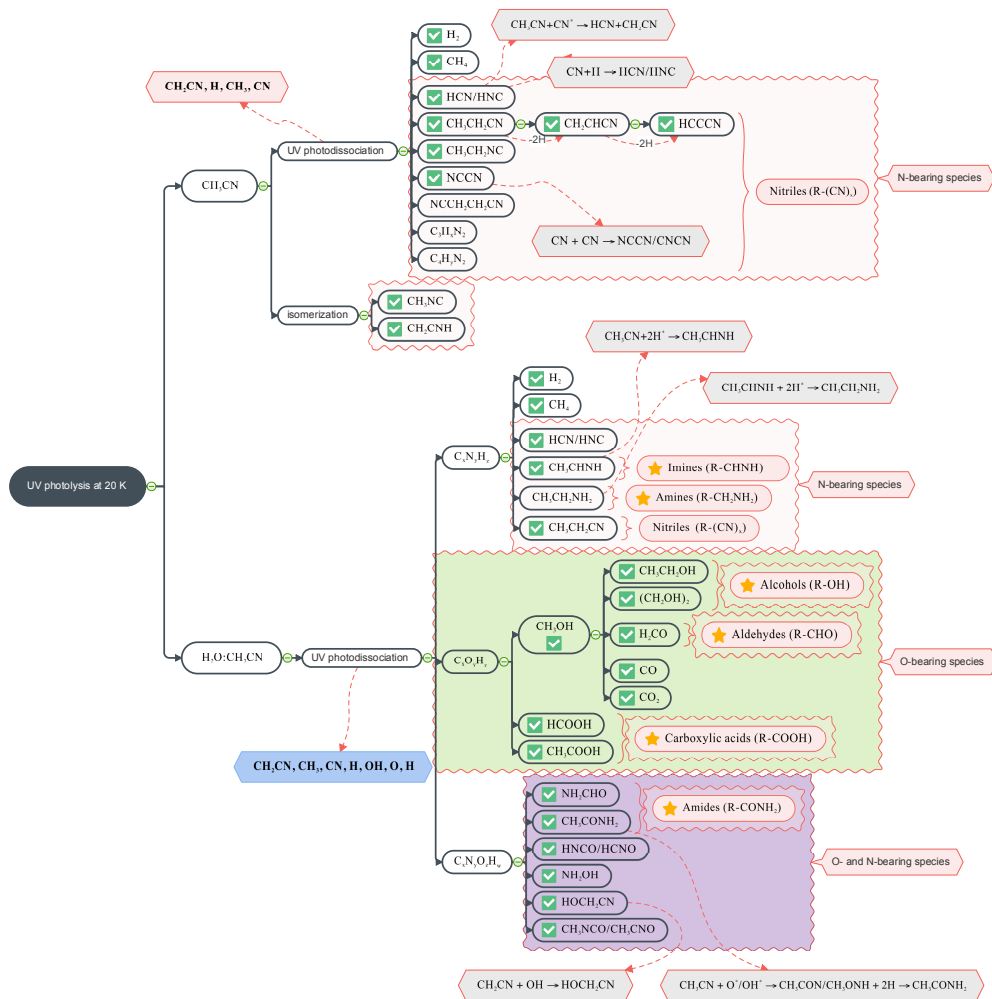
Figure 4.9: An overview of products of UV photolysis of CH_3CN and $H_2O:CH_3CN$ (20:1) ices at 20 K. Groups of molecules uniquely produced in the ice mixtures are marked by a yellow star. The species marked with a check mark have been detected in the ISM. NCCN is marked as detected due to observations of other species which are chemically related and imply its presence in the ISM (Agúndez et al. 2015).

reaction: $CN+HCN \rightarrow NCCN+H$ (Petrie et al. 2003). Alternatively, it is suggested that it might be also formed on dust grains through recombination of two CN radicals. This is indeed the case in our experiments. It is important to note, that the formation of NCCN/CNCN, as well as $NCCH_2CH_2CN$, is only visible for the pure CH_3CN ice photolysis, thus both species could be used as tracers of an ice that is rich in CN.

In a more realistic case, the CH_3CN is diluted in a H_2O ice, and this mixture yields significantly more complexity (shown in the lower part of Fig. 4.9). Even though it is not possible to assign all observed mass peaks unambiguously to specific carrier molecules, the mass spectra reveal trends that can be connected to chemical families. It is clear that a diverse number of larger N-containing COMs is formed upon UV irradiation of H_2O:CH_3CN ice. In the presence of water, the CN bond of acetonitrile can be hydrogenated, leading to the formation of imines and amines. In the study by Loomis et al. 2013, CH_3CHNH was observed towards Sgr B2(N) and now its formation pathway is demonstrated to be possible via hydrogenation of CH_3CN. The hydrogenation process continues until $CH_3CH_2NH_2$ is formed, which has the highest abundance towards the end of the UV photolysis. However, this molecule is yet to be detected in the ISM.

The reactivity of O and OH radicals with the CN bond provides a chemical link between the O- and N-bearing chemical networks. Specifically, formation of amides is suggested to proceed via the O/OH radical interacting with the parent nitrile molecule, which, when followed by hydrogenation reaction, yields CH_3CONH_2. Other formed N- and O-bearing species include HNCO/HCNO, NH_2OH, CH_3NCO and $HOCH_2CN$. All of these molecules, except for an CH_3NCO isomer, namely, CH_3CNO, have been observed in the ISM. The formation mechanism of $HOCH_2CN$, observed in IRAS-16293B (Zeng et al. 2019) and in Serpens SMM1-a (Ligterink et al. submitted), is suggested to have a solid state route. In our experiments it most likely proceeds via OH + $CH_2CN \rightarrow HOCH_2CN$, as both of these radicals are immediately available to react. Alternatively, this product might be formed through reactions of NH_3 with H_2CO and $NH_4^+OCN^-$ (Danger et al. 2012).

To conclude, the UV photolysis of pure CH_3CN ice yields larger nitriles including NCCN/CNCN, CH_3CH_2CN and $NCCH_2CH_2CN$. In addition, it is demonstrated that H atom abstraction reactions are an efficient formation pathway of HCN. The UV photolysis of an astronomically relevant H_2O:CH_3CN ice at 20 K, leads to formation of larger (at least up to 6-7 C/N/O-containing) molecules with the functional groups of: imines, amines, amides, large nitriles, carboxylic acids and alcohols. Photodissociation products of H_2O play a key role in this chemical network. Hydrogenation of the CN bond leads to formation of imines and amines, whereas the interaction of O- and OH with the CN bond results in formation of amides. The identification of photoproducts (see Fig. 4.9), provides a tool to link astronomical observations of (N- and O-bearing) COMs to the underlying solid state processes in which these are formed. In this study it is shown that CH_3CN can play a central role in the chemical network that ultimately results in a further increase of molecular complexity in space. Many of these species already have been identified in recent studies (van Gelder et al. 2020b, Ligterink et al. 2020, submitted and Nazarri et al. 2020, in preparation) other species not identified yet, may be well present in the ISM, following the work presented here.

5 | UV PHOTODESORPTION AND PHOTOCONVERSION RATES OF H_2O ICE - MEASURED WITH LASER DESORPTION POST IONIZATION MASS SPECTROMETRY

Abstract

Ultraviolet (UV) photodesorption of water (H_2O) ice is a non-thermal desorption mechanism required to account for detected abundances of gas-phase water (H_2O) towards cold regions within the interstellar medium (ISM). Previous experimental and theoretical studies provide a range of photodesorption rates for H_2O ice, and point to a convoluted competition between molecular processes following an absorption of a UV photon in the ice. A quantitative measurement allowing for separation of the effect of photodesorption and photoconversion during the photolysis of H_2O ice is still lacking. Here we aim to quantify the effects of photodesorption and photoconversion upon UV photolysis of a H_2O ice. A porous amorphous H_2O ice at 20 K is processed with UV photolysis (photon energy of 7-10.2 eV) and compared to an identical experiment with an additional layer of argon coating. To trace the ice composition and thickness, laser desorption post ionization time-of-flight mass spectrometry (LDPI TOF MS) is utilized. A comparison between (un)coated experiments allows to derive information about the photoconversion and photodesorption of the ice and quantify the latter. We derive the total photodesorption rate for a porous amorphous H_2O ice at 20 K to be $(1.0 \pm 0.2) \times 10^{-3}$ per incident UV photon ($7 - 10.2$ eV), in agreement with the available literature. Based on this value, we place an upper limit on the intact (H_2O) and dissociative (OH) desorption rates, equal to 1.0×10^{-3} per incident UV photon, while for reactive desorption (O_2), this limit is equal to 0.5×10^{-3} per incident UV photon. Photoconversion depletes the H_2O ice at a rate of $(2.3 \pm 0.2) \times 10^{-3}$ per incident UV photon.

5.1   Introduction

Water (H_2O) is ubiquitous in the interstellar medium (ISM) and plays a key role in the physics and chemistry of the star- and planet-forming regions. It is the most abundant constituent of the interstellar ice mantles (Gibb et al. 2004; Boogert et al. 2008), and has an observed gas-phase trail in different environments, including diffuse and translucent clouds (Flagey et al. 2013), prestellar cores (Caselli et al. 2012), star-forming regions (Ceccarelli et al. 2010), protoplanetary disks (Hogerheijde et al. 2011), and comets (Hartogh et al. 2011). The observed abundances of water in the ice and gas are intricately linked, and provide information on local physical conditions.

The majority of water in the ISM resides in interstellar ices with an average abundance of solid H_2O with respect to gas-phase H_2 equal to 1.0×10^{-4} (e.g., Pontoppidan et al. 2004; Boogert et al. 2015; Whittet et al. 2013). Water ice is mainly formed on cold dust grains (10 – 20 K) via surface hydrogenation reactions with O, OH, O_2, and O_3 (Tielens & Hagen 1982; Bergin et al. 2000; Ioppolo et al. 2008, 2010; Miyauchi et al. 2008; Lamberts et al. 2013). An additional low-temperature formation channel is available via gas-phase chemistry. This contribution is limited by the efficiency of the involved ion-molecule reaction scheme, and is capable of reproducing the water abundances of H_2O/H_2 only at the level of $(0.5 - 1.5) \times 10^{-8}$, equivalent to abundances found in translucent clouds (Bergin et al. 1995; Jensen et al. 2000; Hollenbach et al. 2009). An alternative gas-phase formation pathway via neutral-neutral chemistry becomes efficient only above temperatures of 250 K (Harada et al. 2010).

The ice chemistry is coupled with processes in the gas-phase via accretion and desorption processes. In regions with temperatures between 10 – 20 K, observed gas-phase water abundances cannot be accounted for by gas-phase formation or thermal desorption, hence non-thermal desorption mechanisms need to be considered (Willacy & Langer 2000; Boonman et al. 2003; Öberg et al. 2009d; Hollenbach et al. 2009; Walsh et al. 2010; Oka et al. 2012). This has been the case for observations towards photon dominated regions of molecular clouds (Snell et al. 2000; Wilson et al. 2003), prestellar cores (Caselli et al. 2012), outer parts of protostellar envelopes (Schmalzl et al. 2014) and protoplanetary disks (Dominik et al. 2005; Willacy 2007; Hogerheijde et al. 2011). The non-thermal desorption mechanism that is used to explain these observations is UV photodesorption of water ice. This mechanism, initiated by a UV photon absorption (6 – 13.6 eV), allows species in the ice to be transferred into the gas-phase. For this process to take place, UV photons are required, which originate from the interstellar radiation field (ISRF) and nearby protostars. In regions where ISRF is attenuated by dust grains (i.e., cores of dense clouds or protoplanetary disks), the (lower) photon flux originates from interactions of cosmic rays with H_2, resulting in a secondary UV field, with emission peaking at Ly-α (Prasad & Tarafdar 1983; Gredel et al. 1989). For these reasons photodesorption of interstellar ice analogues has been studied in detail, both experimentally and theoretically for a number of different molecules, including CO, CO_2, CH_4, CH_3OH, and also H_2O.

An experimental determination of the photodesorption rate is inherently challenging due to the convoluted competition between photodesorption and photoconversion in UV-irradiated interstellar ices (see Fig. 1 in Bulak et al. 2020). Photoconversion is characterized by a combination of the following two solid state processes: photodissociation, followed by recombination reactions into photoproducts (defined as photochemistry), and reactions of nondissociated, photoexcited molecules, with neighboring

neutral species. Both types of reactions provide formation pathways of many of the observed simple and complex species (e.g., Gerakines et al. 1996; Garrod et al. 2008; Öberg et al. 2009c; Paardekooper et al. 2016b; Bulak et al. 2021). The competition between photodesorption and photoconversion usually takes place for species with a bond dissociation energy below the energy of impacting UV photons, which applies to most constituents of interstellar ices found in the dense molecular clouds, H_2O, CO_2, CH_4, NH_3, CH_3OH. The common exceptions are CO and N_2, which have a bond dissociation energy above 10.2 eV.

The photodesorption and photoconversion of H_2O ice have been extensively studied experimentally (Westley et al. 1995a; Gerakines et al. 1996; Öberg et al. 2009d; DeSimone et al. 2013; Cruz-Diaz et al. 2018), and with molecular dynamics simulations (Andersson et al. 2006; Andersson & van Dishoeck 2008; Arasa et al. 2010, 2011, 2015; Koning et al. 2013). In the original laboratory studies, a quartz micro-balance was used to monitor the depletion of H_2O ice upon UV irradiation and used to derive the photodesorption rate. Simultaneously, photodesorbed gas phase species, H_2 and O_2, were monitored by quadrupole mass spectrometry (QMS). In a study focusing on the photoconversion of H_2O ice, Gerakines et al. (1996) used infrared spectroscopy (IR) to detect the formation of HO_2, H_2O_2, and OH in the ice. In the work by Öberg et al. (2009d), the photodepletion upon UV radiation (7 – 10.2 eV) of the H_2O and D_2O ices was monitored using reflection-absorption infrared spectroscopy (RAIRS) while the gas-phase species were probed by a QMS. Based on the collected RAIRS data, the photodesorption rate of H_2O ice was derived. Mass spectrometry measurements allowed to detect photodesorption of OH, a gas-phase product of solid water photodissociation, as well as other photoproducts (H_2, O_2). In more recent studies (Cruz-Diaz et al. 2018; Fillion et al. 2021), a QMS was used to measure the gas-phase signal during the photolysis of H_2O (D_2O) ice. Based on the calibration of the QMS, the signal was converted to a photodesorption rate of H_2O, OH and O_2. In the work of Fillion et al. (2021) a wavelength selective (and not a broad band) approach was used, as originally introduced by Fayolle et al. (2011).

The aforementioned diagnostic tools, IR spectroscopy and QMS, have been proven capable tools to quantify the photon - triggered processes, providing a range of photodesorption rates for H_2O ice at different low temperatures between $(1-4) \times 10^{-3}$ mol. photon^{-1}. However, a method capable of simultaneously characterizing the effect of photodesorption and photoconversion in water ice is still missing. IR spectroscopy allows to trace photodepletion of the parent species, which is a combined effect of both processes. It is a method which requires molecules to have an IR-active transition, which means that a-polar species, such as one of the photoproducts, O_2, are simply invisible. In addition, there is an uncertainty associated with the interpretation of the IR data, linked to a possible overlap of vibrational features of the parent species (H_2O) with photoproducts (OH) and the mathematical deconvolution of the photodesorption rate. Mass spectrometry (QMS) offers a solution to these issues with a direct measurement of photodesorbed species, however, it also comes with limitations. QMS measures an equilibrated gas-phase composition in the chamber, which means that molecules, prior to being detected, may interact with the walls and other inner parts of the setup. In addition, the conversion of the gas-phase signals to a photodesorption rate is challenging (Fayolle et al. 2011; Martín-Doménech et al. 2015b; Bertin et al. 2016); also, with a QMS-only approach, the effect of photoconversion in the ice remains unconstrained.

In this study of UV photolysis of amorphous water ice, we apply a different experimental approach, which has been previously used to measure the photodesorption of CO (Paardekooper et al. 2016c) and that was shown to separate photodesorption effects from photoconversion in pure ices of CH_4, CH_3OH, and CH_3CN (Bulak et al. 2020). To determine the effect of each process, pure H_2O ice photolysis experiments are compared to measurements with an additional argon coating. The role of the argon layer is to quench any type of photon-triggered desorption, with a minimal effect on the photoconversion. Laser desorption post ionization time of flight mass spectrometry (LDPI TOF MS) is used to probe the ice composition and thickness as a function of UV fluence. The comparison of (un)coated experiments is used to trace both processes, photoconversion and photodesorption, and to quantify the latter. This offers a fully independent method to derive the photodesorption rate of H_2O ice. The next section includes a summary of the experimental procedure, while the results, discussion and astrophysical implications are described in sections 5.3, and 5.4, and 5.5, respectively.

5.2   Experimental

A detailed description of MATRI^{2}CES (Mass Analysis Tool to study Reactions in Interstellar ICES) is provided in Paardekooper et al. 2014. The experimental procedure that has been used is described in Bulak et al. 2020. In this section we only briefly discuss the relevant details.

5.2.1   Experimental system

MATRI^{2}CES consists of a main and time of flight mass spectrometer (TOF MS) chamber with a base pressure in the $\sim 10^{-10}$ mbar range. In the main chamber, ices are deposited onto a chemically inert gold surface, cooled with a closed cycle helium cryostat to 20 K. The cryostat is mounted on a two dimensional translation stage which allows to manipulate the position of substrate along the horizontal and vertical axis. The temperature of the substrate is regulated in the 20 - 300 K range (relative precision of $\pm$ 0.25 K) using a thermocouple and a resistive heater in thermal contact with the substrate, controlled by a Lakeshore temperature controller. Prior to deposition, liquid water samples of $H_2^{16}O$ (miliQ) or $H_2^{18}O$ (Sigma-Aldrich, 97%^{18}O) are purified from air contamination via three freeze-pump-thaw cycles. Argon gas ($\geq$ 99,999 % purity, Linde) is used without further purification. The deposition of (H_2O and Ar) vapors proceeds through a capillary pointed at 85 degrees with respect to the substrate. The ice growth rate is controlled via a calibrated high precision needle valve. As a result of deposition at 20 K, we form a thin film of porous amorphous solid water (ASW) with an ice column density of 20×10^{15} molecules cm^{-2} (20 monolayers, ML, assuming 1 ML = 1×10^{15} molecules cm^{-2}). The uniformity of the ice thickness across the substrate is $\pm$ 1.5 ML. The thickness of the deposited argon coating is 50 ML, sufficient to prevent any forms of photodesorption of the underlaying ice (see Bulak et al. 2020).

The photolysis is performed with a microwave discharge hydrogen lamp (MDHL), which emits UV photons in the range between 121.6 - 170 nm. This corresponds to an energy range of 7.2 – 10.2 eV. The spectral energy distribution (SED) of the lamp

is given in Ligterink et al. 2015 (see Fig. 4 therein) and the UV photon flux was calibrated at the location of the substrate using a Si diode to be $(2.5 \pm 0.5) \times 10^{14}$ photons cm^{-2} s^{-1}.

A laser desorption post ionization time of flight mass spectrometry (LDPI TOF MS) is used to quantitatively probe the composition of the ice. An unfocused laser shot (Nd:YAG, Polaris II, 4-5 ns) trimmed to a beam diameter of ∼1.5 mm with a typical pulse energy of ∼ 55 mJ per cm^2, is guided onto the deposited ice at an incident angle of 30 degrees with respect to the plane perpendicular to the substrate. This pulse, optimized to trigger a complete local desorption, transfers the species from the ice into the gas phase. The resulting plume is subsequently ionized via a continuous electron impact ionization source with a mean electron energy of 70 eV. As the ionized plume travels through the ion optics, a part of it is extracted with a short voltage pulse (typical duration of 4 μs), which guides the charged species into the field free TOF MS (operated in reflectron mode). During the drift, ions are separated based on their mass to charge ratio (m/z). Their time of flight, from the ion extraction area to the Z-gap micro channel plate detector (MCP), is recorded with a data acquisition card (DAQ) at a sampling rate of 2.5×10^8 Hz. This probing technique is synced with an automated translation of the substrate along the vertical direction which allows to probe 100 fresh locations on the substrate (along z-axis). To track changes in the ice as a function of UV photon fluence, the substrate is translated along the x-axis, the probing scheme is repeated for each UV dose along a fresh column of the ice. The TOF traces are collected and averaged using a Labview routine.

The probing sequence of the laser shot, the ion extraction pulse and the data acquisition is controlled with a delay generator (DG 535, Stanford Research System). A variation in a relative time delay between the laser shot and the ion extraction pulse (between 17 and 80 μs) allows to sample the complete profile of the plume. The collected TOF traces are subsequently converted to mass spectra, with a mass resolution of Δm/m ∼ 250.

The LDPI TOF MS signature of H_2O ice consists of mass peaks at m/z = 16, 17, and 18, which are fragments formed upon the electron impact ionization event: O^+, OH^+ and H_2O^+, accordingly (Kim et al. 2014). Due to the low relative intensity of the mass peak at m/z = 16 (1% of m/z = 18), only peaks at m/z = 17 and 18 are used for quantified analysis. For control experiments with $H_2^{18}O$, peaks at m/z = 19, and 20 are used.

The sum of the calculated intensities of H_2O features in the plume profile is proportional to the thickness of the ice (Paardekooper et al. 2014; Bulak et al. 2020). To demonstrate this, H_2O ices of different initial thickness (10 - 60 ML) were deposited and analyzed with LDPI TOF MS. In Figure 5.1, the total intensity of the recorded plume profile is shown as a function of the deposited ice thickness. The plot includes data from two separate calibration experiments, which probe ices with different initial ice thickness. The demonstrated linear relationship allows to use the integrated plume profile obtained with LDPI TOF MS as a direct measurement of the ice thickness.

5.2.2   Experimental overview

The UV photolysis experiments are aimed to separate the effect of photoconversion from photodesorption in a porous amorphous water ice. Following the approach of Bulak et al. 2020, the first type of experiment probes the photodepletion of pure H_2O
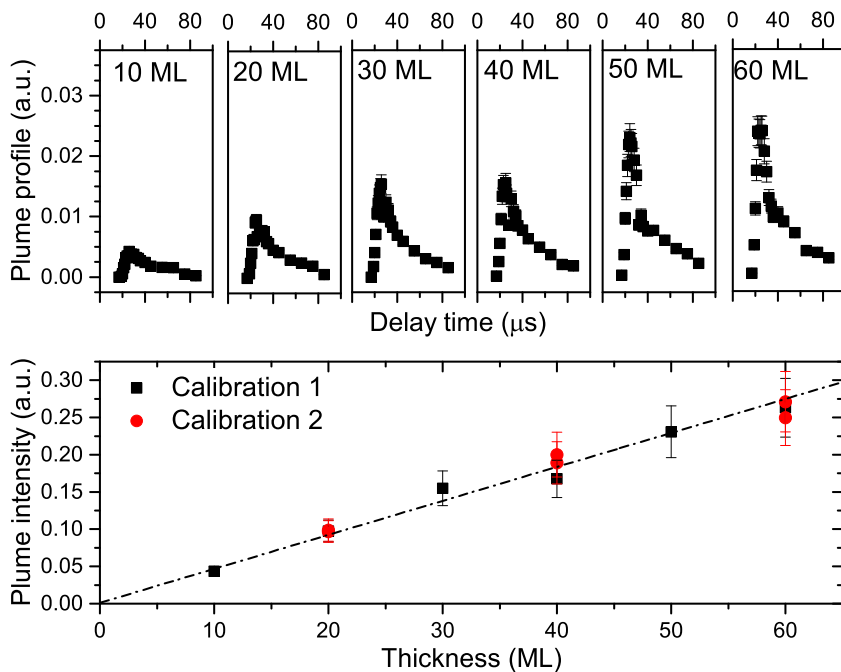
Figure 5.1: *Top panel:* LDPI TOF MS plume profiles for different initial H$_2$O ice thickness at 20 K. Profiles are collected as a function of the delay time between laser desorption and ion extraction. *Bottom panel:* Total signal of the integrated plume profiles (top panel) as a function of initial ice thickness of amorphous H$_2$O ice, collected during two independent calibration measurements. Data is fitted with a linear function ($R^2 = 0.98$).

ice. The measured loss of H$_2$O is linked to the photodissociation (photoexcitation) of the parent species followed by formation of photoproducts (photoconversion) as well as photodesorption of the water molecules, its fragments and the photoproducts. The second type of experiment is performed with an additional layer of argon (50 ML) deposited on top of the H$_2$O ice. The role of the coating is to quench photodesorption processes, including intact, dissociative, and reactive photodesorption (being surface or subsurface processes). Argon, as a noble gas, does not interact with the photodissociation products of H$_2$O. In addition, the argon coating is transparent in the UV range (Schnepp & Dressler 1960), allowing for a direct comparison of the two experiments. The difference in the photodepletion of H$_2$O between (un)coated experiments is used to derive a total photodesorption rate in the H$_2$O ice.

A challenge associated with measuring the photodesorption of water ice, is to exclude the contribution from the residual gas phase water, present in the vacuum chamber even at UHV conditions. The H$_2$O freeze out is most efficient immediately after the ice deposition, and it continues during the UV photolysis (see Westley et al. 1995a and Öberg et al. 2009d), which is also the case in our system. The issue is circumvented by considering the relative difference in the photodepletion rate between (un)coated experiments, both of which include the contribution from the residual gas freeze out. Hence, the contamination is present, however, its impact on the derived

photodesorption rate is limited. The same reasoning is applied to the uncertainty related to other experimental parameters: UV photon flux and ice thickness calibration. Under the assumption that the argon layer has a minimum effect on the photon flux reaching the H_2O ice, these main sources of uncertainty (photon flux and ice thickness), during the derivation of the photodesorption yield, cancel each other out. Hence, the error margin in this work is based on the reproducibility of the repeated measurements (15% for both coated, and uncoated experiments), which leads to a final uncertainty of 21% on the photodesorption yield.

The experimental parameters were constrained in the following way. The initial ice thickness is set within the characterized linear range (see Fig. 5.1), that is above the threshold (4 - 5 ML), at which the photodesorption is no longer expected to be a zeroth order process (Öberg et al. 2009d; Muñoz Caro et al. 2010; Fayolle et al. 2011; Chen et al. 2014). The substrate temperature during the deposition and irradiation is kept at 20 K, the minimum reachable temperature, aiming to represent the "warm" regions of dense molecular clouds. To be able to monitor the photodepletion of H_2O abundance, the ices are exposed to a UV photon fluence (in increments) amounting to 4.5×10^{18} photons cm^{-2}. The experiments with the argon coating are also performed at 20 K, which is well below the sublimation threshold of argon between 30 and 40 K.

5.3 Results

Figure 5.2A. shows the LDPI TOF MS spectra of H_2O ice at 20 K prior to UV irradiation. The recorded plume profile, based on the peaks characteristic for water (OH^+ and H_2O^+), is used as a reference spectrum to track changes in the ice as a function of UV photon fluence. The observed multiple traces of water ions are representative of different parts of the plume, each collected at a separate extraction time (see Section 5.2.1). To demonstrate the evolution of the H_2O ice upon UV irradiation, Figure 5.2B. shows the LDPI TOF MS plume profile recorded after a UV dose of 2.7×10^{18} photons cm^{-2}. The plume (without argon coating) shows the same distribution profile, with a clear decrease in the intensity of the ion signals, which is linked to the photodepletion of the H_2O ice.

To derive the photodepletion rate, LDPI TOF MS plume profiles have been recorded at six increments of UV photon fluence, with the final fluence equal to 4.5×10^{18} photons cm^{-2}. Figure 5.2C. shows the corresponding integrated LDPI TOF MS spectra, which are converted to the ice column density, following the methods described in Section 5.2. The resulting column density (for experiments with both $H_2^{16}O$ and $H_2^{18}O$) are plotted in Fig. 5.2D. The best fit to the data is provided by a linear function ($R^2 = 0.989$), where the slope represents the photodepletion rate of H_2O ice at 20 K. The calculated value is equal to $(3.4 \pm 0.1) \times 10^{-3}$ molecule photon^{-1}. It accounts for losses of amorphous H_2O ice due to photoconversion and photodesorption events. After the maximum photon fluence of 4.5×10^{18} photons cm^{-2}, 75% of the H_2O ice is depleted, yielding a final column density of $(5.1 \pm 1.5) \times 10^{15}$ molecules cm^{-2}.

A similar analysis has been performed on the LDPI TOF MS spectra of H_2O ice capped with an argon layer (50 ML) at 20 K, shown in Figure 5.3(A-D). In the mass spectra prior to UV irradiation, in addition to the features assigned to H_2O, signal representing Ar^+ is traced (Fig. 5.3A). To demonstrate the decrease of the H_2O ice upon UV irradiation, the plume profile after a fluence of 3.6×10^{18} photons cm^{-2} is
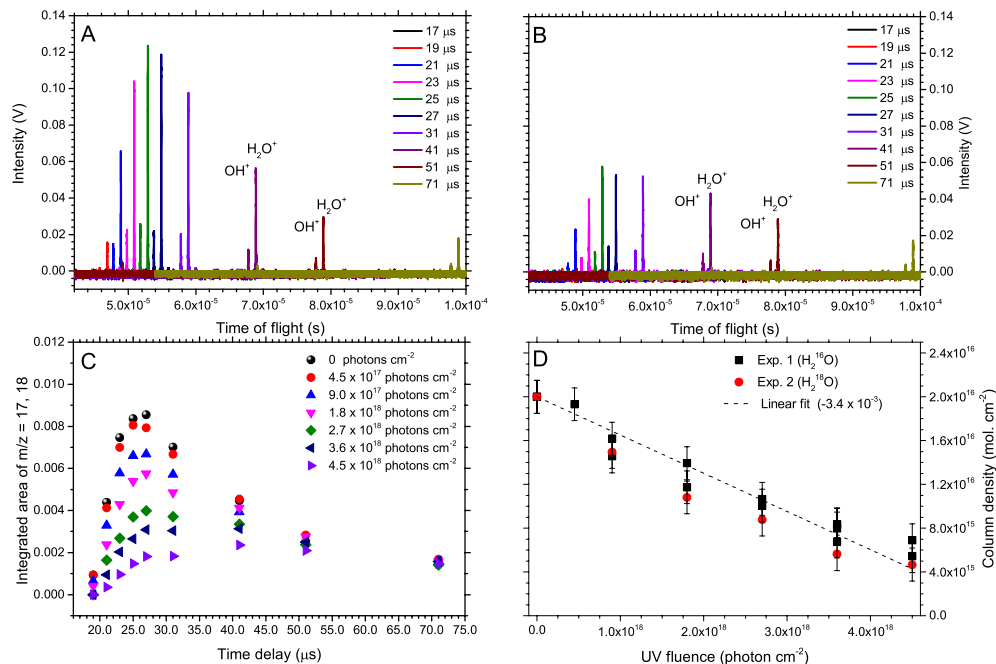
Figure 5.2: *Panel A:* LDPI TOF MS spectra of porous amorphous H_2O ice (20 ML) collected at 20 K, prior to UV photolysis. *Panel B:* LDPI TOF MS spectra of porous amorphous H_2O ice after an UV irradiation with a photon fluence of 2.7×10^{18} photons cm^{-2}. *Panel C:* Integrated plume profiles of LDPI TOF MS signals for different UV photon fluence increments. *Panel D:* Photodepletion of the H_2O column density as a function of UV fluence from repeated experiments with $H_2^{16}O$ and $H_2^{18}O$. Error bars represent the uncertainty on the ice thickness of ± 1.5 ML.

shown (Fig. 5.3B). The integrated mass peaks for all UV fluence increments are then converted into the corresponding ice column density (Fig. 5.3C and 5.3D). The data from two experiments (water with ^{16}O and ^{18}O) is fitted with a linear function with the slope equal to $(2.3 \pm 0.3) \times 10^{-3}$ molecule photon^{-1} ($R^2 = 0.99$). In the experiment with argon coating, the loss of H_2O via photodesorption channels is quenched, while the loss channel due to photoconversion remains active. After the maximum photon fluence of 4.5×10^{18} photons cm^{-2}, $\sim 55\%$ of the H_2O ice is depleted, resulting in a column density of $(9.2 \pm 1.5) \times 10^{15}$ molecules cm^{-2}. Due to the timing optimized for H_2O we were not able to trace the complete argon plume. This, however, has no effect on the derived H_2O photodepletion.

The difference between the (un)coated experiments in the depletion rate is linked to the total photodesorption efficiency of the ice. Figure 5.4 shows the comparison of the (un)coated results. The difference between them was fitted with a linear function with the slope of the fit corresponding to the photodesorption rate of $(1.0 \pm 0.2) \times 10^{-3}$ molecule photon^{-1}. This value represents the total photodesorption efficiency of porous amorphous H_2O ice at 20 K.
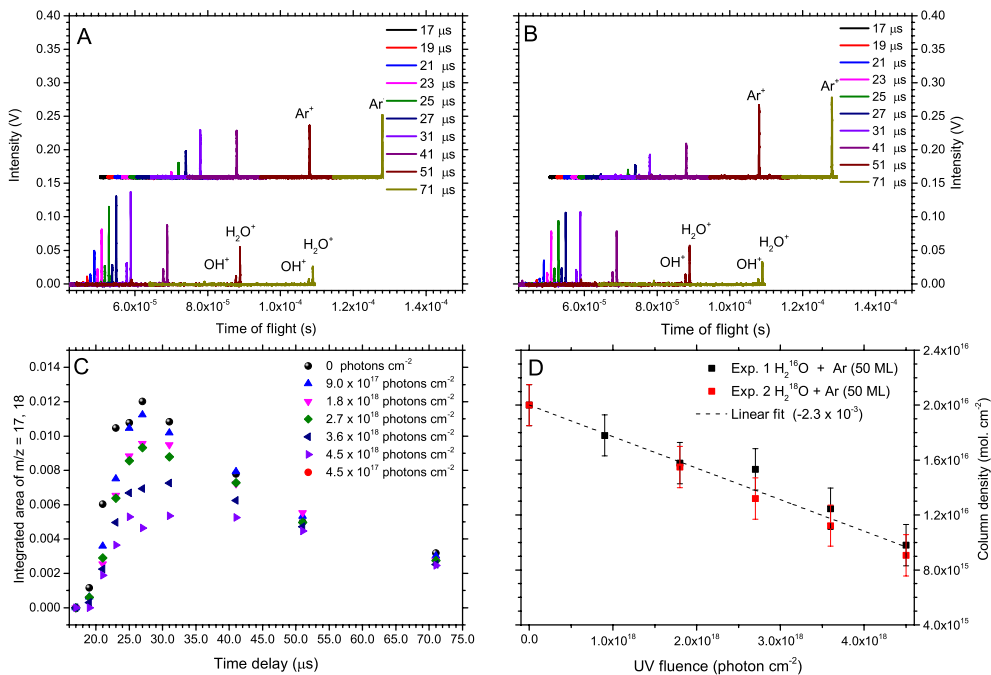
Figure 5.3: *Panel A:*LDPI TOF MS spectra of porous amorphous $H_2^{16}O$ ice (20 ML) coated with an argon layer (50 ML) collected at 20 K, prior to UV photolysis. For clarity of the figure, the plume profile of Ar^+ is separated and vertically offset. *Panel B:* LDPI TOF MS spectra of porous amorphous H_2O + Ar ice after an UV irradiation with a fluence of 3.6×10^{18} photons cm^{-2}. *Panel C:* Integrated plume profiles of LDPI TOF MS for different UV photon fluence increments. *Panel D:* Photodepletion of the H_2O column density as a function of UV fluence from repeated experiments with $H_2^{16}O$ and $H_2^{18}O$. Error bars represent the uncertainty on the ice thickness of ± 1.5 ML.

5.4 Discussion

5.4.1 Types of photodesorption

The derived photodesorption rate of amorphous water ice at 20 K is made up of between contributions from intact desorption (as H_2O), dissociative desorption (H, OH, or O), and reactive desorption (H_2, O_2). We are only able to measure the total photodesorption efficiency, but can provide upper limits for the individual contributions. These values are compared with the outcome of previous studies and an overview of all ASW photodesorption rates, reported in the literature, are summarized in Table 1. It should be noted, that not all experimental settings (temperature, ice thickness, UV SED, level of porosity/compactness) in these studies are fully identical, and one-to-one comparisons, for this reason, should be performed with care.

Intact desorption efficiencies measured experimentally for UV photon energies between 7 – 10.2 eV, at 8 - 20 K, are in the range of $(0.55 – 1.3) \times 10^{-3}$ molecule photon^{-1} (Öberg et al. 2009d; Cruz-Diaz et al. 2018; Fillion et al. 2021). Molecular dynamics studies, which consider photon absorption only into the first excited
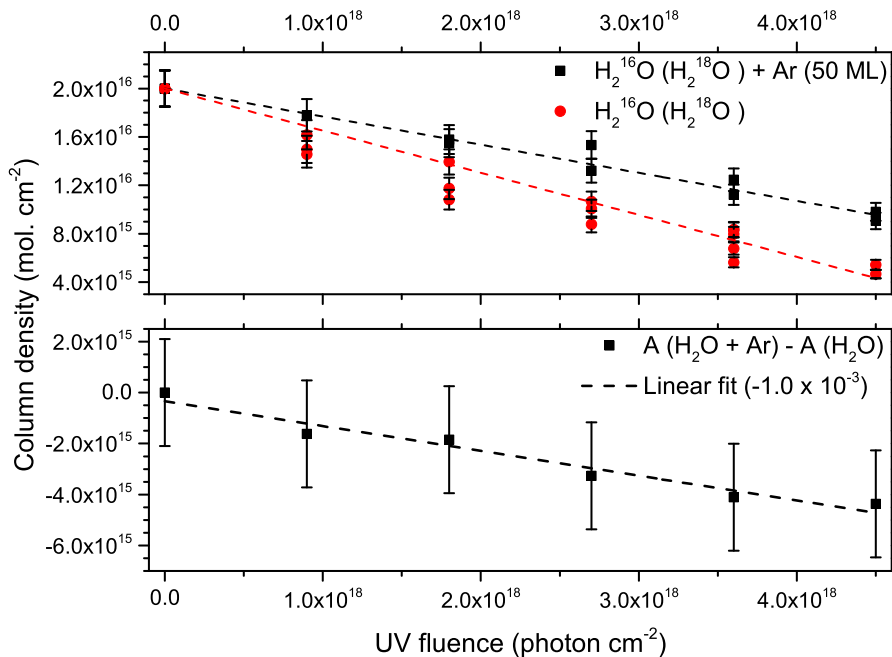
Figure 5.4: *Top panel:* H_2O abundance during the UV photolysis of H_2O with and without the argon coating at 20 K. Error bars represent the uncertainty on the ice thickness of ± 1.5 ML. *Bottom panel:* The difference in the H_2O abundance between the H_2O and H_2O + Ar experiments resulting in a H_2O photodesorption rate. Error bars represent the propagated uncertainty on the ice thickness, with a final value equal to $\pm$ 2.1 ML. Data is fitted with a linear function ($R^2 = 0.94$).

state of water (8.2 – 9.5 eV), yield lower values between $(0.14 - 0.5) \times 10^{-3}$ molecule photon^{-1} (Kobayashi 1983; Andersson & van Dishoeck 2008; Arasa et al. 2010; Crouse et al. 2015). Based on these theoretical investigations, several mechanisms have been proposed that lead to the intact photodesorption of H_2O. An exothermic surface recombination of photodissociation products, OH and H, can result in the H_2O molecule leaving the ice surface. Alternatively, in a 'kick-out' mechanism, an H atom transfers its kinetic energy (following dissociation) to a surface molecule, resulting in the ejection of the latter. DeSimone et al. (2013) suggests a third mechanism, in which excitons generated in the ice upon absorption of UV photons, are near the surface where the charge redistribution of the surface water molecules results in a repulsive electrostatic force, followed by a desorption of a H_2O molecule (Nishi et al. 1984). A so-called DIET (Desorption Induced by Electronic Transition) mechanism, which was experimentally demonstrated to explain the wavelength dependent photodesorption of CO and N_2, in pure and CO:N_2 mixed ices (Fayolle et al. 2011; Bertin et al. 2013), is not expected to be relevant here, as the favourable process following a UV photon absorption by H_2O molecule is photodissociation (Andersson et al. 2006).

The contribution of dissociative desorption (OH) varies across different studies. Öberg et al. (2009d) derive a value for the OH desorption as roughly equal to the

Table 5.1: Summary of water ice photodesorption rate studies, both experimental (Exp) and theoretical (Theor), compared with our work. All desorption rates are given in $\times 10^{-3}$ mol. photon^{-1}. The derived rate upper limits are marked by the "$<$" notation in front of the value. The "total" column represents the loss of water via all photodesorption channels: intact, dissociative and reactive (desorption of O_2 requires two water molecules)

Reference	Exp / Theor	H_2O	OH	O_2	Total	Temp.(K)	Energy (eV)
This work	Exp	<1.0	<1.0	<0.5	1.0 ± 0.2	20	$7 - 10.2$
Westley et al. 1995	Exp	<3.5	-	-	3.5 ± 1.8	35	10.2
Öberg et al. 2009	Exp	0.7 ± 0.4	0.9 ± 0.5	-	1.6 ± 0.9	10	$7 - 10.2$
Cruz-Díaz et al. 2018	Exp	1.3 ± 0.2	0.7 ± 0.3	0.6 ± 0.1	3.2 ± 0.5	8	$7 - 10.2$
Fillion et al. 2021	Exp	0.55 ± 0.09	<0.1	0.3 ± 0.2	1.25 ± 0.25	15	$7 - 10.2$
Andersson, van Dischoeck 2008	Theor	0.14	0.25	-	0.39	10	8.5
Arasa et al. 2010	Theor	0.15	0.3	-	0.55	10	8.5
Crouse et al. 2015	Theor	0.3 ± 0.2	0.3 ± 0.2	-	0.6 ± 0.3	11	8.5

efficiency of intact water desorption at low temperatures (0.9×10^{-3} photon^{-1}). Cruz-Diaz et al. (2018) provide a yield of 0.7×10^{-3} per incident photon at 8 K, lower than their intact photodesorption by a factor of two. In a study by Fillion et al. (2021), OH desorption at 20 K was found to be below their detection limit ($\sim 10^{-4}$ mol. photon^{-1}). It is important to note that with the applied experimental methods (IR and QMS), it is difficult to quantify the contribution of OH from photolysis. In the ice, the OH signature overlaps with a vibrational band of H_2O while in the gas phase, the corresponding mass peak (m/z = 17) can be created as a byproduct of electron impact ionization, rather than UV photolysis. The theoretical studies (Arasa et al. 2010; Crouse et al. 2015) result in rates higher than intact desorption, with the ratios of desorbing OH/H_2O between $1-2$. The absolute calculated desorption yield of OH is lower than the experimental values, by a factor of $2-3$ (3×10^{-4} photon^{-1}).

Reactive photodesorption from water ice is a mechanism previously detected for photoproducts of H_2 and O_2. The O_2 reactive photodesorption rate has been first reported by Öberg et al. (2009d) at a high temperature (100 K), and first quantified by Cruz-Diaz et al. (2018), who determined the reactive photodesorption rate of O_2 at 8 K of $(0.6 \pm 0.3) \times 10^{-3}$ per incident photon. In the study by Fillion et al. (2021), the reactive photodesorption rate of O_2 at 15 K, was found to be $(0.3 \pm 0.2) \times 10^{-3}$ per incident photon. It is noted that the reactive desorption of other photoproducts, such as HO_2 and H_2O_2, is yet to be detected. While these are not expected to be major desorption channels, we provide a generous upper limit for both species, equal to 5.0×10^{-4} per incident photon. Theoretical studies were not able to trace O_2 (or other species) formation/desorption, due to the short timescales of the modelled processes.

To sum up, the literature provides a range of values for total UV photodesorption of water, between $(0.37-3.5) \times 10^{-3}$ per incident photon. These values span an order of magnitude and there is a systematic difference between theoretical and experimental studies. The results of the most recent experimental studies, including this work, agree within a factor of three of each other. This level of agreement is quite acceptable, given the involved uncertainties and differences in ice temperature, used UV photon sources and probing techniques. Photodesorption is a wavelength-dependent process (e.g., Fayolle et al. 2011), hence, the different spectral energy distributions of the applied UV sources can be a reason for differences in measured photodesorption rates. The temperature of the ice during the deposition and irradiation is another parameter that impacts the efficiency of photodesorption. A relative increase in the total photodesorption rate for ices irradiated at temperatures between $8-30$ K was experimentally measured and found to yield values differing by 15 % (Cruz-Diaz et al. 2018) up to 40 % (Öberg et al. 2009d). A theoretical study by Arasa et al. (2010) is in agreement with these measurements, deriving a relative increase in the total photodesorption rate between $10-30$ K to be 15%. Furthermore, it should be noted that all derived photodesorption rates come with relatively high uncertainties. In case of experiments it is a combination of errors related to ice column density, UV photon flux, (IR) band strength, or varying pumping efficiencies for different species, adding up to a large error margin on the final photodesorption rates that can be as high as 50 %. In theoretical calculations, a difference of a factor of a few can be due to the use of gas-phase potential energy surface for modelling the interactions between H_2O molecules, using a short time scale, and only exciting the water molecules in the first excited state (Arasa et al. 2010).

The value derived here puts the most accurate upper limit on an experimentally

derived total photodesorption rate of ASW, and it is well within the uncertainty of other experimental studies and a factor of 2 above theoretical results. It provides a basis to constrain each type of photodesorption, intact, dissociative and reactive, with an upper limit for the first two types equal to the total derived photodesorption rate, 1.0×10^{-3} molecule photon^{-1}. For the reactive desorption, the upper limit is at 0.5×10^{-3} molecule photon^{-1}, as for each desorbed O_2, a loss of two H_2O molecules is required. These upper limits are based on the assumption that the total photodesorption is dominated by a contribution from only one channel, while the others are set to zero.

5.4.2 Photoconversion of H_2O ice

Figure 5.4 allows to distinguish between the effects of photodesorption and photoconversion, during the UV photolysis of H_2O ice. It is worth noting that in the coated experiments, where the depletion due to photodesorption is excluded, after the final UV fluence dose, the remaining column density of H_2O is only about 50% of the initial value. Clearly, upon extended UV irradiation the ice is subject to more processing than photodesorption only.

The photoconversion is a dominant loss channel, depleting the H_2O molecules at a rate of $(2.3 \pm 0.3) \times 10^{-3}$ per UV photon. The depletion of the parent species is expected to result in the formation of photoproducts, H_2, OH, O_2, HO_2, and H_2O_2. Considering that water is a dominant species in the interstellar ices, it is somewhat surprising that there is very limited literature on the photoproduct formation yields upon UV photolysis of H_2O ice. Only recently, a first quantitative study of the formation of typically elusive O_2 and H_2O_2, was reported, also applying LDPI TOF MS (Bulak et al., in press). In experiments favoring bulk processes, a H_2O ice (100 ML thickness) deposited at 20 K was exposed to a UV photon fluence of 1.8×10^{18} photons cm^{-2}. The formation of both O_2 and H_2O_2 reaches a balance with available destruction pathways after a UV fluence between $(4.5 - 9.0) \times 10^{17}$ photons cm^{-2}, at roughly equal abundances of 1% ($\sim$1 ML) with respect to H_2O. Both O_2 and H_2O_2, require two oxygen atoms to be formed (i.e., two H_2O molecules). As these were the only detected products, the corresponding depletion of the parent species should be 4%. If we assume the same efficiency of photoproduct formation in the experiments with argon coating presented here, exposed to the same irradiation dose, the consumption of water due to photoconversion should be 0.8 ML. This allows us to account for the loss of H_2O via photoconversion into O_2 and H_2O_2, at least at the early, and from an astronomical point of view, most relevant photolysis stages.

At higher photon fluence, the depletion of H_2O continues at a linear rate, while the abundances of detected photoproducts are expected to remain on the same level or decrease (Bulak et al., in press). This means that the formation of O_2 and H_2O_2 cannot account for the continuing loss of H_2O. In the absence of other detected products, it is not fully clear what exactly happens. Considering the total UV photon fluence in our experiments and the absorption cross section of water ice (Cruz-Diaz et al. 2014b), we estimate a ratio of water molecules in the ice to the number of absorbed photons of $\sim$20. A part of this lost oxygen budget can be locked in the OH and HO_2 radicals trapped in the ice. Indeed, H atoms and produced H_2 molecules are mobile and can diffuse into the Ar cap, leaving the OH and HO_2 radicals in the bulk of the H_2O ice. Nevertheless, this can only account for the limited fraction of the lost budget. Another

possibility is the diffusion of H_2O molecules into the spots ablated by the previous laser pulses. This is due to considerably longer irradiation time (5 hours) than during our previous experiments, resulting in a higher amount of heat dissipated in the ice. This will be addressed in the future studies. This unaccounted loss of H_2O does not affect the low UV fluence data and can only further reduce our reported photodesorption and photoconversion rates, keeping them as strong upper limits.

5.5   Astrophysical implications

The values used in the past in gas-grain models for the photodesorption rate of ASW are very close to the value derived here, and that has been measured in a fully independent way. Our value offers a somewhat more strict upper limit and this could be taken into account for future work. A detailed astrochemical model of molecular clouds by Hollenbach et al. (2009), shows that photodissociation and photodesorption are the dominant physical processes impacting the gas-phase abundances from the edges until intermediate depths into the cloud. In their model, at the onset of water ice freeze-out, the water vapour abundance is in 98% due to photodesorption of H_2O which has been formed on grains, with the remainder (of the gas-phase abundance) formed through low temperature gas-phase chemistry. Deeper into the cloud, the percentage drops to 70%, and at intermediate depths into the cloud, goes up again to 92%. In this model, the intact (H_2O) and dissociative (OH from H_2O ice) photodesorption rates are set to 1×10^{-3}, and 2×10^{-3} per incident UV photon, respectively. The photodesorption of O_2 was considered only from pure O_2 ices at 1×10^{-3} mol. photon^{-1}. These rates were used to reproduce the gas-phase H_2O and (when applicable) O_2 abundances towards molecular cloud B68, a star forming cloud in Orion, NGC 2024, and ρ Ophiuchus (Hollenbach et al. 2009; Larsson et al. 2007). In a less-detailed model by Schmalzl et al. (2014), the same intact photodesorption rate, combined with photodissociation and freeze-out rates, successfully matches the abundances of water vapour towards the cold regions of pre- and protostellar cores. Also in this study, the reactive photodesorption (of O_2) was not taken into account.

These models use previous laboratory values for intact photodesorption that are largely in line with our work. However, the values for dissociative desorption rate (OH), seem to be consistently lower (see Table 1) than adapted in models. We recommend that these values are updated, as the OH radical, released from the grains via a non-thermal mechanism, contributes to the formation of simple molecules such as CO, CO_2, NO, H_2O, as well as complex organic molecules, such as $HCOOCH_3$ (Charnley et al. 2001; Vasyunin & Herbst 2013; Shannon et al. 2013; Vasyunin et al. 2017). In addition, based on the work presented here, we propose for future work that the reactive photodesorption rate of O_2 is added to the astrochemical models.

In our experiments the photoconversion depletes the H_2O column density twice as fast as the photodesorption. Formation of photoproducts, O_2 and H_2O_2 can account for the initial photoconversion of water, until a UV fluence of 9.0×10^{17} photon cm^{-2}, each at a formation level of 1% of H_2O (Bulak et al., in press). At higher photon fluence, the continuing formation of OH radicals can be of significance for further ice chemistry, opening pathways towards oxygen-carrying molecules, such as CO_2, CH_3OH, HCOOH, or $HCOOCH_3$ (Öberg et al. 2009c, 2010b; Garrod et al. 2008).

It is important to note, that while water is the dominant component of interstellar

ices, other species, including CO_2, CH_4, NH_3, CH_3OH are present and expected to impact the photoconversion as well as photodesorption rates derived for pure water ice. The inclusion of less abundant constituents of interstellar ices in water ice, strongly affects the observed photoconversion. These effects are outlined by Öberg et al. (2010b), where it is demonstrated that the recombination reactions of water are inhibited by up to an order of magnitude due to competitive reactions with other radicals in the ice. In a recent study of photolysis of mixed ices of $H_2O:CO_2$, an increasing amount of CO_2 in the initial composition, resulted in a more efficient photodepletion of water, a shift in the photoproduct yields to carbon bearing species, and a corresponding decrease in the absolute formation yield of O_2 and H_2O_2 (Bulak et al., in press). It is also expected that the photodesorption rates of species in mixed ices will differ from its pure equivalents. This will be the topic of future work; the method presented here has the potential to also derive photodesorption rates for different species in mixed ices.

5.6   Conclusions

A quantification of photodesorption rates and separating this process from the photoconversion of ASW, is crucial as it allows to balance water abundances between ice and gas in astronomical environments such as dense molecular clouds.

Here we apply an alternative, independent measuring technique of LDPI TOF MS to separate the effect of photodesorption from photoconversion during the UV photolysis of porous amourphous water ice at 20 K. We derive the total photodesorption rate to be $(1.0 \pm 0.2) \times 10^{-3}$ per incident UV photon. This is an average value for the photon energy range equivalent to the secondary UV field in the ISM (7 – 10.2 eV). Based on this value, we place an upper limit on the relative contribution of three channels. Both, the intact (H_2O) and dissociative (OH) desorption rates, have an upper limit equal to 1.0×10^{-3} per incident UV photon, while for reactive desorption (O_2), the limit is equal to 0.5×10^{-3} per incident UV photon. It should be noted, that these values apply for pure water ice. Even though water is the dominant species in interstellar ices, also other species will be present that can affect these values. For this also photodesorption rates of mixed ices will be needed and with the new technique presented here, this will be possible.

6 | QUANTIFICATION OF O_2 FORMATION DURING UV PHOTOLYSIS OF WATER ICE - H_2O AND H_2O:CO_2 ICES

Abstract

The *Rosetta* and *Giotto* missions investigated the composition of the cometary comae of 67P/Churyumov-Gerasimenko and 1P/Halley, respectively. In both cases, a surprisingly large amount of molecular oxygen (O_2) was detected and was well correlated with the observed abundances of H_2O. Laboratory experiments simulating chemical processing for various astronomical environments already showed that formation of solid state O_2 is linked to water. However, a quantitative study of O_2 formation upon UV photolysis of pure H_2O and H_2O dominated interstellar ice analogues is still missing. The goal of this work is to investigate whether the UV irradiation of H_2O-rich ice produced at the earliest stages of star formation is efficient enough to explain the observed abundance of cometary O_2. The photochemistry of pure $H_2^{16}O$ ($H_2^{18}O$) as well as mixed H_2O:CO_2 (ratio of 100:11, 100:22, 100:44) and H_2O:CO_2:O_2 (100:22:2) ices was quantified during UV photolysis. Laser desorption post-ionisation time of flight mass spectrometry (LDPI TOF MS) was used to probe molecular abundances in the ice as a function of UV fluence. Upon UV photolysis of pure amorphous H_2O ice, deposited at 20 K, formation of O_2 and H_2O_2 is observed at abundances of, respectively, $(0.9 \pm 0.2)\%$ (O_2/H_2O) and $(1.3 \pm 0.3)\%$ (H_2O_2/H_2O). To the best of our knowledge, this is the first quantitative characterisation of the kinetics of this process. During the UV photolysis of mixed H_2O:CO_2 ices, the formation of the relative amount of O_2 compared to H_2O increases to a level of $(1.6 \pm 0.4)\%$ (for H_2O:CO_2 ratio of 100:22), while the (H_2O_2/H_2O) yield remains similar to experiments with pure water. The resulting O_2/H_2O values derived for the H_2O and H_2O:CO_2 ices may account for a (substantial) part of the high oxygen amounts found in the comae of 67P and 1P.

6.1 Introduction

A major development in observations of O_2 beyond our Earth was made in 2015 with the *Rosetta* space mission (Bieler et al. 2015). The composition of the cometary coma of 67P/Churyumov-Gerasimenko (67P) was measured utilising mass spectrometry. A relatively large amount of O_2 was detected with its abundance well correlated with H_2O. The average concentration of O_2/H_2O in the ice was determined as $(3.1 \pm 1.1)\%$, well above the expected gas-phase ratio in the interstellar medium (ISM) (Woodall et al. 2007; Yıldız et al. 2013). Motivated by this detection, data collected by the *Giotto* mission, which measured the composition of the cometary coma of 1P/Halley (1P), was re-analysed. As a result, an average concentration of O_2/H_2O in 1P was derived at $(3.7 \pm 1.7)\%$ (Rubin et al. 2015).

Following these findings, a number of hypotheses have been proposed to explain the unexpectedly high O_2 comet abundances and its scaling with H_2O. Among different scenarios reviewed by Luspay-Kuti et al. (2018), a primordial origin of O_2 and H_2O has been put forward, which is in agreement with the common origin of these dynamically different comets (Rubin et al. 2015). In the primordial scenario, the nuclei of comets are formed via the agglomeration of icy grains that formed during the dark molecular cloud stage or from more processed grains, frozen out during the protosolar nebula stage. In other words, the composition of the comet nuclei is expected to reflect, to a certain extent, the final composition of interstellar ices at the early stages of the star formation sequence.

Water is the main component of interstellar and cometary ices (Whittet et al. 1988; Bockelée-Morvan et al. 2000; Boogert et al. 2008). Solid O_2 has not been detected because of its homo-nuclear diatomic nature, which turns the molecule nearly invisible in the infrared and millimetre-wavelength regime. As an alternative method, an infrared transition induced by O_2 interacting with a surrounding matrix, could offer a detection, but was shown to be too weak for an astronomical identification (Müller et al. 2018). Hence, only generous upper limits of the O_2/H_2O ratio in the solid are available with values of 15% and 39%, towards the low-mass protostar R CrA IRS2 and the massive protostar NGC 7538 IRS9, respectively (Vandenbussche et al. 1999). This is insufficient to test the hypothesis of a primordial origin of cometary O_2.

Constraining observations of the gas-phase species provides a complimentary view of the involved gas-grain chemistry. In this case, however, it is important to note that the majority of water in the ISM resides in the ice, rather than in the gas. In addition, gas-phase chemistry as well as (non) thermal desorption mechanisms complicate the link between ice and gas. Despite low gas-phase abundances and challenging detection methods, a comparison of measured gas-phase abundances of H_2O with respect to O_2 has been made possible for ρ Oph A (Larsson et al. 2007; Liseau et al. 2012; Larsson & Liseau 2017). In the cold and dark regions of ρ Oph A, the derived ratio of O_2/H_2O abundances reaches 10, significantly varying from cometary measurements and further convoluting the understanding of O_2 in the ice.

A different approach to investigate the link between O_2 and H_2O in solid state is with astrochemical modelling. Taquet et al. (2016) explored a grid of physical parameters which demonstrated that under specific dark cloud conditions, the resulting solid O_2/H_2O values and abundances of related species (H_2O_2, HO_2) could match the findings already cited here for 67P. In this model, the high O_2/H_2O value was a direct result of grain surface reactions at temperatures between 10 - 20 K and based

on a formation pathway of O_2 proceeding via recombination of O atoms (Tielens & Hagen 1982; Cuppen et al. 2010). This reaction competes with the hydrogenation of O, O_2 or O_3, which depletes most of the O and O_2 reservoir and eventually leads to efficient formation of H_2O (Ioppolo et al. 2008, 2010; Oba et al. 2009; Miyauchi et al. 2008; Lamberts et al. 2013). An alternative way of linking solid state O_2 and H_2O is through processing by various energetic particles - cosmic rays (CR), electrons, and UV photons. These processes play an important role in altering the solid state chemical reservoir in molecular clouds and protoplanetary discs. The energetic processing of H_2O-rich ice can result in the production of O_2, as shown in a series of laboratory studies (e.g. Johnson 1991; Baragiola et al. 2002; Kimmel & Orlando 1995; Öberg et al. 2009d). The final impact of each irradiation type depends on local parameters, including the density, ice thickness (related to penetration depth), and proximity of radiation sources.

Upon radiolysis of water ice, H_2O molecules may desorb, ionise, or dissociate, with resulting transients reacting to form other products such as O_2, O_3 and H_2O_2 (Johnson & Quickenden 1997). The observed conversion from H_2O to O_2 has been described with a simplified reaction: 2 H_2O (solid) $\rightarrow$ 2 H_2 (gas) + O_2 (gas). The measured sputtered O_2 yields (gas-phase) can vary across 4 orders of magnitude for different particles and energies, from 5×10^{-7} to 5×10^{-3} molecules/eV (e.g. Brown et al. 1982; Bar-Nun et al. 1985; see Teolis et al. 2017 for an overview).

The effects of electron bombardment of H_2O and D_2O ice have been previously studied by, for example, Sieger et al. (1998) and Zheng et al. (2006a). Based on these investigations, processing of water ice with different energy doses (0 - 500 eV molecule^{-1}) was found to result in the formation of H, O, OH, H_2, O_2 , and H_2O_2. Relatively higher yields of stable products were observed for amorphous water ice compared to crystalline ice (Zheng et al. 2007). Moreover, it was shown that the formation efficiency decreases with increasing ice temperature (12 K - 90 K) (Zheng et al. 2006b).

The first study of UV photolysis of water ice demonstrated its photodesorption at temperatures between 35 and 100 K (Westley et al. 1995a). Subsequently, Gerakines et al. (1996) showed that UV photolysis of H_2O ice at 10 K also leads to formation of OH, H_2O_2 , and HO_2. In addition, UV photolysis triggers amorphisation of the ice (Leto & Baratta 2003). In the more recent studies focusing on the UV photodesorption of H_2O, O_2 photodesorption was also detected, but it was not possible to derive its production yield in the solid state (Öberg et al. 2009d; Cruz-Diaz et al. 2018; Fillion et al. 2021). Additionally, the UV-triggered photodesorption and photochemistry of pure O_2 ice was characterised (Zhen & Linnartz 2014).

During the last few decades, the formation of O_2 upon energetic processing of H_2O ice has been strongly supported by experiments. However, the efficiency of this process and the involved chemical pathways remain under debate. As formation of O_2 in the solid state cannot be measured by regular infrared (IR) spectroscopic techniques, to date, only the previously mentioned radiolysis experiments list quantitative yields on the O_2 (gas) formation from water ice. These yields were measured with quadrupole mass spectrometry, which inherently measures an equilibrated gas-phase composition in the experimental chamber. This means that molecules, prior to being detected, may interact with the walls and other inner parts of the setup, which are typically at room temperature. This might affect the measurements as both H_2O_2 and O_3 can decompose on metal surfaces following general equations, $2H_2O_2 \rightarrow 2H_2O + O_2$ and $2O_3 \rightarrow 3O_2$, further complicating the calculation of precise formation yields.

In this work, we revisit the UV photolysis of pure water and water-rich ice mixtures, utilising a recently developed new diagnostic method that studies UV-irradiated ices in-situ and in real time combining laser desorption and mass spectrometry. This allows us to quantitatively trace ice composition, prior to the interaction of the ablated material of the ice with the walls of the setup or the ion optics of the mass spectrometer. The method offers an alternative to spectroscopic techniques to study species with no or weak dipole moments, such as O_2, N_2, C_2, S_2, etc. This paper is organised as follows: a description of the experimental methods is given in Section 6.2, the results and a follow-up discussion are presented in Sections 6.3 and 6.4, the astrochemical implications are discussed in Section 6.5, and the concluding remarks are summarised in Section 6.6

6.2   Experiments

The experiments were carried out in MATRI^{2}CES - Mass Analysis Tool to study Reactions in Interstellar ICES. This section includes a brief description of the setup, a list of completed experiments, and the analysis routine used to quantify the acquired data. A detailed description of the system can be found in Paardekooper et al. (2014).

6.2.1   Experimental setup

MATRI^{2}CES consists of a main chamber connected with a UHV gate valve to a time of flight mass spectrometer (TOF MS) tube. The base pressure in both chambers is in the $\sim 10^{-10}$ mbar range. The main chamber houses a closed-cycle helium cryostat which cools a 2.5 x 5 cm gold-coated copper block used as a chemically inert substrate for ice deposition. A thermocouple and a resistive heater are attached to the base of the substrate, which allows us to set its temperature in the 20 - 300 K range with a relative precision of 0.25 K. In addition, the cryostat (substrate) is mounted on a two-dimensional translation stage, allowing us to shift its position in the horizontal and vertical directions. Upon reaching the deposition temperature, the vapor and gas samples are admitted through a capillary positioned at 85 degrees with respect to the substrate (front deposition) or pointed away from the substrate (background deposition). Pure water (H_2O, milliQ or $H_2^{18}O$, Sigma-Aldrich, 97%^{18}O) and mixtures with carbon dioxide (CO_2, 99.99% purity) and molecular oxygen (O_2, 99.99% purity) are used. Prior to the deposition, liquid samples are purified from the dissolved air contamination by performing three freeze-pump-thaw cycles. A continuous deposition is regulated by a high precision needle valve, which allows the gas-phase sample to go into the main chamber. The growth rate of the ice is determined in advance using He-Ne laser (wavelength 632.8 nm) interference measurements (Baratta & Palumbo 1998; Bulak et al. 2020). To calculate the deposition rate for H_2O (background deposition) and CO_2 (front deposition), the refractive indices (1.2, and 1.21) and densities (0.94 g cm^{-3}, 0.98 g cm^{-3}), respectively, are taken from the literature (Kofman et al. 2019; Satorre et al. 2008; Jenniskens et al. 1998). In case of the deposition of H_2O:CO_2:O_2, the mixture was premixed at the intended ratio and deposited through the front deposition capillary following a growth rate calibration for H_2O and CO_2. In all experiments, the deposited ice column density is close to 9×10^{17} molecules cm^{-2} or 90 monolayers

(1 monolayer $= 10^{15}$ molecules cm^{-2}) and its uniformity across the substrate is within $\pm$ 10%. This thickness was chosen to maximise the efficiency of photochemistry in the bulk of the ice. At the same time, a large ice thickness minimises the possible chemical reactions triggered by photoelectrons released from metal substrates upon photolysis. These effects have been restricted to the lower few MLs of the ice (e.g. Jo & White 1991; Smith et al. 2012) or not observed at all (Chuang et al. 2018a).

To simulate the UV field present in the interstellar medium, a microwave discharge hydrogen lamp (MDHL) is used. It is attached to the main chamber via a (MgF$_2$) UHV view port directly facing the substrate. The operating conditions of the lamp (H$_2$ pressure of 1.44 mbar and 80 W of applied microwave power at 2.45 GHz) determine its photon flux and the spectral energy distribution (Ligterink et al. 2015). The corresponding emission spectrum consists of a Lyman-α (121.6 nm) and molecular H$_2$ emission bands (130 - 165 nm). The complete spectral energy distribution of the lamp is given in Fig. 4 in Paardekooper et al. (2016c). The photon flux was measured with a NIST-calibrated silicone photodiode at the location of the substrate, 14 cm away from the lamp. The UV photon flux, after the subtraction of the optical emission, amounts to $(2.5 \pm 0.5) \times 10^{14}$ photons cm^{-2}s^{-1}.

MATRI^{2}CES uses a unique analytical approach to monitor the ice composition before, during, and after UV irradiation by combining laser desorption and mass spectrometry. This method is known as LDPI TOF MS, laser desorption post-ionisation time of flight mass spectrometry. The probing scheme is initiated by an unfocused laser beam of a Nd:YAG Polaris II (4-5 ns pulse, wavelength of 355 nm) which is guided into the main chamber at a 30-degree incidence angle with respect to the substrate (laser shot). Prior to entering the main chamber, the laser beam is trimmed to 1 mm in diameter which allows us to spatially constrain its impact on the ice. An average pulse energy (65 mJ cm^{-2}) is optimised for 90 ML of water ice, as the minimum energy that probes the deposited thickness of the ice. The impact of the laser pulse on the ice triggers a local thermal desorption, creating a plume of species. The composition of the plume represents the composition of the ice at the location of the laser shot (Paardekooper et al. 2014). The plume is ionised via a continuous electron impact ionisation source (mean electron energy of 70 eV), and after an optimised time delay, a part of it is extracted into the TOF MS chamber using ion optics (plume extraction). In addition to the ionisation event, an electron impact induces the dissociation of species in the plume, which results in a molecule-specific fragmentation pattern (see Section 6.2). In the field-free TOF tube, ions with different mass-to-charge ratios (m/z) are spatially separated and redirected (TOF MS in reflectron mode) into a micro-channel plate detector (MCP). This allows us to record the characteristic flight times for all m/z in the plume. This approach has several advantages: TOF MS is a very sensitive detection method, ices are investigated in-situ, and signals are recorded in real time. The use of isotopologues offers a further diagnostic tool to identify newly formed species.

To increase the signal-to-noise ratio of the data, the LDPI TOF MS scheme (laser shot, plume extraction, data acquisition) is repeated at a frequency of 5 Hz, simultaneously with the automated translation of the substrate in the vertical direction. This allows us to collect 100 TOF spectra, each corresponding to a non-overlapping spot on the substrate (a column). An average of the TOF spectra in a column is mass calibrated and used to derive the composition of the ice. This scheme is repeated at an updated horizontal position (column) of the substrate, which allows us to probe

the same ice while increasing the total UV photon fluence.

The acquisition of multiple data points during an irradiation experiment makes it possible to track the formation and destruction kinetics for the involved species within a single experimental run. This provides an advantage over the regular QMS TPD techniques.

6.2.2   Data analysis procedure

Analysis of the averaged TOF data comprises of three steps: mass calibration, integration of the mass peaks, and a conversion of the signal to an abundance (column density) of a molecule in the ice. Mass calibration of the averaged TOF spectra yields a mass resolution of $\Delta m/m \sim 250$, clearly separating each m/z. To calculate the intensity of the peaks, a Pearson IV distribution function is fitted to each feature individually. This function provides an accurate fit to the experimental data as it can account for possible asymmetry within the peak. The errors related to the integration are based on the root mean square (rms) over the residual within one standard deviation from the centre of the peak and are below the uncertainty of the ice thickness determination ($\pm10\%$) (Castellanos et al. 2018).

The calculated mass peak intensities are proportional to a linear combination of species present in the plume (Paardekooper et al. 2014). This allows us to express an integrated mass spectrum, M_t, at a given irradiation time, t, by

$$M_t = \sum_{i=1}^{n} a_i \cdot \sigma_i \cdot M_i, \tag{6.1}$$

where a_i is the molecular abundance of species i, σ_i is the electron impact ionisation cross-section (at 70 eV), and M_i is the corresponding fragmentation fraction. The following cross-sections are used: 2.275 (H_2O), 2.441 (O_2), 2.516 (CO), 3.521 (CO_2) Å^2 (Kim et al. 2014). As there is no available data in the literature for the ionisation cross-section of H_2O_2, its value is derived empirically. It is based on a linear correlation between the electron impact ionisation cross-section and polarisability (α), represented by a formula $\sigma = 1.48 \cdot \alpha$ (Lampe et al. 1957; Bull et al. 2012). The polarisability of H_2O_2 is 1.73 Å^3 (Johnson III 1999), and the derived electron impact ionisation cross-section value for H_2O_2 is 2.5 Å^2. The fragmentation pattern of H_2O_2 is adapted from (Foner & Hudson 1962), where the contribution of fragments (peaks other than molecular ion) towards the total yield is 26 %. The fragmentation patterns of other molecules relevant for this study are available in the NIST spectral database or previous works, but it should be noted that these are (slightly) dependent on the geometry of the experimental system (Kim et al. 2014). The use of these values allows us to solve Eq. 1 for a_i (arbitrary units), which is proportional to the column density of each species (mol. cm^{-2}), i.

In the final step of the analysis, the calculated water abundance (in arbitrary units) is set equal to the known thickness of the deposited ice (9×10^{16} mol. cm^{-2} or 90 ML assuming 1×10^{15} molecules per ML). Subsequently, the signals assigned to other species are converted with respect to the initial column density of water, allowing us to quantify their abundances for different UV fluences. The most significant uncertainty in this conversion is related to the uniformity of the ice thickness ($\pm10\%$), and this value is taken into account when deriving abundances of photoproducts.

To translate the experimental results to environments with different astrochemical conditions, it is useful to describe the efficiency of the photoproduct formation as a molecular yield per amount of energy deposited in the ice. Hence, to calculate the fraction of absorbed photons (I_{abs}), the Beer-Lambert absorption law is used:

$$I_{abs} = I_{inc}(1 - e^{-\sigma(\lambda)_{abs}N}), \tag{6.2}$$

where I_{inc} is the incident UV photon fluence, σ_{abs} is the average photon absorption cross-section of the ice (H_2O: 3.4×10^{-18} cm^{-2}), and N is the ice column density (pure H_2O experiments: 9×10^{16} mol. cm^{-2}) (Cruz-Diaz et al. 2014a). For calculations related to mixed ices, we used the following absorption cross-section values for CO_2 and O_2: 6.7×10^{-19} cm^{-2} and 4.8×10^{-18} cm^{-2} (Cruz-Diaz et al. 2014b). For instance, after a UV irradiation of pure H_2O ice with 4.8×10^{17} photons cm^{-2} (64 minutes), 1.3×10^{17} photons cm^{-2} are absorbed: each carry, on average, 9 eV of energy (Ligterink et al. 2015). Thus, after 64 minutes, a total energy of 1.2×10^{18} eV is deposited in the ice and each water molecule statistically absorbs 1.3 UV photons.

Table 6.1: Summary of the types of performed UV photolysis experiments. The total thickness used in all ices is 9×10^{16} mol. cm^{-2}, which accounts for about 90 ML.

Molecular composition	Composition (%)	Temperature (K)	UV photon fluence (10^{18} photons cm^{-2})
$H_2^{16}O$	100	20	0 - 1.8
$H_2^{18}O$	100	20	0 - 1.8
$H_2^{16}O$:CO_2	100:11	20	0 - 1.8
$H_2^{16}O$:CO_2	100:22	20	0 - 2.9
$H_2^{16}O$:CO_2	100:44	20	0 - 2.9
$H_2^{16}O$:CO_2:O_2	100:22:2	20	0 - 2.9
control (H_2O)	100	20, 190	0 - 1.2

6.2.3   Overview of experiments

In this study, we focus on different ices starting with pure H_2O, the primary constituent of interstellar ices. In a realistic interstellar ice, H_2O molecules are expected to be mixed with CO_2 (Öberg et al. 2007a; Pontoppidan et al. 2008). Based on observations, the ratio of CO_2/H_2O in interstellar ices can vary from 12 - 40 % (Boogert et al. 2015). Only in particular environments (Poteet et al. 2013; Isokoski et al. 2013) have pure CO_2 ices been observed. Consequently, we also investigate the photochemistry of three different H_2O:CO_2 ice mixtures. Finally, as O_2 may be formed as a side product of (non-energetic) water formation (see e.g. Cuppen et al. 2010; Minissale et al. 2014; Taquet et al. 2016), we also investigated H_2O:CO_2 ices enriched with O_2. Once O_2 is formed in an ice, it may start contributing to its overall chemical network. However, as the amount of molecular oxygen in the prestellar phase is not known, the recorded data for the O_2-containing ice are presented in the appendix. Table 1 summarises all performed experiments for pure H_2O ice, H_2O:CO_2 ice mixtures (100:11, 100:22 and 100:44), and H_2O:CO_2:O_2 (100:22:2). The assignment of the main photoproducts follows the $H_2^{16}O$ experiments, and the validity of these results is confirmed using $H_2^{18}O$.

In addition to the $H_2^{18}O$ labeled experiments, another control experiment is performed to exclude error-prone results due to H_2O background contamination. In this experiment, the substrate was exposed to H_2O vapours above the sublimation point (190 K), which allows for the characterisation of the water deposited on the walls or ion optics.

The total and incremental UV fluence with which our ice samples are irradiated are representative of the different regions in the ISM. In the centre of a dark cloud, the photon fluence is estimated to be $(3\text{-}30) \times 10^{17}$ photons cm^{-2}, considering cosmic ray induced secondary UV flux of $(1\text{-}10) \times 10^3$ photons cm^{-2}s^{-1} and an average molecular cloud lifetime of up to 10^7 years (Shen et al. 2004b; Chevance et al. 2020). The UV fluence during a lifetime of a protoplanetary disc was modelled by Drozdovskaya et al. (2014), and, depending on the location within the disc, it varies between 10^{16} - 10^{26} photons cm^{-2}.

6.3 Results

6.3.1 UV photolysis of H_2O ice

The mass spectra obtained during the UV photolysis of pure $H_2^{16}O$ and $H_2^{18}O$ ices are shown in the upper and lower panels of Fig. 6.1, respectively. The bottom trace in each panel (black) is a reference mass spectrum that allows us to track changes from the initial composition of the ice. For $H_2^{16}O$, the unprocessed signature includes peaks at $m/z = 16$, 17, 18, and 19. Peaks at $m/z = 18 \cdot n + 1$, where n = 1, 2, and 3 represent protonated water clusters formed in the ablated plume, that is, these are not a reaction product from the UV irradiation, but result from the laser desorption pulse (Gudipati & Yang 2012).

After UV irradiation of the ice with a fluence of 6×10^{16} photons cm^{-2} (red trace, Fig. 6.1), new peaks appear at $m/z = 32$, 34 in the $H_2^{16}O$ experiment (upper panel) and corresponding features at $m/z = 36$ and 38 in the $H_2^{18}O$ experiment (lower panel). The mass shift of 4 atomic mass units (amu) reveals that the newly formed peaks represent species with two oxygen atoms. Considering the initial composition of the ice (pure $H_2^{16}O$ and $H_2^{18}O$) and the reference mass spectra of possible photoproducts, the only species explaining these observations are O_2 and H_2O_2. In addition, the mass peak at $m/z = 2$ (for both isotopes) is increased, which must be due to the formation of molecular hydrogen (H_2) in the ice.

The mass spectra clearly show that upon UV irradiation of water ice, O_2 is formed in the solid state. The formation of H_2 ($m/z = 2$) and H_2O_2 ($m/z = 33$, 34 in upper panel and $m/z = 37$, 38 in lower panel) is observed simultaneously and it is important to note that the contribution of H_2O_2 towards mass peaks of O_2 due to electron impact ionisation is negligible (Foner & Hudson 1962). As we probe the molecular plume before its interaction with the metal walls of the setup or its ion optics, the intensity of features representing O_2^+ and $H_2O_2^+$ provides a firm base to quantify the formation of both photoproducts. This is shown as a function of UV fluence in Fig. 6.2. The abundances are calculated for multiple experiments with both isotopologues following the method described in Sect. 6.2. Subsequently, an exponential function was used to average the photoproduct yields from repeated experiments (for both isotopologues).
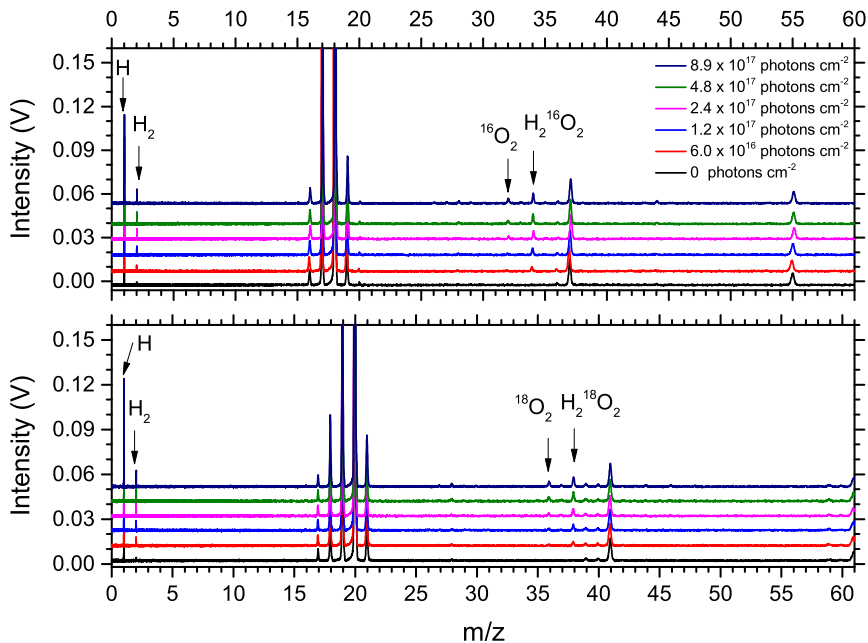
Figure 6.1: LDPI TOF MS signals for a UV-irradiated $H_2^{16}O$ (upper panel) and $H_2^{18}O$ (lower panel) ice at 20 K for increasing photon fluence. The lowest trace in each plot shows the signal without UV irradiation. Besides H_2O and its fragmentation pattern, these spectra reveal the presence of the photolysis products, H_2, O_2 and H_2O_2. In addition, protonated cluster ions $(H_2O)_nH^+$ are seen to form in the desorption process (see text for details).

The formation of O_2 reaches its maximum of $(7.6 \pm 2.0) \times 10^{14}$ molecules cm^{-2} at an incident photon fluence of 8.9×10^{17} photons cm^{-2}. For the O_2 formation relative to the current H_2O abundance, we derive a maximum abundance of O_2/H_2O to be $(0.9 \pm 0.2)\%$. The formation of closely related H_2O_2 is saturated at $(1.1 \pm 0.3) \times 10^{15}$ molecules cm^{-2}, which is converted to a relative maximum abundance of H_2O_2/H_2O equal to $(1.3 \pm 0.3)\%$ (see Appendix A for the water consumption during the experiments in this study).

The observed kinetic curves for O_2 and H_2O_2 show the formation of both products in the early stages of photolysis. The photoproduct abundances reach a saturation level at a fluence of $(4.8 - 8.9) \times 10^{17}$ photons cm^{-2}, the exposure dose that marks the equilibrium between formation and destruction routes.

To calculate the product formation efficiency per energy dose deposited in the ice, for each step of the photolysis, only the absorbed photons are considered. For each of the presented UV irradiation doses, the corresponding fraction of incident photons absorbed by the water ice is calculated using Eq. 2 as $(26.0 \pm 6.5)\%$. The largest uncertainty in the fraction of absorbed photons is based on the error bars related to the UV photon flux (25%). By calculating the yield for each UV dose, an upper limit was determined for the O_2 formation in pure H_2O ice as $(1.3 \pm 0.3) \times 10^{-3}$ mol. eV^{-1}. A similar calculation was done for H_2O_2, which results in a maximum formation yield
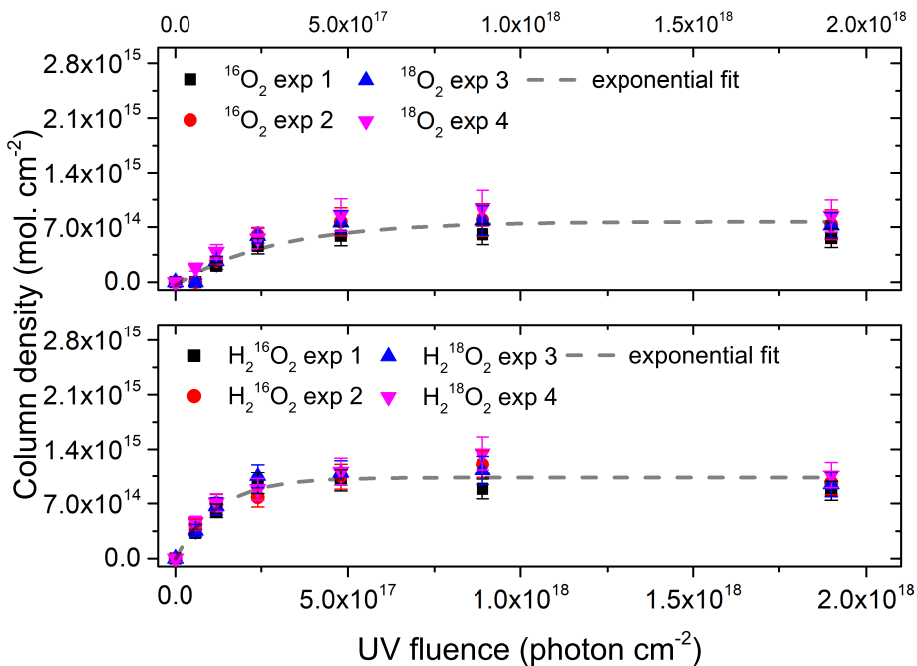
Figure 6.2: Molecular abundances of species during the UV photolysis of $H_2^{16}O$ and $H_2^{18}O$ ices at 20 K as function of photon fluence: $^{16}O_2$, $^{18}O_2$ (*upper panel*) and $H_2^{16}O_2$, $H_2^{18}O_2$ (*lower panel*). The results from four separate experiments are shown. The initial ice thickness is (90 ± 10) ML.

of $(3.7 \pm 0.9) \times 10^{-3}$ mol. eV^{-1}.

6.3.2 UV photolysis of H_2O:CO_2 (100:11, 100:22, and 100:44)

The mass spectra obtained during the UV photolysis of the H_2O:CO_2 = 100:11 ice mixture are shown in Fig. 6.3. The mass spectra for the 100:22 and 100:44 mixtures are presented in Appendix B.

The reference mass spectrum (Fig. 6.3, black trace), in addition to the previously described water signatures (see Fig. 6.2), includes the m/z values characteristic for CO_2, that is, $m/z = 12$, 16, 28 and 44. Upon reaching a UV fluence of 6.0×10^{16} photons cm^{-2} (red trace), a number of new m/z signals is observed. These signals are representative of the formation of H_2O_2 ($m/z = 34$), H_2 ($m/z = 2$) and CO ($m/z = 28$). The formation of O_2, at $m/z = 32$, is detected simultaneously with H_2CO ($m/z = 29$, 30) and HCOOH ($m/z = 45$ and 46). These assignments are based on the available chemical inventory in the ice and available reference mass spectra. The photoproduct formation is consistent with a decrease in the abundances of precursor species as discussed earlier (see Appendix A).

The mass spectra obtained during the photolysis of H_2O:CO_2 (100:22 and 100:44) ices exhibit the formation of the same photoproducts, but at different relative intensities. This change is correlated with the relative increase in the abundance of CO_2
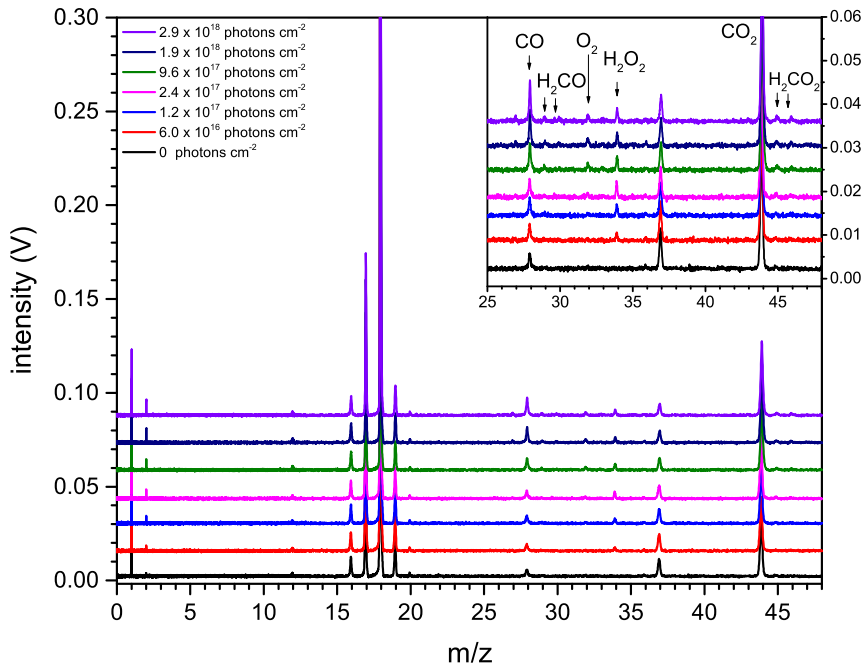
Figure 6.3: LDPI TOF MS signals for a UV-irradiated $H_2O:CO_2$ ice at 100:11 ratio. The lowest trace in each panel shows the signal without UV irradiation. Peaks at $m/z = 18\cdot n+1$, where n = 1, 2 represent protonated water clusters formed upon laser desorption of water ice and do not contribute to the chemistry in the ice. The inset is a zoom on the intensity scale for the higher masses.

which shifts the elemental balance towards carbon-containing species (CO, Appendix A), and also enhances the total oxygen content.

The abundances of the identified photoproducts are derived for the three mixtures following the method described in Sect. 2.2. The formed product abundances for all mixtures are shown as a function of UV fluence in Fig. 6.4. The maximum formation yield of O_2 reaches $(2.4 \pm 0.6) \times 10^{14}$ molecules cm^{-2} (for the $H_2O:CO_2 = 100:11$ mixture), $(3.4 \pm 0.8) \times 10^{14}$ molecules cm^{-2} (100:22), and $(5.1 \pm 1.2) \times 10^{14}$ molecules cm^{-2} (100:44). The formation of H_2O_2 peaks at $(8.5 \pm 2.1) \times 10^{14}$ (100:11), $(3.8 \pm 1.0) \times 10^{14}$ molecules cm^{-2} (100:22), and $(4.2 \pm 1.0) \times 10^{14}$ molecules cm^{-2} (100:44). It can be clearly seen that upon an increase in the abundance of CO_2 in the mixtures with H_2O, the maximum abundance of formed O_2 increases with the amount of CO_2 in the ice. An opposite behaviour is seen for H_2O_2 formation. Its upper limit abundance decreases, or stays constant, as the initial amount of CO_2 in the ice mixture is increased.

In all mixtures, it is found that H_2O depletes more efficiently, compared to pure H_2O ice. The formation yields of the observed species are normalised to the current amount of H_2O for each of the applied UV irradiation doses. Hence, even though the
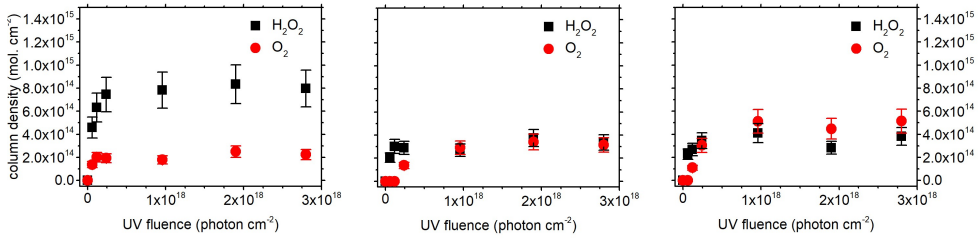
Figure 6.4: Absolute molecular abundances of species during the UV photolysis of mixed ices: H_2O:CO_2 ice at 100:11 ratio (left panel), 100:22 (center panel), and 100:44 (right panel). Initial ice thickness is (90 ± 10) ML.

absolute yields of O_2 and H_2O_2 in mixtures are slightly lower than in pure H_2O ice photolysis, the relative abundance with respect to H_2O is increased. For the 100:11 mixture, the relative abundance of O_2/H_2O and H_2O_2/H_2O reaches, respectively, $(1.1 \pm 0.3)\%$ and $(1.2 \pm 0.3)\%$. For the 100:22 mixture, a relative abundance of O_2/H_2O and H_2O_2/H_2O reaches, respectively, $(1.6 \pm 0.4)\%$ and $(1.8 \pm 0.4)\%$. In the 100:44 mixture, relative maximum abundances of O_2/H_2O and H_2O_2/H_2O are, respectively, $(1.2 \pm 0.3)\%$ and $(1.1 \pm 0.3)\%$.
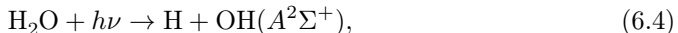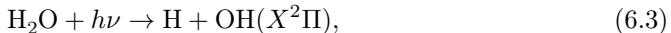
To compare the efficiency of photoproduct formation in the H_2O:CO_2 mixtures with the results obtained for the pure H_2O ice, the peak abundances of products at corresponding UV fluences, have been converted to formation yields per energy dose deposited in the ice. To calculate the fraction of incident photons absorbed by the H_2O:CO_2 ice, we considered the ratio between ice constituents and their respective UV-absorption cross-sections. Consequently, for the H_2O:CO_2 (100:11, 100:22, 100:44) ice mixtures, the fraction of absorbed photons comprise $(24.5 \pm 6.1)\%$, $(22.5 \pm 5.6)\%$ and $(20.8 \pm 5.2)\%$, respectively. Here, the uncertainty in the absorbed photons is again related to the UV flux throughout the photolysis. This results in the maximum formation yields of O_2 equal to $(6.1 \pm 1.8) \times 10^{-4}$ mol. eV^{-1} (100:11), $(9.7 \pm 2.5) \times 10^{-4}$ mol. eV^{-1} (100:22), and $(6.7 \pm 2.1) \times 10^{-4}$ mol. eV^{-1} (100:44). The same calculation for H_2O_2 yields $(3.2 \pm 0.7) \times 10^{-3}$ mol. eV^{-1} (100:11), $(1.5 \pm 0.4) \times 10^{-3}$ mol. eV^{-1} (100:22), and $(3.5 \pm 1.0) \times 10^{-3}$ mol. eV^{-1} (100:44), respectively.

In addition to the mixtures studied above, where O_2 is a product of photolysis of H_2O:CO_2, we investigated the photoevolution of an ice, which already includes O_2 in the initial composition. The initial amount of O_2, at a 2% level, is based on the results of modelling studies by Taquet et al. (2016). The quantitative analysis is presented in Appendix C.

6.4   Discussion

The results presented in the previous section allow us to discuss i) the kinetic curves for O_2 and H_2O_2 during UV irradiation of pure H_2O ice at 20 K, ii) the impact of including CO_2 in the initial ice composition on (absolute and relative) photoproduct formation yields, and iii) the presence of O_2 in the initial mixture and the evolution of its abundance (and H_2O_2) as a function of UV fluence.

The formation of O_2, H_2O_2 in pure H_2O ice is observed immediately upon the onset of UV photolysis. Its efficiency is low, at a level of $X/H_2O \approx 1\%$. To discuss the possible formation pathways, it is useful to recall the main photodissociation channels of H_2O (Stief et al. 1975; Harich et al. 2000; van Harrevelt & van Hemert 2008; Slanger & Black 1982; Harich et al. 2001):

$$H_2O + h\nu \rightarrow H + OH(X^2\Pi), \qquad (6.3)$$

$$H_2O + h\nu \rightarrow H + OH(A^2\Sigma^+), \qquad (6.4)$$

$$H_2O + h\nu \rightarrow H_2 + O(^1D), \qquad (6.5)$$

$$H_2O + h\nu \rightarrow O(^3P) + H + H. \qquad (6.6)$$
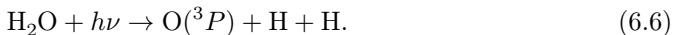
The potential of the newly formed free radicals as precursors for stable molecules is dictated by their abundance, relaxation rates, location within the ice, and diffusion abilities. The abundance of each fragment is given by the wavelength-dependent branching ratios following photodissociation. For H_2O in the gas-phase, relative quantum yields following UV photodissociation within the used wavelength range consistently point to OH (in its ground or first excited state) and H as a dominant channel. This, however, can be different for the solid state (see Öberg et al. 2009d and Lucas et al. 2015 for CH_3OH). It is also expected that the total effective photodissociation yield of radicals in the ice will be lower due to the recombination of fragments into the parent species. A detailed investigation of this process is required, but previous experimental studies show that the radical recombination in the water ice can decrease the photodissociation yield by 43 % – 72 %, compared to the gas phase (Mason et al. 2006; Cruz-Diaz et al. 2014b; Kalvāns 2018).

The location of the photodissociation event within the ice is important; combined with the temperature of the ice, it determines the diffusion abilities of the fragments (Andersson et al. 2006; Andersson & van Dishoeck 2008; Arasa et al. 2010). In particular, if H and OH are formed from photodissociation in the top layers of the ice ($\sim$ 3 ML), both radicals can travel up to a few tens of angstroms within (or on top of) the ice (Andersson & van Dishoeck 2008). However, the average distance travelled by H and OH fragments in the ice is 8 Å and 1 Å, respectively. In a realistic scenario, free radicals are formed randomly throughout the ice and can be formed in two different chemical environments: at the ice and vacuum interface on the surface (including pores) and within the ice bulk. In our experiments, the ice thickness (90 ML) was chosen to maximise the contribution of the radicals created in the ice bulk; however, the exact ratio of radicals created in the bulk versus the surface (and pores) is not known. The presence of such a large parameter space significantly complicates the interpretation of our data. Nevertheless, some important observations can be made.

Under the assumption that photodissociation of H_2O mainly leads to the formation of H and OH (in the ground or excited states), the formation of H_2O_2 and H_2 can be easily accounted for by radical recombination reactions of OH+OH and H+H. However, as formation of O_2 can be observed already during the early stages of irradiation, simultaneously with the formation of H_2O_2 (see Fig. 6.2), the involved O_2 formation routes must be connected to those of H_2O_2 and H_2 and involve the direct products of H_2O photodissociation. Hence, we suggest that O radicals are present in the ice directly upon water photodissociation (reactions 6.5 and 6.6). The formation of $O(^1D)$ via reaction (6.5) was demonstrated experimentally as a primary process upon photolysis of ASW (UV photolysis with 157 nm at 90 K) by Hama et al. (2009a).

This radical can either proceed to react with water via $O(^1D)+H_2O \rightarrow 2\ OH$ (Sayós et al. 2001), or relax to its ground state and react with OH to form O_2 via $O(^3P)$ + $OH \rightarrow O_2+H$ (Hama et al. 2010). Channel (6) has not been observed experimentally; however, its contribution is not excluded as the Ly-alpha photons in our spectrum are capable of dissociating water into $O(^3P)$ (van Harrevelt & van Hemert 2008). During later stages of photolysis, secondary reaction channels, such as photodissociation of OH or recombination of OH radicals can contribute towards the formation of $O(^3P)$, and consequently, O_2 (Hama et al. 2009b, 2010).

It is also important to mention that the photodepletion of water is below $\sim$10%. Such inefficient depletion, even for a relatively large number of absorbed photons per H_2O molecule (i.e. 4 - 5; see Section 6.1), suggests that pure water ice is resilient to UV irradiation, in part due to efficient conversion of the formed products back into H_2O.

The photolysis of H_2O:CO_2 ice mixtures provides additional radical precursors via the following pathways (Slanger & Black 1978; Kinugawa et al. 2011):

$$CO_2 + h\nu \rightarrow O(^3P) + CO(X^1\Sigma^+), \tag{6.7}$$

$$CO_2 + h\nu \rightarrow O(^1D) + CO(X^1\Sigma^+). \tag{6.8}$$
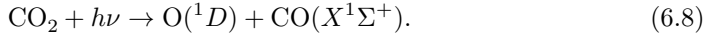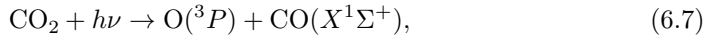
The addition of CO_2 in the ice results in a decreased absolute formation yield of O_2 and H_2O_2 in comparison to pure H_2O ice photolysis (see Fig. 6.2 and 6.4). This could be due to the lower initial abundance of water (90 ML) and/or CO_2 photodissociation products providing reactive radicals leading to competing photoproducts. Indeed, interactions of OH radicals with CO (produced by photodissociation of CO_2) lead to the (re)formation of CO_2 (Hama et al. 2010; Ioppolo et al. 2011). Consistently with fewer OH radicals available, we observe a reduced amount of formed H_2O_2. In addition, if O radicals are present via water photodissociation (see point i) in the discussion), these fragments can also react with CO, to reform CO_2, constraining the absolute formation of O_2.

Increasing the relative CO_2 abundance (H_2O:CO_2 from 100:11 to 100:44) leads to a proportional increase in the O_2 formation. The maximum formation yield of O_2 is increased from $(2.4 \pm 0.6) \times 10^{14}$ molecules cm^{-2} to $(5.1 \pm 1.2) \times 10^{14}$ molecules cm^{-2} for H_2O:CO_2 mixtures with a ratio of 100:11 and 100:44, respectively (see Fig. 6.4). This is in line with the increased production of O atoms, via photodissociation of CO_2 in the ice and formation of O_2 following O+OH and O+O interactions. With more initial CO_2, the formation of H_2O_2 becomes less efficient, which could be simply due to fewer OH radicals available in the ice and the competitive reaction of CO + OH $\rightarrow$ CO_2.

The absolute yields of O_2 and H_2O_2 during UV photolysis of mixed ices (H_2O:CO_2) are lower compared to pure H_2O ice, however, the relative abundances of O_2/H_2O increase. This is due to a more significant photoconversion of H_2O molecules to other species.

The analysis of the most complex H_2O:CO_2:O_2 ice mixture provides hints for more efficient formation pathways towards O_2 and H_2O_2 (see Appendix C). In this mixture, in addition to the previously described fragments, O radicals are available directly upon photodissociation of O_2 (Lambert et al. 2004):

$$O_2 + h\nu \rightarrow O(^3P) + O(^3P), \tag{6.9}$$

$$O_2 + h\nu \rightarrow O(^1D) + O(^3P). \tag{6.10}$$
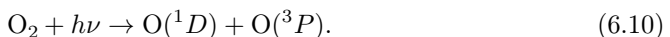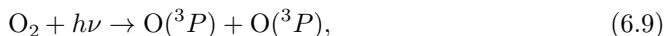
At the early stages of photolysis, the formation efficiency of both O_2 and H_2O_2 (mol. eV^{-1}) is an order of magnitude higher compared to other mixtures or pure water ice. The interpretation of such a result should be performed carefully, as here a precursor is included that in fact is the reaction product the experiment is aiming at. It is found, however, that the maximum abundance observed during the photolysis cannot be accounted for by the initial O_2 injection (Fig. 6.11). The increased formation yield hints for additional chemical mechanisms from the pathways discussed above. These are most likely associated with the presence of a highly reactive radical, $O(^1D)$. The increased formation of O_2 might indeed be partially due to $O(^1D)$ radicals produced via the dissociation of O_2, reacting with CO_2, H_2O or their photodissociation products (Wen & Thiemens 1993; Sayós et al. 2000). A significantly higher abundance (compared to other mixtures) is also observed for H_2O_2. This could be due to a barrierless reaction of $O(^1D)+H_2O \rightarrow 2$ OH, which provides precursor species for the typical radical recombination reaction (OH + OH) leading to H_2O_2 (Sayós et al. 2001). It is also found that $H_2O:CO_2:O_2$ ice mixture is the only ice studied here, where efficient formation of H_2 is not observed. This suggests that H atoms are consumed via reactions with other ice constituents: CO, O, OH, or O_2.

6.5 Astrophysical implications

The majority of water in the ISM exists in the solid state and is formed via atom addition reactions on the grains in the dense molecular clouds (Lamberts et al. 2013; Linnartz et al. 2015; van Dishoeck et al. 2021). In addition to H_2O molecules produced by the hydrogenation of accreting O atoms (O + H $\rightarrow$ OH and OH + H/H_2 $\rightarrow H_2O$), other simple molecules are formed during this stage that contribute to the bulk of observed H_2O-rich ices. These molecules include NH_3 and CH_4, produced by the hydrogenation of N and C atoms, respectively, as well as CO_2, produced through the interaction of accreting CO molecules with OH radicals (Fedoseev et al. 2015b; Qasim et al. 2020; Hama et al. 2010; Ioppolo et al. 2011). Simultaneously, depending on the local physical environment, an O_2 ice reservoir can accumulate (Taquet et al. 2016). Towards the end of the accretion stage in a dense molecular cloud, the increase in chemical complexity of the icy mantles is driven by various types of energetic processing (e.g. cosmic rays, X-rays, UV photons). Later, the chemically enriched icy mantles become part of the material from which a young star, its surrounding planets and other celestial bodies, such as comets, are made from. In fact, the transfer of ices from dark clouds to protoplanetary discs and comets was discussed by Taquet et al. (2016), which showed that the chemical composition of the ices along the comet formation sequence is preserved.

To place our experiments in an astronomical context, Fig. 6.5 (left panel) shows the relative abundance of O_2/H_2O for the four studied ice compositions: pure H_2O and $H_2O:CO_2$ (100:11, 100:22, 100:44). In addition, the abundances detected in the cometary comae of 67P $(3.1 \pm 1.1)\%$ and 1P $(3.7 \pm 1.7)\%$ are marked. In the experiments we show that during the photolysis of pure H_2O ice, the O_2/H_2O ratio can increase up to a level $(0.9 \pm 0.2)\%$, roughly three-four times less than the detected abundances in the cometary comea. For ice mixtures more adequately representing icy mantles ($H_2O:CO_2$), the O_2/H_2O abundance increases with an increasing initial amount of CO_2, up to $(1.6 \pm 0.4)\%$ for the $H_2O:CO_2$ (100:22) ice. This value is within a of factor 2 in the range of the cometary abundances. It is expected that other abun-

dant constituents of interstellar ices may also have an impact on relative formation of O_2/H_2O. As an example, the presence of CO can lead to a decrease in the number of available H atoms in the ice, as its successive hydrogenations lead to efficient formation of H_2CO and CH_3OH (Watanabe & Kouchi 2002). Subsequently, it would inhibit the recombination of water (OH + H), leaving OH radicals that could change the O_2/H_2O ratio. Dedicated astrochemical modelling is needed to understand how these processes combine with each other.

With regard to species that are chemically related, the non-detection of O_3 and HO_2 in our experiments is consistent with low cometary and ISM measurements. The abundance ratio of HO_2/O_2 for both the 67P and ρ Oph A is 2×10^{-3} (Bieler et al. 2015; Parise et al. 2012), while for O_3 there is only an upper limit abundance with respect to O_2 at 2×10^{-5}.

The key discrepancy between our experiments and cometary observations is in the abundance of H_2O_2. Its formation during UV photolysis is at a similar level to O_2, which is two orders of magnitude above the observed values (Bieler et al. 2015). An explanation for this might be in an efficient dismutation of H_2O_2, upon thermal desorption of the water ice as demonstrated by Dulieu et al. (2017). Based on Smith et al. (2011), H_2O_2 is expected to be present in the interstellar ices at an abundance of (9 $\pm$ 4)% with respect to H_2O and to survive the transfer to the nucleus of the comet. Subsequently, when the comet thermally releases species trapped within the cometary ice, including H_2O_2, hydrogen peroxide undergoes a dismutation via $2H_2O_2 \rightarrow 2H_2O + O_2$, which is found to produce O_2/H_2O yields from 1-10% (Dulieu et al. 2017).

Our experiments are set up such that the abundances we record in the gas phase are a direct measure of the ices. The same may not be the case for the gases observed in the comae around comets 1P and 67P. Therefore, dismutation producing O_2 gas from H_2O_2 gas could be a contributing factor to the measured abundance of O_2 in the comets. If O_2 and H_2O_2 ices are produced in similar amounts in the cometary ices (similar to the results from our work), and assuming that all H_2O_2 is processed into O_2 (the H_2O_2 abundance is two orders of magnitude below O_2 in the comet 67P), then the observed abundance of O_2 in the cometary comae may be higher than when it was still in the cometary ice (see also Dulieu et al. 2017; Mousis et al. 2016). If we apply this logic to the experimental yields derived here, then the O_2 abundances are shifted up by the contribution from the H_2O_2 molecules (two H_2O_2 molecules are converted into one O_2). Taking this into account, the experimental values for O_2 abundance (in the gas-phase) for a UV fluence of just under 2×10^{18} photons cm^{-2} and an ice mixture of $H_2O:CO_2$ (100:22) would fall within the observed abundance limits in both comets (see Fig. 6.5, right panel).

For the O_2 -enriched ices, an increase in the O_2/H_2O ratio is seen for all non-zero UV fluences. It varies between $\sim$3% and $\sim$7%, with the maximum yield at a relatively low UV fluence (based on Fig. 6.11). This corresponds to an increase in O_2/H_2O abundance by a factor of 1.5 to 3.5, relatively to the initial O_2 amount. Following this, it can be argued that the icy material in comets 1P and 67P could have started out (prior to the pre-solar nebula-stage) with a smaller O_2/H_2O ice ratio than seen today. Subsequently, during evolution and if subjected to UV photons (or possibly other energetic processing), the initial ratio could have increased by a factor 1.5 - 3.5, to explain the ratio that is derived from the *Rosina* and *Giotto* missions.

It should be noted that UV photolysis is not the only process that affects the composition of the interstellar ices. Other sources of chemical diversity include high-
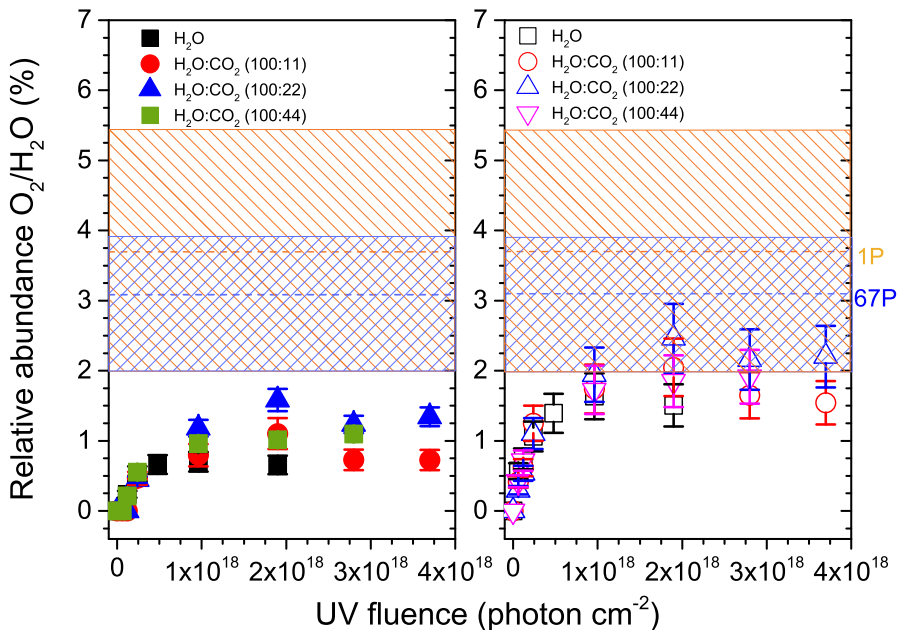
Figure 6.5: Striped areas represent relative O_2/H_2O abundances detected in cometary comae of 67P and 1P from (Rubin et al. 2019). The data points represent the laboratory experiments presented here. *Left panel:* Molecular abundance of O_2 normalised to the amount of H_2O at each UV dose for different initial compositions of the ice. *Right panel:* Molecular abundance of O_2 enhanced by the decomposition of H_2O_2 (see text for details).

energy particles, X-rays, cosmic rays (CR) themselves, or CR-triggered avalanches of secondary electrons. In the last two decades, the effects of these processes have been investigated via experiments and astrochemical models (Gomis et al. 2004; Zheng et al. 2006a; Mousis et al. 2016, 2018; Eistrup & Walsh 2019; Teolis et al. 2017; Shingledecker et al. 2018, 2019; Notsu et al. 2021). These experimental and modelling findings, combined with our novel results, which may (largely) explain the observed cometary O_2/H_2O ratios, stress the importance of precise chemical modelling. The work presented here now provides explicit values as input parameters.

6.6   Conclusions

LDPI TOF MS was applied to quantify the formation of O_2 during UV irradiation of simple interstellar ice analogues (H_2O, $H_2O:CO_2$ and $H_2O:CO_2:O_2$) at 20 K. The main results are as follows.

1. For a UV photon fluence representative of dense molecular clouds and innermost regions of protoplanetary discs ($\sim 10^{18}$ photons cm^{-2}), UV irradiation of porous amorphous H_2O ice at 20 K leads to formation of O_2 and H_2O_2 in the solid

state. The maximum abundances of (O_2/H_2O) and H_2O_2/H_2O are equal to (0.9 ± 0.2)% and (1.3 ± 0.3)%, respectively.

2. The mixing of H_2O with CO_2 ice with the ratios 100:11, 100:22, and 100:44 results in an increased relative formation of O_2/H_2O, with a maximum value of (1.6 ± 0.4)% for the 100:22 mixture. This also shows that CO_2 is involved in the formation of molecular oxygen.

3. The maximum formation efficiency of O_2 and H_2O_2 per energy unit deposited in the pure H_2O ice at 20 K are: (1.3 ± 0.3) × 10^{-3} mol. eV^{-1} and (3.7 ± 1.0) × 10^{-3} mol. eV^{-1}. These yields are similar for the $H_2O:CO_2$ mixtures; for O_2 it is (9.7 ± 0.4) × 10^{-4} mol. eV^{-1} , and for H_2O_2 it is (3.5 ± 0.9) × 10^{-3} mol. eV^{-1}. However, the corresponding maximum photoproduct formation efficiency in the $H_2O:CO_2:O_2$ mixture are almost an order of magnitude higher; for O_2 it is (1.1 ± 0.3) × 10^{-2} mol. eV^{-1} , and for H_2O_2 it is (1.6 ± 0.4) × 10^{-2} mol. eV^{-1}. This is without the contribution of the O_2 already present in the mixture.

4. The abundances of O_2/H_2O found in our experiments are sufficient to account for at least part of the observed cometary abundances.

This work demonstrates the potential of MATRI^{2}CES to investigate the photochemical evolution of interstellar ices analogues, including the infrared-inactive species, upon VUV photolysis at low temperature.

Appendix

6.A   H$_2$O and CO abundance during UV photolysis

The photodepletion of water was derived for all ices investigated in this study and is shown in Fig. 6.6. For the pure H$_2$O ice, the depletion was below the uncertainty related to the initial ice thickness; hence, it was calculated based on the abundances of formed photoproducts. The total abundance of O$_2$ and H$_2$O$_2$ reached $\sim$2 $\times$ 10^{15} molecules cm^{-2}. Under the assumption that each of these species requires two H$_2$O molecules, the lower limit of water consumption was derived to be $(4.0) \times 10^{15}$ molecules cm^{-2}, which is 4% of the initial column density of the ice.
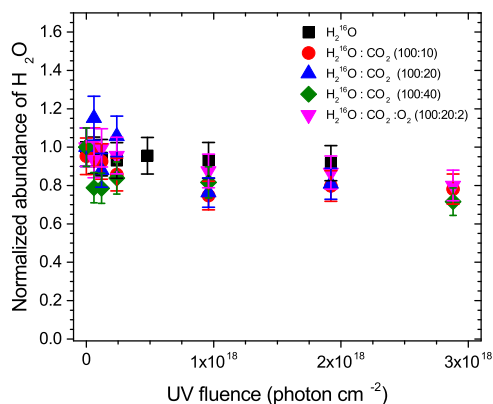

Figure 6.6: Molecular abundance of H$_2$O normalised to its initial amount as a function of UV photon fluence for different initial compositions of the ice.
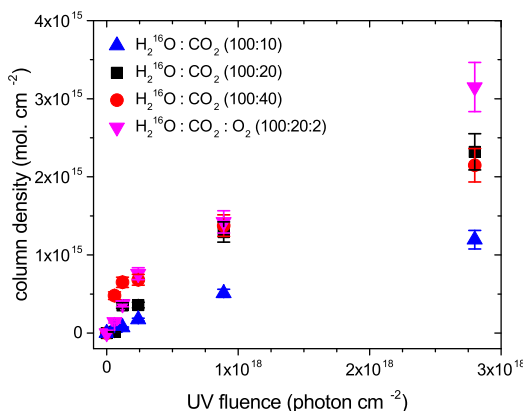

Figure 6.7: Molecular abundance of CO as a function of UV photon fluence for different initial compositions of the ice.

The formation of CO was derived for all mixed ices investigated in this study, shown in Fig. 6.7. Towards the end of UV photolysis, CO was the dominant photoproduct, with a maximum yield in the H_2O:CO_2:O_2 (100:22:2) mixture.

6.B   UV photolysis of H_2O:CO_2 (100:22 and 100:44)

The mass spectra obtained during the UV photolysis of the H_2O:CO_2 = 100:22 and H_2O:CO_2 = 100:44 ice mixtures are shown in Fig. 6.8 and 6.9.

6.C   UV photolysis of H_2O:CO_2:O_2 (100:22:2)

The mass spectra resulting from the UV photolysis of an H_2O:CO_2:O_2 (100:22:2) mixture are shown in Fig. 6.10. The reference mass spectrum (black trace), in addition to the previously described signatures of H_2O and CO_2, also shows the m/z values corresponding to the initial O_2, at $m/z = 16$ and 32.

After UV irradiation of the ice with a fluence of 6×10^{16} photons cm^{-2} (red trace, Fig), new peaks appear at $m/z = 33$, 34, and the intensity of features at $m/z = 28$, 29, 32, and 45 increases. This is representative of the formation of H_2O_2, CO, H_2CO, O_2 and HCOOH. In order to quantify the formation yields of CO and O_2, the signals corresponding to the initial abundances of CO_2 (a fragment overlapping with CO at $m/z = 28$) and O_2 are subtracted, allowing us to trace the contribution from the newly formed molecules. We note that no H_2 signal is observed until a high UV fluence of 1.9×10^{18} photons cm^{-2} is reached.

The abundances of identified photoproducts are calculated following the method described in Sect. 6.2. and are presented in Fig. 6.11 The O_2 abundance increases, reaching $(4.5 \pm 1.1) \times 10^{15}$ molecules cm^{-2}. Upon reaching a UV fluence of 2.4×10^{17} photons cm^{-2}, the O_2 destruction efficiency matches the O_2 formation rate and starts to dominate at higher UV fluence. At a fluence of 3.7×10^{18} photons cm^{-2}, the O_2 abundance continues to decrease, with a final yield below the initial O_2 abundance.

The formation of H_2O_2 in this mixture follows a trend similar to O_2. Its abundance reaches a maximum of $(3.5 \pm 0.9) \times 10^{15}$ molecules cm^{-2} at 2.4×10^{17} photons cm^{-2}. Upon longer irradiation, its abundance decreases to $(1.7 \pm 0.4) \times 10^{15}$ molecules cm^{-2} at 3.7×10^{18} photons cm^{-2}.

The quantified consumption of H_2O (Appendix A) is used to derive an upper limit on the relative photoproduct formation (X/H_2O) during the photolysis of H_2O:CO_2:O_2 ices. The upper limit of the relative abundance of (O_2/H_2O) is calculated to be (6.9 ± 1.6)%, and the corresponding value for (H_2O_2/H_2O) is (5.4 ± 1.4)%.

The H_2O:CO_2:O_2 (100:22:2) ice at each UV dose absorbs (25.7 ± 7.2)% of incident photons. Consequently, the formation yields of O_2 and H_2O_2 reach their maxima equal to $(1.1 \pm 0.3) \times 10^{-2}$ mol. eV^{-1} and $(1.6 \pm 0.3) \times 10^{-2}$ mol. eV^{-1}, respectively. In comparison to the photolysis of pure water ice and mixtures with CO_2, the formation efficiency (in mol. eV^{-1}) of both products in this mixture is higher by one order of magnitude.
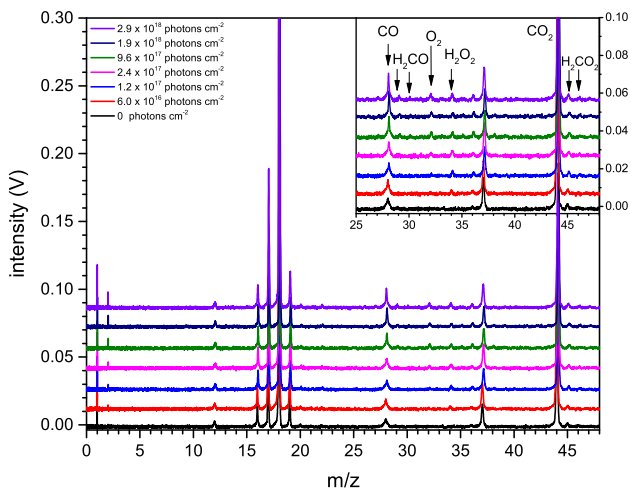
Figure 6.8: LDPI TOF MS signals for a UV-irradiated H_2O:CO_2 ice at 100:22 ratio. The lowest trace in each panel shows the signal without UV irradiation. Peaks at $m/z = 18 \cdot n + 1$, where n = 1, 2 represent protonated water clusters formed upon laser desorption of water ice and do not contribute to the chemistry in the ice. The inset shows a zoomed-in image of the intensity scale for the higher masses.
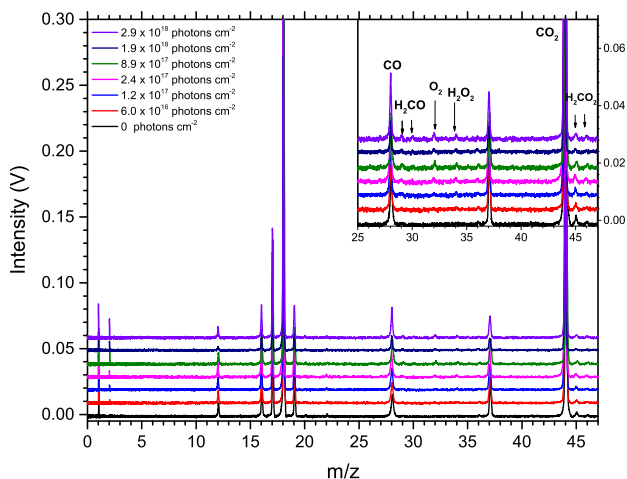

Figure 6.9: LDPI TOF MS signals for a UV-irradiated H_2O:CO_2 ice at 100:44 ratio. The lowest trace in each panel shows the signal without UV irradiation. Peaks at $m/z = 18 \cdot n + 1$, where n = 1, 2 represent protonated water clusters formed upon laser desorption of water ice and do not contribute to the chemistry in the ice. The inset shows a zoomed-in image of the intensity scale for the higher masses.
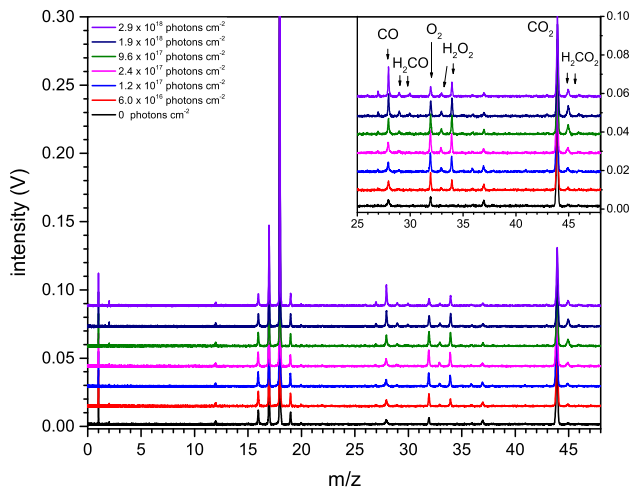
Figure 6.10: LDPI TOF MS signals for a UV-irradiated $H_2O:CO_2:O_2$ ice at 100:22:2 ratio at 20 K. The lowest graph shows the signal without UV irradiation. The inset shows a zoomed-in image of the intensity scale for the higher masses. Peaks at $m/z = 18 \cdot n + 1$, where n = 1, 2 represent protonated water clusters formed upon laser desorption of water ice and do not contribute to the chemistry in the ice.
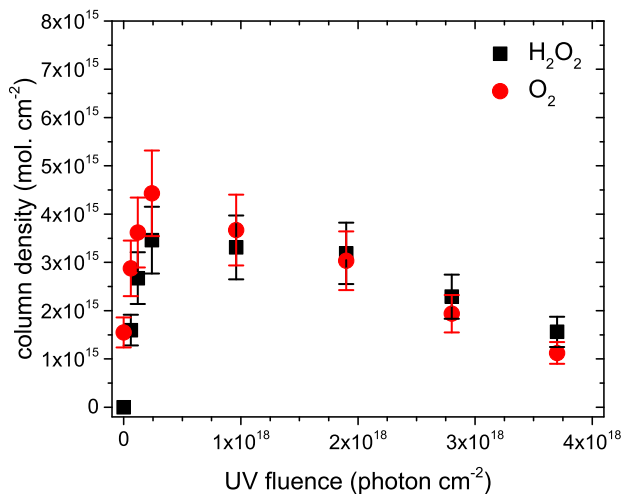

Figure 6.11: Absolute molecular abundances of species during the UV photolysis of mixed ices: $H_2O:CO_2:O_2$ ice at 100:22:2 ratio. Initial ice thickness is (90 ± 10) ML.

Bibliography

Abdulgalil, A. G. M., Marchione, D., Thrower, J. D., et al. 2013, Philos. Trans. R. Soc. A, 371, 20110586

Abplanalp, M. J., Förstel, M., & Kaiser, R. I. 2016, Chem. Phys. L., 644, 79

Abplanalp, M. J. & Kaiser, R. I. 2019, PCCP (Incorp. Far. Trans.), 21, 16949

Abplanalp, M. J. & Kaiser, R. I. 2020, ApJ, 889, 3

Acharyya, K., Schulte, S. W., & Herbst, E. 2020, ApJS, 247, 4

Agúndez, M., Cernicharo, J., de Vicente, P., et al. 2015, A&A, 579, L10

Agúndez, M., Marcelino, N., & Cernicharo, J. 2018, ApJ, 861, L22

Altwegg, K., Balsiger, H., Bar-Nun, A., et al. 2015, Science, 347, 1261952

Altwegg, K., Balsiger, H., Bar-Nun, A., et al. 2016, Science Advances, 2, e1600285

Altwegg, K., Balsiger, H., Berthelier, J. J., et al. 2017, MNRAS, 469, S130

Altwegg, K., Balsiger, H., & Fuselier, S. A. 2019, ARA&A, 57, 113

Andersson, S., Al-Halabi, A., Kroes, G.-J., & van Dishoeck, E. F. 2006, J. Chem. Phys., 124, 064715

Andersson, S. & van Dishoeck, E. F. 2008, A&A, 491, 907

Arasa, C., Andersson, S., Cuppen, H. M., van Dishoeck, E. F., & Kroes, G. J. 2010, J. Chem. Phys., 132, 184510

Arasa, C., Andersson, S., Cuppen, H. M., van Dishoeck, E. F., & Kroes, G. J. 2011, J. Chem. Phys., 134, 164503

Arasa, C., Koning, J., Kroes, G.-J., Walsh, C., & van Dishoeck, E. F. 2015, A&A, 575, A121

Ball, J. A., Gottlieb, C. A., Lilley, A. E., & Radford, H. E. 1970, ApJ, 162, L203

Balsiger, H., Altwegg, K., & Geiss, J. 1995, , 100, 5827

Bar-Nun, A., Herman, G., Rappaport, M., & Mekler, Y. 1985, Surf. Sci., 150, 143

Baragiola, R. A., Atteberry, C. L., Dukes, C. A., Famá, M., & Teolis, B. D. 2002, Nucl. Instr. Meth. in Phys. R. B, 193, 720

Baratta, G. A. & Palumbo, M. E. 1998, J. Opt. Soc. Am. A, 15, 3076

Belloche, A., Garrod, R. T., Müller, H. S. P., et al. 2009, A&A, 499, 215

Belloche, A., Garrod, R. T., Müller, H. S. P., et al. 2019, A&A, 628, A10

Belloche, A., Meshcheryakov, A. A., Garrod, R. T., et al. 2017, A&A, 601, A49

Bennett, C. J., Chen, S.-H., Sun, B.-J., Chang, A. H. H., & Kaiser, R. I. 2007, ApJ, 660, 1588

Bergin, E. A., Hartmann, L. W., Raymond, J. C., & Ballesteros-Paredes, J. 2004, ApJ, 612, 921

Bergin, E. A., Langer, W. D., & Goldsmith, P. F. 1995, ApJ, 441, 222

Bergin, E. A., Maret, S., van der Tak, F. F. S., et al. 2006, ApJ, 645, 369

Bergin, E. A., Melnick, G. J., Stauffer, J. R., et al. 2000, ApJ, 539, L129

Bergin, E. A. & Tafalla, M. 2007, ARA&A, 45, 339

Bergner, J. B., Guzmán, V. G., Öberg, K. I., Loomis, R. A., & Pegues, J. 2018, ApJ, 857, 69

Bernstein, M. P., Dworkin, J. P., Sandford, S. A., Cooper, G. W., & Allamandola, L. J. 2002, Nature, 416, 401

Bernstein, M. P., Sandford, S. A., Allamandola, L. J., Chang, S., & Scharberg, M. A. 1995, ApJ, 454, 327

Bertin, M., Fayolle, E. C., Romanzin, C., et al. 2012, PCCP, 14, 9929

Bertin, M., Fayolle, E. C., Romanzin, C., et al. 2013, ApJ, 779, 120

Bertin, M., Romanzin, C., Doronin, M., et al. 2016, ApJ, 817, L12

Bieler, A., Altwegg, K., Balsiger, H., et al. 2015, Nature, 526, 678

Bisschop, S. E., Fuchs, G. W., Boogert, A. C. A., van Dishoeck, E. F., & Linnartz, H. 2007a, A&A, 470, 749

Bisschop, S. E., Jørgensen, J. K., van Dishoeck, E. F., & de Wachter, E. B. M. 2007b, A&A, 465, 913

Bizzocchi, L., Prudenzano, D., Rivilla, V. M., et al. 2020, arXiv e-prints, arXiv:2006.08401

Blanksby, S. J. & Ellison, G. B. 2003, Acc, 36, 255

Boamah, M. D., Sullivan, K. K., Shulenberger, K. E., et al. 2014, Far. Disc., 168, 249

Bockelée-Morvan, D., Lis, D. C., Wink, J. E., et al. 2000, A&A, 353, 1101

Boogert, A. C. A., Gerakines, P. A., & Whittet, D. C. B. 2015, ARA&A, 53, 541

Boogert, A. C. A., Huard, T. L., Cook, A. M., et al. 2011, ApJ, 729, 92

Boogert, A. C. A., Pontoppidan, K. M., Knez, C., et al. 2008, ApJ, 678, 985

Boonman, A. M. S., Doty, S. D., van Dishoeck, E. F., et al. 2003, A&A, 406, 937

Booth, A. S., Walsh, C., Terwisscha van Scheltinga, J., et al. 2021, Nature Astronomy, 5, 684

Borget, F., Müller, S., Grote, D., et al. 2017, A&A, 598, A22

Bossa, J. B., Paardekooper, D. M., Isokoski, K., & Linnartz, H. 2015, PCCP (Incorp. Far. Trans.), 17, 17346

Bouwman, J., Paardekooper, D. M., Cuppen, H. M., Linnartz, H., & Allamandola, L. J. 2009, ApJ, 700, 56

Brown, W., Augustyniak, W., Simmons, E., et al. 1982, Nucl. Instr. Meth. in Phys. R., 198, 1

Brunetto, R., Caniglia, G., Baratta, G., & Palumbo, M. 2008, ApJ, 686, 1480

Bulak, M., Paardekooper, D. M., Fedoseev, G., & Linnartz, H. 2020, A&A, 636, A32

Bulak, M., Paardekooper, D. M., Fedoseev, G., & Linnartz, H. 2021, A&A, 647, A82

Bull, J. N., Harland, P. W., & Vallance, C. 2012, J. Phys. Chem. A, 116, 767

Calcutt, H., Jørgensen, J. K., Müller, H. S. P., et al. 2018, A&A, 616, A90

Caselli, P., Keto, E., Bergin, E. A., et al. 2012, ApJ, 759, L37

Castellanos, P., Candian, A., Zhen, J., Linnartz, H., & Tielens, A. G. G. M. 2018, A&A, 616, A166

Ceccarelli, C., Bacmann, A., Boogert, A., et al. 2010, A&A, 521, L22

Cernicharo, J., Marcelino, N., Roueff, E., et al. 2012, ApJ, 759, L43

Charnley, S. B., Rodgers, S. D., & Ehrenfreund, P. 2001, A&A, 378, 1024

Chase Jr, M. & Tables, N.-J. T. 1998, Journal of Phys. and Chem. Ref. Data. American Institute of Physics, New York

Chen, Y.-J., Chuang, K.-J., Caro, G. M., et al. 2013, ApJ, 781, 15

Chen, Y. J., Chuang, K. J., Muñoz Caro, G. M., et al. 2014, ApJ, 781, 15

Chevance, M., Kruijssen, J. M. D., Hygate, A. P. S., et al. 2020, MNRAS, 493, 2872

Chiar, J. E., Adamson, A. J., & Whittet, D. C. B. 1996, ApJ, 472, 665

Chuang, K. J., Fedoseev, G., Ioppolo, S., van Dishoeck, E. F., & Linnartz, H. 2016, MNRAS, 455, 1702

Chuang, K. J., Fedoseev, G., Qasim, D., et al. 2017, MNRAS, 467, 2552

Chuang, K. J., Fedoseev, G., Qasim, D., et al. 2018a, A&A, 617, A87

Chuang, K. J., Fedoseev, G., Qasim, D., et al. 2018b, ApJ, 853, 102

Cleeves, L. I., Bergin, E. A., Alexander, C. M. O. D., et al. 2014, Science, 345, 1590

Collings, M. P., Anderson, M. A., Chen, R., et al. 2004, MNRAS, 354, 1133

Congiu, E., Chaabouni, H., Laffon, C., et al. 2012, J. Chem. Phys., 137, 054713

Cordiner, M. A., Palmer, M. Y., Nixon, C. A., et al. 2015, ApJ, 800, L14

Crouse, J., Loock, H. P., & Cann, N. M. 2015, J. Chem. Phys., 143, 034502

Crowley, J. N. & Sodeau, J. R. 1989, J. Phys. Chem., 93, 3100

Cruz-Diaz, G., Caro, G. M., Chen, Y.-J., & Yih, T.-S. 2014, A&A, 562, A119

Cruz-Diaz, G. A., Martín-Doménech, R., Moreno, E., Muñoz Caro, G. M., & Chen, Y.-J. 2018, MNRAS, 474, 3080

Cruz-Diaz, G. A., Martín-Doménech, R., Muñoz Caro, G. M., & Chen, Y. J. 2016, A&A, 592, A68

Cruz-Diaz, G. A., Muñoz Caro, G. M., Chen, Y. J., & Yih, T. S. 2014a, A&A, 562, A119

Cruz-Diaz, G. A., Muñoz Caro, G. M., Chen, Y. J., & Yih, T. S. 2014b, A&A, 562, A120

Csengeri, T., Belloche, A., Bontemps, S., et al. 2019, A&A, 632, A57

Cuppen, H. M. & Herbst, E. 2007, ApJ, 668, 294

Cuppen, H. M., Ioppolo, S., Romanzin, C., & Linnartz, H. 2010, PCCP (Inc. Far. Trans.), 12, 12077

Danger, G., Bossa, J. B., de Marcellus, P., et al. 2011, A&A, 525, A30

Danger, G., Duvernay, F., Theulé, P., Borget, F., & Chiavassa, T. 2012, ApJ, 756, 11

Dartois, E., Augé, B., Boduch, P., et al. 2015, A&A, 576, A125

Darwent, B. d. 1970, Natl. Stand Ref. Data System - Natl. Bur. Stand, U.S. Gov., NSRDS-NBS 31

Das, A., Sil, M., Gorai, P., Chakrabarti, S. i. K., & Loison, J. C. 2018, ApJS, 237, 9

DeSimone, A. J., Crowell, V. D., Sherrill, C. D., & Orlando, T. M. 2013, J. Chem. Phys., 139, 164702

Dobbs, E. R., Figgins, B. F., Jones, G. O., Piercey, D. C., & Riley, D. P. 1956, Nature, 178, 483

Dominik, C., Ceccarelli, C., Hollenbach, D., & Kaufman, M. 2005, ApJ, 635, L85

Draine, B. T. 2010, Physics of the interstellar and intergalactic medium, Vol. 19 (Princeton University Press)

Drozdovskaya, M. N., van Dishoeck, E. F., Rubin, M., Jørgensen, J. K., & Altwegg, K. 2019, MNRAS, 490, 50

Drozdovskaya, M. N., Walsh, C., Visser, R., Harsono, D., & van Dishoeck, E. F. 2014, MNRAS, 445, 913

Dulieu, F., Minissale, M., & Bockelée-Morvan, D. 2017, A&A, 597, A56

Dulieu, F., Nguyen, T., Congiu, E., Baouche, S., & Taquet, V. 2019, MNRAS, 484, L119

Dupuy, R., Bertin, M., Féraud, G., et al. 2018, Nat. Astr., 2, 796

Dupuy, R., Bertin, M., Féraud, G., et al. 2017, A&A, 603, A61

Eddington, A. S. 1937, The Observatory, 60, 99

Ehrenfreund, P., Boogert, A. C. A., Gerakines, P. A., et al. 1996, A&A, 315, L341

Ehrenfreund, P., Dartois, E., Demyk, K., & D'Hendecourt, L. 1998, A&A, 339, L17

Eistrup, C. & Walsh, C. 2019, A&A, 621, A75

Fayolle, E. C., Bertin, M., Romanzin, C., et al. 2011, ApJ Letters, 739, L36

Fayolle, E. C., Bertin, M., Romanzin, C., et al. 2013, A&A, 556, A122

Fedoseev, G., Chuang, K. J., Ioppolo, S., et al. 2017, ApJ, 842, 52

Fedoseev, G., Cuppen, H. M., Ioppolo, S., Lamberts, T., & Linnartz, H. 2015a, MNRAS, 448, 1288

Fedoseev, G., Ioppolo, S., Lamberts, T., et al. 2012, J. Chem. Phys., 137, 054714

Fedoseev, G., Ioppolo, S., Zhao, D., Lamberts, T., & Linnartz, H. 2015b, MNRAS, 446, 439

Fillion, J.-H., Dupuy, R., Féraud, G., et al. 2021, arXiv e-prints, arXiv:2103.15435

Fillion, J.-H., Fayolle, E. C., Michaut, X., et al. 2014, Far. Disc., 168, 533

Flagey, N., Goldsmith, P. F., Lis, D. C., et al. 2013, ApJ, 762, 11

Foner, S. N. & Hudson, R. L. 1962, J. Chem. Phys., 36, 2676

Fourikis, N., Takagi, K., & Morimoto, M. 1974, ApJ, 191, L139

Fourré, I., Matz, O., Ellinger, Y., & Guillemin, J. C. 2020, A&A, 639, A16

Fuchs, G. W., Cuppen, H. M., Ioppolo, S., et al. 2009, A&A, 505, 629

Gans, B., Peng, Z., Carrasco, N., et al. 2013, Icarus, 223, 330

Garrod, R. T. & Herbst, E. 2006, A&A

Garrod, R. T. & Pauly, T. 2011, ApJ, 735, 15

Garrod, R. T., Widicus Weaver, S. L., & Herbst, E. 2008, ApJ, 682, 283

Gerakines, P. A., Moore, M. H., & Hudson, R. L. 2004, ICARUS, 170, 202

Gerakines, P. A., Schutte, W. A., & Ehrenfreund, P. 1996, A&A, 312, 289

Gerakines, P. A., Schutte, W. A., Greenberg, J. M., & van Dishoeck, E. F. 1995, A&A, 296, 810

Gibb, E. L., Whittet, D. C. B., Boogert, A. C. A., & Tielens, A. G. G. M. 2004, ApJS, 151, 35

Gibb, E. L., Whittet, D. C. B., Schutte, W. A., et al. 2000, ApJ, 536, 347

Gillett, F. C. & Forrest, W. J. 1973, ApJ, 179, 483

Goesmann, F., Rosenbauer, H., Bredehöft, J. H., et al. 2015, Science, 349, 2.689

Gomis, O., Leto, G., & Strazzulla, G. 2004, A&A, 420, 405

Goto, M., Vasyunin, A. I., Giuliano, B. M., et al. 2021, A&A, 651, A53

Gratier, P., Pety, J., Guzmán, V., et al. 2013, A&A, 557, A101

Gredel, R., Lepp, S., Dalgarno, A., & Herbst, E. 1989, ApJ, 347, 289

Greenberg, J. M. 1983, Advances in Space Research, 3, 19

Gudipati, M. S. & Yang, R. 2012, ApJ, 756, L24

Guzmán, V. V., Goicoechea, J. R., Pety, J., et al. 2013, A&A, 560, A73

Guzmán, V. V., Pety, J., Gratier, P., et al. 2014, Faraday Discussions, 168, 103

Hagen, W., Allamandola, L. J., & Greenberg, J. M. 1980, A&A, 86, L3

Halfen, D. T., Ilyushin, V. V., & Ziurys, L. M. 2015, ApJ, 812, L5

Hama, T., Yabushita, A., Yokoyama, M., Kawasaki, M., & Watanabe, N. 2009a, J. Chem. Phys., 131, 114510

Hama, T., Yabushita, A., Yokoyama, M., Kawasaki, M., & Watanabe, N. 2009b, J. Chem. Phys., 131, 114511

Hama, T., Yokoyama, M., Yabushita, A., & Kawasaki, M. 2010, J. Chem. Phys., 133, 104504

Harada, N., Herbst, E., & Wakelam, V. 2010, ApJ, 721, 1570

Harich, S. A., Hwang, D. W., Yang, X., et al. 2000, J. Chem. Phys., 113, 10073

Harich, S. A., Yang, X. F., Yang, X., van Harrevelt, R., & van Hemert, M. C. 2001, , 87, 263001

Hartogh, P., Lis, D. C., Bockelée-Morvan, D., et al. 2011, Nature, 478, 218

Henderson, B. L. & Gudipati, M. S. 2015, ApJ, 800, 66

Herbst, E. & van Dishoeck, E. F. 2009, ARA&A, 47, 427

Hogerheijde, M. R., Bergin, E. A., Brinch, C., et al. 2011, Science, 334, 338

Hollenbach, D., Kaufman, M. J., Bergin, E. A., & Melnick, G. J. 2009, ApJ, 690, 1497

Hollenbach, D. J. & Tielens, A. G. G. M. 1997, ARA&A, 35, 179

Hollis, J. M., Lovas, F. J., Remijan, A. J., et al. 2006, ApJ, 643, L25

Hudgins, D. M., Sandford, S. A., Allamandola, L. J., & Tielens, A. G. G. M. 1993, ApJ Suppl. Series, 86, 713

Hudson, R. L. & Moore, M. H. 2004, ICARUS, 172, 466

Hudson, R. L., Moore, M. H., Dworkin, J. P., Martin, M. P., & Pozun, Z. D. 2008, Astrobiology, 8, 771

Ioppolo, S. 2010, PhD thesis, Surface formation routes of interstellar molecules (Leiden University)

Ioppolo, S., Cuppen, H. M., Romanzin, C., van Dishoeck, E. F., & Linnartz, H. 2008, ApJ, 686, 1474

Ioppolo, S., Cuppen, H. M., Romanzin, C., van Dishoeck, E. F., & Linnartz, H. 2010, PCCP (Inc. Far. Trans.), 12, 12065

Ioppolo, S., Fedoseev, G., Chuang, K. J., et al. 2021, Nature Astronomy, 5, 197

Ioppolo, S., van Boheemen, Y., Cuppen, H. M., van Dishoeck, E. F., & Linnartz, H. 2011, MNRAS, 413, 2281

Isokoski, K., Bossa, J. B., Triemstra, T., & Linnartz, H. 2014, PCCP, 16, 3456

Isokoski, K., Poteet, C. A., & Linnartz, H. 2013, A&A, 555, A85

Isokoski, K. M.-R. 2013, PhD Thesis, Physics and Chemistry of Interstellar Ice (Leiden University)

Jenniskens, P., Blake, D. F., & Kouchi, A. 1998, Amorphous Water Ice. a Solar System Material, ed. B. Schmitt, C. de Bergh, & M. Festou, Vol. 227, 139

Jensen, M. J., Bilodeau, R. C., Safvan, C. P., et al. 2000, ApJ, 543, 764

Jiménez-Serra, I., Vasyunin, A. I., Caselli, P., et al. 2016, ApJ, 830, L6

Jin, M. & Garrod, R. T. 2020, ApJS, 249, 26

Jo, S. K. & White, J. M. 1991, J. Chem. Phys., 94, 5761

Johnson, R. E. 1991, , 96, 17553

Johnson, R. E. & Quickenden, T. I. 1997, , 102, 10985

Johnson III, R. D. 1999

Jones, B. M., Bennett, C. J., & Kaiser, R. I. 2011, ApJ, 734, 78

Jørgensen, J. K., Belloche, A., & Garrod, R. T. 2020, ARA&A, 58, 727

Jørgensen, J. K., Favre, C., Bisschop, S. E., et al. 2012, ApJ, 757, L4

Jørgensen, J. K., van der Wiel, M. H. D., Coutens, A., et al. 2016, A&A, 595, A117

Kahane, C., Ceccarelli, C., Faure, A., & Caux, E. 2013, ApJ, 763, L38

Kaifu, N., Morimoto, M., Nagane, K., et al. 1974, ApJ, 191, L135

Kalescky, R., Kraka, E., & Cremer, D. 2013, J. Phys. Chem. A, 117, 8981

Kalvāns, J. 2015, ApJ, 803, 52

Kalvāns, J. 2018, MNRAS, 478, 2753

Kanda, K., Nagata, T., & Ibuki, T. 1999, Chemical Physics, 243, 89

Kim, Y. K., Irikura, K. K., Rudd, M. E., & Ali, M. A. 2014, Electron-Impact Ionization
    Cross Section for Ionization and Excitation Database (version 3.0)

Kimmel, G. A. & Orlando, T. M. 1995, , 75, 2606

Kinugawa, T., Yabushita, A., Kawasaki, M., Hama, T., & Watanabe, N. 2011, PCCP
    (Inc. Far. Trans.), 13, 15785

Kobayashi, K. 1983, J. Phys. Chem., 87, 4317

Kofman, V., He, J., Loes ten Kate, I., & Linnartz, H. 2019, ApJ, 875, 131

Koning, J., Kroes, G. J., & Arasa, C. 2013, J. Chem. Phys., 138, 104701

Lambert, H. M., Dixit, A. A., Davis, E. W., & Houston, P. L. 2004, J. Chem. Phys.,
    121, 10437

Lamberts, T., Cuppen, H. M., Ioppolo, S., & Linnartz, H. 2013, PCCP (Inc. Far.
    Trans.), 15, 8287

Lampe, F., Franklin, J., & Field, F. 1957, J. Am. Chem. Soc., 79, 6129

Larsson, B. & Liseau, R. 2017, A&A, 608, A133

Larsson, B., Liseau, R., Pagani, L., et al. 2007, A&A, 466, 999

Lattelais, M., Pauzat, F., Ellinger, Y., & Ceccarelli, C. 2010, A&A, 519, A30

Lee, J.-E., Lee, S., Baek, G., et al. 2019, Nat. Astron., 3, 314

Leto, G. & Baratta, G. A. 2003, A&A, 397, 7

Ligterink, N. F. W., Coutens, A., Kofman, V., et al. 2017, MNRAS, 469, 2219

Ligterink, N. F. W., Paardekooper, D. M., Chuang, K. J., et al. 2015, A&A, 584, A56

Ligterink, N. F. W., Terwisscha van Scheltinga, J., Taquet, V., et al. 2018a, MNRAS,
    480, 3628

Ligterink, N. F. W., Walsh, C., Bhuin, R. G., et al. 2018b, A&A, 612, A88

Linnartz, H., Ioppolo, S., & Fedoseev, G. 2015, Int. Rev. Phys. Chem., 34, 205

Liseau, R., Goldsmith, P. F., Larsson, B., et al. 2012, A&A, 541, A73

Liszt, H. & Lucas, R. 2001, A&A, 370, 576

Lo, J.-I., Lin, M.-Y., Peng, Y.-C., et al. 2015, MNRAS, 451, 159

Loomis, R. A., Cleeves, L. I., Öberg, K. I., et al. 2018, ApJ, 859, 131

Loomis, R. A., Zaleski, D. P., Steber, A. L., et al. 2013, ApJ, 765, L9

Lucas, M., Liu, Y., Bryant, R., Minor, J., & Zhang, J. 2015, Chem. Phys. Lett., 619, 18

Luna, R., Molpeceres, G., Ortigoso, J., et al. 2018, A&A, 617, A116

Luspay-Kuti, A., Mousis, O., Lunine, J. I., et al. 2018, Space Sci. Rev., 214, 115

Lykke, J. M., Coutens, A., Jørgensen, J. K., et al. 2017, A&A, 597, A53

Mackay, D. D. S. 1999, MNRAS, 304, 61

Maity, S., Kaiser, R. I., & Jones, B. M. 2014, Far. Disc., 168, 485

Martín-Doménech, R., Manzano-Santamaría, J., Muñoz Caro, G. M., et al. 2015a, A&A, 584, A14

Martín-Doménech, R., Manzano-Santamaría, J., Muñoz Caro, G. M., et al. 2015b, A&A, 584, A14

Martín-Doménech, R., Muñoz Caro, G. M., Bueno, J., & Goesmann, F. 2014, A&A, 564, A8

Martín-Doménech, R., Muñoz Caro, G. M., & Cruz-Díaz, G. A. 2016, A&A, 589, A107

Mason, N. J., Dawes, A., Holtom, P. D., et al. 2006, Far. Disc., 133, 311

Mathis, J. S., Mezger, P. G., & Panagia, N. 1983, A&A, 500, 259

McGuire, B. A. 2018, ApJS, 239, 17

Minissale, M., Dulieu, F., Cazaux, S., & Hocuk, S. 2016, A&A, 585, A24

Miyauchi, N., Hidaka, H., Chigai, T., et al. 2008, Chem. Phys. Lett., 456, 27

Mousis, O., Ronnet, T., Brugger, B., et al. 2016, ApJ, 823, L41

Mousis, O., Ronnet, T., Lunine, J. I., et al. 2018, ApJ, 858, 66

Muñoz Caro, G. M., Dartois, E., Boduch, P., et al. 2014, A&A, 566, A93

Muñoz Caro, G. M., Jiménez-Escobar, A., Martín-Gago, J. Á., et al. 2010, A&A, 522, A108

Muñoz Caro, G. M., Meierhenrich, U. J., Schutte, W. A., et al. 2002, Nature, 416, 403

Müller, B., Giuliano, B. M., Bizzocchi, L., Vasyunin, A. I., & Caselli, P. 2018, A&A, 620, A46

Mumma, M. J. & Charnley, S. B. 2011, ARA&A, 49, 471

Nazari, P., van Gelder, M. L., van Dishoeck, E. F., et al. 2021, A&A, 650, A150

Nguyen, T., Fourré, I., Favre, C., et al. 2019, A&A, 628, A15

Nishi, N., Shinohara, H., & Okuyama, T. 1984, J. Chem. Phys., 80, 3898

Notsu, S., van Dishoeck, E. F., Walsh, C., Bosman, A. D., & Nomura, H. 2021, A&A, 650, A180

Oba, Y., Miyauchi, N., Hidaka, H., et al. 2009, ApJ, 701, 464

Oba, Y., Tomaru, T., Lamberts, T., Kouchi, A., & Watanabe, N. 2018, Nat. Astr., 2, 228

Oba, Y., Watanabe, N., Kouchi, A., Hama, T., & Pirronello, V. 2010, ApJ, 712, L174

Öberg, K. I. 2009, PhD thesis, Complex processes in simple ices (Leiden University)

Öberg, K. I. & Bergin, E. A. 2021, Phys. Rep., 893, 1

Öberg, K. I., Boamah, M. D., Fayolle, E. C., et al. 2013, ApJ, 771, 95

Öberg, K. I., Boogert, A. C. A., Pontoppidan, K. M., et al. 2008, ApJ, 678, 1032

Öberg, K. I., Boogert, A. C. A., Pontoppidan, K. M., et al. 2011a, ApJ, 740, 109

Öberg, K. I., Bottinelli, S., Jørgensen, J. K., & van Dishoeck, E. F. 2010a, ApJ, 716, 825

Öberg, K. I., Fayolle, E. C., Cuppen, H. M., van Dishoeck, E. F., & Linnartz, H. 2009a, A&A, 505, 183

Öberg, K. I., Fraser, H. J., Boogert, A. C. A., et al. 2007a, A&A, 462, 1187

Öberg, K. I., Fuchs, G. W., Awad, Z., et al. 2007b, ApJ, 662, L23

Öberg, K. I., Furuya, K., Loomis, R., et al. 2015, ApJ, 810, 112

Öberg, K. I., Garrod, R. T., van Dishoeck, E. F., & Linnartz, H. 2009b, A&A

Öberg, K. I., Garrod, R. T., van Dishoeck, E. F., & Linnartz, H. 2009c, A&A, 504, 891

Öberg, K. I., Guzmán, V. V., Furuya, K., et al. 2015, Nature, 520, 198

Öberg, K. I., Linnartz, H., Visser, R., & van Dishoeck, E. F. 2009d, ApJ, 693, 1209

Öberg, K. I., Murray-Clay, R., & Bergin, E. A. 2011b, ApJ, 743, L16

Öberg, K. I., van Dishoeck, E. F., & Linnartz, H. 2009e, A&A, 496, 281

Öberg, K. I., van Dishoeck, E. F., Linnartz, H., & Andersson, S. 2010b, ApJ, 718, 832

Oka, A., Inoue, A. K., Nakamoto, T., & Honda, M. 2012, ApJ, 747, 138

Paardekooper, D. M., Bossa, J. B., Isokoski, K., & Linnartz, H. 2014, Rev. Sci. Instr., 85, 104501

Paardekooper, D. M., Bossa, J. B., & Linnartz, H. 2016a, A&A, 592, A67

Paardekooper, D. M., Bossa, J. B., & Linnartz, H. 2016b, A&A, 592, A67

Paardekooper, D. M., Fedoseev, G., Riedo, A., & Linnartz, H. 2016c, A&A, 596, A72

Paardekooper, D. M., Fedoseev, G., Riedo, A., & Linnartz, H. 2016d, A&A, 596, A72

Pagani, L., Bacmann, A., Cabrit, S., & Vastel, C. 2007, A&A, 467, 179

Pandya, S. H., Shelat, F. A., Joshipura, K. N., & Vaishnav, B. G. 2012, International Journal of Mass Spectrometry, 323-324, 28

Parise, B., Bergman, P., & Du, F. 2012, A&A, 541, L11

Pearson, K. 1895, Nature, 52, 317

Petrie, S., Millar, T. J., & Markwick, A. J. 2003, MNRAS, 341, 609

Pontoppidan, K. M., Boogert, A. C. A., Fraser, H. J., et al. 2008, ApJ, 678, 1005

Pontoppidan, K. M., van Dishoeck, E. F., & Dartois, E. 2004, A&A, 426, 925

Poteet, C. A., Pontoppidan, K. M., Megeath, S. T., et al. 2013, ApJ, 766, 117

Prasad, S. S. & Tarafdar, S. P. 1983, ApJ

Purcell, C. R., Balasubramanyam, R., Burton, M. G., et al. 2006, MNRAS, 367, 553

Qasim, D., Fedoseev, G., Chuang, K. J., et al. 2020, Nat. Astr., 4, 781

Rachid, M. G., Terwisscha van Scheltinga, J., Koletzki, D., & Linnartz, H. 2020, A&A, 639, A4

Raunier, S., Chiavassa, T., Marinelli, F., & Aycard, J.-P. 2004, Chemical Physics, 302, 259

Raut, U., Teolis, B. D., Loeffler, M. J., et al. 2007, J. Chem. Phys., 126, 244511

Ribeiro, F. d. A., Almeida, G. C., Wolff, W., et al. 2020, MNRAS, 492, 2140

Riddick, J. A., Bunger, W. B., & Sakano, T. K. 1986, Organic solvents: physical properties and methods of purification (John Wiley and Sons, New York, NY)

Rivilla, V. M., Martín-Pintado, J., Jiménez-Serra, I., et al. 2020, ApJ, 899, L28

Roux, J. A., Wood, B. E., Smith, A. M., & Plyer, R. R. 1980, Final Report, ARO, Inc., Arnold Air Force Station, TN.

Rubin, M., Altwegg, K., Balsiger, H., et al. 2019, MNRAS, 489, 594

Rubin, M., Altwegg, K., van Dishoeck, E. F., & Schwehm, G. 2015, ApJ, 815, L11

Ruscic, B. 2015, J. Phys. Chem. A, 119, 7810

Ruscic, B., Pinzon, R. E., Morton, M. L., et al. 2004, J. Phys. Chem. A, 108, 9979

Salahub, D. R. & Sandorfy, C. 1971, Chem. Phys. Letters, 8, 71

Satorre, M. Á., Domingo, M., Millán, C., et al. 2008, Planet. Space Sci., 56, 1748

Sayós, R., Oliva, C., & González, M. 2000, J. Chem. Phys., 113, 6736

Sayós, R., Oliva, C., & González, M. 2001, J. Chem. Phys., 115, 8828

Schmalzl, M., Visser, R., Walsh, C., et al. 2014, A&A, 572, A81

Schnepp, O. & Dressler, K. 1960, The J. of Chem. Phys., 33, 49

Schwell, M., Jochims, H.-W., Baumgärtel, H., & Leach, S. 2008, Chem. Phys., 344, 164

Shannon, R. J., Blitz, M. A., Goddard, A., & Heard, D. E. 2013, Nature Chemistry, 5, 745

Shen, C. J., Greenberg, J. M., Schutte, W. A., & van Dishoeck, E. F. 2004a, A&A

Shen, C. J., Greenberg, J. M., Schutte, W. A., & van Dishoeck, E. F. 2004b, A&A, 415, 203

Shingledecker, C. N., Tennis, J., Le Gal, R., & Herbst, E. 2018, ApJ, 861, 20

Shingledecker, C. N., Vasyunin, A., Herbst, E., & Caselli, P. 2019, ApJ, 876, 140

Shu, F. H., Adams, F. C., & Lizano, S. 1987, ARA&A, 25, 23

Sieger, M. T., Simpson, W. C., & Orlando, T. M. 1998, Nature, 394, 554

Sinnock, A. C. & Smith, B. L. 1968, Phys. Lett. A, 28, 22

Slanger, T. G. & Black, G. 1978, J. Chem. Phys., 68, 1844

Slanger, T. G. & Black, G. 1982, J. Chem. Phys., 77, 2432

Sleiman, C., González, S., Klippenstein, S. J., et al. 2016, PCCP (Incorporating Faraday Transactions), 18, 15118

Smith, R. G., Charnley, S. B., Pendleton, Y. J., et al. 2011, ApJ, 743, 131

Smith, R. S., May, R. A., & Kay, B. D. 2015, J. Phys. Chem. A B, 120, 1979

Smith, R. S., Petrik, N. G., Kimmel, G. A., & Kay, B. D. 2012, Acc. Chem. R., 45, 33

Snell, R. L., Howe, J. E., Ashby, M. L. N., et al. 2000, ApJ, 539, L101

Snow, T. 2013, Proc. IAU, 9, 3

Snow, T. P. & McCall, B. J. 2006, ARA&A, 44, 367

Snyder, L. E. & Bhul, D. 1971, in Bulletin of the American Astronomical Society, Vol. 3, 388

Solomon, P. M., Jefferts, K. B., Penzias, A. A., & Wilson, R. W. 1971, ApJ, 168, L107

Stief, L. J., Payne, W. A., & Klemm, R. B. 1975, J. Chem. Phys., 62, 4000

Suto, M. & Lee, L. C. 1985, , 90, 13,037

Taquet, V., Furuya, K., Walsh, C., & van Dishoeck, E. F. 2016, MNRAS, 462, S99

Teolis, B. D., Plainaki, C., Cassidy, T. A., & Raut, U. 2017, J. Geophys. Res. (Planets), 122, 1996

Terwisscha van Scheltinga, J., Ligterink, N. F. W., Boogert, A. C. A., van Dishoeck, E. F., & Linnartz, H. 2018, A&A, 611, A35

Theule, P., Borget, F., Mispelaer, F., et al. 2011, A&A, 534, A64

Theulé, P., Duvernay, F., Danger, G., et al. 2013, Adv. Space Res., 52, 1567

Thrower, J. D., Abdulgalil, A. G. M., Collings, M. P., et al. 2010, Journal of Vacuum Science Technology A: Vacuum Surfaces and Films, 28, 799

Tielens, A. G. 2005, The physics and chemistry of the interstellar medium (Cambridge University Press)

Tielens, A. G. G. M. & Hagen, W. 1982, A&A, 114, 245

van Broekhuizen, F. A., Keane, J. V., & Schutte, W. A. 2004, A&A, 415, 425

van Broekhuizen, F. A., Pontoppidan, K. M., Fraser, H. J., & van Dishoeck, E. F. 2005, A&A, 441, 249

van Dishoeck, E. F. 2014, Faraday Discuss., 168, 9

van Dishoeck, E. F., Kristensen, L. E., Mottram, J. C., et al. 2021, A&A, 648, A24

van Gelder, M. L., Tabone, B., Tychoniec, Ł., et al. 2020a, A&A, 639, A87

van Gelder, M. L., Tabone, B., Tychoniec, Ł., et al. 2020b, A&A, 639, A87

van Harrevelt, R. & van Hemert, M. C. 2008, J. Phys. Chem. A, 112, 3002

van Hemert, M. C., Takahashi, J., & van Dishoeck, E. F. 2015, J. Phys. Chem. A, 119, 6354

Vandenbussche, B., Ehrenfreund, P., Boogert, A. C. A., et al. 1999, A&A, 346, L57

Vastel, C., Ceccarelli, C., Lefloch, B., & Bachiller, R. 2014, ApJ, 795, L2

Vasyunin, A. I., Caselli, P., Dulieu, F., & Jiménez-Serra, I. 2017, ApJ, 842, 33

Vasyunin, A. I. & Herbst, E. 2013, ApJ, 769, 34

Vigren, E., Kamińska, M., Hamberg, M., et al. 2008, PCCP (Incorporating Faraday Transactions), 10, 4014

Walsh, C., Herbst, E., Nomura, H., Millar, T. J., & Weaver, S. W. 2014a, Far. Disc., 168, 389

Walsh, C., Loomis, R. A., Öberg, K. I., et al. 2016, ApJ, 823, L10

Walsh, C., Millar, T. J., & Nomura, H. 2010, ApJ, 722, 1607

Walsh, C., Millar, T. J., Nomura, H., et al. 2014b, A&A, 563, A33

Watanabe, N. & Kouchi, A. 2002, ApJ, 571, L173

Watanabe, N., Shiraki, T., & Kouchi, A. 2003, ApJ, 588, L121

Weast, R. C. 1972, Handbook of Chem. and Phys. 53rd ed., The Chem. Rubber Co.,
    26

Wen, J. & Thiemens, M. H. 1993, , 98, 12,801

Westley, M. S., Baragiola, R. A., Johnson, R. E., & Baratta, G. A. 1995a, Nature,
    373, 405

Westley, M. S., Baragiola, R. A., Johnson, R. E., & Baratta, G. A. 1995b,
    Planet. Space Sci., 43, 1311

Whittet, D. C. B., Bode, M. F., Longmore, A. J., et al. 1988, MNRAS, 233, 321

Whittet, D. C. B., Poteet, C. A., Chiar, J. E., et al. 2013, ApJ, 774, 102

Whittet, D. C. B., Smith, R. G., Adamson, A. J., et al. 1996, ApJ, 458, 363

Willacy, K. 2007, ApJ, 660, 441

Willacy, K. & Langer, W. D. 2000, ApJ, 544, 903

Willacy, K., Williams, D. A., & Minh, Y. C. 1993, MNRAS, 263, L40

Williams, J. P. & Cieza, L. A. 2011, ARA&A, 49, 67

Wilson, C. D., Mason, A., Gregersen, E., et al. 2003, A&A, 402, L59

Wolszczan, A. & Frail, D. A. 1992, Nature, 355, 145

Woodall, J., Agúndez, M., Markwick-Kemper, A. J., & Millar, T. J. 2007, A&A, 466,
    1197

Woodney, L. M., A'Hearn, M. F., Schleicher, D. G., et al. 2002, ICARUS, 157, 193

Yıldız, U. A., Acharyya, K., Goldsmith, P. F., et al. 2013, A&A, 558, A58

Zeng, S., Jiménez-Serra, I., Rivilla, V. M., et al. 2018, MNRAS, 478, 2962

Zeng, S., Quénard, D., Jiménez-Serra, I., et al. 2019, MNRAS, 484, L43

Zhen, J. & Linnartz, H. 2014, MNRAS, 437, 3190

Zheng, W., Jewitt, D., & Kaiser, R. I. 2006a, ApJ, 639, 534

Zheng, W., Jewitt, D., & Kaiser, R. I. 2006b, ApJ, 648, 753

Zheng, W., Jewitt, D., & Kaiser, R. I. 2007, Chem. Phys. Lett., 435, 289

Zhou, W., Wilkinson, L., Lee, J. W. L., Heathcote, D., & Vallance, C. 2019, Molecular
    Physics, 117, 3066

Zinnecker, H. & Yorke, H. W. 2007, ARA&A, 45, 481

Samenvatting

Ster- en planeetvorming

Tot 1992 was onze kennis van planeten beperkt tot de negen planeten die het zonnestelsel toen kende. Sindsdien is onze kijk revolutionair veranderd door de detectie van duizenden zogenaamde exoplaneten die hun banen rond andere sterren draaien. Deze exoplaneten hebben sterk verschillende eigenschappen in termen van grootte, temperatuur en samenstelling, geïllustreerd in Figuur 1. Onder hen bevinden zich ook planeten die op de aarde lijken: met een vergelijkbare rotsachtige samenstelling en een temperatuur die het mogelijk maakt om vloeibaar water vast te houden. In onze eigen Melkweg en in andere sterrenstelsels moeten er miljarden planeten zijn en daarom is het zeer waarschijnlijk dat de omstandigheden ook elders gunstig zijn geweest voor het ontstaan van leven.
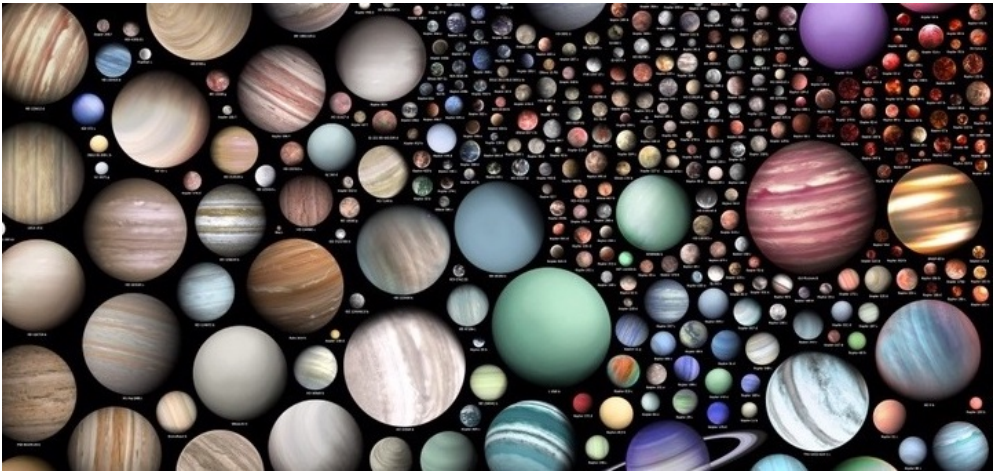
Figuur 1: Diversiteit van werelden. Nagemaakt met toestemming van de kunstenaar: Martin Vargic.

Om hierop verder in te kunnen gaan, is het belangrijk dat we de chemische evolutie van materie tijdens het proces van ster- en planeetvorming begrijpen. Deze vindt plaats in de ruimte tussen de sterren, beter bekend als het interstellaire medium (ISM). Het proces begint in diffuse interstellaire wolken die door hun eigen zwaartekracht ineenstorten waarbij donkere wolken ontstaan met daarin prestellaire kernen en protoplanetaire schijven. Uiteindelijk resulteert dit in de vorming van een jong stellair object (YSO) omringd door puin dat gas en stof omvat waaruit een of meer planeten kunnen ontstaan. Al het overgebleven materiaal wordt opgesloten in andere hemel-

lichamen, zoals kometen of asteroïden. Meer specifiek moeten we begrijpen hoe de
fysische omstandigheden langs dit evolutionaire spoor de chemische processen bepalen
die resulteren in stoffen die nodig zijn om leven te creëren, zoals we dat kennen, b.v.
kleine moleculen zoals water, maar ook complexere organische moleculen, waaronder
suikers en aminozuren.

Het ISM bestaat uit regio's die kunnen worden gekoppeld aan bepaalde stadia van
een stervormingscyclus. De relevante lokale fysische omstandigheden variëren flink in
dichtheid (10^2 - 10^6 deeltjes cm^{-3}), temperatuur (10 - 10^3 K) en blootstelling aan
verschillende soorten straling en deeltjes (kosmische straling, ultraviolette (UV) foto-
nen, vrije atomen en energetische elektronen). De massa van het ISM omvat vooral
gas (99%) en stof (1%). De gasfasecomponent wordt gedomineerd door waterstof
en helium, met slechts een kleine fractie (0,1%) zwaardere elementen (bijvoorbeeld
zuurstof, koolstof, stikstof). De stofkorrels zijn meestal gemaakt van silicaten of kool-
stofhoudend materiaal en dienen in koude gebieden als een oppervlak waarop atomen
en moleculen uit de gasfase kunnen vastvriezen (accretie). Dit leidt tot de vorming
van (meerdere lagen dik) interstellair ijs, dat een belangrijke rol speelt in de fysische
en chemische processen tijdens het proces van ster- en planeetvorming. Het evenwicht
in moleculaire abundanties tussen ijs- en gasfase wordt gecontroleerd door accretie- en
desorptieprocessen, en deze laatste worden veroorzaakt door een temperatuurstijging
(sublimatie), of via andere, niet-thermische processen: desorptie gestimuleerd door
absorptie van UV-fotonen (fotodesorptie), elektronen of het vrijkomen van energie na
een chemische reactie.

Het interstellaire stralingsveld, in het bijzonder in het vacuüm-UV (VUV) bereik,
speelt een tweezijdige rol in elk stadium van de stellaire evolutiecyclus. Het kan ervoor
zorgen dat moleculen fragmenteren (dissociatie), waarbij de resulterende fragmenten
reageren en de chemische complexiteit in het ijs vergroten (fotoconversie), of het ver-
oorzaakt een niet-thermische desorptie van ijsmantels (fotodesorptie). Dit proefschrift
beschrijft experimenteel onderzoek om de invloed van VUV-straling op interstellaire
ijs-analogen kwantitatief te bepalen. Onderwerpen die aan bod komen, richten zich
op de vorming van nieuwe complexe moleculen, nauwkeurige fotodesorptiesnelheden
en een verklaring voor de grote hoeveelheden moleculair zuurstofijs die worden aange-
troffen op kometen in ons zonnestelsel.

Interstellaire ijsjes

De identificatie van interstellaire ijscomponenten evenals een afschatting van de hoe-
veelheden waarin deze voorkomen is voornamelijk gebaseerd op infrarood (IR) ab-
sorptiespectroscopie. Moleculen die in het ijs aanwezig zijn, absorberen het licht dat
wordt uitgezonden door een achtergrondbron, zoals een protoster (of YSO), op mo-
lecuulspecifieke golflengten in het nabij- en ver-infraroodregime. Elk molecuul heeft
een reeks karakteristieke absorptiekenmerken. De volledige signatuur daarvan, wordt
een spectrum genoemd. Interstellaire ijsvorming wordt meestal waargenomen met te-
lescopen in de ruimte of hoog in onze atmosfeer, met ruimtetelescopen of vliegtuigen,
omdat waarnemingen vanaf de grond worden belemmerd door absorptie van atmosfe-
risch water (H_2O) en koolstofdioxide (CO_2). Twee telescopen die de vereiste infrarood
spectrale vensters hebben geopend, zijn de Infrared Space Observatory (ISO) en de
Spitzer Space Telescope (SST). De meest voorkomende componenten van interstel-
laire ijssoorten, zoals weergegeven in Figuur 2, omvatten: water (H_2O), koolstofdi-

oxide (CO_2), koolmonoxide (CO), methaan (CH_4), methanol (CH_3OH) en ammoniak (NH_3). Sommige andere bestanddelen komen minder vaak voor of zijn nog niet met volledige zekerheid toegekend (bijv. acetonitril, CH_3CN, moleculaire zuurstof, O_2). De verwachting is dat met de James Webb Space Telescope (JWST) nieuwe ijsbestanddelen zullen worden geïdentificeerd, mogelijk ook complexe organische moleculen. Dit laatste zou een belangrijke stap voorwaarts zijn om te bewijzen dat dergelijke soorten een vaste stof oorsprong hebben.
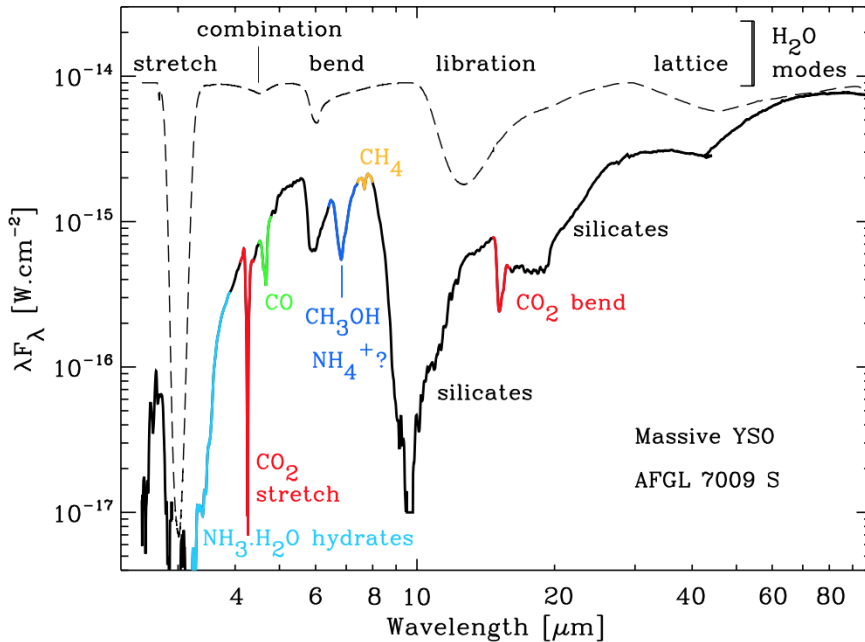
Figuur 2: Een ijsspectrum in de richting van de enorme YSO AFGL 7009S vastgelegd door ISO. De belangrijkste interstellaire ijscomponenten worden geïdentificeerd met de gemarkeerde moleculaire handtekeningen. Figuur gepubliceerd door Boogert et al. 2015.

De ijssamenstelling in regio's buiten het zonnestelsel wordt grotendeels afgeleid op basis van haar IR-spectra. Dichter bij de aarde, bv. voor het onderzoek naar de samenstelling van kometen, bestaan er alternatieven. De ruimtemissies *Giotto* en meer recentelijk *Rosetta* onderzochten respectievelijk de kometencomae van de kometen 1P/Halley (1P) en 67P/Churyumov-Gerasimenko (67P). De *Rosetta* missie volgde de komeet 67P, weergegeven in Figuur 3, langs zijn baan rond de zon, waarbij de uitstoot van gas en stof werd gemeten tijdens de verschillende fasen van zijn reis. De samenstelling van de vrijgekomen coma werd gebruikt om de samenstelling van de kern van de komeet te bepalen. Deze kan worden beschouwd als een grote vuile sneeuwbal, opgebouwd uit het meest oorspronkelijke materiaal dat in ons zonnestelsel voorhanden is. De metingen werden verricht met een massaspectrometer, de Rosetta Spectrometer for Ion and Neutral Analysis (ROSINA). Voor *in-situ* metingen biedt
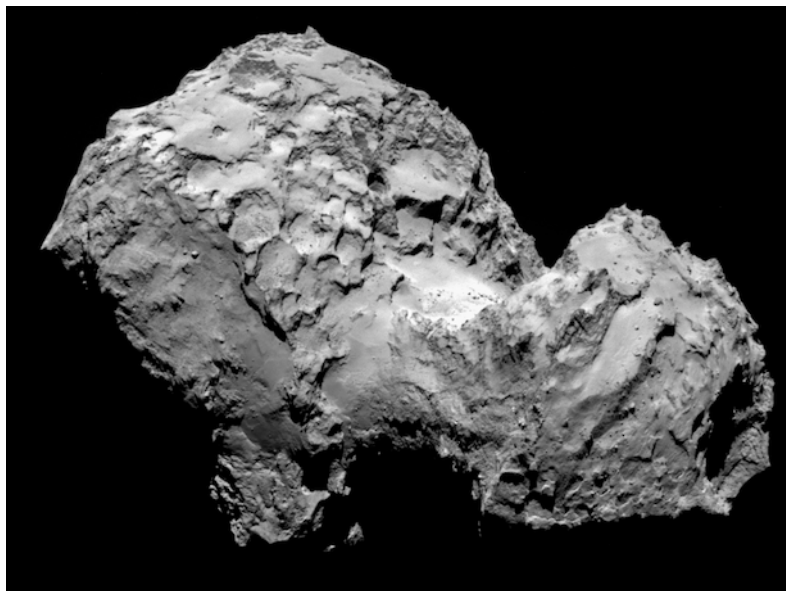
Figuur 3: Afbeelding van komeet 67P/Churyumov-Gerasimenko genomen tijdens de Rosetta-missie. Auteursrecht: ESA/Rosetta/MPS

massaspectrometrie een zeer competitief alternatief voor IR-ijsspectroscopie. De analyse van de gegevens van de *Rosetta*-missie resulteerde in een indrukwekkend aantal geïdentificeerde moleculen, een verdubbeling van het aantal eerder gedetecteerde komeetmoleculen (momenteel 66), inclusief kleine complexe organische moleculen (bijv. CH_3OH, CH_3CN), suikers (glycolaldehyde, $HC(O)CH_2OH$) en zelfs het eenvoudigste aminozuur (glycine, NH_2CH_2COOH). Ongeveer tweederde van de moleculen die in kometen zijn gedetecteerd, is eerder gedetecteerd in gebieden die verband houden met stervorming. Dit is in lijn met een scenario waarin de samenstelling van kometen (en planeetschijven) grotendeels is gekoppeld aan de chemische processen die plaatsvinden tijdens de vroege stadia van stervorming.

Een van de verrassende resultaten van de *Rosetta*-missie was de detectie van een grote hoeveelheid moleculaire zuurstof (O_2), op een niveau van 3% ten opzichte van H_2O ijs. De O_2/H_2O verhouding van 67P lag significant boven de verwachte gasfase verhouding in het interstellaire medium (ISM). Over de oorsprong van deze hoge kometaire O_2 abundantie wordt nog steeds gedebatteerd. Een van de besproken theorieën is dat het zuurstof zijn oorsprong vindt in de UV geïnduceerde dissociatie van water ijs. Dit kan echter niet observationeel worden geverifieerd, aangezien O_2 een homogeen diatomisch molecuul is, waardoor het bijna onzichtbaar is in het infrarood- en millimetergolflengteregime. In **Hoofdstuk 6** wordt experimenteel ingegaan op de mogelijkheid dat de hoge abundanties rechtstreeks te koppelen zijn aan de voorhanden hoeveelheden water op een komeet.

IJzige stofkorrels in de ruimte vormen een oppervlak waar moleculen 'accrete, meet and greet', dat wil zeggen waar ze vastvriezen, een moleculair reservoir vormen, en waar ze kunnen interageren, direct of na diffusie in het ijs. De ijsmantel ondersteunt de toename van chemische complexiteit op twee belangrijke manieren. Het fungeert als een ontmoetingsplek van gasfase-atomen en -moleculen, waar deeltjes een grotere

kans hebben om elkaar te ontmoeten (vergeleken met de gasfase). Bovendien fungeert het ijzige oppervlak ook als een derde lichaam dat het mogelijk maakt om energie die overblijft na een reactie te absorberen. Er zijn verschillende chemische triggers in het spel, die leiden tot de vorming van reactieve fragmenten in het ijs, en die onderverdeeld worden in zogenaamde 'niet-energetische' en 'energetische' processen. De niet-energetische worden aangedreven door opeenvolgende atoomadditiereacties. Zo zorgen atoomreacties tussen zuurstof- en waterstof atomen bv. voor de vorming van water. Dit soort reacties is dominant tijdens de vroege stadia van stervorming. De 'energetische' bewerking van ijs, veroorzaakt door de impact van kosmische straling, röntgenstralen, UV-fotonen of energetische elektronen, spelen een grotere rol in de latere stadia van stellaire evolutie. Deze processen worden in de volgende paragraaf kort samengevat.

Energetische processen

Verschillende vormen van energetische deeltjes (kosmische stralen, fotonen, elektronen) kunnen interageren met interstellair ijs. Figuur 3.1 (Hoofdstuk 3) toont een vereenvoudigd overzicht van mogelijke processen na VUV-fotolyse van interstellaire ijsanalogen. Onderzoek hiervan is relevant om zowel de fotofysische (bv. desorptie) en chemische (bv. vaste stof reacties) te begrijpen. Een molecuul in het ijs absorbeert een VUV-foton en wordt geëxciteerd. Deze energie kan worden gedeeld met de buren zonder dat dat een netto-effect heeft op het ijs, maar er zijn ook andere mogelijkheden. Het geëxciteerde molecuul kan uit het ijs ontsnappen naar de gasfase, of als de energie wordt overgedragen aan het naburige molecuul, kan dit leiden tot indirecte desorptie van dat naburige molecuul. Als alternatief kan het molecuul zijn energie gebruiken om te fotodissociëren in reactieve fragmenten. Deze fragmenten kunnen ook van het ijs desorberen, en in de gas fase reageren. Ten slotte kan de vorming van fragmenten ook resulteren in hun recombinatie tot nieuwe moleculen (fotochemie), die ofwel stabiliseren in het ijs danwel desorberen. Fotoconversie wordt gekenmerkt door een combinatie van fotochemie en reacties van geëxciteerde soorten met naburige moleculen. Beide soorten reacties bieden vormingsroutes van veel van de in het ISM waargenomen eenvoudige en complexe soorten.

De hierboven beschreven desorptieprocessen concurreren met fotoconversie van het ijs. In het ISM is desorptie vereist om de waargenomen gasfase-abundanties te verklaren en fotoconversie wordt gebruikt om vormingsroutes van verschillende soorten moleculen te verklaren, zoals alcoholen, suikers en de bouwstenen van het leven - aminozuren. De scheiding en kwantificering van deze concurrerende processen (fotodesorptie en foto- conversie) is een experimentele uitdaging voor puur ijs, en nog meer voor ijsmengsels. In dit proefschrift wordt deze uitdaging aangegaan.

Laboratorium Astrochemie

Een hoofddoel van astrofysische laboratoriumstudies is het vastleggen van spectrale vingerafdrukken van moleculen die het mogelijk maken die deeltjes te identificeren in de ruimte. Hiervoor worden bijzondere apparatuur gebruikt. Enkele decennia geleden, bestond een typisch laboratoriumsysteem om interstellaire ijsvorming te bestuderen,
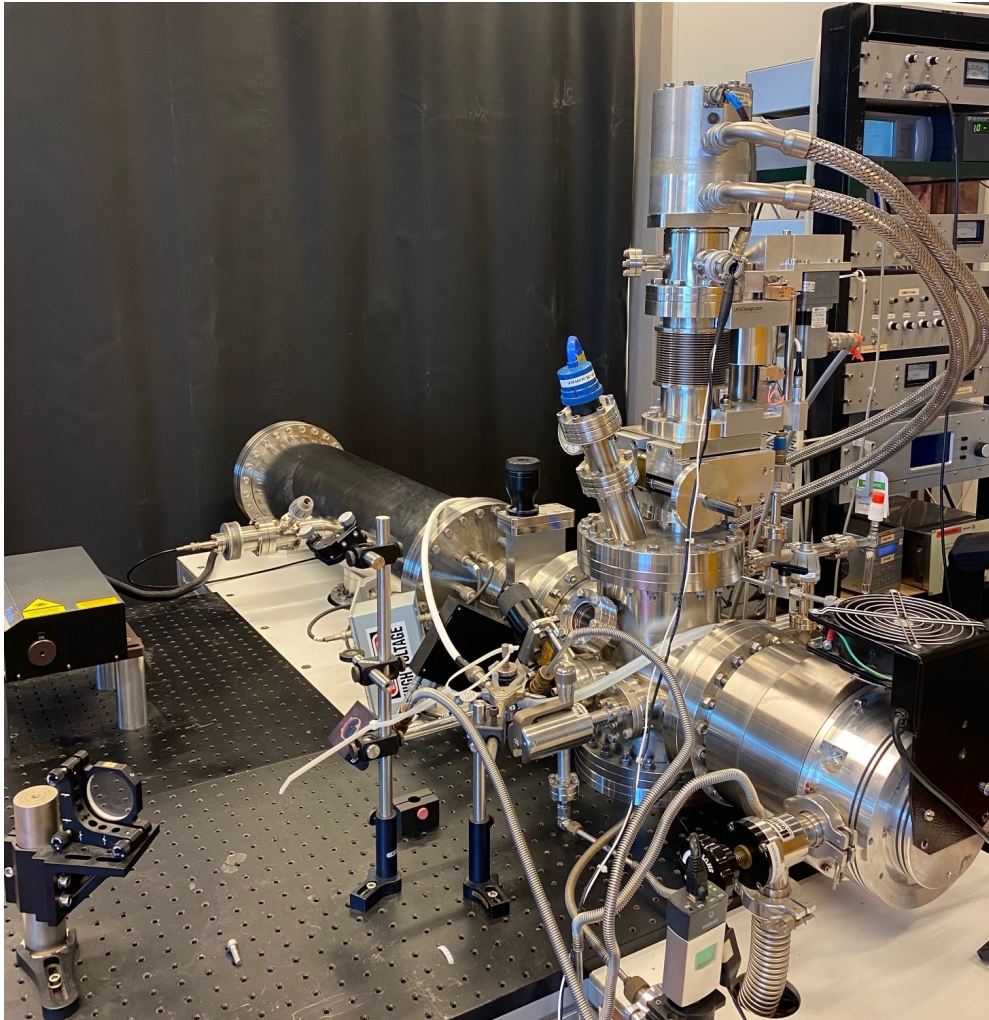
Figuur 4: Experimenteel systeem MATRI2CES in het Laboratorium voor Astrofysica in Leiden. Een gedetailleerde beschrijving wordt gegeven in **Hoofdstuk 2**.

uit een kamer onder hoog vacuüm (10^{-7} mbar, of 10^9 deeltjes cm^{-3}) met een tot 10 K afgekoeld substraat en een IR-spectrometer. In een dergelijk experiment werden, na afzetting van een puur of gemengd ijs, infraroodspectra van verschillende ijscomponenten opgenomen met behulp van een Fourier-transform-infraroodspectrometer (FTIR) en gebruikt voor interpretatie van waarnemingen, zoals weergegeven in Fig. 2. Tegenwoordig zijn deze systemen geüpgraded naar ultrahoog vacuüm (UHV) (10^{-10} mbar, 10^6 deeltjes cm^{-3}) en de UHV-omstandigheden maken het mogelijk ook dun ijs (enkele monolagen dik) te laten groeien, waarbij watervervuiling vanuit het achtergrondgas grotendeels kan worden uitgesloten. Dit levert nauwkeurigere spectra van ijssoorten op ter voorbereiding op de lancering van de James Webb Space Telescope, gepland voor eind 2021.

Sinds de identificatie van de belangrijkste componenten van het interstellaire ijs zijn dynamische studies uitgevoerd in laboratoria, waarbij de nadruk lag op de betrokken chemische processen in vaste toestand, bijvoorbeeld door ijsanalogen te bestralen met microgolfontladingswaterstoflampen (MDHL), een bron van VUV-straling, die lijkt op het UV-veld in de ISM. Fotoconversie van eenvoudige ijssoorten werd onderzocht en de vorming van nieuwe soorten tijdens de UV-fotolyse werd getraceerd, aanvankelijk vooral met behulp van IR-spectroscopie. In complexe ijsmengsels is deze techniek minder krachtig omdat de identificatie en kwantificering van soorten lijdt aan overlappende spectra van moleculen met een vergelijkbare samenstelling. Om deze reden wordt IR-spectroscopie vaak gebruikt in combinatie met massaspectrometrie, wat meer vertrouwen geeft in de interpretatie van data, vooral wanneer ook isotoop verrijkte stoffen worden gebruikt.

De resultaten van dit proefschrift zijn gebaseerd op experimenten met MATRI^{2}CES - Mass Analytical Tool for Reactions in Interstellar ICES, getoond in Fig. 4. Deze UHV- opstelling volgt een andere experimentele benadering om de samenstelling van het ijs kwantitatief te onderzoeken als een functie van VUV-bestraling bij lage temperaturen (tot 20 K). De meetsequentie wordt gestart met de desorptie van ijs met niet gefocusseerd laserlicht, hetgeen resulteert in een gasfasepluim die de samenstelling van het ijs vertegenwoordigt. De pluim wordt geanalyseerd in een time-of-flight massaspectrometer, die het mogelijk maakt om de soorten te scheiden op basis van hun moleculaire massa. Dit schema wordt Laser Desorptie Post Ionisatie Time-of-Flight Mass Spectrometry (LDPI TOF MS) genoemd, een ultra-gevoelige methode die het mogelijk maakt om tegelijkertijd de effecten van fotoconversie en fotodesorptiesnelheden te onderzoeken. Veel van het werk dat in de volgende hoofdstukken wordt beschreven, is alleen mogelijk geworden dankzij de experimentele mogelijkheden die MATRI2CES biedt. Deze opstellingen en de gevolgde meetprocedures worden in detail beschreven in **Hoofdstuk 2**.

Dit proefschrift

Dit proefschrift vat een aantal laboratoriumstudies samen die zich richten op de karakterisering van interstellaire ijsanalogen door vacuüm UV-straling. Dit werk is relevant om de processen te begrijpen die de chemische evolutie in het heelal bepalen voor verschillende stadia tijdens de vorming van sterren en planeten. Het beschrijft in detail fotodesorptie- en fotoconversieprocessen en draagt als zodanig bij aan wereldwijde inspanningen die gericht zijn op het begrijpen hoe chemie in de ruimte de moleculaire inventaris buiten onze dampkring bepaalt en daarmee ook de omstandigheden

waaronder het leven op aarde en mogelijk elders zou kunnen zijn begonnen. In dit proefschrift wordt het potentieel van UV-fotolyse van astronomisch relevante soorten in de vaste stof beschreven, als mogelijke voorlopers van chemisch complexe moleculen, en moleculen die als prebiotisch worden beschouwd (fotoconversie van H_2O en CH_3CN, **Hoofdstukken 4** en **6**). Parallel aan fotoconversie, activeert UV-fotolyse een niet-thermisch desorptiemechanisme dat, gekwantificeerd, bijdraagt aan de ijs-gasbalans in koude (en UV bestraalde) gebieden in het ISM (zie fotodesorptie van bijv. H_2O en CH_3CN, **Hoofdstukken 3** en **5**). De resultaten van deze hoofdstukken worden gebruikt als directe input voor astrochemische modellen, die het op hun beurt mogelijk maken om laboratoriumastrofysica en astronomische waarnemingen te koppelen.

List of Publications

1. *Effect of molecular structure on the infrared signatures of astronomically relevant PAHs*
Bouwman, J., Castellanos, P., **Bulak, M.**, Terwisscha van Scheltinga, J., Cami, J., Linnartz, H., Tielens, A. G. G. M., 2019, A&A 621, A80

2. *Novel approach to distinguish between vacuum UV-induced ice photodesorption and photoconversion. Investigation of CH_4, CH_3OH, and CH_3CN*
Bulak, M., Paardekooper, D.M., Fedoseev, G., Linnartz, H., 2020, A&A 636, A32

3. *Gas-phase infrared spectroscopy of the rubicene cation ($C_{26}H_{14}^{\bullet+}$). A case study for interstellar pentagons.*
Bouwman, J., Boersma, C., **Bulak, M.**, Tielens, A. G. G. M., Linnartz, H., 2020, A&A 636, A57

4. *Photolysis of acetonitrile in a water-rich ice as a source of complex organic molecules: CH_3CN and $H_2O{:}CH_3CN$ ices*
Bulak, M., Paardekooper, D.M., Fedoseev, G., Linnartz, H., A&A 647, (2021) A82

5. *Quantification of O_2 formation during UV photolysis of water ice - H_2O and $H_2O{:}CO_2$ ices*
Bulak, M., Paardekooper, D.M., Fedoseev, G., Chuang, K.-J., Terwisscha van Scheltinga, J., Eistrup, C., Linnartz, H., A&A, in press

6. *UV photodesorption and photoconversion rates of H_2O ice - measured with laser desorption post ionization mass spectrometry*
Bulak, M., Paardekooper, D.M., Fedoseev, G., Samarth, P., Linnartz, H., in preparation

7. *Inverse Kinetic Isotope Effect in Superdeuteration of Pentacene - A Possible Catalytic Pathway to Formation of Deuterium Enriched Interstellar Molecules*
Simonsen, F. D. S., Banhatti, S., **Bulak, M.**, Maddii Fabiani, L., Jaganathan, R., Wenzel, G., Thrower, J.D., Hornekær, L., in preparation

8. *Experimental toolbox of MATRI^{2}CES applied to interstellar ice analogues*
Bulak, M., Paardekooper, D.M., Fedoseev, G., Samarth, P., Bouwman, J., Chuang, K-.J., Linnartz, H., in preparation

About the author

Michał was born to Adam and Ewa Bulak on the 1st of January, 1992 in Zamość, Poland. Growing up, he spent most of the time between school and a local swimming pool. A decision to enroll into the I Społeczne Liceum Ogólnokształcące was made to accommodate for this duality. He continued to develop an inclination towards physics and mathematics as well as his passion for swimming. Upon high school graduation, both worlds, of science, and of sport, were equally exciting and promising. To continue the progress in both, he moved to the United States. At Missouri State University (MSU), he pursued a Bachelor degree in Science majoring in Applied Physics & Engineering, while being a member, and eventually a captain of a Division I swimming team. In 2015, as the swimming journey ran its course, he graduated with a Bachelor degree and science became his dominant passion, which has eventually turned into a career. Michał continued his education at MSU in the Master of Science program in Materials Science. During this period, he acquired experimental skills while working on a project with an astrophysical context. In his master's thesis he studied laboratory analogues of atmospheres of the hot rocky super-Earths. The acquired skillset combined with a thrill and satisfaction that comes from designing and running experiments, was a clear motivation to continue in this field. In 2017, Michał accepted a PhD position in the Laboratory for Astrophysics in Leiden, under supervision of Prof. dr. Harold Linnartz. The research project was focused on quantifying chemical and physical processes triggered upon an interaction of ultraviolet light with interstellar ice analogues. This thesis presents the PhD research results acquired over the last four years in Leiden. In his free time, Michał nurtures his connection to sports by coaching crossfit and weightlifting.

ACKNOWLEDGEMENTS

Looking back at the last four years at the Laboratory for Astrophysics, it seems like the time flew by. Yet, so much has happened and just as much has changed. This has been a time of personal and professional growth which are typically triggered by challenges along the way. To overcome these challenges, write this thesis, and become who I am today would not be possible without an incredible net of support from colleagues, friends and family. Here, I would like to express my gratitude and acknowledge by name those involved. If there are omissions (and there will be), please forgive me, and know it is not out of disregard.

Let me begin with taking a step back. The skills and background which made me eligible to apply for a PhD position in the first place, were largely developed during my time as a research assistant with Dr. Dave Cornelison. His message was to apply the attitude I had for swimming to science and the fun and results would follow. To this day I go by that rule, and I do not expect that will ever change. Lyle, I know you are always there. You have been an inspiration. Please don't change.

My PhD supervisor and promotor Prof. dr. Harold Linnartz made me feel welcome and placed his trust in me. Within reasonable boundaries, I had the freedom to explore the lab and work on my own terms. It took me a while to understand that this is how one becomes independent. Harold patiently forged my writing skills, which are still far from great, but believe me, I have come a long way. My co-promotor, Prof. dr. Xander Tielens. Thanks to you there was a balance between the lab and everything else. Besides invaluable scientific feedback, I truly appreciate you checking on how I was currently feeling.

Daniel, I wish our time in Leiden overlapped more. Without your support, knowledge, enthusiasm for science, and questions you asked me, I would not be able to complete all the projects. You should consider giving a course on how to efficiently work with your supervisors. Pushing the boundaries of Matrices was the most fun I had in the lab, and tuning the system to its current sensitivity was a mutually shared success. I sure hope you enjoyed it as well. Gleb, you were there along most of my journey. Multiple times, when in doubt, or too enthusiastic, you would steer me back to reason. Your bluntness, expertise and sentiment for the slavic culture made me enjoy your company while working together.

Jordy, you are a great scientist who also knows how to have fun. Please don't forget the latter. I learned tons from you, also by being around you. It would be a shame not to mention the fun we had with Pablo and Jeremiah, during and in between the FELIX shifts. I wish you and your family all the best in Colorado. Every lab scientist needs 'a martijn' - that's clear. More importantly, though, Martijn, you are a good spirit - I appreciate you, your attitude, and your passions, stay young forever.

The PhD in the lab cannot be done without a group with whom you exchange ideas, look for tools and solutions to problems, and after work, have a borrel. This

includes: Jeroen, Ko-Ju, Niels, Danna, Vincent, Kirstin, Thanja, Andreas, Marina, Sanjana, Nicolas, Yugu, Pranjal, Tara, Will, Carlos, Julia, Helgi. Pranjal, I trust that you can take care of the baby and I hope you embrace all the successes and challenges that come with it. Jeroen, you have redefined a few things for me, including, tidiness and attention to detail. I am grateful for your company during all the ups and downs of living and working together. Keep you attitude, and make sure to enjoy life.

It is impossible to be an astrochemist without a little bit of astronomy. Thank you, Ewine, for letting me join your group meetings. To the group members: Łukasz, Christian, Martijn, Sierk, Pooneh, Alice, Arthur, Merel, Alex, Benoit, thanks for coffee breaks, borrels and answering all my astronomy questions. Łukasz, together with Marta, you have been a grounding friendly Polish presence. I am cheering for you two and hoping to see you soon. Lydia, we have had a great connection since our first chat about sports. Thank you for being a patient friend. Keep growing! Dario, my companion from day one in Leiden. We went all over Europe together, we grew together, made memories for a lifetime, and we graduated (almost) together. Thank you for always being there. Cheering for you from across the big pond. Chris, how cool is that we have an article together? I hope you and Iris stick around. To all ESRs of the training network EUROPAH - what a group we are! I look back on all our trips with a big smile, and I wish you all the best along the professional and personal paths you have chosen.

Sports has opened up a lot of opportunities for me. A huge thank you to the crew from Crossfit 071 - Peter-Jan, Rob, all the coaches and friends. I owe you. You transformed the gym, from a place of excercise, to a place where I made friends and felt at home, away from home.

Mama, tata, dziękuje za wiarę we mnie i bezwarunkowe wsparcie. Nie ma mnie na miejscu, ale chcę żebyście wiedzieli że często jestem z wami myślami. Kilka lat temu, jak bylem w gimnazjum i w głowie miałem tylko pływanie, kto by pomyślał że będę robił doktorat z astrochemii? Ja na pewno nie... i wy pewnie też nie. Mimo że bez takich planów, okazało się że była to świetna przygoda. Waldi, Artur i Ania — dalej stopniowo do mnie dociera (albo już dotarło) jak ważne jest rodzeństwo i szczególna jest nasza więź. Cale szczęście że was mam, tacy przyjaciele od urodzenia. Każde z was dołożyło swoja cegiełkę. Dziadkowe i babcine mądrosci też zrobiły swoje. Pamiętam i dziekuję. Kocham was wszystkich bardzo!

At last, and the opposite of least, to my rock, Lisanne. You have brought so much energy, so much love, strength and activity to my life, I cannot see it any other way. You know it better than anyone, that you have pushed me through the last bit and supported me on all fronts, from listening to my astrochemistry presentations, to making sure that we have enough sweets to satisfy our cravings. This book is here thanks to you. Kocham Cię!

<div align="right">Michał Bulak</div>